Cranfield University

Luca Gallo

Design Space Exploration of Distributed Propulsion HALE UAVs Burning Liquid Hydrogen

School of Aerospace, Transport and Manufacturing

PhD Thesis

Cranfield University
School of Aerospace, Transport and Manufacturing
PhD Thesis

November 2015

Luca Gallo

Design Space Exploration of Distributed Propulsion HALE UAVs Burning Liquid Hydrogen

Supervisors: P. Laskaridis, R. Singh

Abstract

High altitude long endurance (HALE) unmanned aerial vehicles (UAV) could serve as a platform to promote disruptive aircraft technologies in addition to set the stage to sustain week-long flights with electronic equipment. Hydrogen fuel is essential to meet the long-endurance requirement of low-speed HALE UAVs due to its high energy content per unit mass—2.8 times greater than that of kerosene.

Hydrogen fuel could also be used to cryogenically cool the electric transmission system in a turbo-electric and/or hybrid-electric distributed propulsion system. This advanced propulsion system has the potential to affect all the aspects of a HALE UAV, from how much power is required to sustain flight to how power is produced, managed and distributed. However, in the literature there are no indications or design rules about how an integrated airframe/distributed propulsion system should be designed to maximise the integration synergies.

The aim of this research was to identify a multi-disciplinary and multi-fidelity methodology for design space exploration studies of distributed propulsion low-speed HALE UAVs burning liquid hydrogen. The purpose of this methodology was to assess how the aircraft power requirement, production, management, and distribution are affected by the airframe selection, the distributed propulsion system and the energy management system.

The results indicate that the slipstream-wing interaction of distributed propellers could increase the maximum endurance by nearly 60% on a tube-and-wing airframe for a given engine cycle. Superconductivity was assumed for the hydrogen-cooled electric transmission system that links the core engine to the distributed propulsors. These endurance benefits were three to four times greater than that of the series-hybrid energy management strategy and of the wave rotor hybrid cycles. As such, the distributed propellers technology should be furthered investigated for both low-speed HALE UAVs and other low-Mach applications.

Acknowledgements

I once read in a book that very few people succeed entirely on their own. Needless to say, I came to the same conclusion that the author reached: I am no exception.

First of all, I would like to thank Prof Pericles Pilidis, Prof Riti Singh, and Dr Vassilios Pachidis for giving me the opportunity to conduct this research project. I am very grateful to them for they trusted that I could strive besides the many uncertainties of such a forward-looking project.

This work could have not been completed without the constant support of my supervisor Dr Panos Laskaridis. He set very ambitious targets from the beginning of this project, which had a great influence on the final outcome of this research. I really appreciated being encouraged in any aspect of this PhD, from applying to the Coachmakers Eric Beverly Award to joining the 2015 SAE Aero Tech conference in Seattle. The light at the end of the tunnel might have been another train approaching without his contribution.

My officemate Dr Eduardo Anselmi Palma immensely affected the outcome of this research. His endless knowledge about nearly any engineering subject has been an invaluable help throughout my PhD. Notably, he always shared a word of encouragement even in the most difficult moments of my journey. His friendship is certainly a privilege.

A sincere thanks also goes to the "small army" of MSc students that supported this research project: Mauro Righi, Thibaut Le Boulaire, Marcel Roig Medina, Manuel Furlanello, Jose Romero Trinidad Arechiga, and Miguel Angel De La Cruz Arevalo. They helped me to expand the scope of this research well beyond what I could have ever imagined at the beginning of my PhD. I could not have done it without them. Ultimately, I learnt from them more than what they learnt out of my guidance throughout their MSc projects.

I cannot forget to thank Guillermo Guevara Nieto for his invaluable friendship and guidance in the last three years. The impact that he had on my life and on this research project simply cannot be expressed with words. Thank you for constantly reminding me that *"our Lord has plans to prosper us and not to harm us, to give us a future filled with hope"* (Jeremiah 29:11).

A very special acknowledgement goes to my beloved Cheng Meifang, who made this journey a lot easier. Thank you for your immeasurable patience in the last three years, and for never doubting of my abilities to complete this PhD and beyond.

Last, but not least, I would like to thank my family, and my parents in particular, who encouraged me to be part of an educational environment where my talents could shine. I will always be grateful for their support in every single idea, desire, and ambition I have tried to turned into reality.

Contents

List of Figures

List of Tables

Nomenclature

Abbreviations

APU	Auxiliary Power Unit
AR	Aspect Ratio
BWB	Blended Wing Body
CFD	Computational Fluid Dynamics
COT	Combustor Outlet Temperature
DOC	Direct Operating Cost
DoH	Degree of Hybridisation
DP	Distributed Propulsion
ESAR	Energy Specific Air Range
FAR	Fuel to Air Ratio
GT	Gas Turbine
HE	Hybrid Electric
HEV	Hybrid Electric Vehicle
LE	Leading Edge
LHV	Lower Heating Value
LRMLI	Load Responsive Multilayer Insulation
MLI	Multilayer Insulation
OPR	Overall Pressure Ratio

PEFC	Polymer Electrolyte Fuel Cell
PEN	Positive-Electrolyte-Negative
PR	Pressure ratio
RC	Resistor-Capacitor network
RF	Reverse-flow wave rotor
SFC	Specific Fuel Consumption
SOC	State Of Charge, battery
SOFC	Solid Oxide Fuel Cell
T&W	Tube and Wing airframe
TET	Turbine Entry Temperature
TF	Through-flow wave rotor

Greek Symbols

β	Activation overpotentials symmetry factor
Δg	Variation of Gibbs free energy
Δ	Difference between two values
ϵ	Insulation layer emissivity or wave rotor bypass flow
η	Efficiency
η_{act}	Fuel cell activation overpotential
η_{conc}	Fuel cell concentration overpotential
η_{ohm}	Fuel cell ohmic overpotential
γ	c_P/c_V
γ_{anode}	Anode pre-exponential coefficient for exchange current density calculations
$\gamma_{cathode}$	Cathode pre-exponential coefficient for exchange current density calculations

Λ_{inner}	Inner wing leading edge sweep
Λ_{LE}	Wing leading edge sweep
Λ_{outer}	Outer wing leading edge sweep
μ	Propeller velocity ratio, defined as V_0/V_{jet}
Φ	Hybrid system supplied power ratio
ϕ	Hybrid system activation ratio
ρ	Material density or resistivity or battery pack energy density (kW/kg)

Latin Symbols

$\overline{w}$	Hybrid system power control factor
$\bar{c}$	Mean wing chord
$\mathcal{F}$	Faraday constant
$\mathcal{f}$	Molar flow
$\mathcal{h}$	Molar enthalpy
$\mathcal{Q}$	Heat
$\mathcal{R}$	Ideal gas constant
$\overline{V_V}$	Vertical tail volume coefficient
$\overline{V}$	Horizontal tail volume coefficient
C_f	Flat-plate skin friction coefficient
C_l	Lift coefficient
C_P	Propeller power coefficient
c_P	Specific heat at constant pressure
C_T	Propeller thrust coefficient
c_V	Specific heat at constant volume
$C_{battery}$	Battery pack capacity

C_{d0}	Parasite drag coefficient
C_{di}	Lift-induced drag coefficient
E_{act}	Activation energy
f_a	Wing average allowable direct stress level
M_r	Mass of the wing ribs
n_g	Insulation interstitial gas exponent
N_t	Insulation layer density (layers/cm)
N_{fus}	Fuselage slenderness ratio, defined as fuselage length upon fuselage radius
S_H	Horizontal empennage surface area
S_V	Vertical empennage surface area
U_a	SOFC air utilisation factor
U_f	SOFC fuel utilisation factor
V_0	Aircraft flight speed
V_D	Aircraft design maximum diving speed
W_{el}	Electrical power
A	Area
B	Maximum fuselage width
b	Wing span
C	Coefficient
D	Mass of the wing spars
E	Open circuit voltage or energy
e	Oswald span efficiency factor
F	Wing penalty mass due to secondary and miscellaneous items
f	Fuel-to-air ratio

FF	Form factor
g	Gravitational acceleration
H	Maximum fuselage height
h	Enthalpy
i	Fuel cell current density
J	Propeller advance ratio
K	Drag-due-to-lift factor
k	Thermal conductivity
L	Length
l	Length or distance from the aircraft nose
M	Mass or Mach number
N	Number of insulation layers
Nu	Nusselt number
P	Power
Q	Interference factor
q	Heat flux
R	Electrical resistance or universal gas constant
r	radius
S	Surface area
s	Distance
T	Thrust or temperature
t	Time
V	Volume or voltage
v	Velocity

W	Mass flow
w	Wing loading, defined as take-off weight upon wing area
x	Molar fraction

Subscripts and Superscripts

H_2	Hydrogen
0	Flight conditions
3	After wave rotor expansion to the turbine-exhaust port
A	After wave rotor compression, it refers to the mixture of fresh air and hydrogen fuel
B	After wave rotor combustion, it is the highest-temperature point of the cycle
comp	compressor
iso	isolated wing, which refers to only the part of the wing immersed in the slipstream when modelled as if it was an isolated platform immersed in the freestream flow
jet	slipstream jet properties
no prop	unaffected by the propeller slipstream, or clean wing conditions
prop	affected by the propeller slipstream
rA	After wave rotor compression, it refers to the residual gases from the previous combustion
rotor	wave rotor
static	static conditions, namely no forward speed or null flight speed
V	Vertical
w,jet	wing immersed in the slipstream jet
wj	wing immersed in the slipstream jet

Chapter 1

Introduction

The aerospace industry has undergone distinctive advances in the past decades, which have influenced many other industry sectors. Novel and disruptive technologies have been nurtured by a very competitive market, and creative thinking will be the sovereign strategy towards the sustainable development of aviation. The by-product of innovation is yet risk, and taking a gamble would be an unfortunate option: billions of human lives—as well as trillions of pounds—have to be cushioned from it. Pilotless aircraft, nonetheless, could be the stepping stone to make change permeate to the aviation industry by safeguarding it at the same time. Unmanned systems could serve as a platform to promote disruptive technology and set the stage to sustain week-long flights with electronic equipment.

The idealistic notion of a carbon-free aviation business could become reality thanks to the use of hydrogen as a fuel. Cryogenic storage ($-250°C$) is required to pack an otherwise bulky gaseous fuel into a flying machine, which poses practical and budgetary challenges. Preserving the environment, however, is an overriding requirement that cannot be subordinated to cost. The high specific energy of hydrogen is its added value as experience suggests that it is possible to carry only a finite amount of fuel. A power source that contains nearly three times more energy than kerosene would then be favourable to fly for a lengthy period of time.

Today's air transport is constrained by noise regulations, which restrict night flights and hinder the use of local aerodromes and the opening of new airports. Rotating blades are one of the main sources of disturbance, particularly the turbine-driven fan as it is placed at the face of the engine. The vibrations produced by a compressing device such as a fan are proportional to the extent to which the air is

compressed, i.e. its pressure ratio. This in turn depends on the speed at which it rotates. The very low pressure ratio required to minimise noise can only be achieved by means of a slow-rotating fan, which is unhappily coupled with a compact and fast-spinning turbine. An intermediate rotational speed has to be chosen to compromise between the two, which guarantees adequate fuel consumptions at the expense of a noisier engine. Within a distributed propulsion system, however, multiple propulsors are driven by electric motors and are decoupled from the turbine to spin at the most favourable speed. Electric power is produced by the gas turbine, which is linked to the fans by an electrical network. Unmanned systems in particular benefit from this configuration as the engine has to act as a power source for the electronic equipment. This requires a power that is of the same magnitude as the energy that is needed to propel the aircraft.

1.1 Research aims and project specifications

The aim of this research is to explore the potential of novel and disruptive technologies and the benefits offered by their close interaction. An example of the latter is the synergy between liquid hydrogen and distributed propulsion. In fact, the electrical network that links the gas turbine to the fans has to let the current flow nearly in the absence of any energy loss. Some substances, often called superconductors, have the property of zero electrical resistance when they are cooled at very low temperatures. Thus, the very-low-temperature hydrogen that is necessary for airborne storage can also be used to cool the superconductors required by a distributed propulsion system.

The following specifications were considered for the present low-speed HALE UAV application:

- Loiter altitude 50,000 ft
- Loiter Mach 0.3 – 0-2
- Target endurance 7 – 10 days
- Payload weight 800 kg
- Payload power 200 kW
- Expected life 10 years

It is worth noticing that the payload weight is four to five times heavier than that of existing low-speed HALE UAVs. Also, the payload secondary power requirement is unusually big and it is comparable to that of a large turbofan engine. The aircraft expected life was limited to 10 years as it constrained by that of the on-board advanced electronics.

1.2 Contribution to knowledge

The design space exploration of distributed propulsion HALE UAVs burning liquid hydrogen represents the contribution to knowledge of the present PhD thesis. In the literature there are no indications or design rules about how an integrated airframe, distributed propulsion, and energy management system should be designed to maximise the integration synergies. There are also many uncertainties on what are the variables that mostly influence the design and performance of the integrated aircraft system. As such, the multi-disciplinary and multi-fidelity methodology that was built can fill the knowledge gap present in the literature.

In addition to the methodology, the design space exploration study benchmarks technological advancements in areas that are usually not comparable. The power requirement benefits of advanced airframes were compared to those of the power production, management and distribution offered by unconventional engine cycles, battery technology, energy management strategies, and distributed propulsors—both fans and propellers were considered. Thus, the comparison of the benefits and penalties of dealing with aircraft technologies of a different nature also represents a contribution to knowledge.

1.3 Thesis structure

The present thesis comprises nine chapters and three appendixes:

- **Chapter 1 – Introduction** The research background and aims are presented along with the contribution to knowledge.
- **Chapter 2 – Literature Review** The brief introduction to HALE UAVs is followed by a review of the most significant studies on hydrogen fuel and distributed propulsion.

- **Chapter 3 – Multi-disciplinary and Multi-fidelity Methodology** The integrated airframe, distributed propulsion, and energy management methodology is explained along with the details of the integration synergies between hydrogen fuel, the airframe, and distributed propulsion.
- **Chapter 4 – Aircraft Conceptual Design** The aircraft conceptual design methodology that was built for endurance aircraft is presented, along with a design and performance comparison of conventional and disruptive airframes.
- **Chapter 5 – Wave Rotor Hybrid Cycles** The benefits of hybrid wave rotor gas turbine hybrid cycles are investigated at an aircraft level.
- **Chapter 6 – Solid Oxide Fuel Cell Hybrid Cycles** The benefits of hybrid solid oxide fuel cell gas turbine hybrid cycles are investigated at an aircraft level.
- **Chapter 7 – Energy Management** The influence of the series-hybrid and climb-and-glide energy management strategies on the design and performance of the present HALE UAV are investigated.
- **Chapter 8 – Distributed Propellers** The distributed propellers slipstream-wing interaction is assessed to enhance the design and performance of long endurance unmanned aircraft.
- **Summary and Conclusions** The main conclusions of the present research project are presented.
- **Appendix A** The limitations of the take-off mass build-up approach for endurance aircraft are assessed.
- **Appendix B** The assumptions on the core engine and distributed fans size and weight are exposed, which are used throughout the thesis.
- **Appendix C** The specifications of the electric system architecture are presented, along with a critical review of why superconductivity was assumed for the present project.

A distributed propulsion HALE UAV comprises three main areas of analysis: the airframe, the distributed propulsion system, and the energy management system. Their mutual interactions affect the integrated system power requirement, production, management and distribution. As such, the main chapters of the thesis— from 4 to 7—were grouped into three parts:

- **Power requirement** Chapter 4, Aircraft Conceptual Design
- **Power production** Chapters 5 and 6, Wave Rotor and Solid Oxide Fuel Cell Hybrid Cycles
- **Power management and distribution** Chapters 7 and 8, Energy Management and Distributed Propellers

Chapter 2

Literature Review

2.1 Low-speed HALE UAVs

High altitude long endurance (HALE) aerial vehicles have been the focus of significant research and development efforts for decades [Nickol et al. 2007]. They offer the potential to be used for both civil and military applications, from surveillance and reconnaissance to communication relay and fire detection. Satellites and lighter-than-air-aircraft are the direct competitors of HALE UAVs, but their usefulness is limited by low manoeuvrability, slow transit speeds and limited observation envelopes.

Satellites in particular deny the flexibility to change the on-board equipment according to the mission, and modifying their orbit is often impossible and always time-consuming, complex, and expensive. On the other hand, lighter-than-air-aircraft are slow-moving machines, which makes them vulnerable to hostile actions and incapable of all-weather operations [Jenkinson and Marchman 2003]. Unmanned platforms have the potential to overcome these constraints by providing measurements that complement the current space and ground based systems.

As declining budgets are the main concern in the defence sector [Roland Berger 2013], it is not surprising that the UAV market is expected to grow by more than 60% of the 2012 reference value up to the $7.31 billion forecast for the 2020 [Wilson 2013]. The United States and Israel are currently the biggest players, and Europe is expected to show the highest growth.

Previous low-speed HALE UAV designs are usually characterised by a high-aspect ratio wing, between 22 and 34 [Altman 2000], which is required to minimise lift-induced drag at low air densities and low Mach numbers. However, this results in an aircraft empty mass penalty as the overall aircraft structures can be as heavy as 40% of its take-off mass [Jenkinson and Marchman 2003].

The Boeing Phantom Eye (fig. 2.1) and the Aerovironment Global Observer (fig. 2.2) are recent examples of low-speed HALE UAVs. Both designs rely on liquid hydrogen as a primary fuel, whose high energy content per unit mass becomes a necessity to achieve an endurance of four to seven days with payloads of five to ten per cent of their take-off mass. Although hydrogen fuel has a low energy content per unit volume, its drag penalty is partially offset by the low air density due to the high-altitude requirement.

Figure 2.1: Boeing Phantom Eye

Figure 2.2: Aerovironment Global Observer

2.2 Hydrogen as an aviation fuel

The present section reviews the most significant studies on hydrogen as an aviation fuel. An introduction to the most attractive applications for hydrogen fuel is initially presented (sect. 2.2.1), where the focus is mostly on the outcome of the studies from an aircraft performance perspective (i.e. energy consumption). This is then supported by the influence of hydrogen fuel on both the aircraft design (2.2.2) and

the propulsion system (sect. 2.2.3), as both effects determine the final aircraft performance. A remark is also made on the environmental implications of hydrogen as an aviation fuel (sect. 2.2.4).

It was the author's choice not include more information on many other aspects of hydrogen as an aviation fuel. In fact, the present research mainly quantifies the performance benefits of hydrogen as a fuel for low-speed HALE UAVs. However, a more thorough review should include—just to mention a few—aspects such as hydrogen production, storage, and the overall aircraft and infrastructure economics.

2.2.1 Attractive applications

Brewer investigated the use of hydrogen as an aviation fuel in the 1960s and 1970s at the Lockheed company [Brewer 1991]. He showed that hydrogen fuel would become a necessity for hypersonic reconnaissance applications (Mach > 5). The calculations showed that at hypersonic speeds the airframe could only be cooled with a cryogenic coolant given the tremendous cooling requirement. In addition, only hydrogen fuel would provide enough energy per unit time to sustain flight due to the hypersonic thrust requirement. However, the hypersonic studies were later abandoned as satellites became available.

Brewer also found out that hydrogen fuel would provide benefits for supersonic aircraft. Conceptual design calculations showed that the overall mission energy requirement would reduce when hydrogen fuel is used (sect. 2.2.2). However, the same benefits were not found for the subsonic transport case. This is due to the interaction of many effects on both the airframe (sect. 2.2.2) and the propulsion system (sect. 2.2.3).

In the early 2000s, the European Cryoplane project looked at the use of hydrogen as an aviation fuel for commercial subsonic applications [Cryoplane 2003]. The study, which involved several industrial and academic institutions throughout Europe, was structured in working packages that covered issues from aircraft conceptual design for hydrogen integration to how the engine performance, the emissions, and the overall economics would be affected. The main conclusion of the study is that hydrogen would not be convenient neither to save fuel/energy nor to the economics. In addition, hydrogen fuel becomes more and more attractive as the mission range is increased.

On the other hand, in 2009 Verstraete found benefits for a longe range (4,000 nm) mission on a 380-passenger aircraft [Verstraete 2009]. A 7.6% energy saving could be achieved by re-designing the fuselage to accommodate hydrogen fuel compared to the kerosene baseline. The study also included the effect that hydrogen fuel has on the engine performance (sect. 2.2.3).

The diverging outcomes of the last two studies highlight that the attractiveness of hydrogen fuel heavily depends on the assumptions of the study. It is generally not possible to thoroughly compare the studies assumptions as not all of them are made available. However, it is also clear that the more recent the study the more likely it is that benefits can be found due to technology advancements.

The public domain information on the attractive applications for hydrogen fuel can be summarised by the following quote from Brewer [Brewer 1991]:

"Naturally, the more fuel required for an aircraft to fly its design mission, the more opportunity there will be for the better fuel to display its advantage."

This is why hydrogen as an aviation fuel is attractive for long-endurance applications.

2.2.2 Aircraft considerations

Hydrogen as a fuel has the potential to lighten the aircraft take-off mass and to reduce its direct operating cost. The mission energy consumption, defined as the mission fuel burn times its lower heating value, would also be affected as the storage of bulky hydrogen results in a drag penalty.

The aircraft take-off mass reduces when hydrogen fuel is used to replace kerosene for a given missions requirement [Brewer 1991; Verstraete 2009; Westenberger 2003]. This effect can be captured even in the early stages of the aircraft conceptual design. Hydrogen fuel has an energy content per unit mass that is three times greater than that of kerosene. Thus, for a given mission energy less fuel mass needs to be stored, so that the aircraft can be downsized and its take-off mass reduced.

The wing area reduces as the aircraft take-off mass reduces—for a given wing loading. This results in a lighter wing structural mass, which has a positive effect on fuel consumption. However, all the public domain studies report that the hydrogen tanks are so heavy that the overall aircraft empty mass increases. In fact, the tank

mass increases more than the structural mass reduces.

The hydrogen low energy content per unit volume results in a drag penalty as the fuselage needs to be oversized. This effect more than counteracted the lighter aircraft take-off mass—from an energy consumption perspective—in the Cryoplane study [Westenberger 2003]. Although not explicitly highlighted in the study, it should be noticed that a non-negligible contribution on the aircraft performance also comes from the heavier aircraft empty mass due to the hydrogen tanks.

Top-level conceptual design studies [Verstraete 2009] as well as detailed design studies [Cryoplane 2003] highlighted that the hydrogen drag penalty and the weight of its tanks can more than offset the reduced take-off mass effect. However, hydrogen fuel should still be attractive for low-speed HALE UAVs as the drag penalty would not be as significant as for civil aircraft due to the high altitude requirement. In addition, similarly to the hypersonic-aircraft application using hydrogen fuel should be a necessity to achieve a very long endurance due to its high energy content per unit mass.

Verstraete also looked at the direct operating cost (DOC) of hydrogen-fuelled commercial aircraft [Verstraete 2009]. The author concluded that the DOC of hydrogen fuelled aircraft is lower than that of kerosene aircraft due to the lighter take-off mass. This is because the equations that were used to assess the DOC relate this parameter to the aircraft mass. It is true that acquiring and operating a lighter aircraft is beneficial from a cost perspective. However, no conclusion on the economics of a hydrogen aircraft should be drawn unless the hydrogen production and distribution costs are considered.

Hydrogen fuel needs to be produced by means of steam methane reforming and then liquefied. Even by including economies-of-scale effects, the hydrogen production and distribution cost would still be higher than that of kerosene for commercial applications. Thus, only by means of regulations (e.g. carbon tax) that "artificially" increase the price of kerosene would hydrogen become attractive [Westenberger 2003]. This may not be necessarily true for military UAVs, however, where the cost of transporting kerosene to the front line may be as significant as that of locally producing hydrogen.

2.2.3 Engine considerations

A hydrogen-fuelled gas turbine, when compared to the kerosene case, offers benefits such as reduced combustion chamber cooling requirements and improved turbine life due to the lower turbine entry temperature—for a given thrust/power output.

The hydrogen properties positively affect the combustion process within a gas turbine engine. First of all, hydrogen has a wider flammability range, which means that a stable combustion can be achieved over a greater range of off-design conditions [Lefebvre and Ballal 2010]. Secondly, hydrogen has a higher flame speed, and experiments showed that the combustion chamber can be redesigned to be 2/3 shorter than that of a kerosene combustor [Brewer 1991]. Hydrogen also has a low flame emissivity, which reduces the cooling requirement [Lefebvre and Ballal 2010]. This has the potential of increasing the engine power output for a given intake mass flow. However, there is no study to date that went beyond zero-dimensional performance calculations to quantify these potential benefits.

From an emissions perspective, hydrogen eradicates carbon and sulphur emissions. Also, hydrogen combustion NOx emissions can be reduced by nearly 80% with a tailored injection system [Dahl and Suttrop 1998]. It was experimentally demonstrated on a APU-size gas turbine engine, where a micro-mix combustor was used in lieu of a conventional injection system. By injecting gaseous hydrogen through multiple injection points it is possible to avoid the presence of rich pockets of fuel, which lead to high NOx emissions. However, experiments also showed that hydrogen fuel needs to be preheated before being combusted. In fact, below 60 K the gas turbine combustion would experience instabilities [Sosunov and Orlov 1990].

Looking at gas turbine performance, when the same thrust/power output is retained the specific fuel consumption of a hydrogen-fuelled gas turbine engine reduces by 2/3 due to hydrogen high energy content per mass—2.8 times greater than that of kerosene [Payzer and Renninger 1979]. It is the lower engine SFC that, from a computational standpoint, causes a reduction in aircraft fuel mass to achieve a given mission.

The combustor outlet temperature also reduces—by about 4%— when hydrogen fuel is used for a given thrust/power output. This is due to the higher energy available in the exhaust products as shown by calculating the specific heat at constant pressure of the hydrogen combustion products [Boggia and Jackson 2002]. The turbine life consequently improves as an increase in turbine entry temperature of 10 K

represents a decrease in turbine life of about 25% [Corchero and Montañes 2005]

Hydrogen heat sink capabilities can also be used to intercool or precool the compressor cooling air, cool the turbine cooling air, and recuperate heat from the exhaust pipe [Boggia, Jackson and Singh 2001; Hewitt 1984; Payzer and Renninger 1979]. However, zero-dimensional performance calculations showed that the performance benefits (specific fuel consumption reduces by 1-4%) do not justify the additional weight and complexity. In addition, different studies found different "optimum" cycle arrangements. This highlights the importance of the underlying assumptions on the outcome of a particular study.

2.2.4 Environmental considerations

Hydrogen fuel eliminates carbon and sulphur emissions and has the potential to dramatically reduce NOx emissions as explained in the previous section. However, hydrogen combustion releases 2.6 more water vapour than the kerosene alternative. Similarly to carbon emissions, H_2O is a greenhouse gas but it has a reduced impact from a global warming perspective. It has to be noticed that CO_2 emissions last in the upper atmosphere for about 100 years, whereas water vapour lasts nearly six months [Westenberger 2003]. This is why simulations concluded that the global warming potential of aviation could be reduced by 40-50% when using hydrogen fuel [Cryoplane 2003; Svensson 2005]. However, the global warming mechanism is too poorly understood to draw any significant conclusion on the potential of hydrogen fuel.

Similar conclusions also apply to the contrail and cirrus clouds formation. At present, there is not enough experimental evidence to determine whether the radiative forcing of hydrogen-fuelled aircraft will be smaller or larger than that of kerosene contrails. In fact, the contrails radiative forcing depends on the amount of water vapour released in the engine exhaust as well as on the effective mean radius of the ice particles within the contrail itself. A bigger mean effective radius of the ice particles can offset, from a radiative forcing perspective, a greater amount of water vapour should the two effects be of the same order of magnitude. This effect would occur, as numerical simulations revealed, when moving from kerosene to hydrogen fuel [Marquart et al. 2005]. However, a sensitivity analysis showed that different particle properties models lead to different scenarios in terms of radiative forcing impact, and so experimental evidence is needed for a conclusive assessment.

2.3 Distributed Propulsion

Low-speed HALE UAVs are generally unable to carry a payload that demands an electric power as big as the power required to sustain flight. In fact, to meet such a constraint a piston-prop engine would become significantly heavier and less efficient. Conversely, a lightweight gas turbine engine could be tailored for power generation to supply energy to both the payload and the electric-driven propulsors. This turboelectric Distributed Propulsion (DP) system would be able to achieve a very low specific thrust, which leads to a low specific fuel consumption (SFC) and thus long endurance, by at the same time coping with greater payload powers. Additional synergies might also arise by including the effect of electrical energy storage (Chapter 7) as well as because of the additional degree of freedom of distributing the propulsors virtually anywhere on the airframe (Chapter 8).

The present section reviews the most significant studies on distributed propulsion, which can be intended as either distributing the propulsors or distributing the core engines. As such, the initial part focuses on the effects of distributing the electric-driven fans on large civil aircraft (sect. 2.3.1). The second part focuses on the effect of adopting multiple gas turbine engines (sect. 2.3.2).

The studies on distributed propellers, which might be more relevant to low Mach applications, are discussed in section 8.1.1. Hybrid-electric systems, which are an option made available by turboelectric distributed propulsion, are reviewed in section 7.1. The electric transmission system, which is the key technology enabler of the turboelectric concept, is discussed in Appendix C.

2.3.1 Distributing the electric-driven propulsors

Felder, Brown and Kim predicted that turboelectric distributed propulsion, coupled with a blended-wing-body (BWB) airframe, would reduce the mission fuel burn by over 70% relative to the Boeing 777-200LR baseline aircraft [Felder, Brown and Kim 2011]. This NASA study, which is referred to as the N3-X concept, was conducted to identify solutions to mitigate the environmental impact of aviation. The benefits arise due to the advanced airframe structures and aerodynamics, the increase in propulsion system bypass ratio, and boundary layer ingestion.

According to the authors, all of the required thrust would be delivered by 15

electrically-driven fans. These would be mounted on the back of the BWB fuselage, so that its boundary layer could be ingested. The aircraft drag would consequently reduce, a benefit that could also be quantified as a propulsors-power drop. The electric power would be generated on-board by two turboshaft engines, which would be mounted on the wing tip to enhance the wing bending-relief effect.

The core engines and the distributed propulsors were linked by means of a superconducting electric network [Brown 2011]. This is the key technology enabler of the N3-X concept as it gives the designer the freedom to distribute the propulsors where the aircraft boundary layer can be ingested. However, the weight and the efficiencies that were used to model the electric components assume that the superconducting technology would significantly advance by the 2030-2035 time frame. As such, these values should be intended as targets to be achieved, and uncertainties remain to when the technology would advance to such extent.

The N3-X study assumed that the fan pressure ratio (FPR) was fixed, so that the propulsion system bypass ratio would depend on the required propulsors mass flow at design point. It is for this reason that a FPR that gives a minimum thrust specific fuel consumption cannot be found [Felder, Tong and Chu 2012]. Also, the fans intake width was considered fixed and linked to the aircraft geometry, whereas the fan diameter—and consequently the intake height—could be varied to match the thrust requirement. However, this solution would make the propulsors ingest a mixture of both boundary layer and freestream flow. This could also be ingested by non-electric driven fans mounted on the core engines, which would decrease the electric transmission system mass and improve the overall mission fuel burn.

The main ambiguities of the aforementioned study lie into where the benefits come from and how the baseline reference aircraft was chosen. First of all, it is not possible to distinguish how the 70% fuel burn reduction is shared between the advanced airframe, the greater bypass ratio, and boundary layer ingestion. Thus, it is hard to identify which technology is the main driver of these benefits. Secondly, the Boeing 777-200LR may not be the most appropriate reference aircraft to benchmark the N3-X concept. Future advancements of both conventional tube-and-wing airframes and turbofan engines should be expected in the near future. As such, the N3-X concept should also be compared against less disruptive but still advanced reference aiframe/propulsion concepts.

Kirner investigated the benefits of turboelectric distributed propulsion on long range aircraft [Kirner 2014]. The aim was to identify the key parameters that mostly

influence the benefits of the integrated airframe/distributed propulsion system. This study looked into the benefits of boundary layer ingestion for both the tube-and-wing and BWB airframes. Advanced airframe and turbofan baselines were considered to benchmark the turboelectric distributed propulsion concept.

It was found that distributed propulsion offers a 4.1% and a 5.2% fuel burn reduction on the tube-and-wing and BWB airframes respectively. Differently from the study of Felder et al., these benefits can be directly attributed to the increase in bypass ratio and boundary layer ingestion. These results highlight how important it is to choose the baseline airframe/propulsion configuration to benchmark disruptive technologies.

The present study also investigated the influence of replacing the power-producing turboshaft engines with turbofan engines that deliver both thrust and power. This concept was named the "thrust-split" as generating the required thrust would be divided to both the core engines and the electrically-driven fans. A further 2.5% fuel reduction benefit was achieved by optimising the thrust-split for minimum fuel burn rather than for minimum thrust specific fuel consumption.

This further benefit arose from ingesting the distributed-fans freestream mass flow with the core engines. In fact, for the considered application the main advantage of distributed propulsion is boundary layer ingestion. Any additional freestream mass flow that is needed to meet the thrust requirement could be ingested with the core engines. In this way the electric system weight would be reduced and the overall transmission losses (electrical plus boundary layer pressure drop) could be mitigated.

The study also highlighted that the optimum thrust split would vary depending on the electric system transmission properties and the boundary layer pressure losses in the fans intake. As such, it is important to adopt a multidisciplinary methodology to integrate all these effects. In addition, a multi-fidelity methodology should also be considered as the results of detailed methods for the electric system and the boundary layer properties could be translated into simple outputs to be integrated with the airframe and propulsion calculations.

2.3.2 Distributing the core engines

Ameyugo investigated the influence of distributing small gas turbine engines along the wing span of a conventional tube-and-wing airframe [Ameyugo 2007]. Using multiple gas turbine engines could lighten the wing mass due to the bending-relief effect. Also, from a manufacturing standpoint a higher number of units could reduce the overall production cost due to economies of scale.

However, it was reported that the thermal efficiency deteriorates with a smaller engine size due to scaling effects. In fact, the overall pressure ratio and turbine entry temperature would be limited by the turbomachinery blade height as the mass flow reduces. Also, the overall propulsion system weight should increase due to auxiliary and non-scalable parts. Similar effects also reported by Leifsson et al., where they estimated the weight and specific fuel consumption of small gas turbine engines by interpolating a database of existing engines [Leifsson et al. 2013].

Chapter 3

Integrated Airframe, Distributed Propulsion, and Energy Management Methodology

The aim of the present chapter is to introduce the methodology that was built to capture the synergies offered by integrating advanced and disruptive aircraft technologies. The integrated HALE UAV system is initially defined and its component parts are highlighted (sect. 3.1). The integration synergies between the considered technologies are then analysed (sect. 3.2), along with the requirements that a methodology should possess to capture them (sect. 3.3). The detailed multi-disciplinary and multi-fidelity methodology is finally presented as a top-level flow of calculations between the different sub-systems (sect. 3.4).

3.1 Integrated airframe, distributed propulsion, and energy management system

The integrated HALE UAV under consideration comprises three main areas of analysis: the airframe, the distributed propulsion system, and the energy management system (fig. 3.1). Their mutual interactions affect the integrated system power requirement, production, management, and distribution.

An aircraft platform needs to be defined, so that its size and thrust requirement

can be used to define the distributed propulsion system. This influences the integrated system design and performance because of its performance, size, weight, and aerodynamics effects (sects. 3.2.3 and 3.4.2). The energy management strategies influence the integrated system due the presence of the battery and/or a variation in the aircraft flight path (sect. 3.4.3).

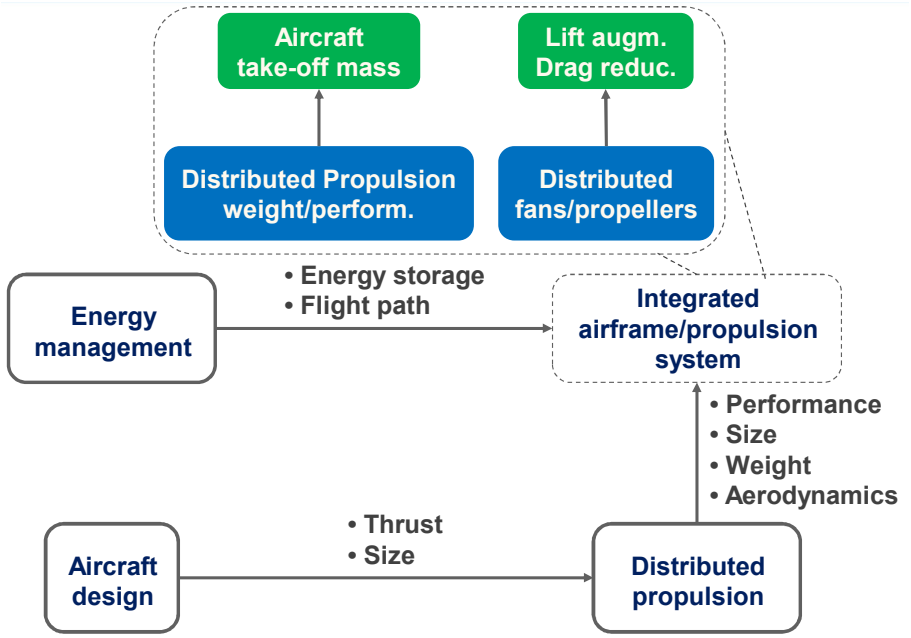

Figure 3.1: Schematic representation of the integrated airframe/propulsion system and of its component parts

Two main effects should be captured by integrating the aforementioned systems. First of all, there is a weight/performance trade-off due to the use of heavier but more efficient technologies (e.g. electric transmission, batteries, fuel cells). Secondly, the installation of the distributed propulsors would result in a drag reduction and/or lift augmentation.

3.2 Integration synergies

Hydrogen fuel, unconventional airframes, and distributed propulsion were selected to meet the given long-endurance requirement. The individual technologies by themselves enhance the performance of a HALE UAV. However, their integration leads to some strategic synergies. As such, the endurance of the integrated system will be greater than what could be achieved by simply superimposing the individual technologies. The following sections describe the integration synergies of hydrogen fuel,

unconventional airframes, and distributed propulsion.

Figure 3.2: Hydrogen fuel, airframe, and distributed propulsion synergy diagram

3.2.1 Hydrogen fuel affects power requirement and distribution

Hydrogen fuel is essential to sustain long endurance flight on low-speed HALE UAVs. Its high energy content per unit mass allows the aircraft to store three times more energy than kerosene. On the other hand, hydrogen is bulky due to its low energy density per unit volume. This would result in a drag penalty due to the oversized fuselage, which would affect the system power requirement. However, this should play a secondary effect as at altitudes over 50,000 ft the air density is low. It might be argued that the volume occupied by hydrogen fuel could be filled with enough kerosene to achieve the desired endurance. However, an aircraft designer would point out that this solution is unfeasible. In fact, in this way the aircraft fuel fraction would be well in excess of half of the UAV take-off mass. This would lead to an excessively small structural fraction, so that the aircraft would become unfeasible to be designed.

Hydrogen fuel could also be used to cryogenically cool the electric transmission system in a turbo-electric and/or hybrid-electric distributed propulsion system. The distributed propulsion concept is feasible only if the electric system weight and losses are mitigated. Cryocooling is a viable solution for both conventional and superconducting electric components. This could be achieved by circulating a cryogenic liquid within the parts to be cooled with either a dedicated refrigerating device—a cryocooler—or by adopting a cryogenic fuel. Cryocoolers would result in an extra

weight and complexity, which would penalise the aircraft endurance. As such, liquid hydrogen fuel is a key technology enabler that affects the power distribution to the propulsors.

Hydrogen fuel would also offer some operational flexibility as it can be produced on site. This could be particularly attractive in military applications, where there is a high cost of transportation of kerosene to the front line. There are many challenges related to hydrogen fuel, such as its cryogenic storage and its mass production from processes other than steam-methane reforming. Addressing all these challenges would go beyond the scope of this thesis.

3.2.2 Unconventional airframes impact on power requirement

Unconventional airframes improve the system endurance due to their structural and aerodynamic efficiency. These advancements would be synergistic with hydrogen fuel and advanced propulsion systems as they reduce the system power requirement.

The blended wing body (BWB) airframe is characterised by a lighter structural weight and an improved lift-to-drag ratio. The BWB airframe is divided in two sections: the centre body, which is the inner part of the wing where the payload and the fuel are stored, and the outer wing. Distributing the payload and the fuel inside the centre body counteracts the wing bending due to lift. Thus, the structures can be redesigned to be lighter as ultimately their weight depends on how much they are bent upwards because of lift. The BWB airframe also offers a better volumetric efficiency, defined as its surface-to-volume ratio. The lower surface leads to a reduced wetted area for a given volume, and so drag is reduced. This effect counteracts the low aspect ratio of the overall BWB wing planform, which in a conventional airframe would be detrimental in terms of drag. In addition, its volumetric efficiency would mitigate the drag penalty of storing bulky hydrogen fuel.

A multiple-fuselage airframe distributes additional bodies sidewise from the aircraft centrelines. Similarly to the BWB airframe, this effect counteracts the wing bending because of lift. Thus, a multiple-fuselage airframe can be considered an advanced tube-and-wing airframe from a structural point of view. However, the extra fuselages result in a greater drag as multiple bodies have a wetted area that is greater than that of a single body. Thus, the structural benefits may be partially

or completely offset by the drag penalty.

3.2.3 Distributed propulsion influences power requirement, production, management and distribution

A distributed propulsion system gives the designer the possibility to distribute the propulsors nearly anywhere on the airframe. Thus, this advanced propulsion system has the potential to affect all the aspects of the integrated system, from how much power is required to sustain flight to how power is managed and distributed.

A distributed propulsion system can alter the lift/drag characteristics of the airframe. Thus, the integrated system power requirement would vary depending on how the power is distributed over the airframe. Ingesting the fuselage boundary layer is one of the options as re-accelerating the low momentum flow results in a reduced drag. Ultimately drag is caused by a momentum deficit that the aircraft imparts to the flow, or a wake. Re-energising this wake would allow the aircraft drag to be reduced.

Another possibility is blowing over the wing with the propulsors exhaust. This would result in an increased wing lift coefficient, so that either the wing area can be reduced for a given field performance constraint or the aircraft take-off and landing performance can be improved. Reducing the wing area would decrease drag as the aircraft wetted area would be smaller. In addition, the wing mass would be lighter and more fuel could be stored for a given take-off mass.

Decoupling the propulsors from the core engine also affects how fuel-efficiently power is produced. First of all, distributed propulsion allows virtually any bypass ratio or propeller disc loading to be achieved. This would decrease the specific thrust of the propulsion system, and consequently its fuel flow. Low-specific thrust engines usually incur in a drag and weight penalty. However, these effects could be offset by adopting a synergistic propulsors installaton such as boundary layer ingestion or blowing over the wing. Secondly, a low specific thrust could be achieved with as little as one core engine. This is particularly important in small engines, such as the ones of UAVs, where using multiple cores to deliver a given thrust would reduce the engine mass flow. As a consequence, a constraint in the engine overall pressure ratio and turbine entry temperature would arise, which would limit the cycle thermal efficiency and the propulsion system fuel consumption.

Electrifying the propulsion system opens the door to hybrid-electric systems. These integrate a battery within the propulsion system, which can be used as an energy buffer to either downsize the engine and optimise it for cruise/loiter (instead of take-off or top-of-climb) or to mitigate its off-design fuel penalty. However, using batteries increases the aircraft empty mass and allows less fuel to be stored. Thus, a trade-off exists between the fuel savings of a given energy management strategy and the fuel penalty of carrying the battery itself. This effect becomes particularly pronounced when a long endurance requirement needs to be met. The trade-off between these two effects would also depend on the assumed battery energy density.

3.3 Capturing the integration synergies

A multi-disciplinary and multi-fidelity methodology is required to capture the synergies between hydrogen fuel, the airframe, and the distributed propulsion system. It is worth noticing that such a methodology could not be identified in the public domain. The present literature does not give any indication or design rule about how an integrated system should be designed to maximise the benefits offered by the integration synergies. There are also many uncertainties on what are the key variables that mostly influence the design and performance of the integrated aircraft system.

The aim of the present methodology is to capture the integration synergies for the purpose of design space exploration studies. Assuming a fixed design for any of the considered sub-systems would not allow the benefits of the aforementioned synergies to be fully quantified. As such, a trade-off is required between accuracy and complexity when representing the integrated system component parts.

A multi-disciplinary methodology is required when different sub-systems need to be integrated. Only through a careful analysis of the individual modules it is possible to study the overall system. In addition, once the models of the different disciplines are defined it is also possible to couple them with an optimiser so that an optimum design can be found for a given set of constraints. However, the automated nature of optimisers leads to a black-box approach that would not highlight the trade-off between opposing effects (e.g. trade-off between lower SFC and increase in engine weight and drag when the bypass ratio is increased). As such, parametric studies should be preferred in the early stages of exploring advanced and disruptive technologies.

The multi-fidelity concept is the backbone of a multi-disciplinary methodology. In its simplest form, a multi-fidelity methodology is able to represent the individual components of a system with different levels of accuracy, which is usually traded with computational time [Lukaczyk et al. 2015]. A more strategic approach to multi-fidelity modelling is to map a high-fidelity representation (e.g. computational fluid dynamics) of one of more sub-systems into low-fidelity numeric tables and response surfaces [Choi et al. 2008]. Thus, a multi-fidelity methodology should allow accurate results to be achieved without incurring in a computational burden.

A multi-fidelity methodology also forces the designer to check that all the governing variables fall within a meaningful range. Some checks could be implemented should an automated link between high-fidelity methods of different disciplines be realised. However, at the early stages of investigating disruptive technologies the designer may not be aware of which variables need to be checked. It is clear that not all of them can be monitored, or the computational time would increase exponentially. As such, a multi-fidelity methodology allows the designer to quickly identify meaningful designs that meet the given system specifications.

Avoiding the need to establish an automated link between different software platforms is also an advantage of a multi-fidelity methodology. Software programs are usually not conceived to exchange an inflow and outflow of information with other simulation tools. Should this be possible, it may not offer to the designer the required trade-off between accuracy and computational time given their order of fidelity. Conversely, a simplified representation of high-fidelity results could be applied to any software platform independently of its current or future versions.

3.4 Multi-disciplinary and multi-fidelity methodology definition

A multi-disciplinary and multi-fidelity methodology was built to capture the synergies between hydrogen fuel, the airframe, and the distributed propulsion system (fig. 3.3). The purpose of this methodology is to capture the mutual interactions between the sub-systems and assess their impact on the design and performance of the integrated system.

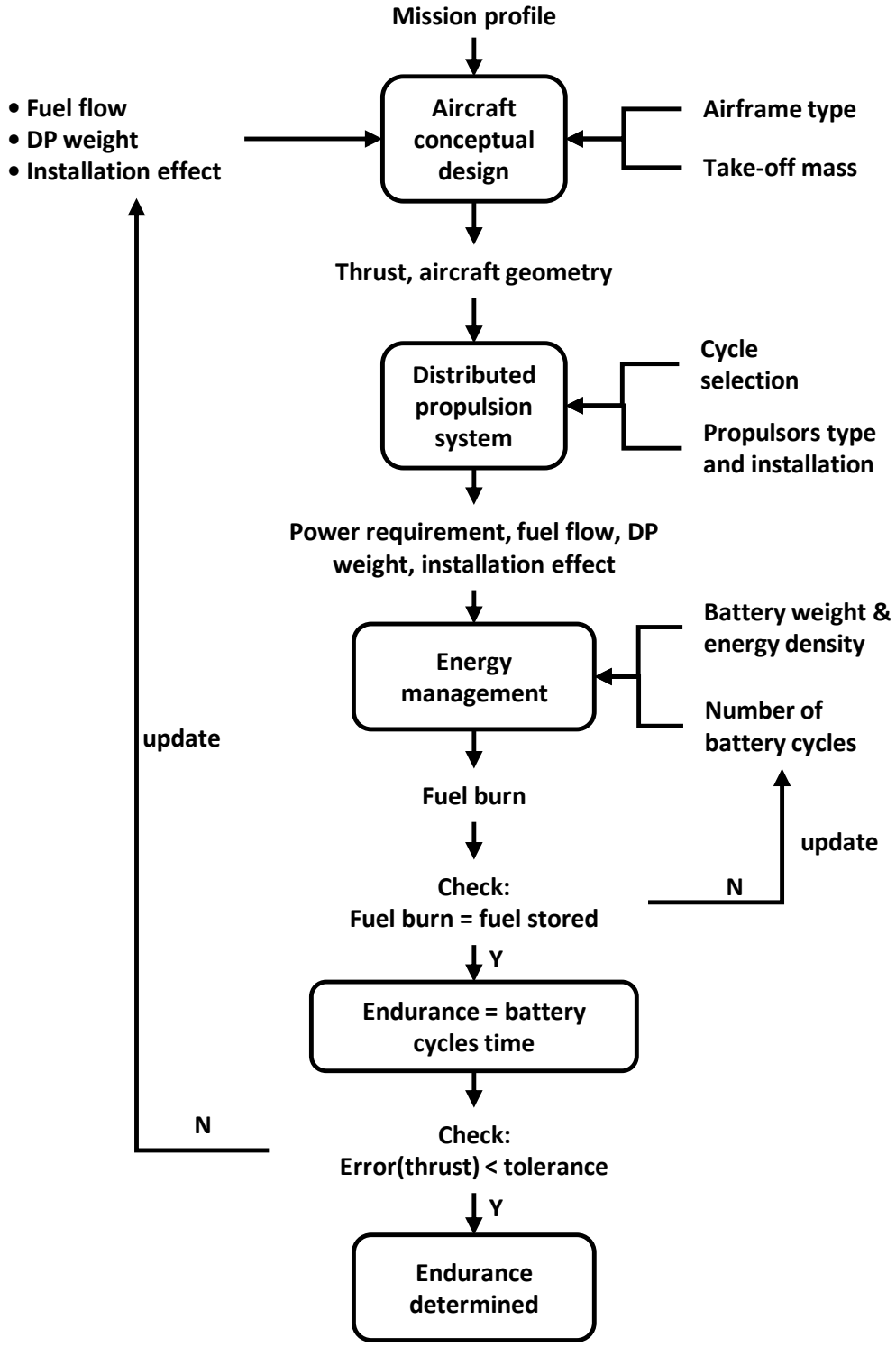

Figure 3.3: Integrated airframe, distributed propulsion, and energy management methodology layout

3.4.1 Aircraft Conceptual Design

A mission profile needs to be initially defined. For the present project, a fixed-altitude and variable-Mach loiter were chosen (Chapter 1). An airframe is also selected, which could be a conventional (i.e. tube and wing) or an unconventional one (e.g. blended wing body (BWB) , multiple-fuselage design), along with its take-off mass. These inputs allow the aircraft conceptual design and performance calculations to be assessed, which are discussed in Part I (Chapter 4).

The aircraft platform also needs the main propulsion system parameters (fuel flow, weight, and installation effect) to be defined, which are initially guessed and then iteratively changed. The fuel flow information needs to account for the off-design penalty to predict an accurate fuel burn. The weight is mainly a function of the design point thrust, which for the present project it was assumed to be the top-of-climb requirement. The installation effect would vary depending on the propulsor type (fan, propeller) and where the propulsors are distributed on the airframe.

The main output of the aircraft conceptual design calculations are the aircraft design-point thrust requirement, the airframe 3D geometry, its take-off mass fractions (e.g. fuel, structures), and its drag characteristics. These are the main inputs for the propulsion system calculations and ultimately to assess the mission fuel burn.

3.4.2 Distributed Propulsion system

The system designer should then select a distributed propulsion system architecture, namely the cycle and the propulsors. The electric system properties (e.g. weight, efficiency) were assumed to be fixed for the present project (Appendix C). However, future studies should assess its properties into more detail.

The main outputs of the distributed propulsion system calculations are its fuel flow (both at design and off-design), its weight, and its impact on the aircraft structures and aerodynamics due to its installation. The aircraft power requirement is also determined, which is required for energy management calculations.

3.4.2.1 Cycle selection

Wave rotor and solid oxide fuel cell (SOFC) hybrid cycles were considered in addition to the baseline Brayton cycle (Part II, Chapters 5 and 6). The wave rotor would allow to reach higher peak pressures and temperatures being a non-bladed component. Conversely, the SOFC generates electric electric power more efficiently by complementing the hydrogen combustion with its oxidation. In addition to their intrinsic benefits, investigating unconventional cycles allow the advantages of distributed propulsors to be put into perspective.

3.4.2.2 Propulsors selection

Both distributed fans and propellers were considered for the present project. Each type of propulsor could be installed on the airframe to either ingest the fuselage boundary layer or to augment lift. However, ingesting boundary layer would not be a viable option for the present HALE UAV due to the low-speed requirement. This results in an insufficient boundary layer mass flow, which would not be enough to generate the required aircraft thrust. As such, the propulsor power drop (or the aircraft drag reduction) would not significantly affect the design and the performance of the integrated system.

Lift augmentation, on the other hand, would also work at low Mach numbers. This could be achieved with both fans and propellers. However, a fan would need to be installed on the wing upper surface or the wing leading edge would obstruct the fan nozzle and alter the flow expansion. Conversely, the propeller hub could be buried into the wing leading edge (assuming that the electric motor would fit). A propeller generates thrust by accelerating the flow rather than by imparting a pressure differential. Thus, cutting the propeller exhaust with the wing leading edge should not be as significant as for a fan.

The advantage of leading-edge mounted distributed propellers is that their exhaust would influence both the wing upper- and lower-surface flow. This would enhance the lift-augmentation effect compared to blowing only over the upper surface as in the case of a fan. In addition, the propeller power decreases as the propulsors number increases for a given thrust to deliver (Part III, Chapter 8). This effect would not occur with distributed fans as their power is unaffected by the number of propulsive devices. As such, only lift-augmentation by means of distributed

propellers was considered for the present project. The fans were simply considered as podded on the wing as a baseline configuration to benchmark the distributed propellers architecture.

3.4.3 Energy Management

The energy management calculations start by specifying the battery weight and its energy density (in kWh/kg). The weight is expressed as a fraction of the aircraft take-off mass, so that its influence becomes comparable between different take-off masses. The energy density can be varied to assess the influence of future advancements in battery technology and their impact on the design and performance of the integrated system.

The battery performance were represented by means of battery charge and discharge cycles (Part III, Chapter 7). Each cycle has a finite time and depends on the aircraft power requirement (discharge) and the core engine power output (charge). The aircraft power requirement depends on both the considered airframe and the type of propulsor along with its installation. Thus, the charge and discharge cycles depend on both the airframe and the distributed propulsion system characteristics—for a given energy management strategy.

The endurance was determined as the number of the battery cycles times the unit cycle time. In fact, the aircraft design calculations iteratively assess the maximum endurance for a given take-off mass (Chapter 4). Thus, it was convenient to link the aircraft endurance to the charge/discharge cycles time, so that the maximum endurance would be determined once the number of charge/discharge cycles is found by iterating on its initial guess.

The maximum endurance is determined when the aircraft top-of-climb thrust converges to a stable solution. In fact, this fixes the distributed propulsion system fuel flow, weight, and installation effect, which were initially guessed and iteratively changed. Fixing the engine design-point with the aircraft top-of-climb thrust is one of the main assumptions of the present project. Further studies should look at a propulsion system design for multiple design points (i.e. variable cycles) as the off-design fuel penalty becomes rather significant when the endurance requirement is of 7 to 10 days.

Part I

Assessing the Integrated System Power requirement

Chapter 4

Aircraft Conceptual Design

4.1 Introduction

It is essential to answer basic questions about the aircraft configuration arrangement, size and weight, and performance [Raymer 1992] to assess the benefits of innovative propulsion systems. However, the design methods available in the literature rely on previous aircraft designs to extrapolate the required information. This would be unfeasible for low-speed HALE UAVs that include a distributed propulsion system and rely on liquid hydrogen as a primary fuel. Also, existing aircraft design tools were not explicitly built to capture the aerodynamic and structural effects of unconventional propulsion systems and fuels.

The aim of the present chapter is to build a tailored aircraft conceptual design methodology for low-speed HALE UAVs. This should be flexible enough to capture the mutual interactions between unconventional airframes, fuels, and propulsion systems. The multidisciplinary approach to conceptual design that was adopted is initially presented (sect. 4.2.1). The individual disciplines, which are the foundations of the multidisciplinary method, are then introduced. The aircraft geometry (sect. 4.2.1.1), structures (sect. 4.2.1.2), drag (sect. 4.2.1.3), and performance (sect. 4.2.1.4) assessment is described. This is followed by the assumptions on the liquid hydrogen storage system (sect. 4.2.1.5). The results highlight the influence of the main airframe and propulsion system parameters on the design and performance of the integrated airframe/propulsion system.

4.2 Methodology

The aim of the present study was to build a flexible aircraft platform to assess the effect of integrating a distributed propulsion system on the design and performance of hydrogen-fuelled low-speed HALE UAVs. A multidisciplinary approach to the aircraft conceptual design was adopted, which was tailored to endurance-aircraft design (sect. 4.2.1). A 3D dimensional geometrical representation of the airframe was considered, which is particularly useful to estimate the available volume of the BWB centrebody (sect. 4.2.1.1). The analytical and/or empirical correlations that were adopted to assess the aircraft structural mass (sect. 4.2.1.2), drag (sect. 4.2.1.3), and performance (sect. 4.2.1.4) are then presented. The hydrogen storage system assumptions are also described (sect. 4.2.1.5).

Three airframes were included in the present study (fig. 4.1). The T&W airframe was considered the baseline design. The triple-fuselage airframe was modelled as an advanced T&W configuration, in which the mass of the wing would be lightened by the bending-relief effect of the outer fuselages. However, the increase in aircraft drag may partially or completely offset the structural benefit. The BWB airframe was also assessed for two reasons. First of all, the BWB airframe is volumetrically efficiency due to its reduced surface-to-volume ratio [Liebeck 2004]. This results in a greater aerodynamic efficiency. Secondly, distributing the payload and the fuel within the wing root increases the bending-relief effect on the centrebody. Thus, the overall wing planform becomes lighter, so that more fuel could be stored for a given take-off mass.

4.2.1 Multidisciplinary aircraft conceptual design

A multidisciplinary approach to aircraft conceptual design was selected. In fact, previous designs of hydrogen-fuelled HALE UAVs are unavailable to extrapolate enough information to define an aircraft platform. Also, recent studies on distributed propulsion systems highlighted the need for a re-scalable platform as part of the benefits of distributed propulsion arise from the reduced fuel load, which leads to a smaller and lighter aircraft [Felder, Tong and Chu 2012].

Figure 4.2 shows the structure behind the aircraft conceptual design calculations, which is flexible enough to account for unconventional airframes such as a blended-wing-body (BWB) and a multiple-fuselage design. The proposed iterative layout

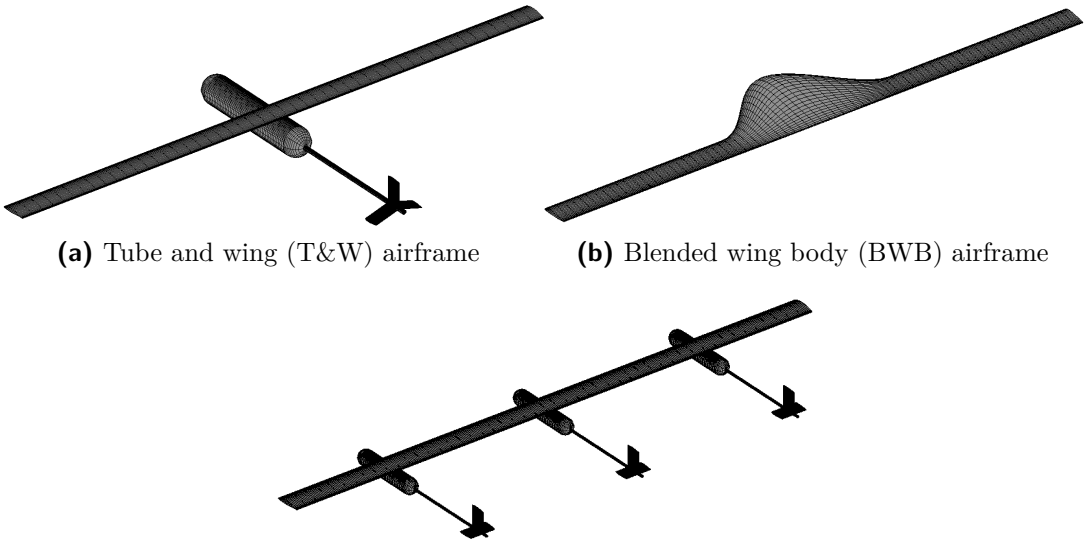

(a) Tube and wing (T&W) airframe

(b) Blended wing body (BWB) airframe

(c) Triple-fuselage airframe

Figure 4.1: 3D view of the selected airframes

differs from the take-off mass build-up approach that is usually adopted to design larger aircraft. In fact, the take-off mass build-up method was found to exhibit divergent trends with an increase in the endurance requirement (see Appendix A). Thus, it was decided to iteratively increase the endurance requirement—for a given take-off mass—until the maximum endurance is determined. With this "endurance build-up" approach the take-off mass is used as a handle to define the boundaries of the design space, and the maximum endurance is determined for each take-off mass [Altman 2000].

The iterative aircraft conceptual design and performance procedure works as follows. For a given take-off mass, the wing is sized based on a calculated wing loading, which depends on the loiter altitude, minimum flight speed, and maximum lift coefficient. The fuselage is sized based on the internal volume requirement, and the fuel volume is initially guessed and iteratively changed. Once the geometry is available, it is possible to estimate both the aircraft drag and structural mass. The hydrogen tanks were assumed to be a fraction of the stored fuel. Then, aircraft performance calculations lead to the mission fuel burn estimate for a given endurance requirement. Starting from an underestimate of the maximum endurance, this is iteratively changed until the end-of-loiter mass matches the fuel required to complete the descent phase. This procedure is repeated for each take-off mass within the considered range. The following sections provide the details of the aircraft geometry, structures, drag, and performance calculations.

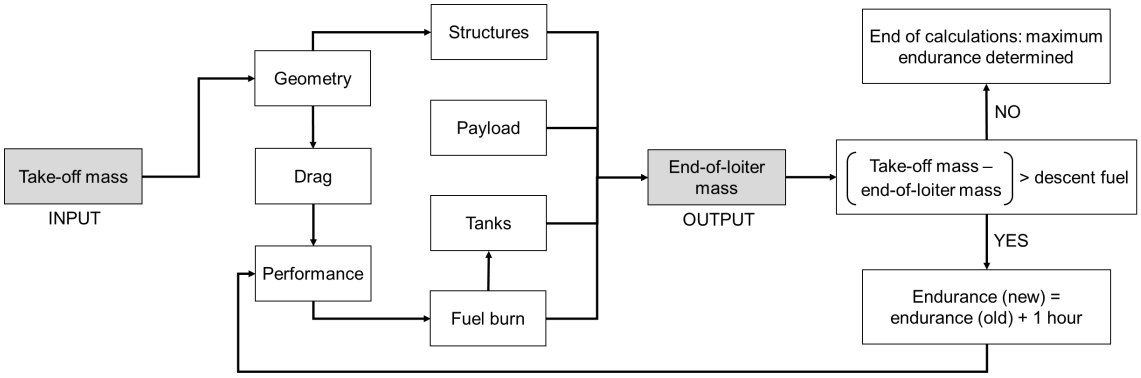

Figure 4.2: Iterative method layout for long-endurance aircraft conceptual design

4.2.1.1 Aircraft geometry

The aircraft geometry module provides a 3D model of a given UAV configuration. As it will be explained below, the wing area is sized based on the take-off mass and the wing loading. In the case of the tube and wing configuration, the fuselage is shaped to enclose the fuel and payload volume. The fuel volume depends on the fuel mass, which needs to be assessed by means of aircraft performance calculations. Its value is initially guessed by assuming the fuel to be a certain fraction of the take-off mass. In the case of a BWB configuration, the centre body is shaped to account for both the wing area requirement—as both the centre body and the outer wing generate lift—and the storage constraint.

Wing sizing The wing span can be calculated, for a given aspect ratio, by knowing the wing surface area (eq. 4.1). The wing area is calculated as the ratio of the take-off weight upon the wing loading (eq. 4.2). Thus, knowing the take-off mass is essential to estimate the wing area. As shown in equation 4.3, the wing loading can be calculated combining the minimum flight speed, the maximum wing lift coefficient, and the air density [Austin 2010].

$$b = \sqrt{AR\, S_{wing}} \tag{4.1}$$

$$S_{wing} = \frac{M_{takeoff}\, g}{w} \tag{4.2}$$

$$w = \frac{v_{min}^2\, \rho\, C_l}{2} \tag{4.3}$$

Fuselage sizing The radius of a tubular fuselage with hemispherical heads can be sized by knowing the fuselage radius r_{fus}, its slenderness ratio N_{fus}, and the fuselage internal volume requirement V_{tot} (eq. 4.4). V_{tot} is the sum of the fuel and payload volumes, and the slenderness ratio N_{fus} is defined as the fuselage length upon its radius. This was set to 10 based on structural and drag considerations [Torenbeek 1976]

$$r_{fus} = \frac{V_{tot}}{\pi(N_{fus} + \frac{4}{3})} \tag{4.4}$$

$$N_{fus} = \frac{L_{fus}}{r_f us} \tag{4.5}$$

Tail sizing The horizontal and vertical empennages surface areas can be sized as follows by means of empirical and geometry parameters [Howe 2000]. In addition to the wing chord $\bar{c}$, the distance between the aircraft nose and the tail plane l_{tail} and the distance of the aircraft centre of gravity from the nose l_{CG} need to be known (eqs. 4.6 and 4.7). $\overline{V}$ and $\overline{V_V}$ are the tail volume coefficient, whose values can be obtained from existing designs and as they are defined according to equations 4.8 and 4.9. On a large civil aircraft, the tail empennages are usually mounted at the back of the fuselage. The UAV high altitude and low speed requirement, however, would make such an arrangement inconvenient as it would result in an excessively large empennages surface area. This would lead to an increase in tail drag and mass, which has a detrimental effect on the endurance of an unmanned system. Thus, both the horizontal and vertical empennages were assumed to be mounted on a tail boom, which increases the tail moment arm and so decreases the empennages surface area. Its length can be determined by taking the moments around the nose of the aircraft (eq. 4.10).

$$S_H = \frac{\overline{V}\, S_{wing}\, \bar{c}}{0.9 l_{tail} - l_{CG}} \tag{4.6}$$

$$S_V = \frac{\overline{V_V}\, S_{wing}\, b}{0.9 l_{tail} - l_{CG}} \tag{4.7}$$

$$\overline{V} = \frac{S_H \, l}{S \, \overline{c}} \tag{4.8}$$

$$\overline{V_V} = \frac{S_V \, l_V}{S \, b} \tag{4.9}$$

$$M_{take-off} \, l_{CG} = M_{wing} \, l_{wing} + M_{fus} \, l_{fus} + M_{payload} \, l_{payload} + M_{tanks} \, l_{tanks} + M_{tail} \, l_{tail} \tag{4.10}$$

BWB sizing The 2D planform of a BWB aircraft can be represented by a set of 10 parameters as shown in figure 4.3. Assigning an airfoil at each spanwise location allows the 3D geometry to be defined. The selected airfoil was the Eppler E344, a reflexed airfoil designed for flying wings that has a thickness-to-chord ratio of 15%. The internal volume available within the centre body of a BWB is not as easily

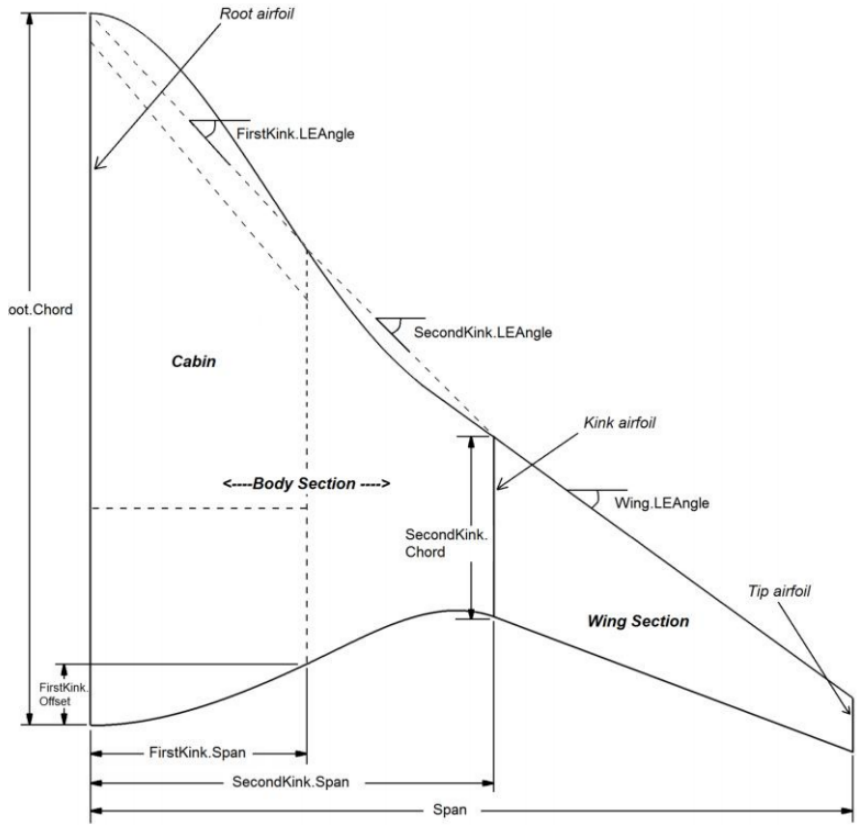

Figure 4.3: Parametric definition of the BWB planform [Brenner et al. 2012].

definable as in the case of a tubular fuselage. Thus, it was decided to parameterise

such volume as shown in figure 4.4, which can be described as follows:

1. Define the portion of airfoil that is allocated to the available internal volume.
2. Define the span length within the centre body that is allocated to available internal volume, b2.
3. Define the following centre body parameters:
    - Sweep
    - Taper ratio (kink chord upon root chord)
    - B2, which is the ratio of b_2 upon the root chord.

For a given set of sweep, taper ratio, and B2 parameter, the centre body internal volume depends uniquely on its root chord. Thus, its value must be initially guessed and iteratively varied until the difference between the required volume (fuel and payload) and the available volume becomes smaller than a given tolerance. Assuming that a BWB is represented by a centre body (or inner wing) and an outer wing, then the inner wing area is determined by the internal volume requirement. This is because the centre body must be shaped to store a certain amount of fuel and payload. Thus, the outer wing area is obtained as the difference between the overall wing area, which is based on wing loading considerations and the inner wing area.

4.2.1.2 Aircraft structures mass estimation

For a tube and wing UAV configuration, the main structural components are:

- Wing
- Fuselage
- Empennages and tail boom

The wing mass is determined with the F-method, which is an empirically weighted theoretical approach [Howe 1996]. The main assumptions behind this method are:

1. The mass of the wing is assumed to be equal to the sum of the mass of the spars (D), the mass of the ribs (M_r), and a penalty factor that accounts for secondary and miscellaneous items (eq. 4.11).

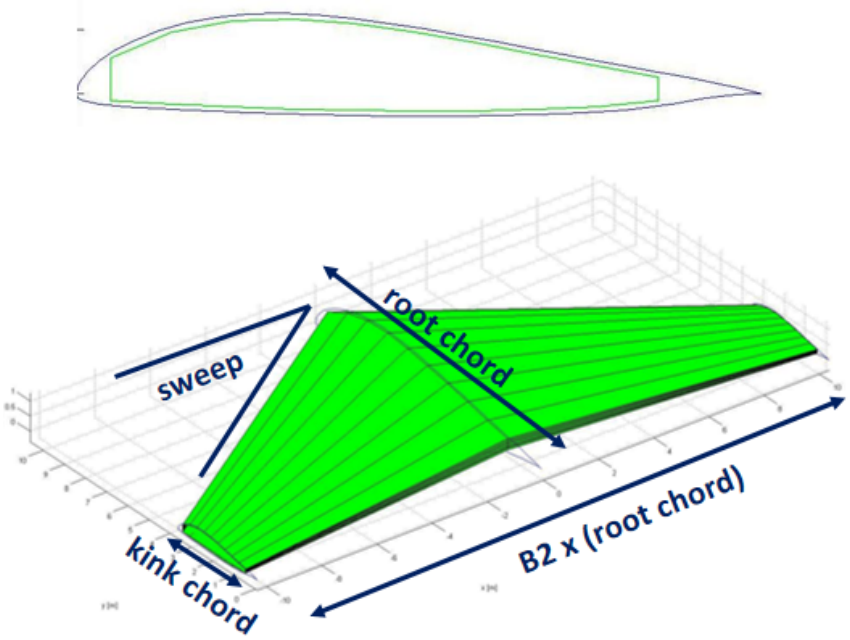

Figure 4.4: Visual representation of the available volume within the BWB centre body. In the airfoil at the top the green area is allocated to the internal volume.

$$M_{wing} = D + M_r + F \tag{4.11}$$

The ribs and spars masses are represented by linear equations that depend on the take-off mass, the wing geometry, and its material properties. Some examples of penalty factors, which are expressed as fractions of the take-off mass, are given in table 2 of Howe 1996.

2. The spanwise lift distribution is semi-elliptical.

3. The average allowable direct stress level f_a is constant everywhere.

4. The ratio of the allowable shear stress upon the allowable direct stress is assumed to be 0.5.

5. Any discrete or distributed mass on the wing (engines, pods, etc.) lightens the mass of the spanwise structures (D) because it counterbalances the bending moment due to lift; this effect is quantified by means of a bending relief factor (see Appendix 2 of Howe 1996).

The masses of the fuselage and the empennages are calculated with equations 4.12 and 4.13 respectively. They are based on empirical data and rely on the primary design parameters (geometry and maximum design speed)[Howe 2000]. The tail

boom mass is arbitrarily assumed to be a 10% of the fuselage mass. Regarding the mass of a Y tail arrangement, the horizontal and vertical projections of the inclined empennages were treated as individual tail planes (eq. 4.14).

$$M_{fus} = [L_{fus}\,(B+H)(V_D)^{0.5}]^{1.5} \tag{4.12}$$

$$M_H = 0.047\,V_D\,(S_H)^{1.24} \qquad M_V = 0.047\,V_D\,(S_V)^{1.15} \tag{4.13}$$

$$M_H = 0.047\,V_D\,(S_{H1}^{1.24} + S_{H2}^{1.24}) \qquad M_V = 0.047\,V_D\,(S_{V1}^{1.15} + S_{V2}^{1.15} + S_{V3}^{1.15}) \tag{4.14}$$

For what concerns the BWB configuration, its structural components mass is predicted with a modified F-method [Howe 2001]. This assumes that the airframe comprises an inner and outer wing as shown in figure 4.5. The equations to calculate the wing mass are used twice: once for the inner wing, and once for the outer wing. However, the inner wing spars mass equation is modified to account for the structural continuity between the centre body and the outer wing: one of its input values, in fact, is the outer wing bending relief factor. Nonetheless, there is independence between the outer and inner wing ribs mass and penalty factor.

4.2.1.3 Aircraft drag

Zero-lift drag is determined with the component build-up method, which calculates the subsonic parasite drag of each component using a flat-plate skin friction coefficient (C_f) and a component form factor (FF) that estimates the pressure drag due to viscous separation [Raymer 1992]. The interference drag effects are also included with a correction factor Q that is equal to 1.0 for a fuselage or a wing, becomes 1.03 for a tail surface, and 1.5 for a nacelle or external store mounted on the fuselage or wing. The parasite drag coefficient for a given component is then given by:

$$C_{d0} = \frac{C_f\,FF\,Q\,S_{wet}}{S_{ref}} \tag{4.15}$$

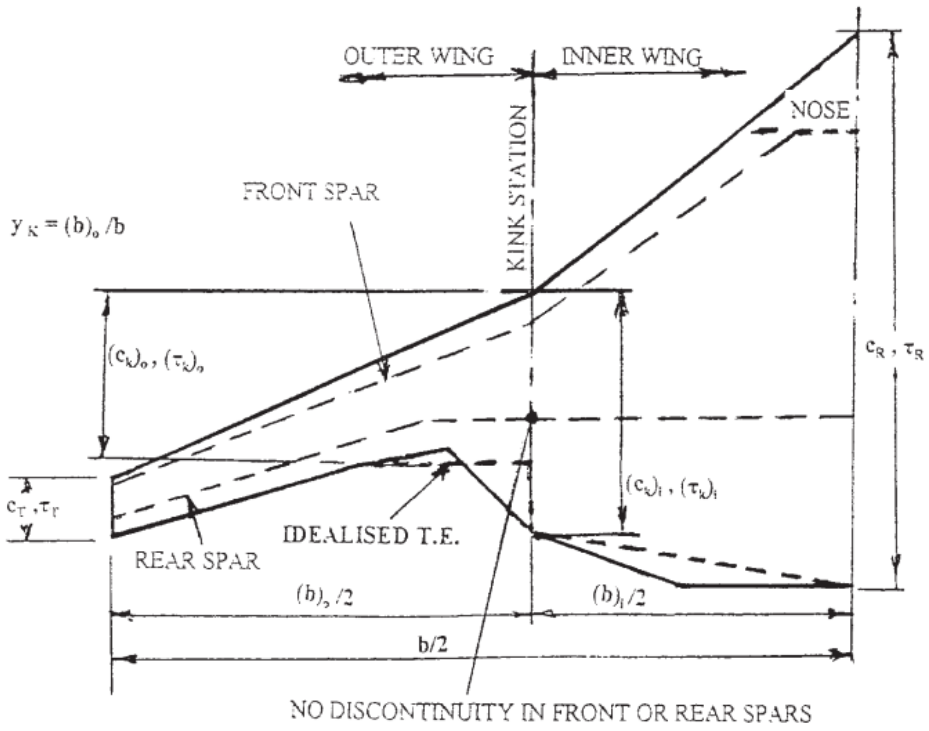

Figure 4.5: Idealisation of BWB geometry [Howe 2001].

Where the reference surface area S_{ref} usually coincides with the wing surface area, and S_{wet} is the wetted surface area of the considered component. Lift-induced drag is assumed to be proportional to the square of the lift coefficient for low angles of attack with a proportionality factor called "drag-due-to-lift factor" or K:

$$C_{di} = K\, C_l^2 \tag{4.16}$$

The K factor is equal to the reciprocal of the product of the wing aspect ratio and π according to the classical wing theory. However, this must be corrected by a factor "e" to account for effects such as flow separation and non-elliptical lift distribution:

$$K = \frac{1}{\pi\, AR\, e} \tag{4.17}$$

Where "e" is the Oswald span efficiency factor that can be estimated based upon actual aircraft data as follows:

$$\Lambda_{LE} < 30\,\text{deg} \qquad e = 1.78(1 - 0.045\, AR^{0.68}) - 0.64 \tag{4.18}$$

$$\Lambda_{LE} > 30\,\text{deg} \qquad e = 4.61(1 - 0.045\,AR^{0.68})(cos\,\Lambda_{LE})^{0.15} - 3.1 \tag{4.19}$$

In order to assess the lift-induced drag of the BWB configuration, the airframe planform was treated as a flying wing. Thus, it was assumed that the BWB aircraft could be treated as a wing whose sweep is equal to the leading-edge-averaged sweep between the inner and outer wing (eq. 4.20).

$$\Lambda_{LE\,BWB} = \frac{LE_{inner}\,\Lambda_{inner} + LE_{outer}\,\Lambda_{outer}}{LE_{inner} + LE_{outer}} \tag{4.20}$$

To account for the effect of natural laminar flow, a weighted-average skin friction coefficient between the laminar and turbulent flow was considered. Assuming a tailored airfoil design, a 50% laminar flow fraction was considered for the present study as the Reynolds number is below 30 million and the wing is unswept [Green 2008]. For the BWB airframe, natural laminar flow was assumed only on the straight outer wing as the Reynolds number on the swept centrebody is very close to the boundaries where natural laminar flow could be achieved.

The effect of the podded-fans axisymmetric nacelle drag was also included in the calculations [Williams 2011]. Both the NACA-1 series forebody and the 8-degree circular arc afterbody drag coefficients were estimated with experimental correlations REF, and an interference factor of 1.5 was considered assuming that the fans are mounted directly on the wing [Raymer 1992].

4.2.1.4 Aircraft performance

Take-off The take-off performance was modelled with a simplified empirical approach that relates the take-off length and the required thrust (eq. 4.21), which neglects the aerodynamic drag and rolling friction [Jenkinson, Simpkin and Rhodes 1999]. Such a linear relationship between the take-off length and the thrust requirement relies on the assumption that the average value of thrust at the mean energy speed is considered.

$$s = \frac{v^2}{2a} = \frac{(v_2^2)}{2\frac{T}{M_{takeoff}\, g}} \tag{4.21}$$

Climb and descent The path between sea level and the loiter altitude was discretised in steps to assess climb and descent performance [Jenkinson, Simpkin and Rhodes 1999]. The average fuel burn between two altitude steps can be calculated by means of the following iterative procedure (fig. 4.6):

1. Guess a fuel burn between two altitude steps to guess an aircraft mass reduction for drag calculations.
2. Calculate an average rate of climb (at the average altitude between the two steps) thanks to the above drag calculations and assuming a thrust variation with altitude.
3. Determine the time to climb as the ratio of the altitude variation between two steps upon the average rate of climb.
4. Calculate the segment fuel burn as the product of the average SFC, the time to climb, and the required thrust.
5. Repeat the steps from 1 to 4 updating the initial guess for the fuel burn until convergence is achieved by means of fixed point iterations.

Once the average fuel burns between all the altitude steps has been assessed, their values can be summed to calculate the overall climb/descent fuel burn.

Loiter For large civil aircraft cruise performance is usually assessed with the Breguet equation (eq. 4.22), which relates the aircraft mass reduction due to the fuel consumption to the main cruise parameters.

$$\frac{M_1}{M_2} = \exp\left(\frac{time\, SFC}{L/D}\right)_{cruise} \tag{4.22}$$

However, in the case of a HALE UAV there is a significant mass reduction when loitering for seven to ten days. Thus, assuming a constant SFC and lift-to-drag ratio might be unacceptable. It was then decided to discretise the loiter in steps of one

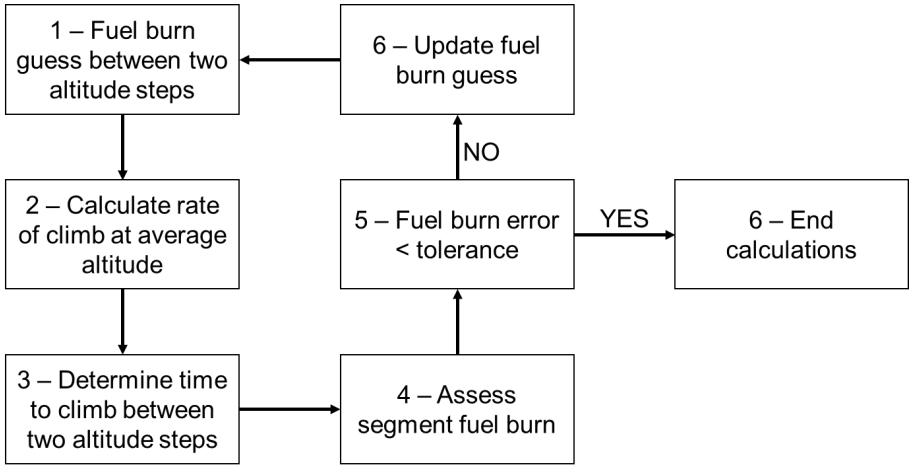

Figure 4.6: Iterative climb/descent fuel burn calculations flow chart.

hour each, and to calculate the fuel burn at every step with an iterative method similar to the climb/descent performance calculations: a mass reduction is initially guessed, and fixed-point iterations are repeated until convergence is reached. The loiter was assumed to occur at constant altitude, with the Mach number decreasing to compensate for the aircraft mass reduction. The loiter iterative calculations are schematically shown in 4.7 and are exposed below.

1. Guess the reduced aircraft mass after one hour of loitering, M_2.

2. Calculate the new velocity v_2 at which the aircraft loiters due to the aircraft mass reduction as follows:

$$v_2 = \sqrt{\frac{2\, M_2\, g}{\rho\, S_{wing}\, C_l}} \tag{4.23}$$

3. Determine the new Mach number at which the aircraft loiters due to the aircraft mass reduction dividing v_2 by the speed of sound.

4. Assess the segment average drag ($D = 0.5\, \rho\, v_{mean}^2\, S_{wing}\, C_d$) and fuel burn (product of SFC, drag, and time), where v_{mean} is the average between the start-of-segment velocity (i.e. prior to the mass reduction) and v_2.

5. The steps from 1 to 4 can be repeated until the error on the fuel burn becomes smaller than a given tolerance.

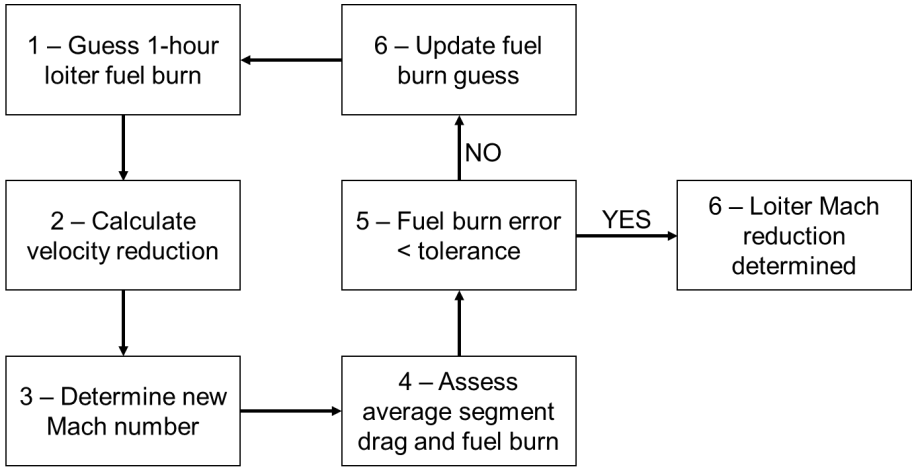

Figure 4.7: Iterative loiter performance calculations flow chart for fixed altitude and variable Mach number.

4.2.1.5 Hydrogen storage assumptions

The hydrogen fuel was assumed to be stored in its liquid state within cryogenic tanks. Gaseous hydrogen could be pressurised in tanks, stored in metal alloys that are able to absorb it (metal hydrides), or trapped in carbon nanotubes and glass microspheres [Colozza 2002]. However, all these solutions would be far too heavy for weight-sensitive applications.

Composite cryotanks The hydrogen cryotanks were assumed to be made of composites due to the recent development in composite materials for cryogenic hydrogen storage in space applications. In addition, they were assumed to be shaped as cylinders with hemispherical heads. For the present study, it was assumed that the weight of each composite cryotank is the 6.74% of the weight of the stored hydrogen—i.e. fuel weight upon tank weight is equal to 0.0674. The present value is based on public domain information about the Boeing composite cryotank design [Johnson, Sleight and Martin 2013]. This was sized to store 634.3 m^3 $(22,400 ft^3)$ of fuel, which is equivalent to 45,035 kg of liquid hydrogen assuming its density to be 71 kg/m^3; the published weight of the cryotank is 3,037 kg (6,696 lbs).

Load responsive multilayer insulation The available options to achieve an acceptable hydrogen boil-off are foams, aerogels, and multilayer insulation (MLI). Nonetheless, for a given number of insulation layers the MLI thermal performance is one order of magnitude better than foams [Verstraete et al. 2010] and gives a

sixteen-fold improvement over aerogels [Dye, Kopelove and Mills 2012].

However, MLI performance rapidly deteriorates for ambient pressures above 100 mPa, which means that a heavy vacuum shell is required. To minimise the overall weight of the insulation, Load-Responsive MLI (LRMLI) has been recently developed: a flexible 5-times-lighter vacuum shell can be integrated within the insulation layers, which is linked to a dynamic beam spacer that allows vacuum to be obtained when altitude is varying. As a result, for a given heat leak LRMLI is lighter than foams and aerogels [Dye, Kopelove and Mills 2010].

Thermal performance and weight Accurate thermal performance modelling and weight prediction for the cryogenic hydrogen storage system are beyond the scope of this thesis. However, it would be useful to estimate its boil-off and gravimetric efficiency.

The following equation allows the thermal performance of MLI to be estimated by accounting for the effects of ambient temperature, pressure, and different insulation layer materials [Verstraete 2009]:

$$q = C_1 \frac{N_t^{C_2}(T_H + T_C)(T_H - T_C)}{2(N+1)} + C_3\,\epsilon\,\frac{T_H^{4.67} - T_C^{4.67}}{N} + \frac{C_g\,P}{N}\,(T_H^{n_g} - T_H^{n_g}) \quad (4.24)$$

Where q is the heat flux (W/m^2) across the insulation, $C_1\,C_2\,C_3$ are empirical coefficients that describe the insulation layer materials, T_H and T_C are the hot and cold side temperature respectively, N_t is the layer density of the insulation (layers/cm), N is the total number of layers, C_g and n_g are coefficients that depend on the interstitial gas insulation, P is the ambient pressure, and ϵ is the emittance of the layers.

Hydrogen boil-off calculations can be performed with equation 4.25, where 446,000 J/kg is the hydrogen latent heat and the time is measured in seconds [Rapp 2007]. It was assumed that any heat input within the storage system will directly contribute to hydrogen vaporisation. With an aircraft take-off mass of 5,000 kg and a fuel fraction of 40%, 2,000 kg can be used as a reference hydrogen mass to perform boil-off calculations. Assuming the tank to be cylindrical with hemispherical heads, its size can be determined with equation 4.4. Thus, the tank surface area S_{tank} can

be defined.

$$M_{boil-off} = \frac{q \ t \ S_{tank}}{446,000 \ J/kg} \tag{4.25}$$

With the above information, it was possible to preliminary estimate the thermal performance of LRMLI when storing 2,000 kg of liquid hydrogen. As shown in figure 4.8, boil-off calculations were performed, varying the number of layers, for a 10-day loiter. The "take-off fuel" curve refers to the mass of fuel that needs to be stored within the aircraft to make sure that, after subtracting the boil-off, there will still be enough fuel available to complete the mission. The take-off fuel was computed iteratively, and the "available fuel" line is another output of the computations. Based on the present calculations, 14 layers of LRMLI would guarantee a 1% boil-off over a 10-day loiter.

About the weight of LRMLI, the weight of the insulation layers (in kg/m^2) for liquid hydrogen storage can be obtained from experimental data for one to four layers [Dye, Kopelove and Mills 2010, Table 1]. The insulation weight for a number of layers greater than four was obtained by linearly extrapolating the experimental data (fig. 4.9). Based on these calculations, 14 layers of LRMLI were preliminary estimated to weigh 242 kg. The tank weight, which is the 6.74% of 2,020 kg of fuel, was estimated to be the 135 kg. These figures led to a composite tank/LRMLI gravimetric efficiency of 84%, which is greater than the 60% of a state-of-the-art aluminium tank with foam insulation.

Based on these calculations, a 2% mission boil-off was assumed to also include the effect of climb and descent. In addition, the tank volume was assumed to be 2% greater than the fuel volume to account for contingencies and to permit unforeseen expansion of the liquid hydrogen without causing tank rupture or spills [Verstraete et al. 2010].

4.3 Results

The following sections assess the benefits of a high-bypass ratio distributed-fans propulsion system on the three selected airframes. The importance of the propulsion system design-point selection is initially presented (sect. 4.3.1). This is followed by a

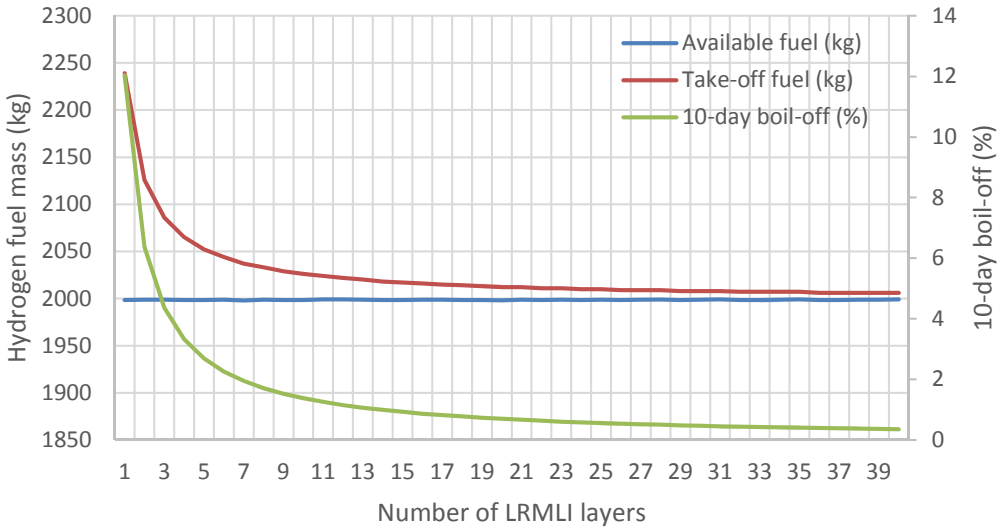

Figure 4.8: Boil-off calculations for a 10-day loiter as a function of the number of LRMLI layers. The take-off fuel is determined iteratively, so that the computed available fuel (take-off fuel minus boil-off) matches the required 2,000 kg to complete the mission.

study of the wing geometry effects on the design and performance of the integrated airframe-propulsion system (sect 4.3.2). The influence of varying the number of distributed fans is then presented (sect. 4.3.3), along with a design and performance comparison of the three selected airframes (sect. 4.3.4).

The distributed propulsion system architecture of Appendix C was considered, which includes a superconducting electric system that links the gas turbine engine with the distributed fans. The assumptions on the weight and size of the turbomachinery components are described in Appendix B. In the present Chapter a turbine entry temperature (TET) of 1,300 K and an overall pressure ratio (OPR) of 28 were considered as a baseline cycle. Conversely, Chapters 5 and 6 investigate the influence of conventional and hybrid Brayton cycles on the selected airframes. A TET of 1,300 K would allow to simplify the turbine design as the blades would be uncooled. The selected OPR would maintain the blade size at the high-pressure compressor exit between 9 and 15 mm throughout the considered range of take-off masses (5,000 kg to 15,000 kg).

4.3.1 Influence of propulsion system mass-flow scaling

The propulsion system scaling effect was found to have a significant impact when the aircraft take-off mass is varied from 5,000 kg to 15,000 kg. In fact, endurance

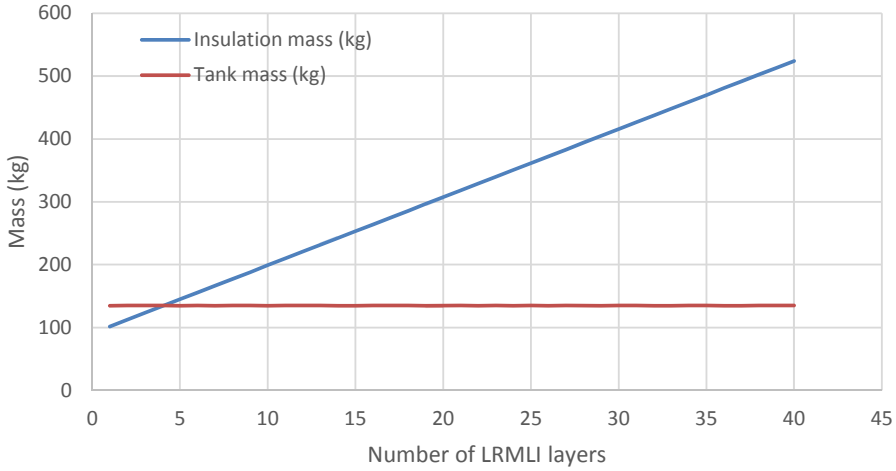

Figure 4.9: Insulation mass and tank mass as a function of the number of LRMLI layers. The insulation mass has been linearly extrapolated from Dye, Kopelove and Mills 2010.

increases by approximately 30% as the take-off mass increases although the fuel fraction remains fairly flat (fig. 4.10a). This is because the optimum SFC drops as the take top-of-climb thrust power requirement increases due to the payload secondary power requirement. Conversely, in the considered range of take-off masses the maximum endurance variation would be of eight hours if a fixed SFC was assumed. It is evident from figure 4.10a that on the T&W airframe one day of endurance would be missed by assuming a fixed SFC and neglecting the propulsion system scaling effect due to the payload power requirement.

The design point of the propulsion system was found to be affected by the 200 kW payload secondary power requirement. In fact, the optimum FPR increases when the propulsion system is scaled from a design point thrust of 2,129 N to 5,893 N, which are the top-of-climb thrust requirement for the T&W airframe with a take-off mass of 5,000 kg and 15,000 kg respectively (figs. 4.10c and 4.10d). This is because the power required by the fan system, which varies between 280 kW and 760 kW, is as big as the payload power. Thus, as the propulsion system is scaled up the greater mass flow makes more energy available in the core to drive the fans. As a consequence, the optimum FPR increases and the optimum SFC decreases. This effect can be observed when comparing figures 4.10c and 4.10d, where for a given core and BPR as the thrust requirement increases the SFC curves as a function of FPR dilates and shift downwards. Thus, for a given TET, OPR, and BPR the optimum SFC decreases as the thrust requirement increases due the payload power requirement (fig. 4.10b).

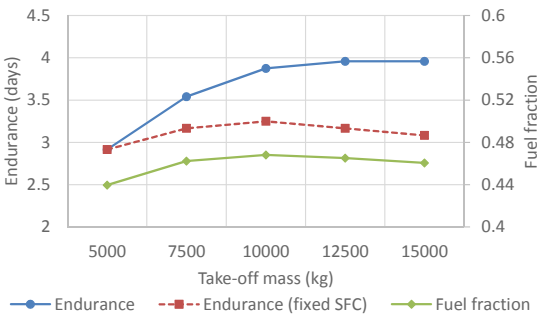

(a) Endurance and fuel fraction as function of take-off mass

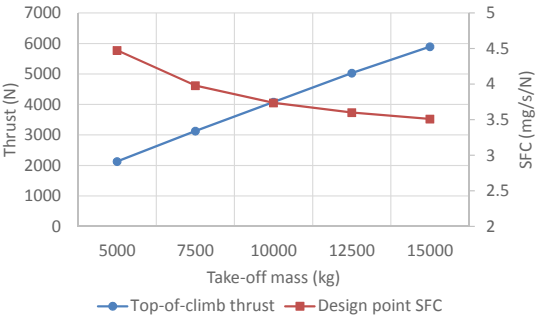

(b) Top-of-climb thrust and minimum SFC as function of take-off mass

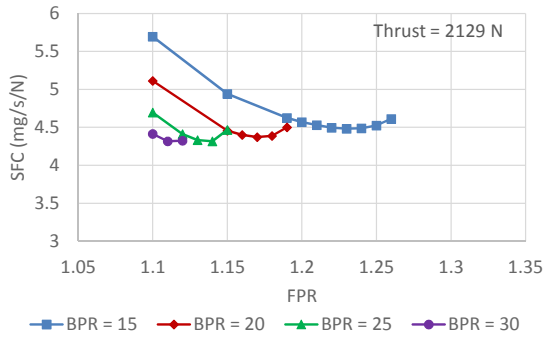

(c) SFC as function of BPR and FPR (thrust = 2129 N)

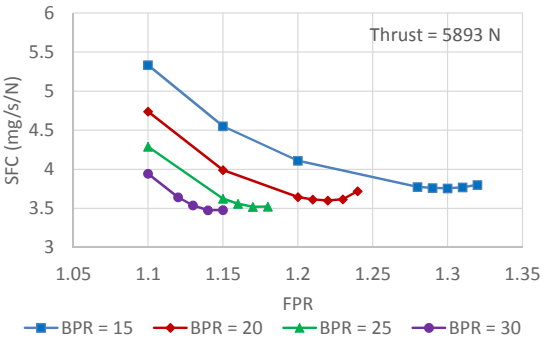

(d) SFC as function of BPR and FPR (thrust = 5893 N)

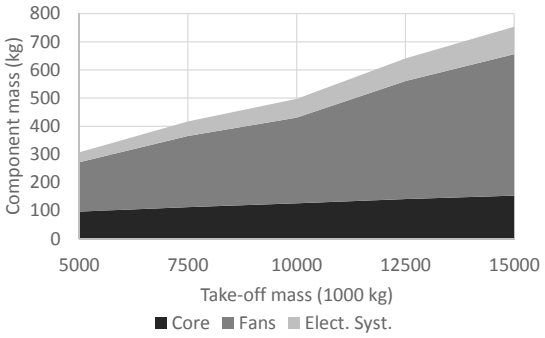

(e) Propulsion system weight breakdown as function of take-off mass

Figure 4.10: Influence of the propulsion system mass-flow scaling effects on the design and performance of the integrated airframe/propulsion system.

The weight of the propulsion system was also scaled as the take-off mass is varied (fig. 4.10e), which is essential to determine the overall aircraft system performance. The fan system accounts for the majority of the propulsion system weight, and the electric system represents the lightest component. This is mainly driven by two effects. Firstly, the selected power densities are of superconducting components

(see Appendix C). Secondly, the high-altitude requirement and the low TET lead to increased size and weight of the turbomachinery components due to the low air density and the increases mass flow.

4.3.2 Wing geometry effects

The influence of the wing loading selection on the overall UAV performance was assessed for all the considered airframes. For a given altitude and Mach, the wing loading depends on the design maximum lift coefficient, which was parametrically varied. For the T&W and triple-fuselage airframes, the wing aspect ratio was also parametrically varied being an independent design parameter. This was not the case on the BWB airframe as the fuel and the payload are stored in the inner wing. Thus the overall wing planform aspect ratio is a trade-off between the wing area and the internal volume requirements. It also worth noticing that the detailed results about the triple-fuselage airframe are not shown as the trends would be similar to those of the T&W airframe.

4.3.2.1 T&W and triple-fuselage design for long endurance

For the T&W airframe, endurance increases with an increase in wing loading and its maximum is achieved at the lowest considered aspect ratio (fig. 4.11a), which is in agreement with the findings of Altman [Altman 2000]. The design maximum lift coefficient was varied from 0.7 to 1.0 [Austin 2010] and 1.3 [Altman 2000] respectively for the considered altitude and Mach, and the wing loading was computed accordingly. The wing aspect ratio was varied in equal steps from 22 to 34, which are figures typical of low-speed HALE UAVs [Altman 2000].

The decrease in wing mass—due to the increase in wing loading and reduced aspect ratio—has the greatest impact on endurance. In fact, for a given take-off mass the lower structural fraction weight allows more fuel to be stored. This is why the point of maximum endurance in figure 4.11a corresponds to the point of maximum fuel fraction in figure 4.11b. The effect of having a lighter wing offsets the aerodynamic efficiency degradation, which drops from 27 to 23 for a wing aspect ratio of 22 (fig. 4.11c). For a given take-off mass, the propulsion system performance scaling due to the payload power requirement was found to be negligible. In fact, a maximum of five hours of endurance difference was found between scaling the

propulsion system properties (performance, size, and weight) and neglecting this effect when changing the wing loading and wing aspect ratio.

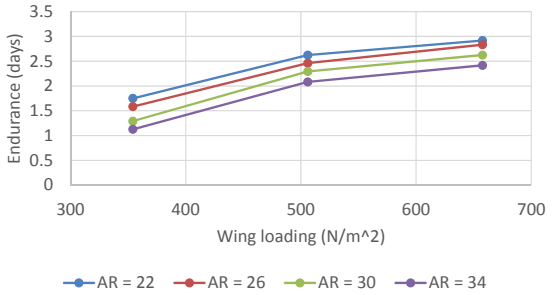

(a) Endurance as function of wing loading and wing aspect ratio

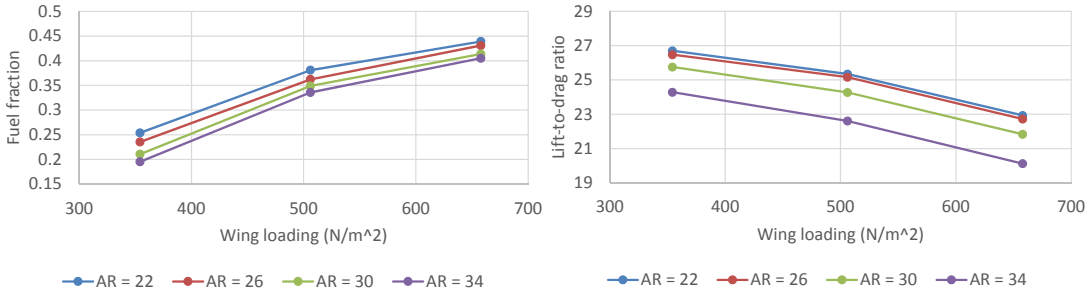

(b) Fuel fraction as function of wing loading and wing aspect ratio

(c) Loiter lift-to-drag ratio as a function of wing loading and wing aspect ratio

Figure 4.11: Influence of the wing geometry on the design and performance of the T&W airframe

4.3.2.2 BWB design for long endurance

The BWB airframe stores fuel in the centrebody of the aircraft, affecting its size and weight. Thus, the overall wing-planform aspect ratio is a trade-off between the internal volume and wing area requirements. This is different from the aforementioned T&W and triple-fuselage designs, where the wing aspect ratio is not constrained by the fuel and payload storage. As a consequence, when endurance is computed as a function of wing loading—for a given take-off mass—the trends are different from the more conventional airframes (fig. 4.12a).

Looking at a take-off mass of 5,000 kg, as wing loading increases the endurance exhibits a maximum and the decreases. This is because when moving from 405 to 455 N/m^2 (corresponding to a wing $C_{L,max}$ of 0.9) the reduced wing area results in a smaller outer-wing area because of the fuel volume constraint. Although the wing becomes structurally more efficiency and more fuel could be stored (fig. 4.12b), at

high wing loadings the lift-to-drag ratio deterioration becomes the prevailing effect fig. 4.12c. It is worth noticing that at 455 N/m^2 the overall wing planform aspect ratio is approximately 8.2, and a further increase in wing loading would result in an excessively small outer wing as the centrebody wing area and aspect ratio are set by the fuel volume requirement. Thus, the mutual interaction between the internal volume and wing area requirements results in an upper limit in wing loading for a practical design to be achieved.

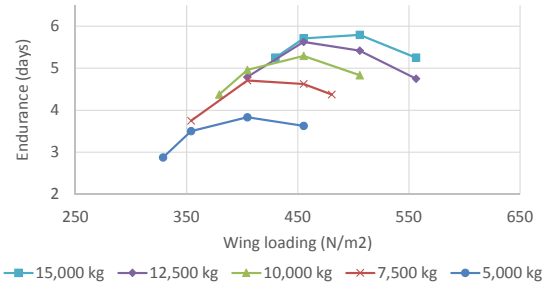

(a) Endurance as function of wing loading

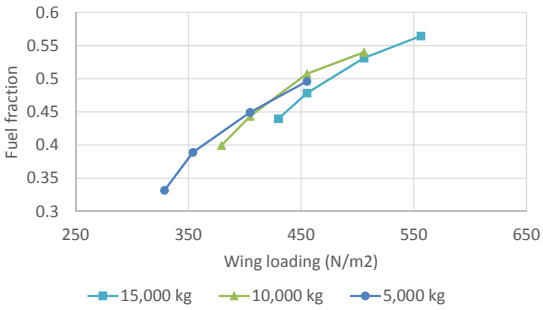

(b) Fuel fraction as function of wing loading

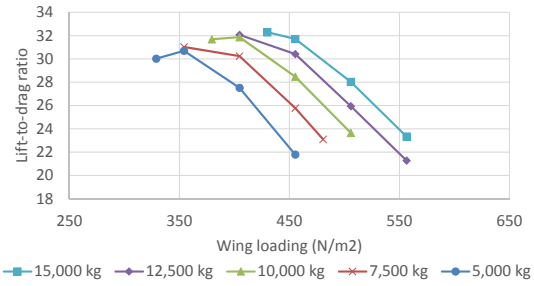

(c) Loiter lift-to-drag ratio as a function of wing loading

Figure 4.12: Influence of the wing geometry on the design and performance of the BWB airframe

Similarly to the T&W and triple-fuselage airframes, the take-off mass increase leads to a longer endurance due to the propulsion system drop in SFC because of the payload power requirement (fig. 4.10a). Differently from the more conventional airframes, the optimum wing loading for maximum endurance is not independent from the considered take-off mass. This is a consequence of the interaction between the internal volume and the wing area requirement.

4.3.3 Influence of distributed fans number

The impact of distributing the motor-driven fans on the considered airframes was found to have a limited impact on endurance. For the T&W airframe, a one-hour increase in endurance was found when increasing the number of fans from 2 to 10 (fig. 4.13b), and similar trends were also obtained for the triple-fuselage design. The fans were spaced from the wing root to the tip assuming a mutual spacing equal to 18% of the wing semi-span, a figure based on the existing low-speed HALE UAV designs. The mass of the wing structures was found to be nearly independent of the number of fans (fig. 4.13c). This is because the mass of the fans drops when their number is increased (fig. 4.13b), and so the change in wing bending-relief is negligible. Eventually, the one-hour improvement in endurance is mainly due to the fact that more fuel can be stored, for a given take-off mass, if the mass of the fans becomes lighter. However, this effect is mitigated by the increase in fans nacelle drag (fig. 4.13c).

For the BWB airframe the endurance increases linearly when the number of fans is increased, and for a given take-off mass the endurance variation depends on the considered wing loading (fig. 4.13a). In fact, the endurance increment varies from 0% to 11% as the wing loading is decreased. Thus, it is possible to observe that the optimum number of fans decreases as the wing loading increases. As for the T&W airframe, the endurance improvement is driven by the reduction in fans mass, which is replaced by fuel for a given take-off mass.

For the BWB airframe the effect of nacelle drag was not included in the calculations as the common-nacelle centrebody installation of the fans has a nearly neutral effect on the overall aircraft drag [Leifsson et al. 2013]. Although not shown in the present results, the effect of ingesting the inner-wing boundary layer with the distributed fans was also investigated and found to have a negligible impact regardless of the number of fans. In fact, the low-momentum flow represents just a small fraction of the fans-intake mass flow due to the low Mach number, and so the fans-power drop would be negligible.

4.3.4 Airframes comparison

It is useful to compare the three selected airframes once the influence of the main design parameters of the distributed propulsion HALE UAV system was established.

Based on the previous analysis, the T&W and triple-fuselage airframes were sized for a wing loading of 658 N/m^2 and a wing aspect ratio of 22, and the number of fans was fixed to two. In the case of the BWB airframe, the optimum wing loading and the fans number were determined for each take-off mass.

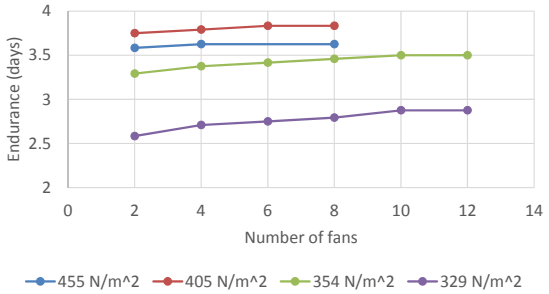

(a) Endurance as a function of the number of distributed fans and wing loading for the BWB airframe with a take-off mass of 5,000 kg

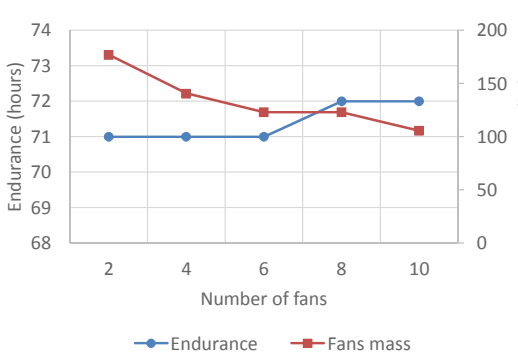

(b) Endurance and fans mass as a function of the number of distributed fans for the T&W airframe with a take-off mass of 5,000 kg and a wing loading of 658 N/m^2

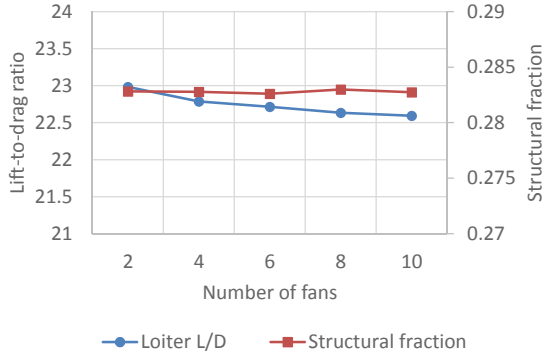

(c) Loiter lift-to-drag and structural fraction as a function of the number of distributed fans for the T&W airframe with a take-off mass of 5,000 kg and a wing loading of 658 N/m^2

Figure 4.13: Influence of the number of distributed fans on the design and performance of the T&W and BWB airframes

For the present low-speed application, the BWB airframe was found to outperform the T&W and triple-fuselage airframes by approximately two days of maximum endurance (fig. 4.14a), which is a 30% increase. This is because the BWB airframe has the greatest fuel fraction and aerodynamic efficiency (fig. 4.14b). Another interesting finding is the fact that the triple-fuselage and T&W endurances are very close. This is because for the triple-fuselage airframe the increase in fuel fraction was offset by the reduced aerodynamic efficiency due to the additional fuselages.

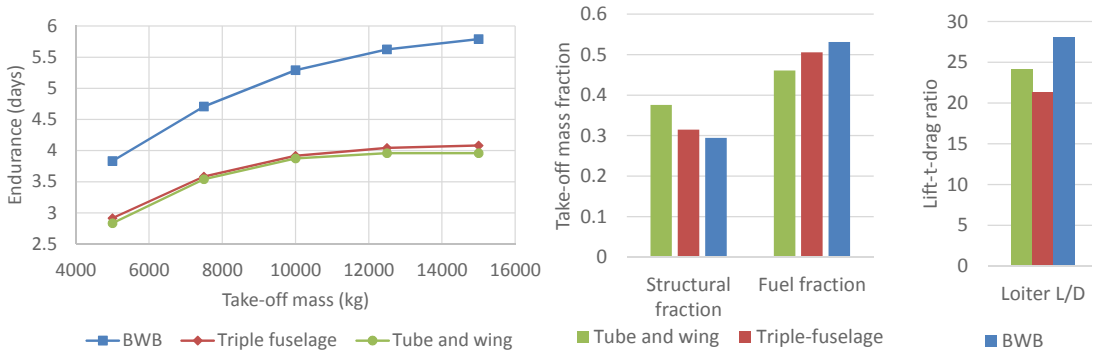

(a) Endurance as a function of take-off mass **(b)** Structural fraction, fuel fraction and loiter L/D

Figure 4.14: Design and performance comparison of the T&W, BWB, and triple-fuselage airframes

4.4 Limitations to the present study

There are three main assumptions that should be highlighted when drawing a conclusion from the present study. First of all, a remark must be made on the semi-empirical structural mass correlations that were used. Secondly, it is necessary to highlight the uncertainties of the BWB design due to the lack of previous designs.

4.4.1 Aircraft structural mass prediction

The present study highlighted that a wing aspect ratio of 22 would give the optimum endurance on the T&W and triple-fuselage airframes. This is because at greater aspect ratios the wing mass offsets any aerodynamic benefit due the reduction in lift-induced drag. However, the present structural correlations were built based on large civil aircraft in addition to light general-aviation aircraft and military fighters. The safety factors typical of civil design may not be applicable to HALE UAVs. As such, the optimum wing aspect ratio should be expected to be higher than what was predicted. This would lead to a greater aerodynamic efficiency of the T&W airframe, which would reduce the endurance gap with the BWB airframe.

4.4.2 BWB wing loading

The same wing lift-coefficient was assumed for both the inner and outer wings. This is usually not the case in passengers aircraft design, where the internal volume requirement results in a centrebody that could not have the same wing loading as the outer wing. However, in a HALE UAV design the internal volume requirement should be less stringent as mainly fuel and payload are stored. Detailed studies are required to assess the lift distribution of the overall BWB wing planform.

4.4.3 BWB hydrogen tanks

It would be difficult to install the hydrogen tanks within the BWB centrebody as they would interfere with the aircraft structures. This would have two effects. First of all, the aircraft structures would become less efficient and consequently heavier to support a given take-off mass. Secondly, smaller tanks might be required to fit into the ribs and spars of the inner wing. This would lead to a greater number of tanks, and so the overall storage system weight would increase.

The present study assumed a 5% volume penalty to account for the tanks installation within the airframe. However, with the present methodology it would not be possible to capture by how much the aircraft structure would become heavier or the tanks lighter. This is because a larger centrebody would reduce the overall structural mass, and so more fuel could be stored and the maximum endurance would increase. Also, a detailed arrangement of the wing structure was not available. Thus, it was not possible to shape the tanks and determine their number and weight with a bottom-up approach. Detailed studies are required to assess the hydrogen tanks integration, which would lower the maximum endurance predictions of the present study and narrow the gap with the baseline T&W airframe.

4.5 Concluding remarks

The aim of the present chapter was to build a flexible aircraft platform to assess the effect of integrating a distributed propulsion system on the design and performance of hydrogen-fuelled low-speed HALE UAV. A multidisciplinary approach to the aircraft conceptual design was adopted, which was tailored to endurance-aircraft

design. Three airframes were included in the present study. The T&W airframe was considered the baseline design. The triple-fuselage airframe was modelled as an advanced T&W configuration, in which the mass of the wing would be lightened by the bending-relief effect of the outer fuselages at the expense of a drag penalty. The BWB airframe was also assessed due to its low surface-to-volume ratio and efficient structures as the payload and the fuel are distributed across the wing root (i.e. the centrebody).

The propulsion system scaling effect was found to cause a 30% endurance improvement when the aircraft take-off mass is increased from 5,000 kg to 15,000 kg on the T&W airframe. The aircraft fuel fraction remains fairly constant when the aircraft take-off mass increases. However, the when the thrust requirement increases a larger mass flow is accelerated by the propulsion system. This leads to a lower SFC as more energy is available within the core, which can drive a higher pressure-ratio fan. The effect is due to the payload secondary power requirement of 200 kW, which is as big as the fans power requirement that varies between 280 kW and 760 kW in the considered range of take-off masses.

The BWB airframe was found to outperform the T&W and triple-fuselage airframes by approximately two days of maximum endurance, which is a 30% increase. This is because the BWB airframe has the greatest fuel fraction and aerodynamic efficiency. Another interesting finding is the fact that the triple-fuselage and T&W maximum endurances are very close. This is because for the triple-fuselage airframe the increase in fuel fraction was offset by the reduced aerodynamic efficiency due to the additional fuselages.

The conclusions of the present study are constrained by the assumptions on the structural mass predictions and on the BWB airframe. The semi-empirical structural correlations were mainly intended for civil applications, whose safety factor would be too stringent for a HALE UAV application. As such, it would be possible to increase the wing aspect ratio, for the given wing mass, to improve the T&W aerodynamic efficiency. In addition, the BWB results should be regarded as optimistic as integrating the hydrogen tanks may lead to a heavier aircraft empty mass. Detailed studies are required to assess the effective endurance benefits of the BWB airframe over more conventional designs.

Part II

Efficient Power Production

Chapter 5

Wave Rotor Gas Turbine Hybrid Cycles

5.1 Introduction

The wave rotor is a set of cylindrically-arranged channels that is able to perform compression, combustion, and expansion. Differently from turbomachinery components, compression and expansion are achieved through pressure waves. The wave rotor was conceived as a turbocharger for either piston engines or gas turbine engines. However, its lower-than-predictions efficiency prevented its wide-spread commercialisation on cars. On gas turbine engines, the turbomachinery components advanced to such a point that the wave rotor would be of little use to increase the engine pressure ratio. On the other hand, the wave rotor could still be useful in relatively small engines, as in the case of a HALE UAV, where the engine pressure ratio would be limited by the reduced blade size of axial turbomachinery.

The aim of this chapter was to build a methodology to assess the benefits of the wave rotor with internal combustion (WRIC) when integrated with a gas turbine engine—at an aircraft-integrated level. Thus, the goal was to assess by how much the performance of the integrated aircraft-propulsion system would be affected because of the cycle selection.

An introduction to the benefits and the limitations of the wave rotor technology is presented, along with an explanation of its inner-working principles. The methodology is then introduced, which focuses on the modelling of the wave rotor and

the centrifugal compressor. This technology was also considered as it would be the most reliable and well-established solution to overcome the size constraints of axial turbomachinery. The results quantify the benefits of the WRIC for a distributed propulsion system and for the integrated aircraft-propulsion system. Prior to the concluding remarks, the limitations to the present study are exposed along with a qualitative assessment of the further non-performance benefits of a wave rotor.

5.1.1 Wave rotor is a turbocharging technology

A wave rotor is an array of rotating cylindrically-arranged channels that compress and expand air by means of pressure waves (fig. 5.1). The wave rotor spins between two stationary end-plates, whose ports allow the inlet and outlet flow to be controlled. Both ends of each channel are periodically exposed to different pressures as the wave rotor spins. The combined effects of pressure differential and rotation cause pressure waves inside the rotor channels, which allow the flow to be compressed or expanded without being deflected by a blade or an impeller. This is the reason why the wave rotor is also referred to as a "pressure exchanger".

The wave rotor was initially conceived as a solution to increase the pressure ratio by topping gas turbine cycles (fig. 5.2). In the early 1940s, the Brown Boveri Company (BBC, which later became Asea Brown Boveri ABB) designed a wave rotor for the British Railways as a topping stage for a 1,640 kW locomotive gas turbine [Akbari, Nalim and Mueller 2006]. In fact, in the early stages of the gas turbine development the compressor components had a limited pressure ratio. Today, on large engines the same benefits could be simply achieved by increasing OPR with axial turbomachinery. The work of BBC later resulted in the Comprex, a wave rotor turbocharger for automotive diesel engines and perhaps one of the most commercialised wave rotor applications. The development of the Comprex started in the early 1970s and was not commercialised until the 1987 on the Mazda 626 Capella diesel engine [Smith et al. 2012]. Although more the 150,000 were built using this technology, the idea was later abandoned as the Comprex efficiency proved to be lower than expected.

Recent wave rotor applications looked at a small gas turbine engines, such as helicopter applications and micro gas turbines for de-centralised power generation. Similarly to a centrifugal compressor stage, in a small engine a wave rotor would be able to increase the cycle OPR as this is limited by the blade size constraints

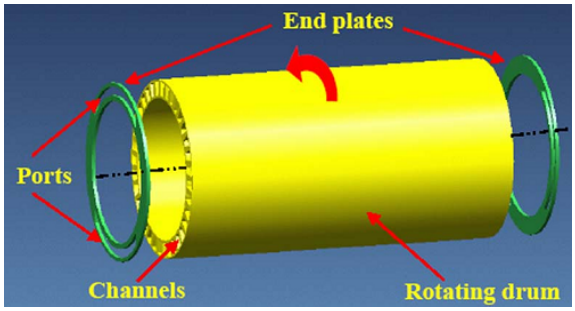

Figure 5.1: Schematic configuration of a typical wave rotor [Akbari, Nalim and Mueller 2006]

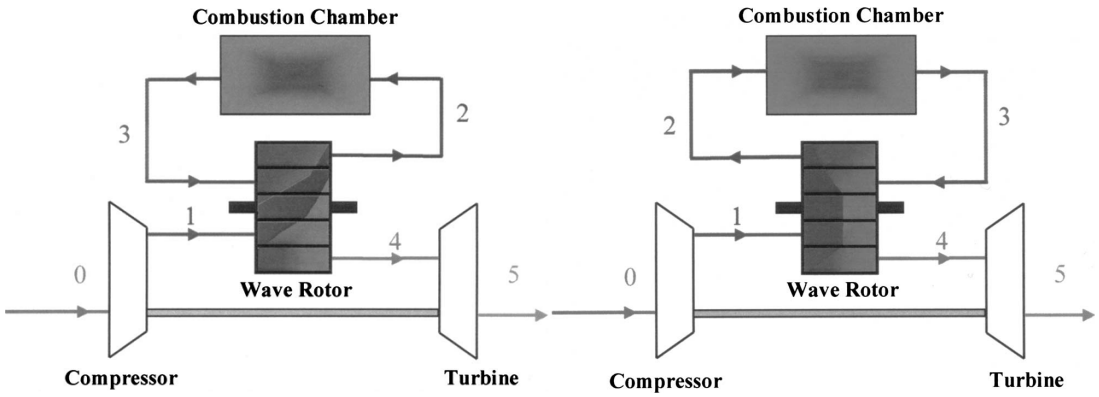

(a) Through-flow four-port wave rotor cycle **(b)** Reverse-flow four-port wave rotor cycle

Figure 5.2: Schematic of a gas turbine topped by a through-flow (left) and reverse-flow (right) four-port wave rotor [Akbari, Nalim and Mueller 2006]

of axial turbomachinery. This is why a wave rotor could be of interest for a HALE UAV due to its reduced thrust/power requirement. A common wave rotor design for GT topping is the four-port layout, where two ports receive air and two ports discharge air. The wave rotor would receive flow form the compressor outlet (1) to compress it and discharge it to the combustion chamber (2). After the combustion process (3), the flow would be delivered back to the wave rotor itself where it is expanded (4) before being delivered to the turbine (fig. 5.2).

This process can occur with the hot flow and the cold flow either moving in opposite directions along the wave rotor channels (fig. 5.2a) or following the same direction (fig. 5.2b). The first configuration is usually referred to as a through-flow (TF) layout, whereas the second one is indicated as a reverse-flow (RF) solution. Although both configuration would give the same performance benefit, in the TF arrangement also makes the wave rotor a self cooled device. This is because a channel where the flow is at his peak temperature (i.e. combustor outlet) is adjacent to a

channel where the air is at the lowest temperature (i.e. compressor outlet). In principle, this would allow the cycle to reach a higher peak temperature compared to the maximum temperature that can be attained with blade cooling. However, moving to higher peak temperatures also affects NO_x emissions, particularly above 1,850 K where the thermal nitrous-oxide emissions start proceeding at a significant rate [Lefebvre and Ballal 2010].

5.1.2 Wave rotor exchanges pressure with scavenging and discharge processes

The inner working of the wave rotor is schematically represented in figure 5.3. The picture represents the flow evolution inside a wave rotor channel, where the rotation effect is represented by moving from the bottom to the top of the figure. The initial conditions at the bottom of the channel refer to that of the combusted gases. The inner working process can be divided in two parts: the scavenging process and the discharge process.

In the scavenging process, the cold air is sucked into the wave rotor channel and compressed while the hot air is discharged to the turbine. Initially, the rotation exposes the channel combusted gases to the turbine exhaust port, which allows the flow to exit. An expansion fan of waves is created because of the sudden exposure to a lower pressure outside of the wave rotor. The waves then cross the channel until they reach the opposite end. At this point, the waves are reflected back and a depression is created in the channel. At the same time, the rotation exposes the channel to the compressor outlet, which is at a higher pressure than that of the channel. Thus, the compressor air is sucked into the wave rotor channel due to a combination of the rotation and depression effects. As soon as the turbine-outlet port closes a pressure wave (called hammer shock) is generated, which compresses the air inside the channel.

In the discharge part the cold air—which has been compressed twice—is delivered to the combustion chamber while the hot combustion chamber air is sucked into the channel. Initially, the channel air is exposed to a high-pressure end as the rotation brings the channel in contact with the combustion chamber gases. A second hammer shock compresses the channel air—which is now at its highest pressure—while the combusted gases enter the channel. After that, the rotation exposes the channel to the combustion-chamber exhaust port. This happens as soon as the hammer

shock has reached the opposite end-plate (i.e. at the end of the second compression process). As a consequence, the high-pressure gases are delivered to the combustion chamber.

It should be clear that the inner working of the wave rotor is a dynamic process, where the hot and the inlet flows exchange pressure by means of pressure waves. The size, timing and position of the inlet and outlet ports, combined with the channel size, are the main variables that govern this process.

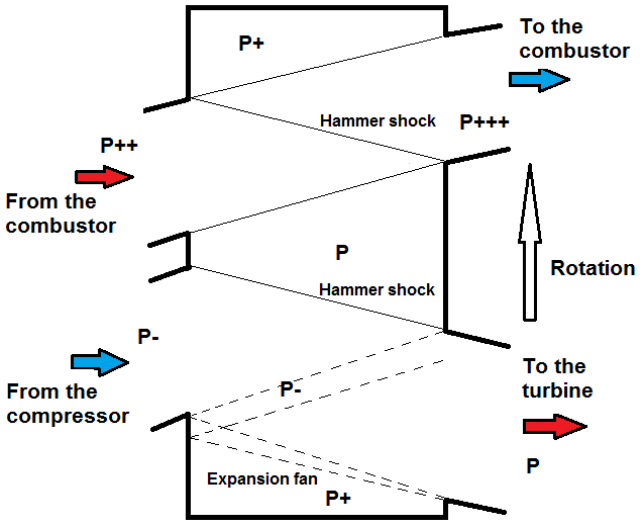

Figure 5.3: Pressure wave system scheme in a 4-port wave rotor [Righi 2014]

5.1.3 Wave rotor with internal combustion

It is also possible to achieve combustion within a wave rotor, so that the pressure-drop typical of a (near) constant-pressure combustor can be replaced by a pressure gain. The wave rotor with internal combustion (WRIC) is characterised by a constant-volume combustion. This is due the fact that the combustion process occurs in a confined volume if both the inlet and outlet ports are closed.

Although constant volume combustion can lead to a lower entropy rise, in the WRIC this is offset by the exhaust gas residuals. In fact, not all the combusted gases inside the channels are delivered to the turbine. As such, when the combustion process occurs the residual gases from the previous combustion are simply heated and compressed. This inefficiency would be further accentuated by an ignition mechanism that relies on recirculating hot gases rather than by a separate ignition source such as a spark plug [Akbari and Nalim 2009].

The WRIC pressure gain is a function of the temperature rise inside the component itself. Thus, by increasing the temperature rise inside the WRIC it is possible to achieve a greater cycle efficiency as both its peak temperature and OPR would increase. However, when a WRIC is used its outlet pressure is greater than that of the compressor delivery air. This would make turbine cooling unfeasible as it would not be possible to discharge the compressor air back into the main gas path after cooling the turbine blades. This would constrain the cycle TET to the operating temperature of uncooled superalloys blades, which is in the order of 1,350 K [Rubini 2014]. The double benefit of having a temperature and pressure gain should lead to greater benefits compared to a pure pressure gain offered by, for example, a traditional centrifugal compressor. In fact, this is the preferred choice on small engines.

If the cycle TET is a constraint, it is possible to increase the WRIC temperature gain by mixing its outlet air with some "cold" air before delivering it to the turbine. This could be done by mixing the WRIC outlet air with the compressor delivery flow if part of this bypasses the WRIC itself (fig. 5.4). Although mixing two flows at different pressures and temperatures is not an ideal process, this mixing loss should be compensated by a sufficiently high WRIC temperature—and consequently pressure—gain.

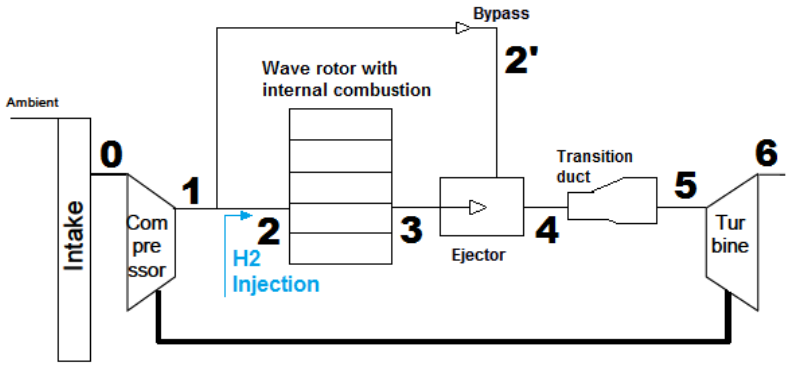

Figure 5.4: WRIC cycle layout including the wave rotor bypass [Righi 2014]

Bypassing the WRIC and mixing its outlet flow with the compressor delivery air was initially proposed in a U.S. patent [Nalim 2003]. This concept relies on the "ejector", a pipe that is able to efficiently mix the WRIC and compressor flows (fig. 5.5). In addition to the different temperatures and pressures, the mixing process is further complicated by the fact that the unsteady WRIC flow is mixed with the continuous compressors flow. The ejector needs to mix the flows so that the turbine would receive a near-constant stream of air.

Feeding a turbine with an unsteady flow has become common in the state-of-the-art automotive piston engines. The WRIC can be assumed to generate a flow non-uniformity similar to that of a piston engine due to its high number of channels and rotational speed [Akbari, Nalim and Mueller 2006]. As such, it should be considered feasible to integrate the WRIC with a turbine in a similar fashion.

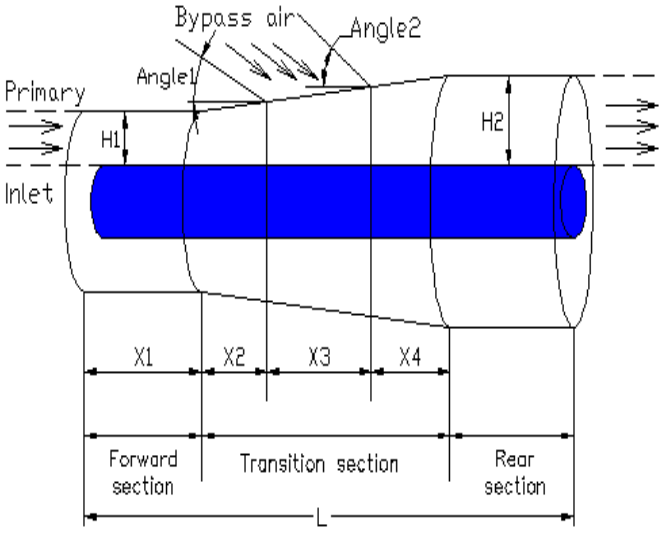

Figure 5.5: Ejector schematic [Geng and Nalim 2004]

5.1.4 Limitations of the wave rotor technology

The wave rotor technology, with and without internal combustion, is limited by the following considerations:

Leakage between the rotor and the end-plates A finite gap exists between the wave rotor and the static end-plates. Thus, a fraction of the flow both at the inlet and at the exit of the wave rotor would leave the main gas path. In addition to improving the sealing, this issue could be mitigated in the WRIC case by introducing a bypass around the wave rotor (sect. 5.1.3).

Ducting Transition ducts are necessary to link the gas turbine components with the wave rotor. Turbomachinery components are characterised by an annular cross-section, whereas the wave rotor exchanges flow with partial-annulus ports. The main issues are the variable shape and area of the ducts as well as turns up to a 180°. Experimental and 3D CFD studies predicted a maximum pressure loss of 6.5% [Weber and Snyder 1998; Welch, Slater and Wilson 2007].

Combusted gas recirculation A fraction of the combusted gases is not delivered to the turbine and remains in the wave rotor channels after the closure of the turbine-exhaust port. Such a source of inefficiency is common to the wave rotor both with and without internal combustion. These "buffer" gases typically account for a 40% to 50% of the total wave rotor flow [Li, Akbari and Nalim 2007].

Unsteady flow Delivering unsteady flow to the turbine hinders its capability to extract work. Experimental tests predicted a performance loss of 10% or worse when a turbine extracts work from non-uniform flow [Ward and Miller 2012]. However, the uniformity of the flow can be controlled by means of the rotational speed and the number of channels. According to Nalim, 50 fast-spinning channels are enough to deliver a nearly uniform wave rotor outlet flow [Akbari, Nalim and Mueller 2006].

Trade-off between friction and swirl losses As the ports of the end-plates do not open and close instantaneously, losses would arise in the form of flow vortices. This could be offset by designing a smaller wave rotor channel, so that the opening and the closure would occur in a reduced time. However, this would increase the friction losses inside the wave rotor channels. Thus, a trade-off between these two loss mechanisms must be found in terms of channel size.

5.2 Methodology

The aim of the present study was to build a methodology to assess the benefits of the wave rotor with internal combustion when integrated with a GT engine—at an aircraft-integrated level. Thus, the goal was to assess by how much the performance of the integrated aircraft-propulsion system would be affected because of the cycle selection.

In a relatively small engine, as in the case of a HALE UAV, the OPR would be limited by the blade size at HPC exit for a given TET. The OPR limit would result in a thermal efficiency limit for the engine itself. The WRIC would act as an extra compressor, and an OPR increase would lead to a higher cycle efficiency. However, this could also be achieved with a centrifugal compressor, which was also included in the study for comparison purposes. The WRIC would also improve the cycle

efficiency because of the higher cycle peak temperature, particularly when part of the compressor air bypasses the WRIC to mix with its outlet flow (sect. 5.1.3).

The present methodology initially focuses on the thermodynamics of the WRIC, which was modelled with a set of zero-dimensional analytical correlations (sect. 5.2.1). The modelling of the centrifugal compressor is then introduced, which was assessed with a set of analytical correlations to account for its losses (sect. 5.2.2). The modelling of the axial compressor efficiency degradation due to the reduced blade height is also described (5.2.3). This allowed to define the performance of the baseline engine with axial turbomachinery components only. The engine size and weight calculations are described in Appendix B. Lastly, the off-design assumptions are discussed as the engine SFC variation at loiter needs to be accounted to predict an accurate aircraft endurance (sect. 5.2.4).

5.2.1 Wave rotor with internal combustion

5.2.1.1 Performance

The model of Li, Akbari and Nalim was considered to assess the performance of the wave rotor with internal combustion [Li, Akbari and Nalim 2007]. The authors proposed a zero-dimensional model based on an analytical formulation. All the wave rotor losses (e.g. leakage, friction) are included by defining appropriate isentropic efficiencies for the compression and the expansion phase. The model was modified to include the effect of the presence of air, fuel, and combusted gases as in the original model only air was considered.

It was assumed that both air and hydrogen fuel enter the WRIC channels. The different flows were assumed to be at the same pressure and to mix instantaneously. The processes inside the WRIC are divided in three phases (fig. 5.6):

- Compression of the inlet air from state 2 to state A
- Combustion of both the inlet air/fuel mixture and the residual gases to from state A to state B
- Expansion from to state B to state 3 as the flow is delivered to the turbine

The calculations start from the exhaust, where an exit Mach number needs to be defined. This usually ranges between 0.3 and 0.7 [Li, Akbari and Nalim 2007], and

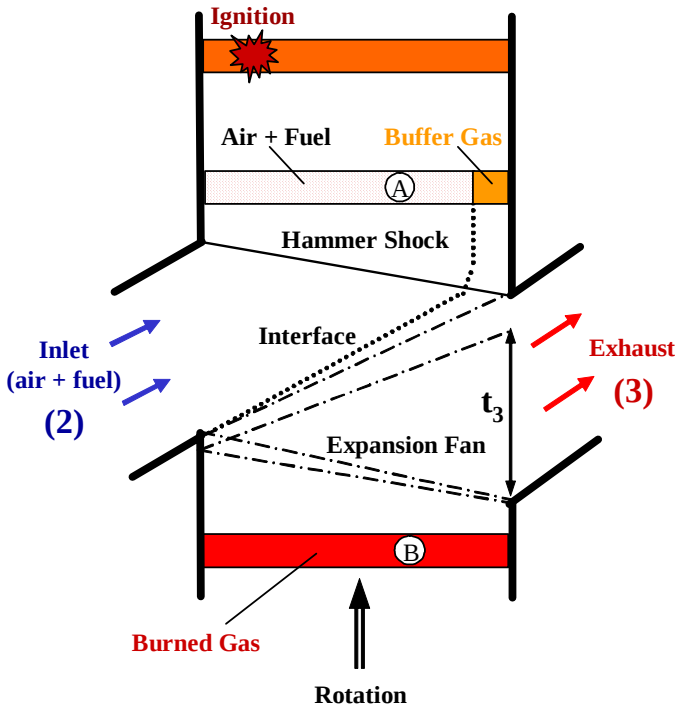

Figure 5.6: Wave pattern in a developed view of the combustion wave rotor [Li, Akbari and Nalim 2007]

a value of 0.7 was chosen in the present project. Choosing the upper bound of this range represents an optimistic assumption. In fact, with a greater exit Mach number the WRIC becomes more efficient as more residual gases can be exhausted to the turbine. This is due to the stronger expansion wave when the turbine-exhaust port opens. Decreasing the amount of residual gases from the previous combustion makes more room available for fresh air to enter the WRIC and improves its combustion efficiency.

It is possible to determine the static temperature at the WRIC exhaust exit (station 3) and the combustion peak temperature (station B) by using the isentropic relations (eqs. 5.1 and 5.2).

$$T_{3,static} = \left(1 + \frac{\gamma M_3}{2c_P}\right)^{-1} \tag{5.1}$$

$$T_B = T_{3,static}\left(\frac{\gamma - 1}{2} M_3 + 1\right)^2 \tag{5.2}$$

The ratio of the exhaust time t_3 over the WRIC channel length is calculated as shown in equation 5.3. This is necessary to calculate the fill fraction μ, which

represents the ratio between the inlet flow (air + fuel) upon the sum of the inlet flow and the residual gases from the previous combustion (5.4).

$$\frac{t_3}{L_{rotor}} = \frac{1}{a_B}\left(\frac{2/(\gamma-1)}{2/(\gamma-1)+M_3}\right)^{\frac{1+\gamma}{2(1-\gamma)}}\frac{2}{1+M_3} \tag{5.3}$$

$$\mu = \frac{M_{fuel+air}}{M_{fuel+air}+M_{residual}} = \frac{t_3}{L_{rotor}}\frac{\rho_3}{\rho_B}M_3 a_3 \tag{5.4}$$

The density ratio $\frac{\rho_3}{\rho_B}$ can be calculated from the ideal-gas equation of state (eq. 5.5), where $\frac{P_B}{P_{3,static}}$ can be assessed as the flow properties at station B and 3 were defined (eq. 5.6).

$$\frac{\rho_3}{\rho_B} = \frac{P_{3,static}}{P_B}\frac{T_B}{T_{3,static}} \tag{5.5}$$

$$\frac{P_B}{P_{3,static}} = \frac{P_B}{P_3}\frac{P_3}{P_{3,static}} \tag{5.6}$$

The isentropic expansion from station B to station 3 allows the stagnation pressure and temperature ratios to be defined (eqs. 5.7 and 5.8), where $T_{3,id}$ is found by introducing the WRIC isentropic efficiency of expansion (eq. 5.9).

$$R_{gas} ln\left(\frac{P_3}{P_{3,static}}\right) = \int_{T3,static}^{T_3} \frac{c_P}{T} dT \tag{5.7}$$

$$R_{gas} ln\left(\frac{P_B}{P_3}\right) = \int_{T3,id}^{T_B} \frac{c_P}{T} dT \tag{5.8}$$

$$\eta_{WRIC,exp} = \frac{\int_{T_{3,id}}^{T_B} c_P dT}{\int_{T_3}^{T_B} c_P dT} \tag{5.9}$$

After the properties of the gases between stations 3 and B were assessed, it is possible to calculate the flow characteristics between stations A and B (i.e. before

and after the combustion process). It was assumed that both the buffer gases and the inlet flow (air + fuel) are at the same pressure P_A, whereas their temperatures differ and were indicated as T_{rA} and T_A respectively. The pressure gain during the combustion process can be expressed as a function of the fill fraction μ and of the flow temperatures (5.10). This allows T_A to be calculated by replacing the ratio P_B/P_A with the isentropic relation for the compression between T_{rA} and T_B)(eq. 5.11)

$$\frac{P_B}{P_A} = \mu\frac{T_A}{T_B} + (1-\mu)\frac{T_{rA}}{T_A} \tag{5.10}$$

$$T_A = \frac{T_B}{\mu}\left[exp\left(\frac{-\int_{T_{rA}}^{T_B}\frac{c_P}{T}dT}{R_{gas}}\right) - (1-\mu)\frac{T_{rA}}{T_B}\right] \tag{5.11}$$

The residual gases temperature after compression T_{rA} was assessed with an energy balance on the wave rotor. In fact, the overall WRIC inlet-to-outlet enthalpy rise to achieve a given outlet temperature depends on the variation of flows internal energy and on the heat addition (eq. 5.12). The outlet temperature would be either the TET (if bypass $\epsilon = 0$) or the temperature that allows the TET to be achieved after mixing with the compressor air that bypassed the WRIC (which has to be guessed and iteratively changed for $\epsilon > 0$) . Equations 5.11 and 5.12 were solved simultaneously to assess the T_A and T_{rA} by means of the Newton-Raphson methods [Righi 2014].

$$h_3 - h_2 = h_{gas} - h_{air+fuel} = [u_{gas}(1+f) - u_{air} - u_{H_2}f] + \frac{1-\mu}{\mu}\int_{T_{rA}}^{T_B} c_V dT \tag{5.12}$$

Similarly to the expansion process, it is possible to introduce a WRIC isentropic efficiency for the compression (eq. 5.13). This allows the pressure ratio of the WRIC compression process from station 2 to station A—i.e. the pure compression process due to the pressure waves and not due to the constant-volume combustion pressure gain—to be determined (eq. 5.14).

$$\eta_{WRIC,comp} = \frac{\int_{T_2}^{T_{A,id}} c_P dT}{\int_{T_2}^{T_A} c_P dT} \tag{5.13}$$

$$R_{gas} ln\left(\frac{P_A}{P_2}\right) = \int_{T_2}^{T_{A,id}} \frac{c_P}{T} dT \tag{5.14}$$

Finally, the overall WRIC pressure ratio can be calculated by combining the initial compression ratio (2 to A), the pressure gain (A to B), and the expansion ratio (B to 3) (eq. 5.15).

$$\frac{P_3}{P_2} = \frac{P_A}{P_2}\frac{P_B}{P_A}\frac{P_3}{P_B} \tag{5.15}$$

The fuel to air ratio is calculated as the enthalpy difference between the exhaust products and the inlet flow (air + fuel), which is divided by the LHV of hydrogen fuel to make it non-dimensional (eq. 5.16).

$$f = \frac{h_{gas} - h_{air} - h_{H_2}}{LHV_{H_2}} \tag{5.16}$$

The key efficiency parameters of the cycle are reported in table 5.1. A 90% isentropic efficiency was assumed for both the compression and the expansion of the WRIC [Li, Akbari and Nalim 2007]. The effect of mixing the steady flow from the compressor with the discontinuous WRIC flow, which would also be at different temperatures and pressures, was modelled by assuming a mixing efficiency of 43% [Ward and Miller 2012]. This mixing occurs within the ejector (figs. 5.4 and 5.5), which then delivers flow to a transition duct that exhausts the mixed flow to the turbine. A pressure loss of 6.5% was assumed based on experimental results [Welch, Slater and Wilson 2007].

Parameter	**Value**
WRIC expansion isentropic efficiency	90%
WRIC compression isentropic efficiency	90%
Ejector efficiency	43%
Transition duct pressure loss	6.5%

Table 5.1: Key efficiencies and losses of the hybrid GT/WRIC cycle

5.2.1.2 Sizing and weight

The wave rotor with internal combustion was sized by assuming a four-port design with a hub-to-tip ratio of 0.7 and a tip speed of 100 m/s [Wilson and Paxson 1996]. The exhaust time is calculated as the time that the wave rotor needs to complete a 45° rotation, which is a reference literature value for the exhaust port angular width [Welch, Slater and Wilson 2007]. The exhaust-time-to-rotor-length ratio can be calculated as to equation 5.3. Multiplying this ratio by the exhaust time allows the rotor length to be determined.

The weight of the wave rotor was estimated by assuming two main components: the wave rotor itself and its casing. The wave rotor was assumed to be made of Nimonic superalloy given the high temperatures it should withstand. The casing was assumed to be made of aluminium. An 8 mm thickness was assumed for the wave rotor inner/outer cylindrical walls and the for the end plates. This is because they would be exposed, although intermittently, to high peak temperatures and also rotation-induced mechanical stresses for the rotor itself. A 2 mm thickness was assumed for the thickness of the casing, which acts as a pressure vessel for the bypass flow. A thickness of 1 mm was assumed for the walls separating the wave rotor channels, smaller than that of the outer walls as the radial pressure distribution along the rotor would compress the channels on both sides. The number of channels was calculated by assuming a height-to-width ratio of 5 [Wilson and Paxson 1996].

5.2.2 Centrifugal compressor

The centrifugal compressor performance was modelled with a set of optimum loss models [Oh, Yoon and Chung 1997]. These analytical correlations were selected out of all the empirical models available in the literature for each loss mechanism. The equations relate each loss mechanism to the main characteristics of the impeller (inlet and outlet hub/tip diameters, length, blade metal angles, RPM) and to the thermodynamic properties of the inlet mass flow (temperature and density). The detailed sizing of the centrifugal compressor is described in [De La Cruz Arevalo 2015].

The correlations selected by Oh, Yoon and Chung, which were validated against experimental data (fig. 5.7), account for the following loss mechanisms:

1 **Incidence loss**, which is due to the difference between the air inflow angle and the blade metal angle.

2 **Blade loading loss**, which is caused by the blade-to-blade circumferential pressure difference and results in a diffusion that produces secondary flows.

3 **Clearance loss**, which is generated by the flow leaking through the clearance gaps and labyrinth seals and moving backwards to the low-pressure regions.

4 **Skin friction loss**, also known as wall friction loss and generated by the fluid flowing over the impeller surface.

5 **Mixing loss**, which is generated by the mixing of the impeller exit flow with the downstream undisturbed flow.

6 **Vaneless diffuser loss**, which is caused by the flow leaving the impeller and being decelerated in the diffuser.

7 **Recirculation loss**, which is a consequence of the extra work that the impeller has to spend to compress the air that flows back from the diffuser due the favourable pressure gradient.

8 **Disc friction loss**, which arises from the friction between the impeller and the flow trapped between the impeller and the casing.

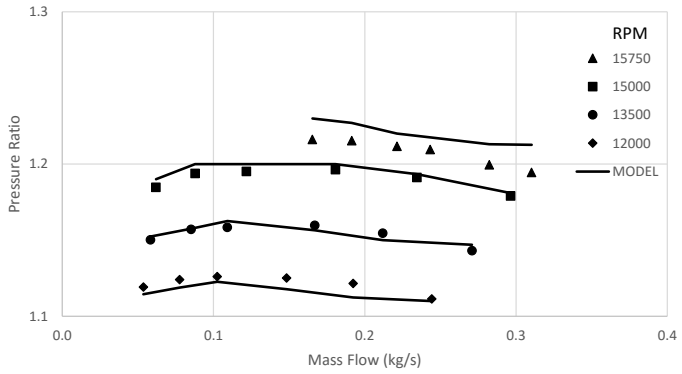

Figure 5.7: Comparison of the centrifugal compressor model of Oh, Yoon and Chung 1997 against experimental results [De La Cruz Arevalo 2015]

5.2.3 Axial compressor tip clearance loss

An analytical correlation was used to predict the compressor efficiency degradation as its annulus area reduces. The selected correlation (eq. 5.20) is presented in section

5.2.3.1 and benchmarked against other public domain correlations. This analytical equation was then implemented into an iterative calculations framework to assess the change in engine size and performance due to the degradation effect (section 5.2.3.2).

5.2.3.1 Public domain correlations

For axial turbomachinery, the public domain includes several correlations to estimate the efficiency degradation effect due to the reduced blade size. Many authors tried to correlate these losses to the main compressor design parameters (e.g. stage loading, flow coefficient, tip clearance as a percentage of the blade height, blade aspect ratio). The correlation proposed by Robinson was selected for the present study (eq. 5.20)[Robinson 1982]. A brief review of the available correlations is proposed below, which clarifies the aforementioned choice.

Lakshminarayana proposed a semi-empirical correlations to estimate the change in blade efficiency $\Delta\eta_b$ (eq. 5.17) [Lakshminarayana 1970]. The equation was built with the lifting-line theory, which is commonly used to model aircraft wings and propeller blades. However, it was found that this correlation is suitable only for low-speed compressors, whereas it would not be appropriate for high-speed compressors [Robinson 1982]. Schmidt concluded that the correlation of Lakshminarayana grossly overpredicts the tip clearance losses after comparing its predictions with experimental results for centrifugal compressors [Schmidt 1985]. The author concluded that the inaccuracy was due to the difference in stage loading as in his experiments he was using values that were five time greater to that of Lakshminarayana (0.5 against an average of 0.1).

$$\Delta\eta_b = \frac{0.7\lambda\psi}{cos\beta_m}\left(1 + 10\sqrt{\frac{\phi}{\psi}\frac{\lambda A}{cos\beta_m}}\right) \tag{5.17}$$

Hasselgreaves presented a correlation that relates the efficiency degradation to the kinetic energy loss in the clearance gap (eq. 5.18) [Hasselgreaves 1969]. However, Schmidt concluded that this correlation gives a good agreement only for single-stage machines.

$$\Delta\eta = \eta_{To}\frac{\Delta\psi_d}{\psi_o} \tag{5.18}$$

Kyprianidis and Rolt recently proposed a correlation to estimate the isentropic efficiency degradation of a large turbofan high-pressure compressor (eq. 5.19) [Kyprianidis and Rolt 2014]. The correlation is simpler than the previous ones as it considers only the blade height of the last stage. However, its simplicity makes it specific only to compressors whose blade size is smaller than 13 mm. In fact, the equation would not return any meaningful result for a blade height greater than 13 mm.

$$\Delta\eta_{HPC} = 0.12 \left\{ 1 - \left[\frac{1}{\left(\frac{h_{b,HPC}}{13}\right)^{0.6}} \right] \right\} \tag{5.19}$$

Lastly, Robinson built a correlation that relates the polytropic efficiency degradation of a compressor stage to its hub-to-tip ratio (r_H/r_T) and its clearance-gap-to-blade-height (g/h) ratio (eq. 5.20) [Robinson 1982]. This correlation was selected for the present project as it offers a trade-off between simplicity and accuracy. Firstly, it takes only the blade, disc, and gap dimensions as an input, which were available from the preliminary sizing of the turbomachinery components (see appendix B). Secondly, this correlation gave the best agreement with the experimental data, which considered stage loadings that are aligned to that of the present work.

$$\Delta\eta = \frac{2.74}{1 + r_H/r_T} \frac{g}{h} \tag{5.20}$$

5.2.3.2 Calculations framework

An iterative framework of calculations was built to assess the efficiency degradation of the high-pressure compressor (fig. 5.8). The selected correlation (eq. 5.20) allows the variation in polytropic efficiency to be assessed for a given annulus geometry. Thus, this correction was applied stage-by-stage throughout the compressor.

Initially, the compressor performance is modelled by assuming a polytropic efficiency of 0.92—a reference value for the 2025-2035 timeframe [Mourouzidis 2015]—with no degradation effects. This allows the compressor to be sized based on its mass flow and thermodynamic properties (see appendix B). As the blade height and hub-to-tip ratios are determined, it is then possible to correct the stage polytropic efficiency with equation 5.20. A clearance gap of 0.5 mm was assumed throughout the compressor. The compressor performance can then be re-assessed with the new

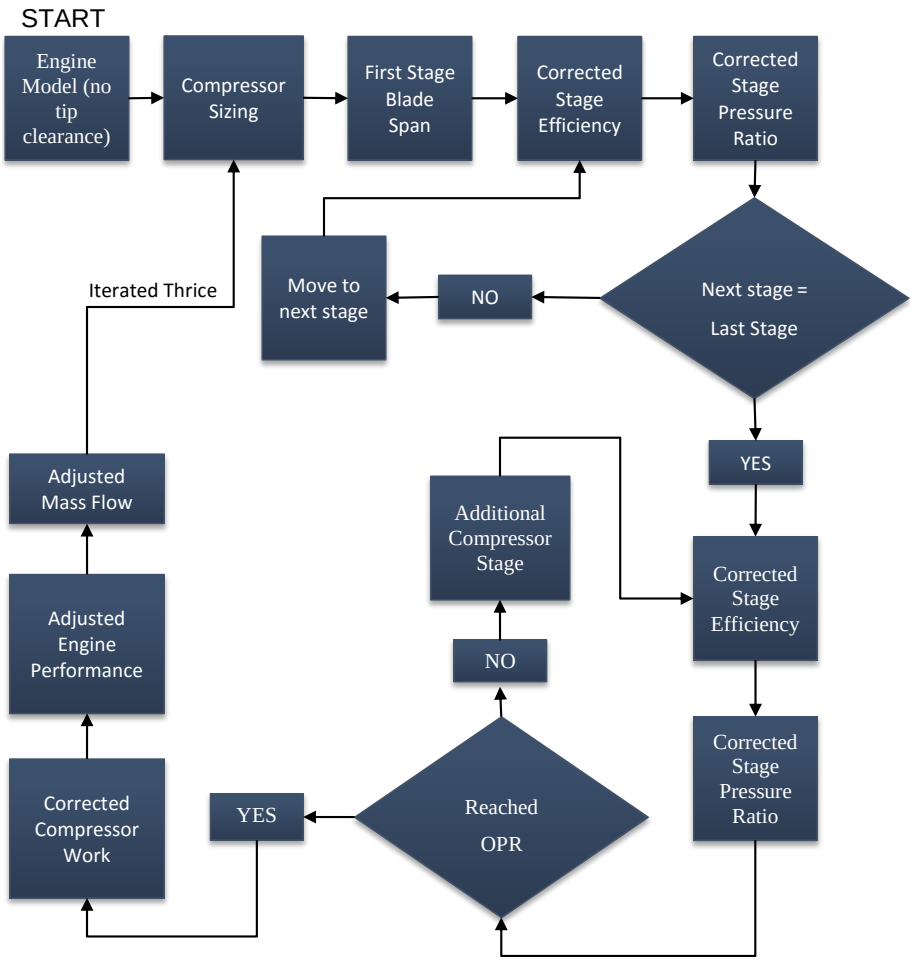

Figure 5.8: Iterative framework of calculations to assess the tip clearance effect on axial compressors [De La Cruz Arevalo 2015]

polytropic efficiencies, so that a new pressure ratio is calculated for each stage. A stage temperature rise of 50 K was considered, and stages were subsequently added to reach the design-point OPR. Consequently, the compressor work and the engine performance need to be re-assessed. An increase in mass flow should occur due to the decrease in the stages polytropic efficiency. The new mass flow can then be fed back into the sizing calculations to repeat the aforementioned steps. It was found that after three iterations the algorithm would converge to a stable solution.

5.2.4 Off-design considerations

The off-design performance of each cycle was modelled with Turbomatch, Cranfield University gas turbine performance simulation software. The engine off-design behaviour was expressed as an SFC variation from the design-point value (fig. 5.9a) as

the loiter thrust reduces (fig. 5.9b). A variation percentage from the design point was considered because the design-point SFC would change every time the aircraft is resized throughout the endurance calculations (see section 3).

The effect of moving towards higher temperatures and pressures was found to have quite an impact on the off-design SFC-variation (fig. 5.9a). Particularly at the end of the loiter (approx. Mach 0.23), the loiter SFC variation doubles when moving from the highest-temperature (1,600 K) to the lowest-temperature (1,200 K) cycle. Ultimately, the SFC variation at off-design is driven by a degradation of the turbomachinery components efficiency. This depends on the quasi non-dimensional mass flow $W\sqrt{T}/P$, and the greater its variation from the design-point the bigger the components efficiency degradation. For a given drop in engine power output (fig. 5.9b), in a high-temperature cycle the $W\sqrt{T}/P$ variation is smaller than that of a low-temperature cycle. This is because in a high-temperature cycle the design-point mass flow is smaller, and consequently its "absolute" off-design variation will be smaller than that of a low-temperature cycle.

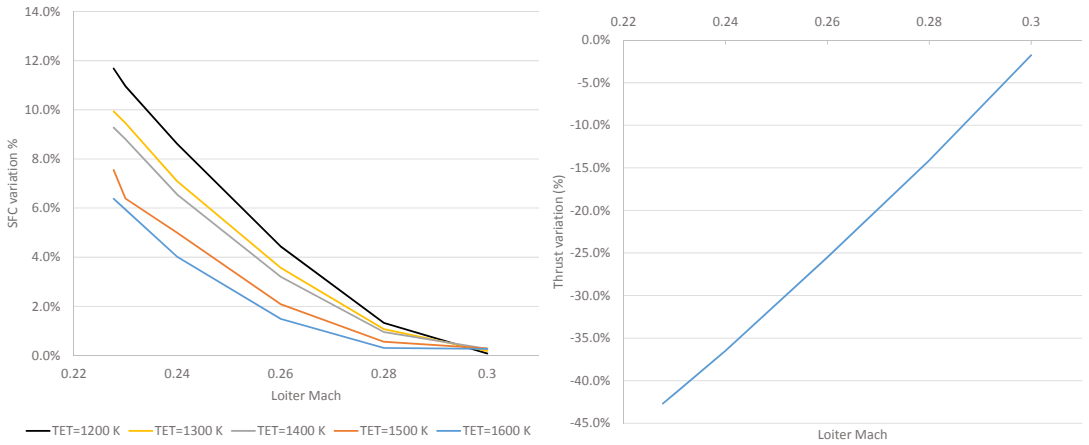

(a) Off-design SFC variation from design point as a function of Mach

(b) Aircraft thrust variation from top-of-climb as function of loiter Mach

Figure 5.9: Core engine off-design and aircraft loiter characteristics

Turbomatch would only be able to assess the off-design behaviour of a Brayton-cycle engine, and the WRIC model of section 5.2.1 would be unable to predict the wave rotor off-design performance. However, Welch, Jones and Paxson explained that when the wave rotor is modelled as a set of compressor and turbine on its own shaft the off-design performance of this fictitious cycle becomes very similar to that of the "real" hybrid WRIC/GT cycle [Welch, Jones and Paxson 1997]. This is because the off-design behaviour of the hybrid WRIC/GT cycle is dominated by the turbomachinery components [Jones and Welch 1996]. Thus, the wave rotor

was modelled in Turbomatch as a third shaft, i.e. as an extra compressors after the axial HPC and as an additional turbine before the axial HPT. In reality, these considerations were strictly valid only for a wave rotor without internal combustion, so that the wave rotor would simply top the GT engine (fig. 5.2). It was assumed that these findings could also be extended to a wave rotor with internal combustion.

5.3 Results

This section quantifies the benefits of the hybrid WRIC/GT cycles compared to that of the Brayton cycles. These also included the option of adding a centrifugal compressor stage at the back of the HPC. In addition, the effect of having two core engines instead of one—which might be a design choice for reliability purposes—is shown.

The results initially focus on a turboshaft engine analysis, which allows the core to be isolated from the propulsors (sect. 5.3.1). This investigation was also used to integrate the present cycles with the distributed propellers (sect. 8.3.6). The turbofan analysis is then presented (sect. 5.3.2), which is followed by the integrated aircraft-cycles studies that assessed the impact of selecting a different cycle on the aircraft endurance (sect. 5.3.3).

5.3.1 Turboshaft results analysis

5.3.1.1 Hybrid WRIC/GT cycles improve thermal efficiency

The hybrid WRIC/GT cycles offered thermal efficiencies up to 64%, approximately 7% greater than a high-temperature Brayton cycle (fig. 5.10a). This result refers to a hybrid WRIC/GT cycle with a TET of 1,300 K, a compressor pressure ratio PR_{comp} of 65, and a WRIC bypass ϵ of 2.

It can be noticed that the effect of introducing a bypass flow around the wave rotor is graphically represented by a vertical shift of the thermal efficiency curves (fig. 5.10a). This is different to what would occur by increasing the TET of a Brayton cycle, where the thermal efficiency curves would overlap for a low PR_{comp} to then diverge for a high PR_{comp}. The vertical shift of the hybrid-cycle thermal efficiency curves is due to the increase in cycle peak temperature (fig. 5.10c), an effect that

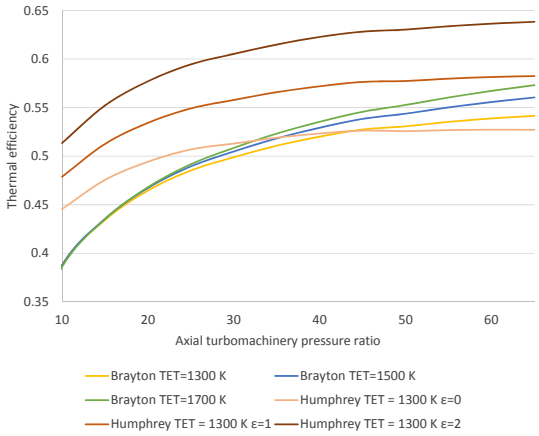

(a) Thermal efficiency for the Brayton and hybrid WRIC/GT cycles

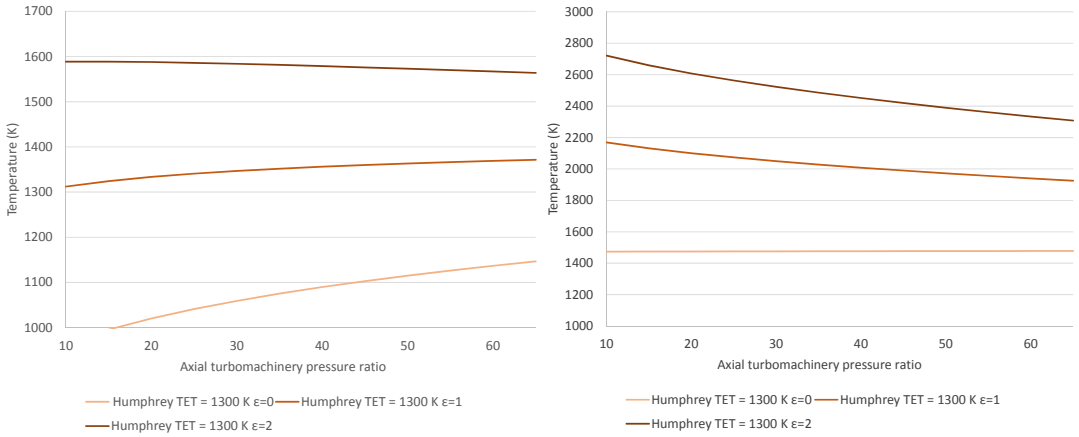

(b) Hybrid WRIC/GT cycles maximum average temperature between WRIC flow and WRIC-bypass flow

(c) Hybrid WRIC/GT cycles peak tempearature

Figure 5.10: Thermal efficiency comparison between the Brayton cycles and the hybrid WRIC/GT cycles as a function of OPR, TET, and WRIC-bypass ϵ. An altitude of 50,000 ft and a Mach of 0.3 were considered.

occurs at any PR_{comp}. However, differently from a high-temperature Brayton cycle the hybrid-cycle thermal efficiency curves are more flat at high pressure ratios. The hybrid-cycles trends preserve the characteristics of a low-temperature (TET = 1,300 K) Brayton cycle. This should not be surprising given the fact that the cycle TET is effectively the same as only a fraction of the core mass flow experiences a greater peak temperature.

The hybrid cycle would offer benefits only when a bypass ϵ greater than zero is considered. In fact, if no bypass is considered the inlet temperature of the wave rotor becomes greater with an increase in PR_{comp}. As explained in section 5.1.3, the TET is limited to 1,300 K due to turbine cooling issues. Thus, the wave rotor outlet-to-

inlet temperature ratio would be limited. This would limit the wave rotor pressure ratio as the two are related, with a consequent reduction in the wave rotor efficiency. It is for this reason that when no bypass ϵ is considered the hybrid WRIC/GT cycle performs worse than the Brayton cycle at high PR_{comp}.

The performance of the hybrid cycle improves and offsets that of the Brayton cycle when a bypass around the wave rotor is introduced. When the bypass ϵ is considered, the wave rotor receives a reduced amount of mass flow. For a given TET, its outlet temperature needs to be greater than if all the compressor flow was delivered to the wave rotor. This is because the wave rotor flow mixes with the "cold" compressor delivery air before being delivered to the turbine. Thus, when a bypass around the wave rotor is introduced its temperature ratio increases. This leads to a higher wave rotor pressure ratio, a greater OPR, and consequently to a gain in thermal efficiency—even when a 6.5% pressure loss in the transition duct is considered (table 5.1).

The greater wave rotor temperature ratio leads to a higher cycle peak temperature (fig. 5.10c). This reduces as the PR_{comp} increases due to the higher compressor delivery temperature when a bypass is considered. The results indicate that a peak temperature of about 2,300 K would be reached inside the wave rotor. It needs to be noticed that above 1,800 K the combustion products become unstable and dissociate into simpler molecular and atomic species. This process absorbs a significant amount of energy, which limits the flame temperature that can actually be achieved [Lefebvre and Ballal 2010]. On the other hand, the engines of military fighter aircraft are able to achieve TETs in excess of 2,000 K. It is clear that the peak temperature that could be achieved inside the wave rotor is limited by operational factors, which at the moment would be difficult to assess in the absence of an actual wave rotor design. As such, a bypass ϵ equal to one should be considered a pessimistic assumption, whereas a bypass of two should be regarded as an optimistic one.

Similarly to a counter-flow heat exchanger design, a four-port wave rotor is a self-cooled device. This implies that the wave rotor integrity would not be compromised even when the peak temperature is well above the operational limits of uncooled superalloys. This was verified by looking at the average temperature between the bypass flow (i.e. the compressor air) and the peak temperature inside the wave rotor. The results indicate the average temperature is always below 1,600 K for the considered WRIC bypasses, which is close to the maximum blade metal temperature of modern cooled blades (fig. 5.10b). Also, the bypass flow would be twice the mass

flow inside the wave rotor when $\epsilon = 2$, meaning that potentially the maximum metal temperature could be below the average of 1,590-1,570 K shown in picture 5.10b.

5.3.1.2 Compressor efficiency degradation leads to 2.5% maximum thermal efficiency loss

The compressor efficiency degradation resulted in a maximum thermal efficiency degradation of 2.5% (fig. 5.11a) if a blade size constraint of 8 mm is imposed (fig. 5.11e). A maximum thermal efficiency degradation of 4% would occur at pressure ratios beyond this blade size limit. The results refer to a 1 MW of engine power output, which is representative of the power requirement of the engine at top-of-climb. If the same power output was delivered by two core engines instead of one, then the maximum thermal efficiency degradation would be 5-6% (fig. 5.11b). This case was considered to examine the effect of using multiple core engines for reliability purposes.

The effect of thermal efficiency degradation due to the reduced blade height is more noticeable on the hybrid WRIC/GT cycles. This occurs regardless of the whether the power output is delivered by one or two core engines (figs. 5.11a and 5.11b). When the compressor performance degrades, the same PR_{comp} is achieved at the expense of a higher exit temperature. This would reduce the WRIC outlet-to-inlet temperature ratio as the outlet temperature is fixed by the TET requirement. The lower temperature ratio leads to a reduced compression ratio inside the wave rotor, which degrades the cycle performance. Thus, the degradation effect is more noticeable on the hybrid cycle because it negatively affects both the turbomachinery and the wave rotor.

The thermal efficiency degradation when PR_{comp} increases is driven by a reduction in the HPC isentropic efficiency (figs. 5.11c and 5.11d) as the blade size reduces (fig. 5.11e and 5.11f). When an 8 mm blade height is considered, the maximum isentropic efficiency degradation ranges between 6% and 7% depending on the power output. As expected, the effect is more noticeable on the Brayton cycles as the TET increases. A similar effect occurs when the WRIC bypass is increased. However, the hybrid cycles have a higher compressor isentropic efficiency compared to the 1,700 TET Brayton cycle although the peak temperature is beyond 2,000 K. This is because in the hybrid cycles the core intake mass flow is greater than that of the high-temperature Brayton cycle as not all the mass flow is combusted.

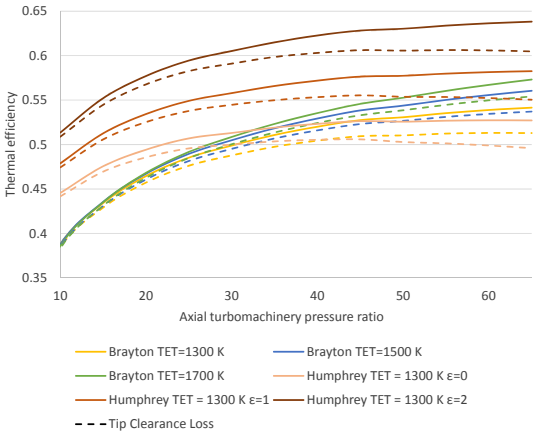

(a) Thermal efficiency for the Brayton and WRIC cycles – 1 MW power output

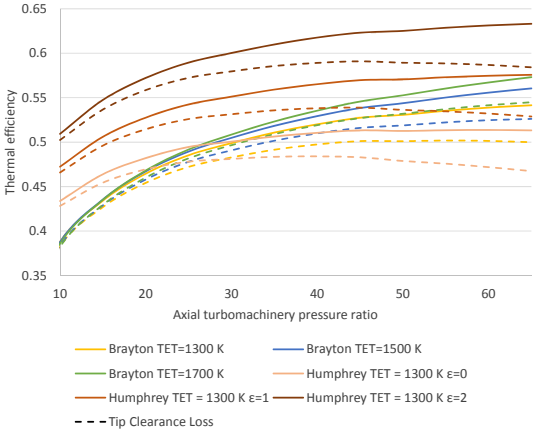

(b) Thermal efficiency for the Brayton and WRIC cycles – 500 kW power output

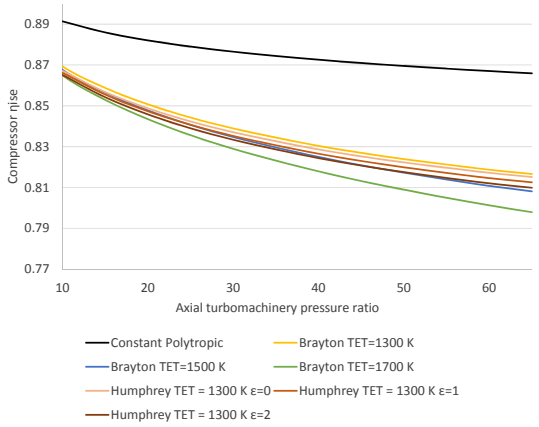

(c) Compressor isentropic efficiency – 1 MW power output

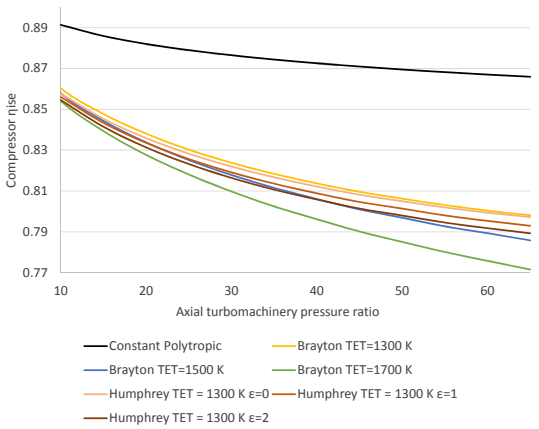

(d) Compressor isentropic efficiency – 500 kW power output

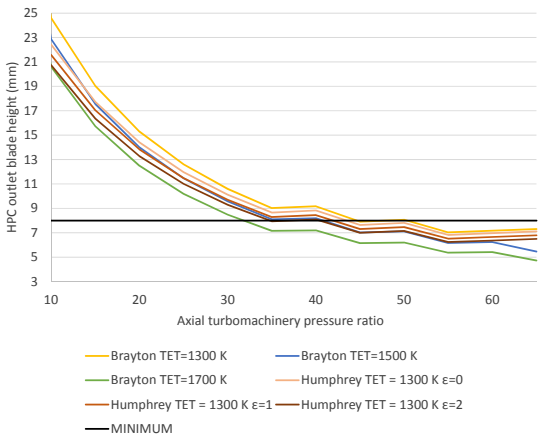

(e) HPC outlet blade height – 1 MW power output

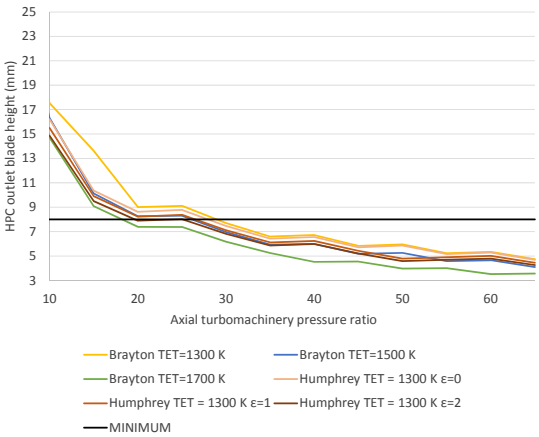

(f) HPC outlet blade height – 500 kW power output

Figure 5.11: The effect of compressor polytropic efficiency degradation on thermal efficiency, compressor isentropic efficiency, and blade height. Both the 1 MW and the 500 kW cores were modelled to study the effect of selecting the number of cores. An altitude of 50,000 ft and a Mach of 0.3 were considered.

The mass flow effect also explains why the blade size of the hybrid cycles is greater than that of the high-temperature Brayton cycle (figs. 5.11e and 5.11f). It is also possible to notice that, as expected, a smaller blade size is achieved at a lower pressure ratio when a 500 kW core is considered instead of a 1 MW one. In addition, the curves show some flat-trend regions whenever a new compressor stage is added.

This study considered an 8 mm blade height as the minimum achievable. In reality, today's engine have a blade height greater than that, usually in the order of 10 to 13 mm, even in very high temperature/pressure and small-size engines. This is usually the case for large high-BPR turbofans or relatively low-mass-flow engines for fighter aircraft or high-speed HALE UAVs. However, a 10-13 mm blade size limit would result in a very stringent PR_{comp} limit, in the order of 10 to 20 for the high-temperature Brayton cycle (TET = 1,700 K) depending on the engine power output.

It was the author's choice to lower this limit to 8 mm. This is because the same hub diameter was considered throughout the LP and HP compressors to keep the preliminary design calculations manageable for a wide range of temperatures and pressures (see Appendix B). In a detailed engine design it might be possible to decrease the HPC hub diameter to increase the blade height, although that would result in a greater tip speed.

5.3.2 Turbofan results analysis

For both the Brayton and hybrid WRIC/GT cycles, the compressor efficiency degradation effect resulted in a higher SFC for a given specific thrust (figs. 5.12 and 5.13). Conversely, for a given SFC the degradation effect results in a reduced specific thrust, which leads to an increase in the propulsion system weight and drag. Ultimately, the major constraint in selecting the design point is the blade height rather than the efficiency degradation. The results refer to a thrust of 5,900 N, which is representative of the top-of-climb thrust of the T&W airframe at an altitude of 50,000 ft and a Mach of 0.3. The BPR was fixed to 25 and the optimum FPR was considered in each case.

On a turbofan engine, the hybrid WRIC/GT cycle offers a double benefit. When the bypass around the wave rotor increases both the specific thrust increases and the SFC decreases (fig. 5.13). This means that increasing the WRIC bypass results in an engine that is lighter, produces less drag, and consumes less fuel. This is quite

different to what occurs in a Brayton-cycle turbofan engine, where a higher TET cycle leads to a higher specific thrust but also to a higher SFC. It is also possible to notice that the hybrid cycle trends have a longer horizontal trait. This means that, compared to the Brayton cycle, a smaller SFC range is achieved in a wider specific thrust variation.

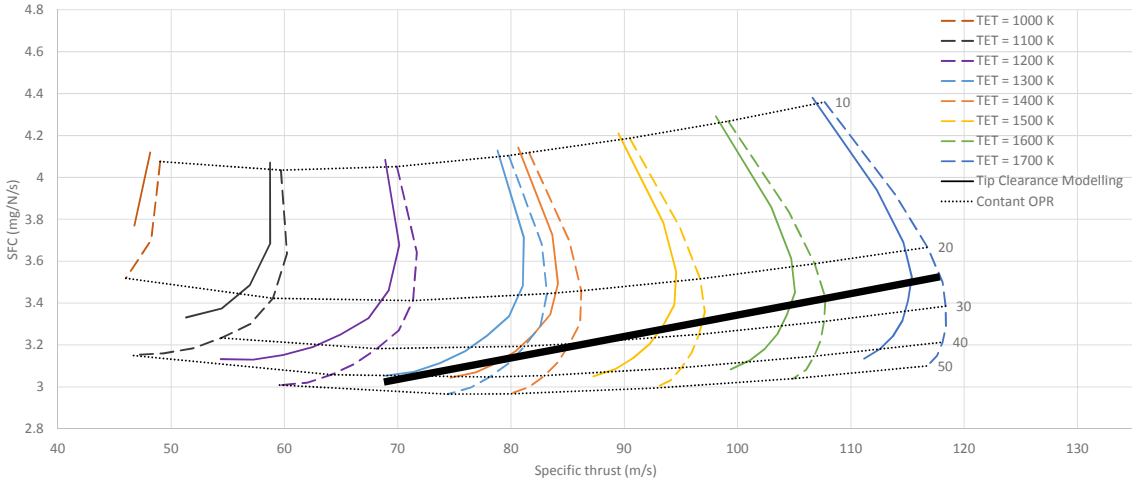

Figure 5.12: SFC as a function of specific thrust with (solid lines) and without (dashed lines) the compressor efficiency degradation effect for the Brayton cycle. The thick black line marks the region of achievable OPRs bases on the component blade size

5.3.3 Integrated aircraft-cycle studies

The aim of this section is to integrate the effects of the propulsion system weight, SFC, and drag on the performance of the integrated aircraft-propulsion system. Both the T&W and the BWB airframes were considered. Different cycles were investigated to assess—at an aircraft-integrated level—the benefits of the hybrid WRIC/GT cycles compared to the Brayton cycles. These also included the effect of adding a stage of centrifugal compressor at the back of the HPC. In addition, the influence of having two core engines instead of one, which could be a design choice for reliability purposes, was also assessed. This resulted in an axial turbomachinery PR limit, which was also complemented by other adding a WRIC or a centrifugal compressor (table 5.2). The first part of this section focuses on the propulsion system BPR selection (sect. 5.3.3.1), which was consequently fixed to 25 to compare all the considered cycles at an aircraft-mission level (sect. 5.3.3.2).

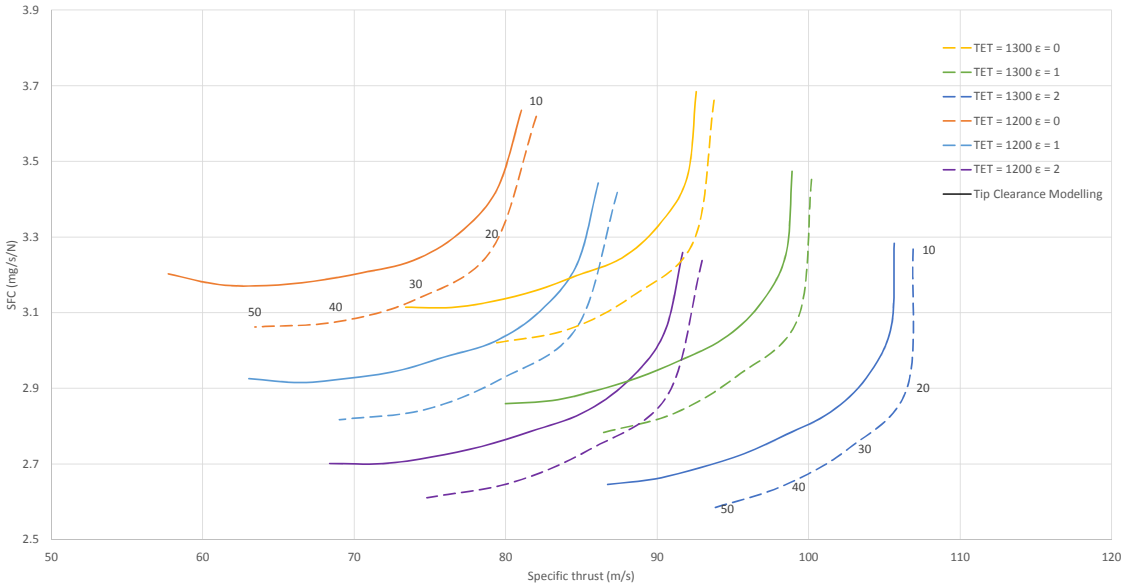

Figure 5.13: SFC as a function of specific thrust with (solid lines) and without (dashed lines) the compressor efficiency degradation effect for the WRIC cycle

TET (K)	1200	1300	1400	1500	1600
Max PR_{axial} (1 core)	45	50	50	40	40
Max PR_{axial} (2 cores)	30	30	25	25	25
Centrif. compr. PR	1.701	1.693	1.752	1.744	1.841
WRIC PR ($\epsilon = 2$)	–	1.148	–	–	–

Table 5.2: Maximum pressure ratio for the combined LP and HP compressors and as a function of the number of core engines that meets the 8 mm blade height limit (first two rows). The additional PR of the centrifugal compressor and of the WRIC is also shown.

5.3.3.1 BPR selection

A study was initially carried out to assess the influence of the BPR on the aircraft performance. In large turbofan engines, the BPR is usually varied to achieve a desired specific thrust, which fixes the engine propulsive efficiency. For low-speed HALE UAVs, however, there are no turbofan designs against which it would possible to benchmark specific thrust and propulsive efficiency. This is why the BPR was treated more like a design parameter rather than a variable to be adjusted and meet a given specific thrust. In addition, the optimum FPR was selected for each design point.

From an endurance perspective, it is possible to observe that the optimum BPR increases at a greater cycle TET (fig.5.14a). This is because a higher-temperature core, for a given bypass, requires less mass flow to generate a certain aircraft thrust

and has more energy available to drive the fan system, whose power increases as the BPR increases. The optimum BPR is a trade-off between three parameters: the propulsion system drag, weight, and SFC.

The overall propulsion system weight increases as the BPR increases (fig. 5.14b). This is due to the increase in the fan system mass, which becomes the dominant weight of the propulsion system. For a low-temperature cycle the propulsion system mass increases faster when greater values of BPR are considered. This is because a low-temperature cycle requires more mass flow to generate a given aircraft thrust. Conversely, for high-temperature cycles the same propulsion system weight would be predicted at a higher BPR. There is a marked difference between the 1,200 K and the 1,400 K cycle weights. This is because the optimum FPR increases, which contributes to a grater specific thrust combined to the higher TET. However, this difference is smaller when moving from 1,400 K to 1,600 K because the variation of optimum FPR reduces.

The aircraft aerodynamic efficiency reduces as the BPR increases due to the smaller engine specific thrust (fig. 5.14c). The reduction in specific thrust is also the reason why the aircraft L/D becomes worse with a low-TET cycle. Conversely, an optimum SFC can be identified for a given set of BPRs if the FPR is optimised for each BPR (fig. 5.14d). For each cycle the maximum optimum FPR was between 1.5 and 1.6, and so a single-stage fan could still be used. The minimum optimum FPR, however, was below 1.3, which may pose a challenge in terms of fan design for efficiency.

5.3.3.2 Cycles comparison on the T&W and BWB airframes

The hybrid WRIC/GT cycles offered an endurance benefit of 6%-18% on the T&W airframe and of 5%-14% on the BWB airframe compared to the best Brayton cycle (figs. 5.15a and 5.16a). The upper bound refers to a WRIC bypass of two, which can be considered an optimistic assumption due to its peak temperature well in excess of 2,000 K (sect. 5.3.1.1). On the other hand, the lower bound refers to a bypass of one, which can be considered a more conservative case. Adding a stage of centrifugal compressor offered an endurance benefit of 7% on the T&W airframe and of 8% on the BWB airframe. Thus, from an endurance perspective the benefit of the of the centrifugal compressor would be aligned to that of the "conservative" WRIC/GT hybrid cycle ($\epsilon = 1$). Conversely, using two core engines instead of one,

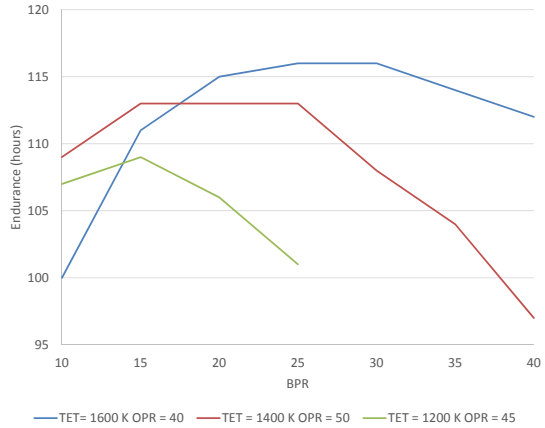

(a) Endurance as function of BPR, OPR, and TET

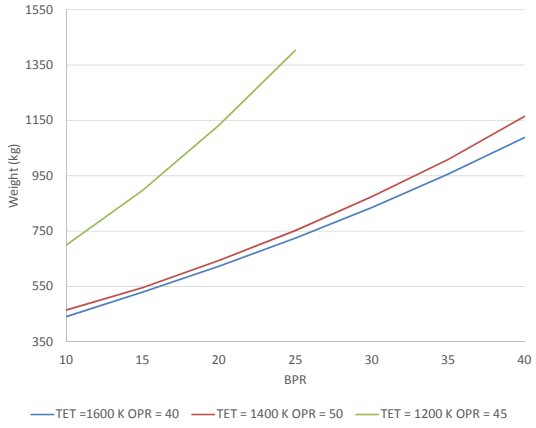

(b) Propulsion system weight as function of BPR, OPR, and TET

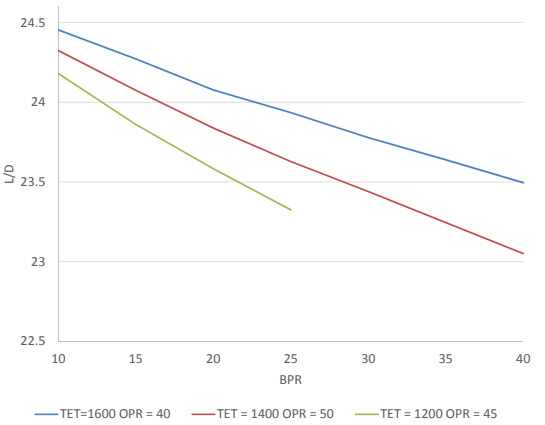

(c) L/D as function of BPR, OPR, and TET

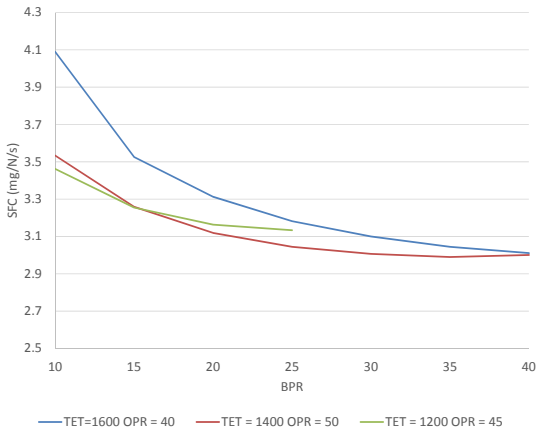

(d) SFC as function of BPR, OPR, and TET

Figure 5.14: BPR selection study for the T&W airframe with a take-off mass of 15,000 kg (thrust = 5,900 N) with a Brayton-cycle core engine

which might be a design choice for reliability purposes, would result in an endurance penalty of 8%. This is due to a reduction in HPC isentropic efficiency and pressure ratio (table 5.2). The benefits or penalties of dealing with different cycles are a trade-off between various airframe and propulsion system effects.

The aircraft aerodynamic efficiency improves on the T&W airframe as the engine moves to a higher-temperature or higher-ϵ cycle for the T&W airframe (fig. 5.15b). This is because the reduced propulsion system intake mass flow results in a smaller fans size and drag. The smaller mass flow also leads to a lighter propulsion system (fig. 5.15c), which allows more fuel to be stored for a given take-off mass. This why the aircraft fuel fraction increases as the propulsion system specific thrust increases (fig. 5.15f).

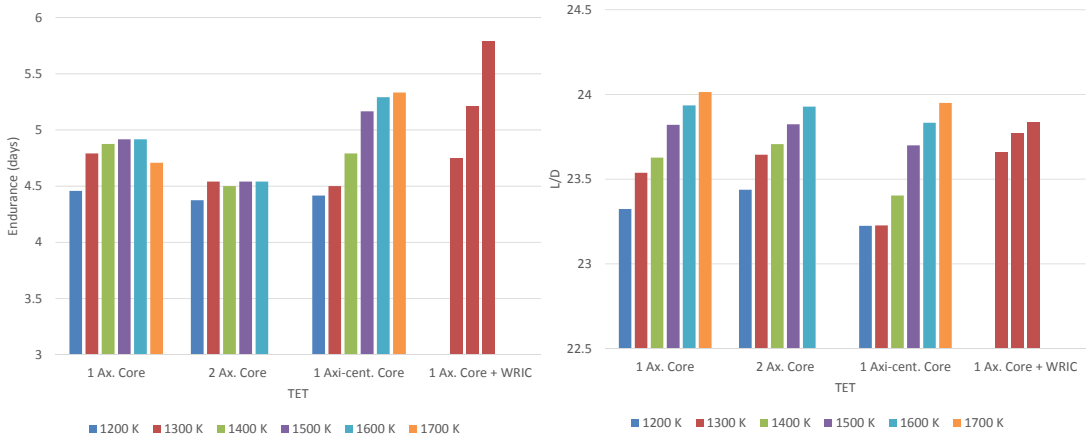

(a) Endurance as a function of cycle and number of cores

(b) L/D as a function of cycle and number of cores

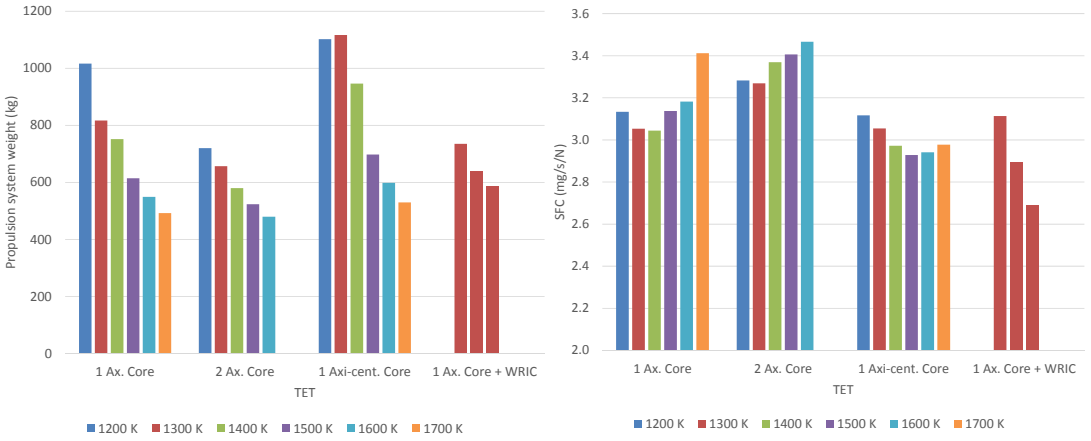

(c) Propulsion system weight as a function of cycle and number of cores

(d) Propulsion system SFC as a function of cycle and number of cores

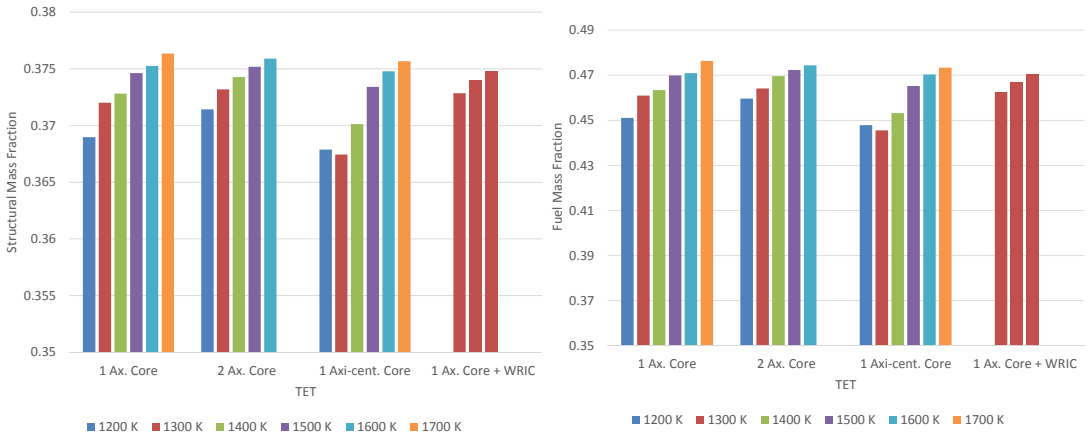

(e) Aircraft structural fraction as a function of cycle and number of cores

(f) Aircraft fuel fraction as a function of cycle and number of cores

Figure 5.15: Integrated airframe/distributed fans study for the T&W airframe with a take-off mass of 15,000 kg (wing AR = 22). The BPR is fixed to 25 and the optimum FPR is considered for each cycle. About the WRIC cycles, for the given TET of 1,300 K a bypass of 0 (left), 1 (middle), and 2 (right) were considered

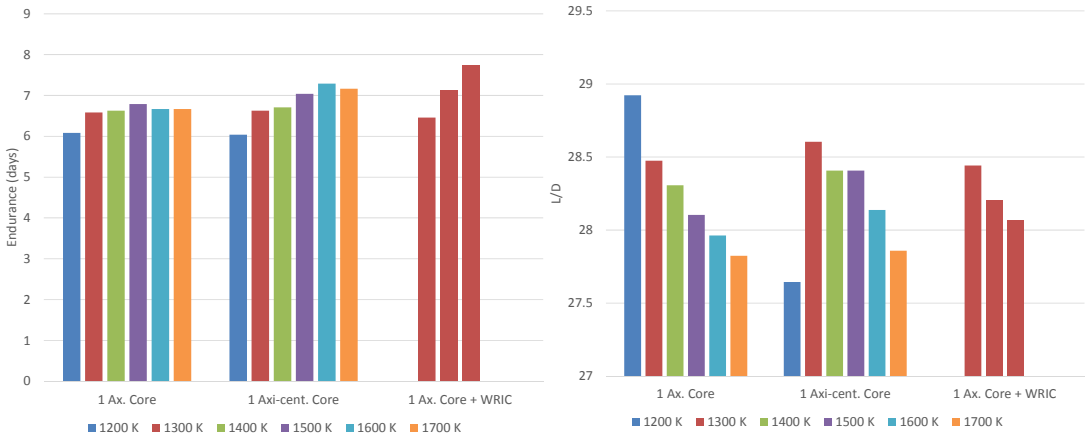

(a) Endurance as a function of cycle and number of cores

(b) L/D as a function of cycle and number of cores

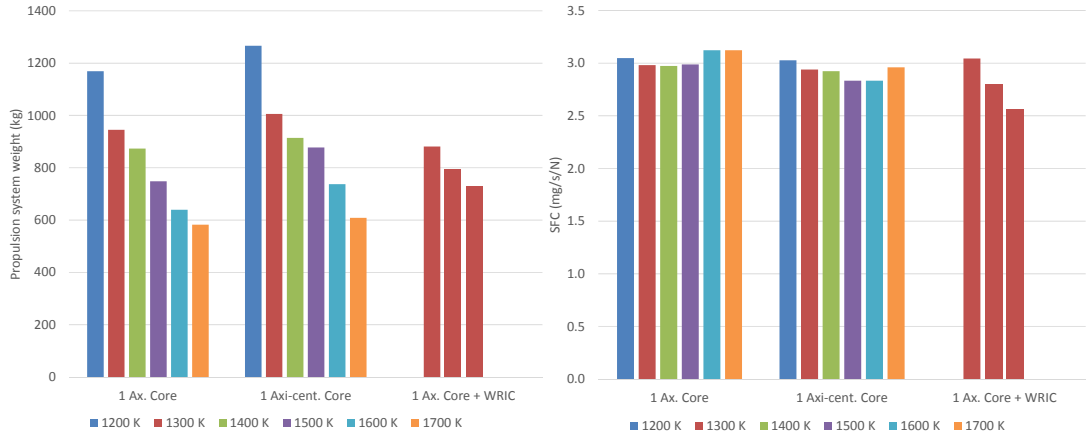

(c) Propulsion system weight as a function of cycle and number of cores

(d) Propulsion system SFC as a function of cycle and number of cores

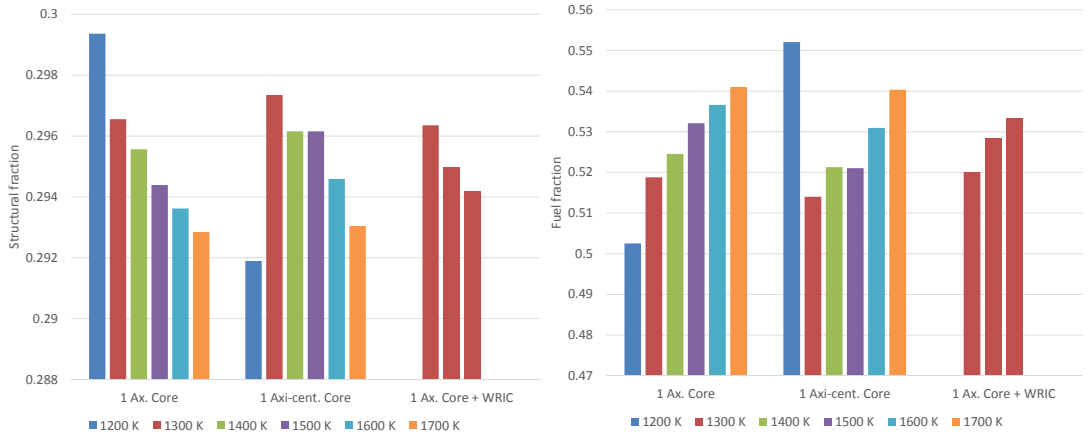

(e) Aircraft structural fraction as a function of cycle and number of cores

(f) Aircraft fuel fraction as a function of cycle and number of cores

Figure 5.16: Integrated airframe/distributed fans study for the BWB airframe with a take-off mass of 15,000 kg. The BPR is fixed to 25 and the optimum FPR is considered for each cycle. About the WRIC cycles, for the given TET of 1,300 K a bypass of 0 (left), 1 (middle), and 2 (right) were considered

The aircraft structural fraction is marginally affected by the propulsion system specific thrust (fig. 5.15e). This is because the greater fuel volume results in an over-sized fuselage, which is of secondary importance compared to the wing mass from a structural standpoint. Compared to the fuel-fraction chart, a smaller y-axis scaling needs to be used to visualise this effect.

A key difference exists between the SFC trends of the Brayton cycles and the hybrid WRIC/GT cycles. As explained in section 5.3.2, the SFC reduces when the wave-rotor bypass increases for the hybrid WRIC/GT cycles, whereas for the Brayton cycles a minimum can be identified when the TET is varied (fig. 5.15d). However, adding a centrifugal-compressor stage allows the minimum SFC (1) to decrease because a higher OPR can be achieved and (2) to shift towards a higher TET. In addition, the SFC variation across the different TET cycles is smaller than that of the axial-turbomachinery-only Brayton cycles.

The endurance trends for the BWB airframe are similar to those of the T&W airframe. However, different effects occur at an airframe level. Compared to the T&W airframe, the opposite occurs on the BWB airframe in terms of L/D (fig. 5.16b). This is because as the engine specific thrust increases its weight reduces (fig. 5.16c). Consequently, more fuel can be stored for a given take-off mass, and so the fuel fraction increases as the propulsion system specific thrust increases (fig. 5.16f). A large fuel volume leads to a greater aircraft centrebody, which means that the centrebody wing area would take a higher fraction of the overall wing area compared to the outer wing. The centrebody is structurally more efficiency than the high-aspect-ratio outer wing as the wing bending-moment is distributed over a larger wing-root area. This is why the aircraft structural fraction decreases as the propulsion system specific thrust increases (fig. 5.16e). However, an undersized BWB outer-wing area leads to a reduced aspect ratio of the overall wing planform, which is why the L/D becomes worse with an increase in engine specific thrust.

Three main conclusions can be drawn from these results:

Axial-turbomachinery-only Brayton cycles For these cycles endurance is a trade-off between the lighter propulsion system weight and its increased drag and SFC when the cycle TET increases. Endurance initially improves when moving towards a higher TET because the smaller propulsion system weight and drag offset the greater SFC. However, the higher SFC becomes the predominant effect for TETs greater than 1,600 K. Also, when two core engines

are considered the SFC effect becomes even more important. In fact, the endurance trends are flat when varying the TET, although the propulsion system weight is lighter due to reduction in the weight of the core due to the smaller PR.

Centrifugal-compressor Brayton cycles As for the aforementioned cycles, endurance is still a trade-off between the propulsion system weight, drag, and SFC. However, the increase in SFC becomes the dominant effect. This is why the endurance steadily improves with an increase in TET, although this effect attenuates for a TET greater than 1,500 K.

Hybrid WRIC/GT cycles The combined effects of reduced propulsion system weight, drag, and SFC lead to an endurance improvement as the WRIC bypass increases.

5.4 Limitations to the present study

Several assumptions were made to assess the benefits of the hybrid WRIC/GT cycles at an integrated-aircraft level. Some of them are related to either the design or the modelling of the individual elements of the system, whereas others concern the study as a whole.

5.4.1 Maximum TET = 1,300 K for hybrid WRIC/GT cycles

From a wave rotor perspective, it was assumed that the engine TET should be limited to 1,300 K. This is because the HPC delivery air would be at lower pressure than that of the WRIC exhaust, and so the turbine could not be cooled according to today's standards. However, other solutions could be adopted for turbine cooling:

1 **A power output could also be extracted from the wave rotor** to lower its delivery pressure and make turbine cooling feasible with the HPC delivery air. This could be achieved by curving the channels around the wave rotor drum, so that the exhaust air would be imparted a swirl that accelerates the wave rotor itself [Akbari, Nalim and Mueller 2006]. The extra rotor acceleration could then be translated into shaft-power to drive an electric generator.

2 **Air could be bled from the wave rotor** by adding an extra port to one of the end-plates [Akbari and Nalim 2009]. The air needs to be extracted after the pressure waves compressed the air. Similarly to GT compressor bleeds, this solution would penalise the wave rotor performance as the WRIC would spend work to compress air that would not be combusted and expanded to support its rotation.

3 **A closed cooling system for the turbine** could be adopted, although this would result in extra weight and complexity. After cooling the turbine blades, the recirculated flow would need to be cooled down with a heat exchanger, which is known to be a heavy technology. It might also be difficult to "pack" a heat exchanger in a small-size engine, as the heat exchanger surface-to-volume area does not scale linearly (i.e. more heat exchange area is proportionally available in a large volume than in a small one).

5.4.2 Practical wave rotor integration challenges

Embedding the wave rotor within a gas turbine engine occurs by means of ducts. Transition ducts are required to connect the annular flow compressor and turbine to the partial-annulus wave-rotor ports, which need to be carefully designed to avoid flow separation and pressure losses [Jones and Welch 1996]. The present study assumed a 6.5% pressure loss based on experimental data [Welch, Slater and Wilson 2007]. Such a high pressure loss on the main gas path translated directly into a thermal efficiency degradation. A sensitivity analysis should be carried out to assess its impact on the aircraft endurance, and further studies are required to optimise the ducts design.

The thermal and mechanical stresses on the wave rotor would be a concern. When a bypass is introduced, the peak temperature of the wave rotors could be up to 2,300 K, although the peak would be reached only for a limited period of time differently from a constant-pressure combustor. Also, when a wave rotor is introduced the overall pressure ratio of the engine would be in the order of 80-90 due to the high outlet-to-inlet temperature gain in the rotor. Rotor channels designs to withstand these pressure might result in a weight penalty.

The present study also assumed that at a cycle peak temperature of 2,300 K combustion would still be feasible, and no dissociation penalty was accounted for (sect. 5.3.1.1). Detailed studies are required to assess the achievable peak temper-

ature limits. Combustion noise would also be of concern as in a non-ideal cycle there combustion process would interfere with the pressure waves when either the compression or the expansion are taking place.

5.4.3 Results analysis and presentation

A remark must also be made on how the results were presented. Great emphasis was placed on how the cycle architectures would affect the endurance of the integrated system. Thus, the results focused on the top-level propulsion system (e.g. thermal efficiency, SFC, weight) and aircraft (e..g endurance, L/D, fractions) parameters.

More emphasis could be placed on the wave rotor itself by showing the results in terms of its pressure or temperature gain. Sensitivity studies could be performed to assess—at an integrated aircraft level—the effect of the key wave rotor parameters such as the compression/expansion isentropic efficiencies and the WRIC exhaust Mach (which determines the recirculation of the combusted gases). In addition, the wave rotor benefits could have also been assessed on the two-core engine case.

It was the author's preference to present the results in a way that could be interpreted by a wider audience as the present research would be of interest of experts and researchers with different backgrounds. Also, given the limited timeframe of the present research it was preferred to benchmark the wave rotor against many different options to truly understand its benefits rather than to focus on the wave rotor itself.

5.5 Further considerations on the benefits of wave rotor technology

The hybrid WRIC/GT cycles could also offer emissions and electric-system weight benefits in addition to an endurance improvement of the integrated aircraft system.

5.5.1 Combusted gases recirculation & emissions

Recirculating the combusted gases is an intrinsic characteristic of the wave rotor. First of all, recirculation happens because of the limited time that the rotor channel

is exposed to the turbine-exhaust port. Secondly, recirculation could also be used as a mechanism to trigger the combustion process [Akbari and Nalim 2009]. This effect clearly penalises the performance of the wave rotor. However, it might also lead to lower emissions—per hour of endurance or nautical mile of range flown—if the combustion occurs with a mixture of fresh air and combusted gases. This is because only the combustion of fresh gases would result in NO_x emissions when hydrogen fuel is burned.

5.5.2 Wave rotor work extraction & electrical system weight

Shaft power can be extracted from the wave rotor by appropriately shaping its channels [Akbari, Nalim and Mueller 2006]. This could be used to make the stator of the electric generator rotate in the opposite direction to that of the rotor, resulting in a contra-rotating generator. The magnetic flux would be "cutting" the stator coils at a higher frequency, and so an increased output current would be induced for a given generator weight. Vice versa, a given power could be produced with a lighter generator. Thus, the wave rotor could help reducing the electric-transmission weight and relax the technological challenges linked to advance the power density of the electric machines. This could contribute to an earlier introduction of the distributed propulsion technology.

In a two-shaft engine the same effect could be obtained by linking the generator to both the HP and LP shafts, although this may result in a reduced engine off-design flexibility as the performance of both compressors would be impaired. However, in a small single-shaft engine (e.g. helicopter engine) the wave rotor would make the contra-rotating option available.

5.6 Concluding remarks

The aim of this chapter was to build a methodology to assess the benefits of the wave rotor with internal combustion (WRIC) when integrated with a GT engine—at an aircraft-integrated level. Thus, the goal was to assess by how much the performance of the integrated aircraft-propulsion system would be affected because of the cycle selection. This would be particularly important in a small engine such as the core of HALE UAV, where the OPR would be limited by the blade size at the HPC exit for

a given TET. The WRIC would act as an extra compressor, and an OPR increase would lead to a higher cycle efficiency. The WRIC would also improve the cycle efficiency because of the higher cycle peak temperature, particularly when part of the compressor air bypasses the WRIC to mix with its outlet flow (sect. 5.1.3).

The hybrid WRIC/GT cycles offered an endurance benefit of 6%-18% on the T&W airframe and of 5%-14% on the BWB airframe compared to the best Brayton cycle (figs. 5.15a and 5.16a). The upper bound refers to a WRIC bypass of two, which can be considered an optimistic assumption due to its peak temperature well in excess of 2,000 K (sect. 5.3.1.1). On the other hand, the lower bound refers to a bypass of one, which can be considered a more conservative case. Adding a stage of centrifugal compressor offered an endurance benefit of 7% on the T&W airframe and of 8% on the BWB airframe. Thus, from an endurance perspective the benefit of the of the centrifugal compressor would be aligned to that of the "conservative" WRIC/GT hybrid cycle ($\epsilon = 1$). Conversely, using two core engines instead of one, which might be a design choice for reliability purposes, would result in an endurance penalty of 8%. This is due to a reduction in HPC isentropic efficiency and pressure ratio (table 5.2).

The benefits or penalties of dealing with different cycles are a trade-off between various airframe and propulsion system effects. The hybrid WRIC/GT cycles reduce the propulsion system weight, drag, and SFC when the wave rotor bypass increases. This is different to what occurs in a Brayton cycle, where the increase in TET leads to a lower weight and drag but to a higher SFC.

In addition to performance benefits, the wave rotor cycles also offer the potential to reduce the engine emissions and the weight of the electric transmission. Emissions would reduce as a consequence of recirculating the gases from the previous combustion. This is an intrinsic characteristic of a non-ideal wave rotor, and might also be used to trigger the combustion process inside the rotor channels. The electric transmission weight would reduce by adopting a contra-rotating generator when linking the wave rotor to the stator of the turbine-driven electric generator. This may help to relax the technological challenges of advancing the electric-machines power density to make the distributed-propulsion concept feasible.

It can be concluded that the wave rotor technology should be further investigated for HALE UAVs. This would also apply to other applications where the engine OPR is limited by blade size constraints typical of small engines. In addition, further studies should focus on the impact of raising the TET limit of 1,300 K with

appropriate turbine-blade cooling techniques. From an endurance perspective, this would offer the potential to reach improvements well above the 14%-18% that were predicted for the T&W and BWB airframes respectively.

Chapter 6

Solid Oxide Fuel Cell Gas Turbine Hybrid Cycles

6.1 Introduction

Solid oxide fuel cells (SOFC) offer efficiencies above 60% when integrated with a gas turbine [Aguiar, Brett and Brandon 2008]. Although their weight can be 10 to 20 times greater than that of a gas turbine, the overall propulsion system weight may become less important than its efficiency to complete very long endurance missions. In addition, the SOFC is characterised by a low technology readiness level and further advancements in its power density should be expected in the near future.

The aim of this chapter was to build a methodology to assess the benefits of the hybrid SOFC/GT cycles at an aircraft-integrated level. Thus, the goal was to assess by how much the design and the performance of the integrated aircraft-propulsion system would be affected by the cycle selection.

An introduction to SOFC/GT systems for airborne applications is initially presented (sect. 6.1.1). This is followed by a methodology section (sect. 6.2) that focuses on the cycle selection for HALE UAV applications, the electrochemical an thermo-fluid dynamic modelling of the SOFC, and its integration with the gas turbine components. In addition to the cycle performance, the results quantify the benefits of a hybrid SOFC/GT system for a distributed-fans propulsion system at an aircraft-integrated level (sect. 6.3). Prior to the concluding remarks (sect. 6.5), the limitations to the present study are exposed (sect. 6.4).

6.1.1 SOFC/GT systems airborne applications

Hybrid SOFC/GT cycles have been mainly investigated for two airborne applications: auxiliary power units (APU) and HALE UAVs [Waters and Cadou 2003]. Fuel cell technology could be attractive in aviation as it reduces noise and emissions in addition to improve fuel consumption. These factors are particularly important at ground level according to the present regulations, which is why fuel cell APUs were investigated [Freeh, Pratt and Brouwer 2004; Steffen, Freeh and Larosiliere 2005]. However, the technology readiness level of fuel cells is low. Their transient response is slower and their weight could be 10 to 20 times heavier than that of gas turbine engines [Roth and Giffin III 2010].

Solid oxide fuel cells are the preferred choice over polymer electrolyte fuel cells (PEFC) to generate powers in the order of kW/MW at high altitude. Once integrated in a GT cycle, a SOFC offers efficiencies in excess of 60% even at high altitude [Aguiar, Brett and Brandon 2008]. Conversely, the PEM cycle efficiency would be in the order of 30-40% because of the altitude effect [Palethorpe 2008]. This is because the SOFC releases enough heat to be expanded in a turbine to drive the compressor. The PEFC exhaust is usually too cold, and so the PEFC itself has to produce the energy to electrically drive the compressor. The air density reduces when altitude increases, and so the high compressor power requirement leads to a low cycle efficiency. In addition, solid oxide fuel cells have a potentially longer durability than PEFCs, which might be an important factor given the long-endurance requirement of HALE UAVs [Aguiar, Brett and Brandon 2008]. Also, PEFCs require careful water management, which becomes challenging at low temperatures as the water might freeze.

Himansu et al. studied a 50 kW hybrid SOFC/GT system for HALE UAVs [Himansu et al. 2006]. It was concluded that long duration missions in the order of 10 to 20 days benefit from having a high-efficiency but heavy power source. This is in contrast to what was found for missions with a shorter endurance of about half a day. Aguiar, Brett and Brandon modelled a 140 kW hybrid SOFC/GT system for a HALE UAV and found benefits in linking the SOFC stacks in series. However, the study did not quantify the endurance benefits of such a system. Waters and Cadou showed that a range improvement of up to 29% could be achieved by generating electric power with a hybrid SOFC/GT system for HALE UAVs [Waters and Cadou 2003]. This range improvement was calculated with the Breguet equation by assuming an electric-to-propulsive power fraction fo 50%. The study also showed that the range

benefits increase as the electric power fraction increases.

It is clear that none of the aforementioned studies assessed the trade-off between the weight and the fuel-efficiency of a hybrid SOFC/GT system when integrated with the aircraft. The aircraft needs to be redesigned to accommodate a heavier propulsion system. This would result in a reduced fuel mass and a greater aircraft empty mass, which would affect the performance of the integrated aircraft-propulsion system. As such, it is still unknown if the hybrid SOFC/GT system would buy its own weight on the aircraft.

.

6.2 Methodology

The aim of the present study was to build a methodology to assess the benefits of the hybrid SOFC/GT cycles at an aircraft-integrated level. Thus, the goal was to assess by how much the design and the performance of the integrated aircraft-propulsion system would be affected because of the cycle selection. The hybrid SOFC/GT cycles are known to offer efficiencies above 60%. However, the weight of the SOFC is a major constraint as the fuel-flow benefits might be offset by the increased weight of the propulsion system from an endurance perspective.

The cycles that were selected for the present HALE UAV application are initially presented (sect. 6.2.1). This section is followed by the electrochemical (sect. 6.2.2) and thermo-fluid dynamic modelling of the SOFC (sect. 6.2.3). These sections describe the one-dimensional finite-volume modelling of a planar co-flow SOFC. A planar design was considered over a tubular one as it results in lower ohmic losses and thermal stresses due its shorter conduction path. A one-dimensional model was selected over, for example, a simplified parametric approach such as the one proposed by Larminie and Dicks 2003. In fact, the SOFC geometry affects its fuel utilisation and outlet temperature. These parameters are essential to explore the benefits of the hybrid SOFC/GT cycles. Also, the mathematical model that was selected could be extended to two and three dimensions for more detailed SOFC stack analysis.

The integration between the SOFC and the gas turbine components is described in section 6.2.4, which also focuses on the hybrid SOFC/GT cycles off-design con-

siderations. The gas turbine components size and weight calculations are described in Appendix B.

6.2.1 Hybrid SOFC/GT cycles selection

The selected hybrid SOFC/GT cycles (fig. 6.1) avoid the use of heat exchangers and place the SOFC in the gas path so that its operating temperature falls within the 600-1,000°C limits [Larminie and Dicks 2003]. Avoiding the use of heat exchangers is quite important in airborne applications as they are known to be a heavy technology. Thus, two cycle layouts were selected for the present HALE UAV study.

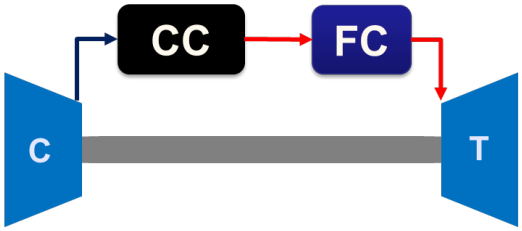

(a) Hybrid SOFC/GT cycle layout 1: SOFC after CC

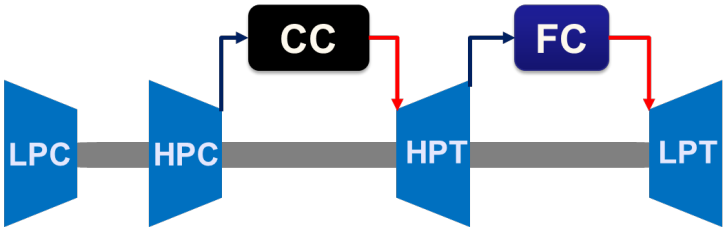

(b) Hybrid SOFC/GT cycle layout 2: SOFC after HPT

Figure 6.1: Layout of the hybrid SOFC/GT cycles selected for the present project

In the first cycle the SOFC is positioned between the combustion chamber and the turbine (fig. 6.1a). This will be referred to as "cycle 1" throughout the chapter. In the second cycle, or "cycle 2", the SOFC is positioned between the HPT and LPT and acts as a turbine reheater (fig. 6.1b).

The selected cycle layouts are not frequently used in the public literature. Industrial cycles usually position the SOFC between the compressor outlet and the combustion chamber, and a heat exchanger is used to preheat the compressor delivery air [Selimovic 2002]. This is because industrial cycles have a low compressor pressure ratio, between 3 and 4, and so the compressor outlet would be too cold for the SOFC—even at sea level. On the other hand, even after the turbine expansion the flow is hot enough to preheat the compressor exit air. In addition, weight is not

a concern in ground-based applications and so a heat exchanger can be adopted. However, at an altitude of 50,000 ft pressure ratios above 80 are required to preheat the compressor delivery flow with the engine exhaust air. This would not be achievable given the turbomachinery size limitations at pressure ratios well below 80 (see sect. 5.3.1.2).

Another solution could be to preheat the compressor delivery flow with the combustor outlet air before it is delivered to the turbine (fig. 6.2) [Aguiar, Brett and Brandon 2008]. However, this solution would still require the use of a heat exchanger, which might be inconvenient for airborne applications due to its weight.

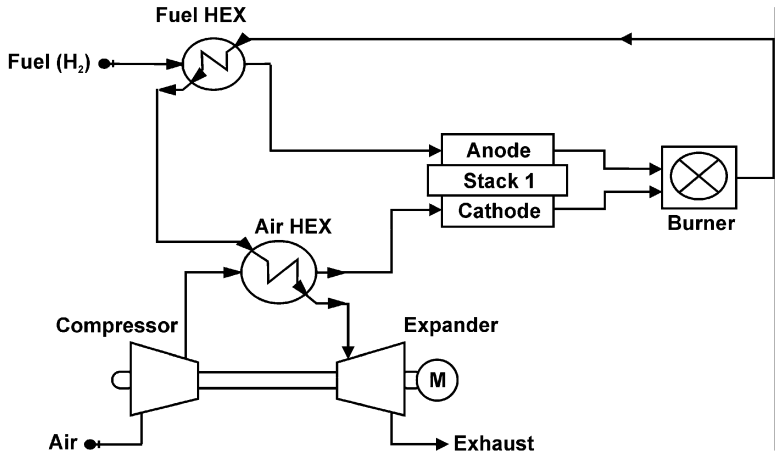

Figure 6.2: Hybrid SOFC/GT cycle layout with the SOFC inlet preheated by the combustor outlet [Aguiar, Brett and Brandon 2008]

The proposed cycles avoid the use of heat exchangers and maintain the fuel cell operating temperature between the 600-1,000$°C$ range (fig. 6.1). However, the combustion process would partially consume the air oxygen content, so that less oxygen would be available in the SOFC air channel. This would limit the SOFC power output and decrease the overall cycle efficiency as in these cycle arrangements part of the electric power would also be produced by a turbine-driven generator. On the other hand, limiting the SOFC power output would decrease its weight, which would have a beneficial impact on the aircraft endurance.

Another consideration on the selected cycles is about the fuel utilisation. In a "real" SOFC not all the hydrogen that enters the fuel channel would be consumed to produce electric power. This means that there would be a hydrogen flow leaving the SOFC, which would simply be expanded in the turbine. However, in the industrial cycle layout any excess hydrogen would be burned in the combustion chamber as this is placed after the SOFC. Thus, in the selected cycles it is important to operate the

fuel cell under high fuel utilisation conditions, otherwise the cycle efficiency would be penalised by the unused hydrogen.

6.2.2 SOFC Electrochemical model

The SOFC voltage is a function of its open circuit voltage and overpotentials (eq. 6.1) [Larminie and Dicks 2003]. The open circuit voltage is the ideal voltage generated by the hydrogen oxidation, which needs to be corrected because of some irreversible loss mechanisms. These are usually referred to as "overpotentials" within the electrochemical modelling of a fuel cell. The open circuit voltage due to the water formation, which depends on the variation of Gibbs free energy (eq. 6.3), was also corrected to account for its dependence on temperature, pressure, and species concentration (eq. 6.2). It is this relationship that allows to evaluate the influence of the fuel cell operating pressure on its performance, particularly within a gas turbine/SOFC hybrid cycle. It is also worth noticing that the same expression also explains why as hydrogen is consumed through a SOFC channel its voltage—and consequently power output—decreases. In fact, a drop in hydrogen molar fraction (x_{O_2}) leads to a lower argument within the logarithmic part.

Electric generating devices are usually rated at a given voltage. For the present study, the cell voltage of each fuel-cell volume was kept constant throughout the SOFC channel length. As such, the current density has to vary, and it was iteratively assessed on each channel volume (fig. 6.3). A current density value is initially guessed, which allowed the overpotentials to be calculated as explained in sections 6.2.2.1, 6.2.2.2, and 6.2.2.3. The SOFC volume voltage can be assessed according to equation 6.1, and so a check is made to assess if the calculated cell voltage differs from its design value. The calculations on each volume are repeated until its voltage matches the design voltage.

$$V = E - \eta_{ohm} - \eta_{act} - \eta_{conc} \tag{6.1}$$

$$E = E_{H_2O} + \frac{\mathcal{R}T}{2\mathcal{F}} \log\left(\frac{x_{H_2} x_{O_2} p^{0.5}}{x_{H_2O}}\right) \tag{6.2}$$

$$E_{H_2O} = -\frac{\Delta g}{2\mathcal{F}} \tag{6.3}$$

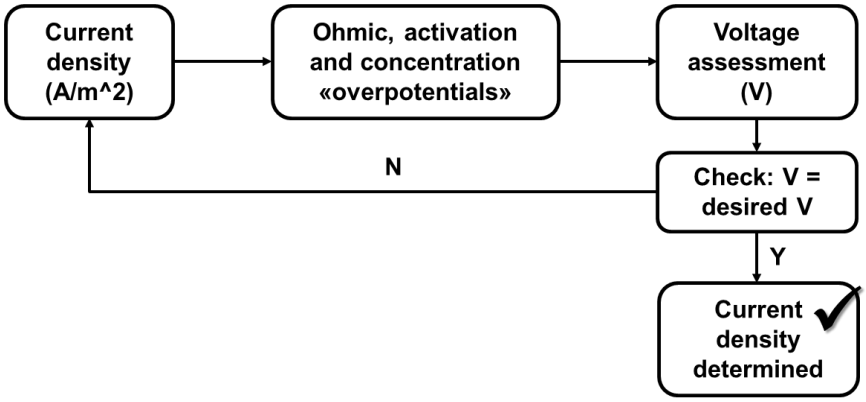

Figure 6.3: SOFC electrochemical model iterative calculation layout

6.2.2.1 Ohmic Overpotentials

The ohmic overpotentials arise because of the resistance that the current encounters when flowing within the SOFC itself. This is usually divided in into two parts, namely the PEN (Positive-Electrolyte-Negative) solid structure and the channel walls (fig. 6.4). The ohmic overpotentials can be expressed as a function of the current density, fuel cell active area and its electrical resistance (eq. 6.4). Within a finite volume approach, the active area coincides with the horizontal cross-sectional area of the considered volume assuming that the current flow is mainly perpendicular to the gas-path flow direction [Campanari and Iora 2005; Mastropasqua 2014].

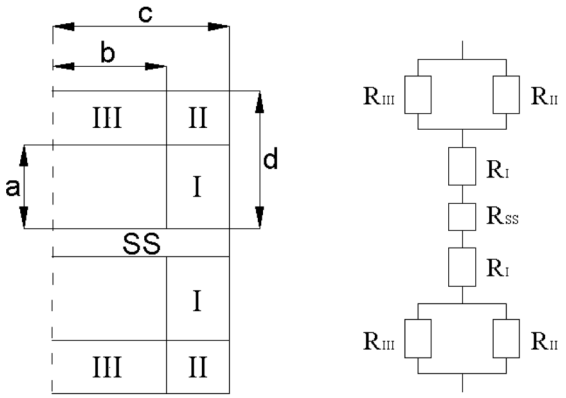

Figure 6.4: Equivalent electrical circuit of half of the SOFC channel [Campanari and Iora 2005]

As its layers are one on top of the other, the PEN resistance is simply the sum of the resistances of the anode, cathode, and electrolyte (eq. 6.5). Each resistance is a function of its material resistivity, thickness and active area (eq. 6.6). The resistivity is a function of the fuel cell operating temperature, or the local temperature of the SOFC volume within a finite-volume approach [Campanari and Iora 2005].

Equation 6.6 was also applied to assess the resistances of the channel portions I and II. However, within the channel part III the current density flux is not perpendicular to the actual cross-sectional area of the SOFC volume element. Thus, an empirical correlation was used to replace the element thickness with a function of the lengths a, b, and d reported in figure 6.4.

$$\eta_{ohm} = R_{FC}\, i\, Area = (R_{PEN} + R_{channel})\, i\, Area \tag{6.4}$$

$$R_{PEN} = R_{anode} + R_{cathode} + R_{electrolyte} \tag{6.5}$$

$$R_i = \frac{\rho\, thickness}{Area} \qquad i = anode, cathode,\ and\ electrolyte \tag{6.6}$$

$$R_{channel} = \frac{R_{III} R_{II}}{R_{III} + R_{II}} + R_I \tag{6.7}$$

6.2.2.2 Activation Overpotentials

The activation overpotentials occur because the current, once generated within the fuel cell itself, has to overcome an energy barrier before start "moving" along the electrically conductive material. It is for this reason that this loss is usually described as due to the charge transfer process. Although in the past it might have been common to neglect the activation losses, modern planar SOFC stacks are characterised by very short conduction paths. As a consequence, the activation losses are expected to be closer in magnitude, or even greater than, the other two loss mechanisms—namely the ohmic and concentration ones [Moren and Hoffman 2005].

The activation overpotentials were described with the Butler-Volmer equation (eqs. 6.8 and 6.9), which assumes the charge transfer as represented by a one-step single-electron process [Campanari and Iora 2004]. As such, the exchange current density i_0 at both the anode and cathode sides (eqs. 6.10 and 6.11) needs to be corrected by a symmetry factor β. This represents the fraction of the activation voltage loss that affects the activation energy barrier, and thus the rate of the electrochemical transformation [Moren and Hoffman 2005]. It is clear from equations 6.8 and 6.9 that the activation overpotentials need to be iteratively determined as

they cannot be expressed as a direct function of the current density.

$$i_{anode} = i_{0,anode}\left[\exp\left((1-\beta)\frac{\mathcal{F}}{\mathcal{R}T}\eta_{act,anode}\right) - \exp\left((-\beta)\frac{\mathcal{F}}{\mathcal{R}T}\eta_{act,anode}\right)\right] \tag{6.8}$$

$$i_{cathode} = i_{0,cathode}\left[\exp\left((1-\beta)\frac{\mathcal{F}}{\mathcal{R}T}\eta_{act,cathode}\right) - \exp\left((-\beta)\frac{\mathcal{F}}{\mathcal{R}T}\eta_{act,cathode}\right)\right] \tag{6.9}$$

$$i_{0,anode} = \gamma_{anode} x_{H_2} x_{H_2O} \exp\left(\frac{-E_{act,anode}}{\mathcal{R}T}\right) \tag{6.10}$$

$$i_{0,cathode} = \gamma_{cathode} x_{O_2}^{0.25} \exp\left(\frac{-E_{act,cathode}}{\mathcal{R}T}\right) \tag{6.11}$$

6.2.2.3 Concentration Overpotentials

The concentration overpotentials arise because of the difference between the molar fractions of the chemical species within the "bulk" flow and at the cell reaction site. In fact, the open circuit voltage (eq. 6.1) is calculated based on the average concentration of the chemical reactants within the SOFC channels. However, the reactants have to migrate from the main gas path to the cell reaction site for the oxidation to occur. Such a process predominantly takes place by diffusion [Mastropasqua 2014], and so a reactant molar fraction lower than the "bulk" flow average is present at the cell reaction site. Thus, the concentration overpotentials are expressed as a correction that accounts for the difference between the bulk flow (x^b) and reaction site (x^r) molar fractions (eq. 6.12).

$$\eta_{conc} = \eta_{conc,anode} + \eta_{conc,cathode} = \frac{\mathcal{R}T}{2\mathcal{F}} \ln\left(\frac{x_{H_2}^b x_{H_2O}^r}{x_{H_2}^r x_{H_2O}^b}\right) + \frac{\mathcal{R}T}{4\mathcal{F}} \ln\left(\frac{x_{O2}^b}{x_{O2}^r}\right) \tag{6.12}$$

There are two types of diffusion processes that occur within a SOFC. First of all, the reactant diffuses in the gas mixture from the bulk flow to the cell surface layer. Secondly, there is a diffusion process from the cell surface layer to its reaction site as

the reactant diffuses through the porous electrode [Campanari and Iora 2004]. The first step of the diffusion process can be calculated as the ordinary diffusion of a gas in a mixture. This can be assessed with the Fuller equation, which evaluates the diffusion coefficient of a binary gas mixture as a function of temperature and the species atomic diffusion volumes [Poling, Prausnitz and O'Connel 2001]. An average absolute error of 4% was reported in approximating the experimental data.

The diffusion through the porous electrode material was modelled with the Knudsen model. In fact, the ordinary diffusion that can be modelled with the Fuller equation occurs when the pore diameter of the material under consideration is greater then the mean free path of the gas molecules. However, in a SOFC the pores are small compared to the mean free path of the gas [Selimovic 2002].

6.2.3 SOFC Mass and Energy Balance

Mass and energy balances are essential to predict the temperature distribution along the SOFC channels, which leads to the flow exit temperature that is necessary for hybrid SOFC/GT cycles performance assessment. It also affects the electrochemical behaviour of the SOFC as both the open circuit voltage and the overpotentials are a function of temperature.

The thermo-fluid dynamics calculations of the SOFC start by assessing the mass transfer between the fuel and the air channels (fig. 6.5). The mass transfer depends on the current density, the fuel cell active area, and the Faraday constant (eqs. 6.13). Secondly, momentum conservation, energy balance—which allows to evaluate the heat transfer between the SOFC solid structure and the flow—and continuity allow the SOFC exit temperatures and velocities to be calculated (eqs. 6.14). These need to be guess and iteratively changed (fig. 6.5).

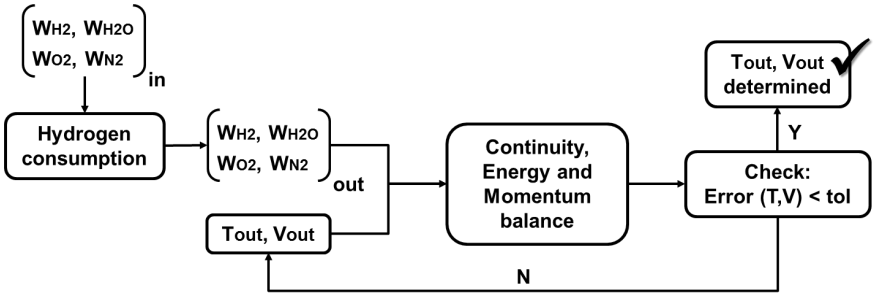

Figure 6.5: SOFC mass and energy balance iterative calculation layout

As the oxidation takes place, two electrons pass around the external circuit for

each water molecule produced and each molecule of hydrogen used [Larminie and Dicks 2003]. Thus, the moles of hydrogen that are consumed—or of water that are produced—can be expressed as the ratio of the current density to twice the Faraday constant as this represents the electric charge of a mole of electrons (eqs. 6.13). Similarly, the moles of oxygen that are consumed correspond to a half of the hydrogen moles that are consumed, whereas the nitrogen molar flow remains unaffected.

$$\begin{cases} f_{H_2,out} = f_{H_2,in} - \Delta f = f_{H_2,in} - \frac{i}{2\mathcal{F}} A_{active} \\ f_{H_2O,out} = f_{H_2O,in} + \Delta f \\ f_{O_2,out} = f_{O_2,in} - \frac{\Delta f}{2} \\ f_{N_2,out} = f_{N_2,in} \end{cases} \tag{6.13}$$

Once the mass transfer between the fuel and the air channels is established, the continuity and momentum conservation (four equations) allow the exit velocities for each chemical species (four variables) to be determined (eqs. 6.14). The equations that are shown represent the simplified version that was used for the actual calculations. They were simplified up to this point by assuming that both volume and surface forces are negligible. Particularly, neglecting viscous forces results in no pressure losses within the SOFC channels. However, this aspect and its influence on the overall cycle performance could be addressed with a parametric study. It is also worth noticing that the density that appears in the continuity equations is a function of temperature, and so the equations 6.14 have to be solved in iterations with the energy balance (eqs. 6.15).

$$\begin{cases} \left(\frac{f_{H_2,out}\, v_{H_2,out} - f_{H_2,in}\, v_{H_2,in}}{A_{cross}}\right) \mathcal{M}_{H_2} + \left(\frac{f_{H_2O,out}\, v_{H_2O,out} - f_{H_2O,in}\, v_{H_2O,in}}{A_{cross}}\right) \mathcal{M}_{H_2O} = 0 \\ \left(\frac{f_{O_2,out}\, v_{O_2,out} - f_{O_2,in}\, v_{O_2,in}}{A_{cross}}\right) \mathcal{M}_{O_2} + \left(\frac{f_{N_2,out}\, v_{N_2,out} - f_{N_2,in}\, v_{N_2,in}}{A_{cross}}\right) \mathcal{M}_{N_2} = 0 \\ A_{cross}(\rho_{H_2,out}\, v_{H_2,out} + \rho_{H_2O,out}\, v_{H_2O,out} + \rho_{O_2,out}\, v_{O_2,out}) = W_{H_2,in} + W_{H_20,in} + W_{O_2,in} \\ A_{cross}\, \rho_{N_2,out}\, v_{N_2,out} = W_{N_2,in} \end{cases} \tag{6.14}$$

The temperature of the gases within the fuel and air channels varies due to the

heat released during the oxidation and the convective heat transfer with the channel walls (eq. 6.15). It was assumed that the heat generated because of the chemical reaction is equally split between the air and fuel channel ($\frac{\mathcal{Q}}{2}$). Also, the PEN and the channel walls were considered as a whole solid structure that is heated up because of the hot gases and the ohmic dissipation due to the electrical flow through it. A more accurate energy balance should separate the heat transfer between the PEN and the channel walls. However, according to the two-dimensional modelling results available in the public literature considering a merged PEN-interconnect solid structure still allows to obtain a good agreement with experimental data [Campanari and Iora 2005]. As such, this assumption was assumed to be acceptable also for the present one-dimensional modelling.

About the convective heat transfer, the logarithmic-mean-temperature was considered for the gases as it was assumed that heat is exchanged between the gases and an average constant-wall-temperature pipe. This assumption is in agreement with what is suggested by most heat transfer textbooks. Also, the heat produced by the fuel cell in each control volume ($\mathcal{Q}$) was assessed based on the difference between the actual cell voltage and the ideal output voltage (1.25 V) that would be achieved if the water product were in the vapour form [Larminie and Dicks 2003].

For the purpose of this initial study, the stacking effects between the different channels were neglected as the present model is one-dimensional. The heat transfer with the adjacent channels and the heat losses between the outer-stack channels and the surrounding ambient-temperature air could be included should the modelling capabilities be expanded to two and three dimensions.

$$\begin{cases} (f_{H_2} h_{H_2} + f_{H_2O} h_{H_2O})_{out} - (f_{H_2} h_{H_2} + f_{H_2O} h_{H_2O})_{in} = \frac{\mathcal{Q}}{2} - \frac{Nu\,k}{l_{volume}} A_{HT} (T_{log,fuel} - T_{ss}) \\ (f_{O_2} h_{O_2} + f_{N_2} h_{N_2})_{out} - (f_{O_2} h_{O_2} + f_{N_2} h_{N_2})_{in} = \frac{\mathcal{Q}}{2} - \frac{Nu\,k}{l_{volume}} A_{HT} (T_{log,air} - T_{ss}) \\ k_{ss} A_{HT} \frac{T_{ss,out} - T_{ss,in}}{l_{volume}} = A_{HT} \left[\frac{Nu\,k}{l_{volume}} A_{HT} (T_{log,air} - T_{ss}) + \frac{Nu\,k}{l_{volume}} A_{HT} (T_{log,fuel} - T_{ss}) \right] + \\ \qquad\qquad\qquad\qquad\qquad\qquad\qquad\qquad\qquad\qquad\qquad\qquad\qquad\qquad + W_{el} \\ \mathcal{Q} = i_{volume} (1.25 - V) A_{active} \end{cases} \tag{6.15}$$

6.2.4 SOFC/GT Integration

The present SOFC model was integrated with Turbomatch, Cranfield University gas turbine performance simulation software. Turbomatch allows the gas turbine design and off-design performance to be assessed, and it also has multi-fuel capabilities. The integration with Turbomatch was necessary to assess the off-design performance of the hybrid SOFC/GT cycle. In fact, if only the hybrid cycle design-point performance was required the GT components could be simply represented by their zero-dimensional thermodynamic equations. However, the aircraft loiter performance are affected by the propulsion system SFC increase as the aircraft thrust reduces (see sect. 5.2.4 and fig. 5.9).

As it will be explained in section 6.3.2.3, only the off-design performance of cycle 1 (fig. 6.1a) was modelled. Thus, the hybrid cycle was simply modelled as a compressor-combustor-turbine arrangement in Turbomatch. The effect of having a SOFC between the combustor and the turbine was simulated by modifying the water vapour content of the combustor outlet, an option that was recently made available in Turbomatch. On the other hand, the overall cycle performance were calculated by assuming that the overall power output and fuel flow equal the sum of the Turbomatch output and of the SOFC model calculations. Fixed isentropic efficiencies of 0.87 and 0.88 were assumed for the compressor and the turbine respectively. This was based on non-dimensional mass flow scaling considerations to account for the blade size effect on the turbomachinery efficiency. Also, the low-DC voltage of the SOFC output needs to be translated into a high-DC voltage output to be integrated into the distributed propulsion system. A DC-DC conversion efficiency of 99.93% was assumed to be consistent with the electric system assumptions of the present study (see Appendix C).

The off-design calculations of the hybrid SOFC/GT cycle start by guessing the Turbomatch cycle mass flow W_{core}, the SOFC outlet temperature $T_{C,out}$ and pressure $P_{C,out}$, and the turbine power output $AUXW$ (fig. 6.6). The main handle of the off-design calculations is the combustion chamber outlet temperature $T_{CC,out}$ in the Matlab SOFC motel. These quantities allow the SOFC calculations to be performed, so that its outlet temperature $T_{SOFC,out}$ and water-vapour mass fraction $\%H_2O$ can be assessed. This information can be fed into Turbomatch, so that the cycle mass flow can be calculated. Also, the fraction of mass flow that needs to be extracted by the cycle ΔW is assessed, where W_{FC} refers to the cycle mass flow calculated in the SOFC model. This is because when water vapour is added in the Turbomatch

combustion chamber the water vapour mass fraction would be higher than that of the SOFC model. Once the cycle mass flow has been corrected, it is possible to update the initial guesses and repeat the calculations until the core mass flow value converges to a stable solution.

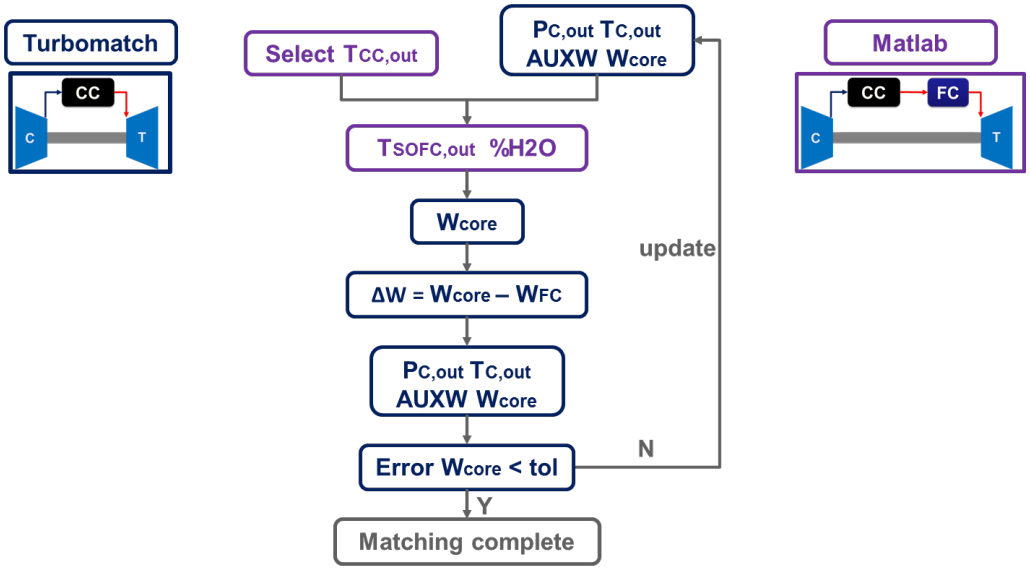

Figure 6.6: Flowchart to explain the integration between Cranfield University Turbomatch and the SOFC model for off-design calculations

6.3 Results

This section quantifies the benefits of the hybrid SOFC/GT cycles at an aircraft-integrated level. The SOFC model introduced in the methodology section is initially verified against public domain results (sect. 6.3.1). The turboshaft analysis of the hybrid cycles is then presented, which allows the cycle efficiency benefits to be assessed as a function of the key fuel cell and turbomachinery parameters (sect. 6.3.2). Finally, the hybrid SOFC/GT cycle was integrated within a distributed fans propulsion system. Its effect on the aircraft endurance was assessed on both the T&W and BWB airframes (sect. 6.3.3).

6.3.1 SOFC model verification

The reliability of the developed SOFC methodology was verified against the simulation results of Campanari and Iora 2005. This choice was based on the lack of detailed experimental results in the public domain. The selected reference, whose

model was calibrated against experimental results, allows to validate the trends of the local properties within a co-flow planar SOFC channel. The reference simulation results, however, include the steam-methane-reforming modelling, whereas pure hydrogen was assumed for the present project. Thus, some discrepancies both in terms of absolute figures and trends should be expected.

For verification purposes, the values reported in tables 6.1, 6.2, and 6.3 were assumed for the channel geometry and the overpotentials assessment [Campanari and Iora 2005]. A mass flow equal to that of the aforementioned reference was assumed in the air channel, whereas this was not possible for the fuel channel. Due to the presence of pure hydrogen as a fuel, the stoichiometric fuel channel mass flow was re-calculated based on the assumption that hydrogen and water vapour are present in the same molar fraction (0.5) at the inlet of the fuel channel. This is a reasonable assumption considering that in the aforementioned reference about half of the fuel-channel inlet-mass-flow molar fraction was represented by water vapour.

Variable	**Value**	**Dimension**
Voltage	0.7	V
Anode thickness	50.0E-06	m
Cathode thickness	50.0E-06	m
Electrolyte thickness	150.0E-06	m
Interconnect thickness	1.28E-03	m
Channel width	0.003	m
Channel height	0.001	m
Channel length	0.1	m
Air channel mass flow	5.69E-05	kg/s
Fuel channel mass flow	(stoichiometric mass flow)/λ	kg/s
λ	6	
Inlet temperature	1173.15	K
Operating pressure	101325	Pa

Table 6.1: SOFC geometry and setting parameters for verification

Activation overpotentials	**Value**	**Dimension**
β	5	
γ_{anode}	7.0E08	A/m^2
$\gamma_{cathode}$	5.5E08	A/m^2
$E_{act,anode}$	100.0E03	J/mol
$E_{act,cathode}$	117.0E03	J/mol

Table 6.2: Activation overpotentials parameters

The present SOFC model was found to match the reference results in terms of hydrogen and water vapour fraction throughout the fuel channel (figures 6.7 and 6.8).

Concentration overpotentials	Value	Dimension
Diffusion path length	0.005	m
Electrode bulk porosity	50	%
Electrode bulk tortuosity	3.0	
Mean pore diameter	1.0E-06	m

Table 6.3: Concentration overpotentials parameters

The main difference between the two is due to the absence of the steam-methane-reforming modelling in the present SOFC model. In fact, when methane reforming takes place at the inlet of the SOFC channel water vapour is initially consumed to break down the natural gas into carbon dioxide and molecular hydrogen. This is why the reference results have a maximum hydrogen molar fraction and a minimum water vapour molar fraction throughout the channel length. As expected, these peaks are absent in the present SOFC model due to the presence of pure hydrogen as a fuel.

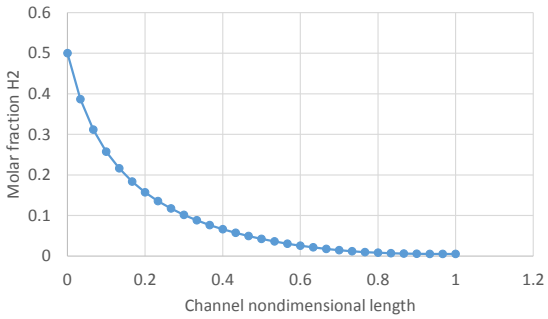

(a) Hydrogen fuel molar fraction results (Co-flow, 900°C)

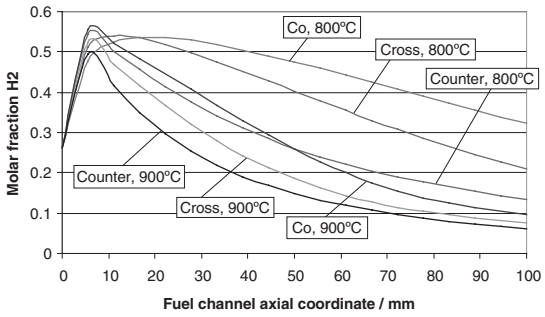

(b) Hydrogen fuel moalr fraction from Campanari and Iora 2005

Figure 6.7: Comparison of the simulated hydrogen fuel molar fraction with the results from Campanari and Iora 2005

The present SOFC model was also found to reasonably predict the ohmic and activation overpotentials (figures 6.9 and 6.10). In terms of absolute figures, the ohmic overpotentials are greater by 10 mV and the activation overpotentials (on the cathode side) are bigger by 25 mV. This difference was due to the fact that pure hydrogen fuel is used. In fact, hydrogen fuel has a higher lower heating value (LHV) compared to the hydrogen-hydrocarbon fuel mixture present in the case of steam methane reforming. As a consequence, the ideal SOFC voltage increases. In order to achieve the same specified operating voltage of 0.7 V, the overpotentials have to increase to compensate for the increase in the ideal voltage (eq. 6.1).

It is for the same reason that the present SOFC model predicts a higher max-

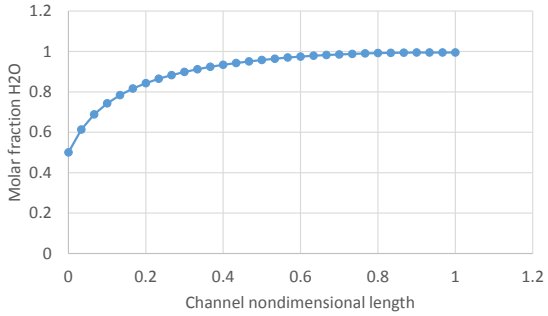

(a) Water vapour molar fraction results

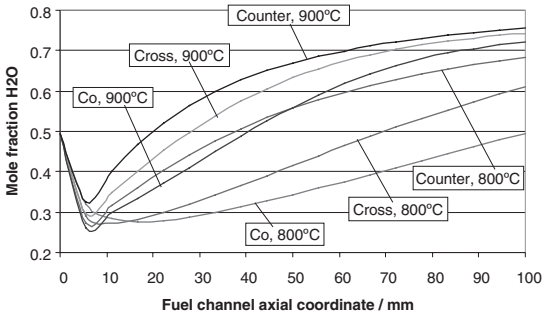

(b) Water vapour moalr fraction from Campanari and Iora 2005

Figure 6.8: Comparison of the simulated water vapour molar fraction with the results from Campanari and Iora 2005

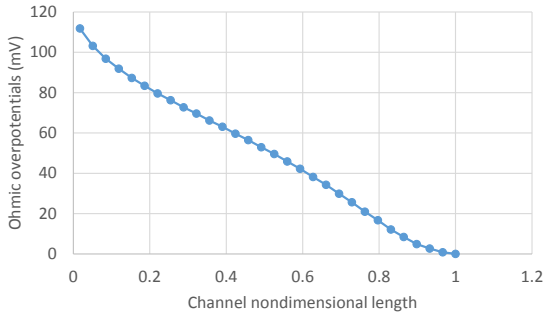

(a) Ohmic overpotentials results

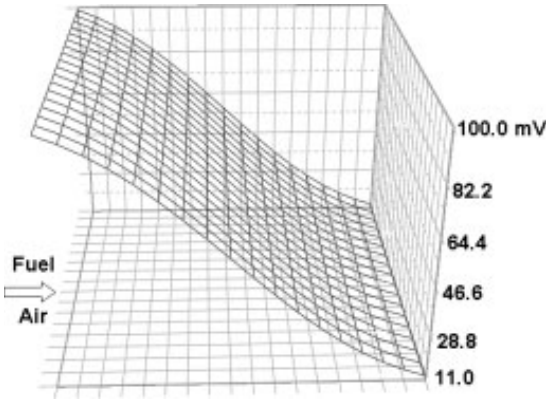

(b) Ohmic overpotentials from Campanari and Iora 2005

Figure 6.9: Comparison of the simulated ohmic overpotentials with the results from Campanari and Iora 2005

imum current density (figure 6.11). The ohmic and activation overpotentials are mainly a function of the channel geometry, operating temperature, molar fractions and current density. As the first three parameters are nearly unaffected by the fuel selection, the current density is the only variable that can change to result in a variation of overpotentials. Being the aforementioned overpotentials linearly dependent on the current density, this has to necessarily increase to achieve greater overpotentials.

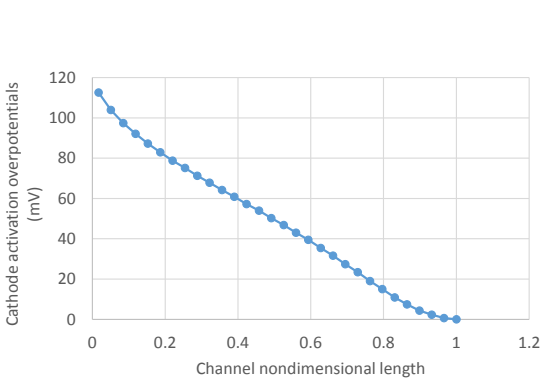

(a) Activation overpotentials results

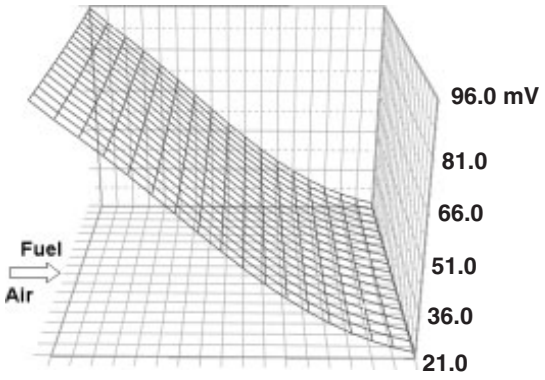

(b) Activation overpotentials from Campanari and Iora 2005

Figure 6.10: Comparison of the simulated activation overpotentials with the results from Campanari and Iora 2005

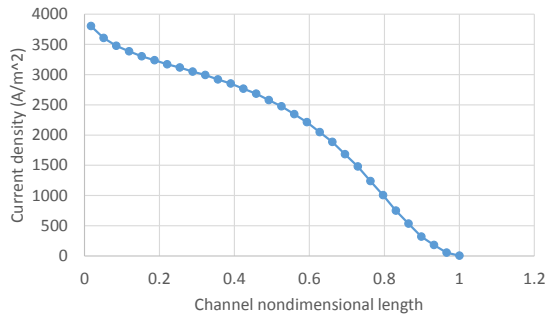

(a) Current density results

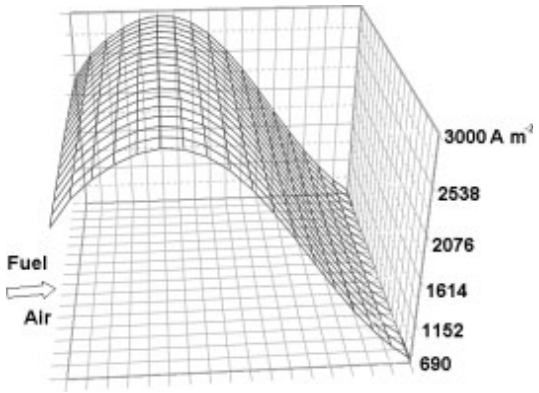

(b) Current density from Campanari and Iora 2005

Figure 6.11: Comparison of the simulated current density with the results from Campanari and Iora 2005

6.3.2 Hybrid SOFC/GT cycle analysis

This section focuses on a turboshaft analysis of the hybrid SOFC/GT cycles. The sensitivity of the cycle efficiency to the key SOFC design parameters, namely its fuel-to-air ratio and its cell voltage, are initially described (sects. 6.3.2.1 and 6.3.2.2). The effect of the combustor outlet temperature and of the engine overall pressure ratio is then presented, along with some key considerations on the cycles off-design performance (sect. 6.3.2.3).

6.3.2.1 SOFC molar FAR selection

The hybrid SOFC/GT cycle efficiency was found to increase at smaller molar fuel-to-air ratios (FAR)(fig. 6.12a). The considered hybrid cycle layout is cycle 1 (fig. 6.1a), where an OPR of 10 and a combustor outlet temperature of 1,000 K were considered.

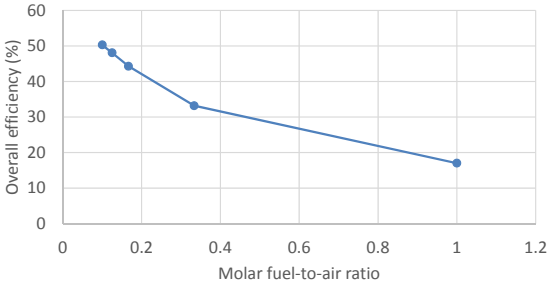

(a) Cycle efficiency as function of molar FAR

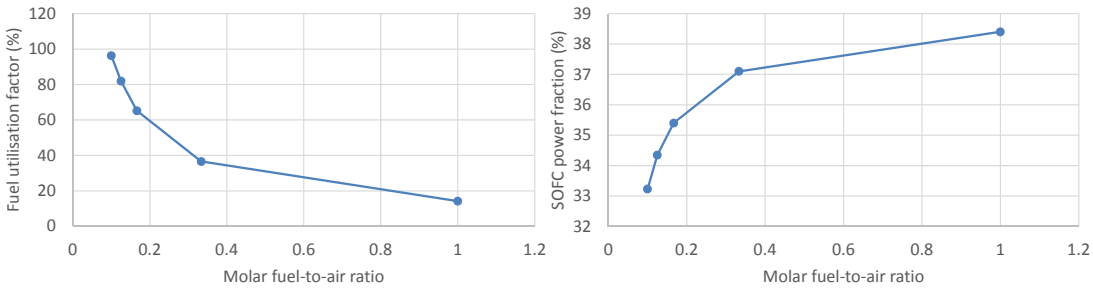

(b) Fuel utilisation as function of molar FAR **(c)** SOFC power fraction as function of molar FAR

Figure 6.12: The effect of SOFC molar fuel-to-air ratio (FAR) selection on the hybrid SOFC/GT cycle design-point performance. Cycle 1 was considered (fig. 6.1a) with OPR = 10 and combustor outlet temperature = 1,000 K

At a high FAR excess hydrogen is introduced in the fuel channel, and so not all the hydrogen is used to produce electric power. As the SOFC is placed after the combustor, the unused hydrogen could not be combusted and differently from an industrial cycle layout it would simply be wasted (sect. 6.2.4). This is reflected by the fuel utilisation factor, which increases as the molar FAR reduces (fig. 6.12b). The fuel utilisation factor is defined as the mass flow of hydrogen that leaves that fuel cell upon its inlet mass flow.

It is possible to observe that the fuel utilisation trend becomes divergent as the molar FAR reduces. This is because at a reduced FAR a small variation, in absolute terms, has a greater impact than at high FAR. The fuel utilisation factor was fixed at 95% for the present study, which is considered a very high value [Costamagna and Honegger 1998]. Such a high value would result in a non-uniform current density

distribution throughout the channel, which would lead to a non-uniform temperature distribution. However, previous studies predicted that the temperature gradients would still be small enough not to damage the SOFC structure [Costamagna and Honegger 1998].

The SOFC power as a fraction of the overall cycle power output (SOFC + turbine-generator) decreases as the molar FAR decreases (fig. 6.12c). This is because at a low FAR less hydrogen is available at the end of the SOFC channel, so that the hydrogen partial pressure would drop along with the ideal cell voltage (eq. 6.2). The reduced voltage would result in a higher current density, although this is not enough to compensate the lower voltage and deliver the same power output as if more hydrogen was available. The SOFC power fraction trend resembles that of the fuel utilisation factor, although its curve converges to zero rather than diverging to infinity. This suggests that there is an inverse relationship between the fuel utilisation factor and the SOFC power fraction.

6.3.2.2 SOFC cell voltage selection

There is an optimum cell voltage that maximises the efficiency of the hybrid SOFC/GT cycle (fig. 6.13a). The cell voltage was varied between 0.5 V and 1 V, which are typical values of solid oxide fuel cells [Campanari and Iora 2005]. The considered hybrid cycle layout is cycle 1 (fig. 6.1a), where an OPR of 10 and a combustor outlet temperature of 1,000 K were considered.

The optimum cycle efficiency is a trade-off between the SOFC efficiency (fig. 6.13b) and its inlet-to-outlet temperature difference (fig. 6.13c). The SOFC efficiency increases as its voltage becomes greater. This is because the operating voltage becomes closer to the ideal voltage of the hydrogen oxidation, and so less heat is released as thermal energy. Ultimately, the heat release is a source of inefficiency of the SOFC. This is why the temperature difference between the inlet and the outlet becomes smaller as the cell voltage increases.

These two effects have an opposite impact on the hybrid SOFC/GT cycle. A high SOFC efficiency improves the cycle efficiency because a greater amount of the cycle power output is produced more efficiently. At the same time, a high SOFC temperature difference improves the cycle performance as the overall efficiency is a function of the cycle peak temperature for a given OPR. At a low cell voltage the cycle efficiency increases as the high SOFC efficiency is the dominant effect.

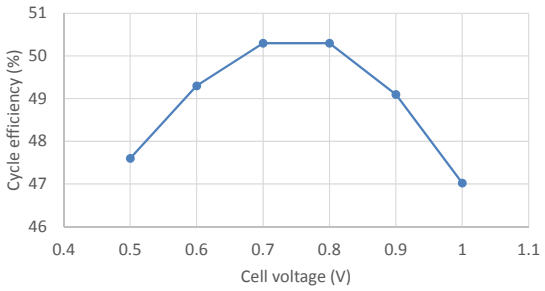

(a) Cycle efficiency as function of cell voltage

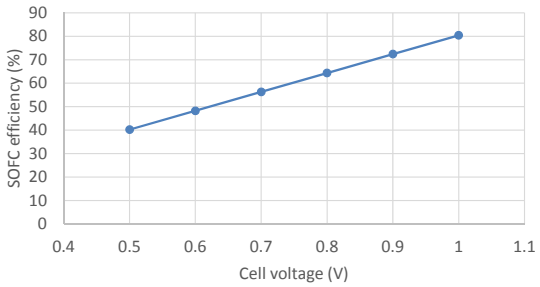

(b) SOFC efficiency as function of cell voltage

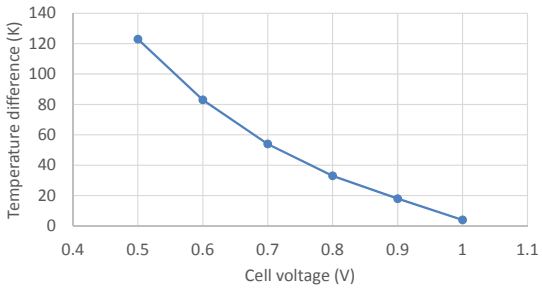

(c) SOFC ΔT as function of cell voltage

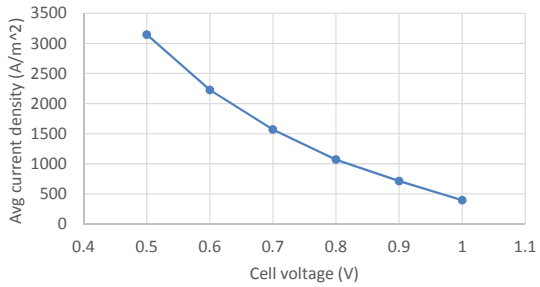

(d) SOFC current density as function of cell voltage

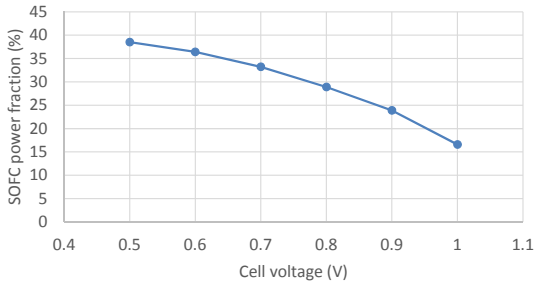

(e) SOFC power fraction as function of cell voltage

Figure 6.13: The effect of SOFC cell voltage selection on the hybrid SOFC/GT cycle design-point performance. Cycle 1 was considered (fig. 6.1a) with OPR = 10 and combustor outlet temperature = 1,000 K.

However, after a cell voltage of 0.8 V the reduced temperature difference prevails and cancels out any benefit of having an efficient source of electricity generation within the cycle.

The SOFC power as a fraction of the overall cycle power output (SOFC + turbine-generator) decreases with an increase in the cell voltage (fig. 6.13e). This is because when the cell voltage increases a fuel utilisation factor of 95% is reached at a smaller molar FAR, which leads to a reduced power output (see sect. 6.3.2.1). At low voltages the SOFC is unable to achieve a high fuel utilisation at high FARs. This is because at low voltages its efficiency is too low, and so most of the hydrogen in the fuel channel would be unused. Thus, the FAR needs to decrease so that the

hydrogen that is consumed throughout the reaction becomes closer to its inlet value. However, as the cell voltage increases the SOFC becomes more efficient, and so it is able to proportionally consume more hydrogen. This is why when the cell voltage increases the molar FAR reduces for a given fuel utilisation factor.

The current density decreases as the cell voltage increases (fig. 6.13d). This is because for a given FAR the ideal voltage is fixed, whereas the overpotentials, which directly depend on the current density, have to decrease to match the imposed cell voltage (eq. 6.1).

6.3.2.3 OPR and TET selection and off-design considerations

There is an optimum combustor outlet temperature (COT) that maximises the efficiency of the hybrid SOFC/GT cycle for a given OPR (fig. 6.14a). As expected, the cycle efficiency increases at greater OPRs for all the considered COTs (fig. 6.14b). It has to be noticed that the cycle 1 arrangement (fig. 6.1a) was used for a COT up to 1,100 K. Above 1,100 K the cycle 2 layout (fig. 6.1b) was used. This is because if the inlet temperature of the SOFC is in excess of 1,100 K its peak temperature would be beyond its maximum operating temperature of 1,273 K (1,000°C). Thus, by placing the SOFC after the HPT its expansion can be used to reduce the flow temperature down to an acceptable value for the SOFC.

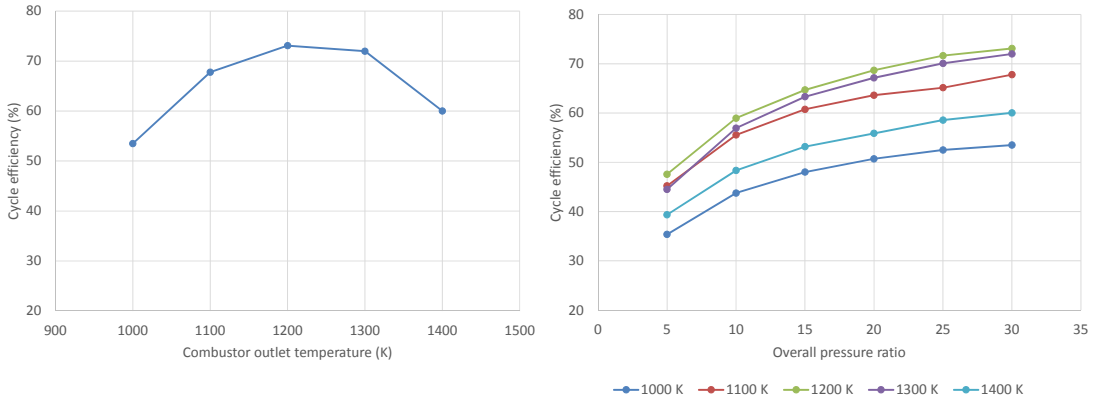

(a) Cycle efficiency as function of COT (OPR = 30)

(b) Cycle efficiency as function of OPR and COT

Figure 6.14: The effect of OPR and TET selection on the hybrid SOFC/GT cycle design-point performance. The optimum COT for a given OPR = 30 is shown.

Cycle 1 was considered when the COT was increased from 1,000 K to 1,100 K. The cycle efficiency improves because both the SOFC efficiency and the cycle peak

temperature increase. The SOFC efficiency is a function of temperature, and so the higher COT leads to a greater SOFC operating temperature. In addition, the higher COT also results in a higher SOFC outlet temperature, which is the peak temperature of the cycle. Thus, the cycle efficiency also improves because its peak temperature is higher.

Cycle 2 was considered when the COT was equal to 1,200 K. The cycle efficiency reaches a maximum at this COT because of the aforementioned factors (high SOFC efficiency and cycle peak temperature) coupled with the turbine reheating. This increases the overall power output of the cycle if power is also extracted from the HPT. At 1,200 K, the effect of reheating offsets the reduction in SOFC efficiency. This reduces because the turbine expansion leads to a lower pressure at the SOFC inlet.

The SOFC efficiency degradation due to its reduction in operating pressure becomes the dominant factor at COTs above 1,200 K. This effect becomes more evident at 1,400 K as a 10% cooling flow for the HPT was bled from the HPC exit. This is why the line between 1,300 K and 1,400 K is steeper than that from 1,200 K to 1,300 K.

The results indicate that a maximum design-point cycle efficiency of 73% could be achieved at a COT of 1,200 K. However, the layout of cycle 2 would be impractical at off-design. During the loiter the aircraft required thrust reduces as a consequence of the fuel that is burnt. Thus, the engine power setting would reduce. With the layout of cycle 2, if its power output reduces so that the COT falls below 1,110 K than the HPT would not be needed. Alternatively, for such a low COT the SOFC efficiency would degrade because of the combined effect of both the low temperature and the low pressure due to the turbine expansion. For cycle 2 to be a viable option, the HPT and HPC should be decoupled at off-design. This would not be possible at off-design as the two components are linked through a shaft.

As such, for the present study the COT was fixed to 1,100 K, limiting the design-point efficiency to 67.8%. The layout of cycle 1 was selected (fig. 6.1a). The OPR was limited to 30 so that the fuel cell operating pressure would be similar to that of the industrial cycles at sea level. This is because higher pressures would compromise the integrity of the SOFC structure.

6.3.3 Integrated aircraft-cycles studies

The hybrid SOFC/GT cycles were found to offer little or no benefits from an endurance perspective on both the T&W and the BWB airframes (figs. 6.15a and 6.16a). This is because the weight of the propulsion system offsets its fuel efficiency—even at SOFC power densities up to 1 kW/kg. The layout of cycle 1 was considered (fig. 6.1a), with an OPR of 30 and a COT of 1,100 K (sect. 6.3.2.3). An aircraft take-off mass of 15,000 kg was assumed (see Chapter 4). The SOFC power density was varied between 0.25 kW/kg, which is representative of today's technology, up to 1 kW/kg to account for future advancements in materials and electrodes architecture. The hybrid SOFC/GT cycle was integrated in a distributed-fans propulsion system, where its architecture is described in Appendix C.

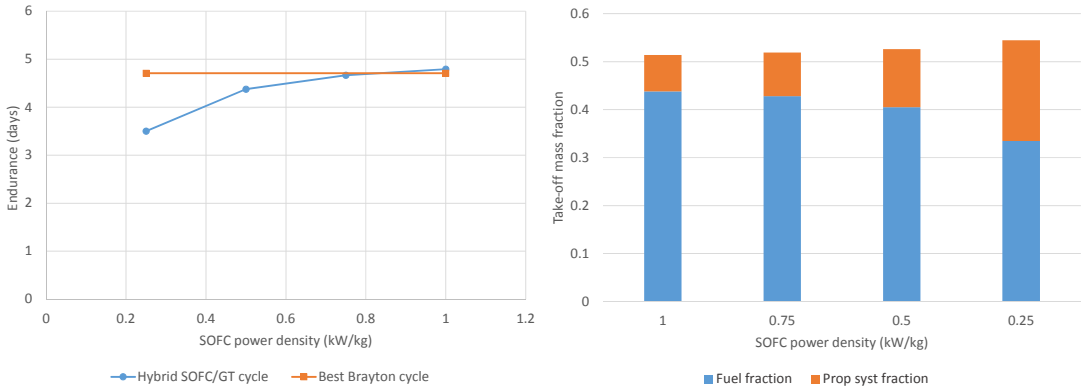

(a) T&W endurance as function of SOFC power density

(b) T&W take-off mass fractions as function of SOFC power density

Figure 6.15: The effect of the SOFC power density on the design and performance of the integrated aircraft-hybrid-cycle system. The T&W airframe was considered.

The study showed that the endurance of the integrated airframe/propulsion system is very similar when either the "best" Brayton cycle or the hybrid SOFC/GT cycle (at power density of 1 kW/kg) are used. The considered Brayton cycle refers to an OPR of 40, a TET of 1,600 K, a BPR of 25 and a FPR of 1.5 (see Chapter 5) For the hybrid SOFC/GT cycle, a BPR of 30 and a FPR of 1.5 were considered.

The considered SOFC/GT cycle would perform worse than the best Brayton cycle at power densities lower than 1 kW/kg. When the power density decreases, the fuel mass is replaced by the propulsion system mass. Thus, for a given take-off mass when the aircraft is re-designed less fuel can be stored as a consequence of the heavier propulsion system. This effect would occur on both the T&W and the BWB airframes (fig. 6.15b and 6.16b). An increase in the propulsion system mass also

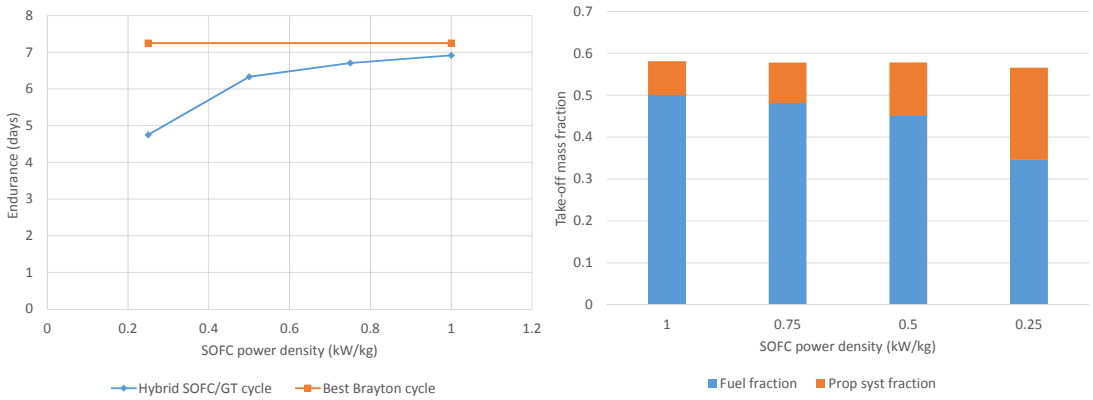

(a) BWB dndurance as function of SOFC power density

(b) BWB take-off mass fractions as function of SOFC power density

Figure 6.16: The effect of the SOFC power density on the design and performance of the integrated aircraft-hybrid-cycle system. The BWB airframe was considered.

leads to a heavier aircraft empty weight, meaning that more fuel would be consumed per time unit.

Ultimately, even at a SOFC power density of 1 kW/kg the propulsion system weight is still twice that of the best Brayton cycle. This effect completely offsets the fuel efficiency of the hybrid SOFC/GT cycle—which offers a 12% reduction in SFC—on the tube-and-wing airframe (fig. 6.15a).

It is also worth noticing that the endurance curves as a function the SOFC power density tend to become quite flat at 1 kW/kg. This suggests that even at higher power densities limited endurance improvements should be expected. Thus, for the SOFC to offer benefits a more efficient hybrid SOFC/GT cycle should be adopted.

6.4 Limitations to the present study

Several assumptions were made to assess the benefits of the hybrid SOFC/GT cycles at an integrated aircraft level. Some of them are related to either the design or the modelling of the individual elements of the system, whereas other concern the study as a whole.

6.4.1 SOFC assumptions and practical considerations

Several assumptions were made on the modelling of the hybrid SOFC/GT cycle and of the SOFC itself in terms of performance, size, and weight.

6.4.1.1 Stacking effects

The stacking effects were ignored when modelling the SOFC channels. As such, it was assumed that all the SOFC channels would behave in a similar fashion and would not affect each other. In reality, when the SOFC channels are placed close to each other they interact, so that the temperature and current density distribution would vary along three dimensions.

At a conceptual design phase, however, it was the author's choice to focus on a one-dimensional model and neglect the stacking effects. This is because such a model is still able to predict under which conditions a high fuel utilisation can be achieved—which strongly affects the cycle efficiency (sect. 6.3.2.1)—rather than imposing its value. However, neglecting two- and three-dimensional effects resulted in higher cycle efficiencies, particularly because the heat transferred from the SOFC boundaries to the ambient air was ignored. As such, the hybrid SOFC/GT cycle efficiencies that were predicted should be regarded as optimistic values.

6.4.1.2 Size and weight

A volumetric density of 0.3 m^3/ MW was considered for the present study, which is comparable to that of a modern gas turbine engine [Roth and Giffin III 2010]. It was also assumed that the geometry of the SOFC would be such that it could be fitted within the aircraft fuselage. However, Waters and Cadou highlighted that a tailored SOFC stack design is required to meet this constraint in the case of a tubular fuselage [Waters and Cadou 2003]. The proposed changes would also contribute to an increase in the SOFC power density.

Rows of SOFC channels should be stacked radially, so that the interconnect between the layers could be removed. Also, it would be possible to feed more mass flow within each channel by increasing its width. Decreasing the SOFC operating voltage and increasing the FAR would also result in a higher proportion of power produced by the SOFC for a given geometry and weight. This would reduce the

cycle efficiency, although this may be offset by the reduced SOFC weight at an aircraft level.

Even with the aforementioned changes, Waters and Cadou estimated that in a traditional turbofan engine for high-speed HALE UAVs the SOFC would be big enough to obstruct the fan bypass duct. However, in a distributed propulsion system the fans could be conveniently positioned elsewhere and they would be unaffected by the SOFC geometry.

6.4.1.3 Off-design considerations

The present study assumed that the layout of cycle 1 (fig .6.1a) should be adopted as the SOFC turbine-reheating would be unfeasible at off-design. During the loiter the engine power setting reduces up to a point that the HPC should be decoupled from the HPT. Otherwise, the low temperature and pressure would compromise the efficiency of the SOFC and of the hybrid SOFC/GT cycle as a whole.

A possible solution would be to drive the HPC with an electric motor and, at low power settings, to bypass the HPT with a duct that would deliver the flow directly to the LPT. Thus, the core would be characterised by a variable cycle. Electric motors are known to be a heavy and inefficient technology for airborne applications compared to a shaft linking the turbomachinery components. However, advancements in the electric machines technology should be expected in the near future as the electric transmission system is the key enabler for the distributed propulsion concept (see Appendix C). In addition to improve the design-point cycle efficiency, at off-design this concept would also offer extra flexibility to the gas turbine components as the HPC and the HPT would be decoupled.

6.4.1.4 Practical SOFC issues

A fuel cell stack requires a relatively complex system of pumps, blowers, sensors, controllers, and fuel processors to deliver appropriate reactants, maintain proper operating temperatures, manage starting and shut down transients [Waters and Cadou 2003]. Several components are required for the proper functioning of the SOFC, which add weight and complexity. The integration of the SOFC within a gas turbine engine simplifies the need for some of these devices. However, a system of variable shape and area ducts is required to link the planar SOFC stacks to the GT

components. Their design need to be carefully assessed, and a practical arrangement of the GT and SOFC components needs to be identified.

6.4.2 Further hybrid SOFC/GT cycle layouts

Other than what proposed in section 6.2.1, different cycles could have also be analysed. A first option would be to stack the SOFC channels in series and not only in parallel. Alternatively, the SOFC could be integrated with a wave rotor with internal combustion (Chapter 5).

6.4.2.1 SOFC stacks in series

Linking SOFC stacks in series could result in a cycle efficiency improvement up to 5% [Selimovic and Palsson 2002]. Similarly, benefits of a series arrangement were also reported in a more recent study [Aguiar, Brett and Brandon 2008]. The improvement is due to a better thermal management, as air flows through two subsequent smaller stacks compared to one larger stack [Selimovic and Palsson 2002]. However, within the present methodology it would not have been possible to capture this effect as the heat transfer between the PEM and the flow was not assessed in detail.

One of the main advantages of linking SOFC channels in parallel is that the cell voltage can be decreased. This would increase the power density of the SOFC at the expense of a lower fuel utilisation. However, the excess fuel could be used in the subsequent SOFC channel. The main challenge of this arrangement lies in the use of heat exchangers. In fact, the output of the first SOFC stack may be too hot to be delivered to the second SOFC, and so cooling would be required.

6.4.2.2 SOFC/wave rotor integration

Integrating the SOFC with a wave rotor with internal combustion (WRIC) would allow the overall cycle efficiency to be increased. In fact, the integration of the WRIC with a gas turbine engine improved the endurance of the integrated aircraft-propulsion system by up to 14%-18% (Chapter 5). The WRIC could replace the combustion chamber of the hybrid SOFC/GT cycles, along with a bypass around the WRIC itself.

The output of the wave rotor is an unsteady flow, and so it may negatively affect the performance of the SOFC. However, this could be counteracted by increasing the WRIC rotational speed and its number of channels. Another main challenge would be to practically integrate both the WRIC and SOFC within a gas turbine engine as several ducts would be required, which introduce losses within the system. Further studies are required to assess if the performance benefits—at an aircraft-integrated level—justify such a complex cycle architecture.

6.4.3 Results analysis and presentation

A remark must also be made on how the results were presented. Great emphasis was placed on how the cycle selection would affect the endurance of the integrated aircraft-propulsion system. Conversely, more focus could be put on the fuel cell itself and how its key design parameters would affect the design and performance of the integrated system.

An insightful study would be to assess the influence of the key SOFC design parameters on the SOFC weight and performance and on the aircraft endurance. This is because both the FAR and the voltage of the SOFC influence the power density of the SOFC itself. However, in the present study the FAR and cell voltage were chosen to maximise the cycle efficiency, and the power density was independently varied within a sensitivity study. A detailed assessment is required to assess how the geometry and the architecture of the SOFC stacks would influence its weight and performance, and consequently the aircraft endurance. The SOFC weight should then be assessed with a bottom-up approach by assessing the weight of its components.

6.5 Concluding remarks

The aim of this chapter was to build a methodology to assess the benefits of the hybrid SOFC/GT cycles at an aircraft-integrated level. Thus, the goal was to assess by how much the design and the performance of the integrated aircraft-propulsion system would be affected because of the cycle selection. The hybrid SOFC/GT cycles are known to offer efficiencies above 60%. However, the weight of the SOFC is a major constraint as the fuel-flow benefits might be offset by the increased weight

of the propulsion system from an endurance perspective.

The SOFC was placed after either the combustion chamber or the HP turbine within the considered cycles layouts (fig. 6.1). These arrangements allow the operating temperature constraints (600-1,000°C) of the SOFC to be met and avoid the use of heat exchangers to preheat the SOFC inlet flow. In fact, heat exchangers would increase the weight and complexity of the core engine. A maximum thermal efficiency of 73% was predicted when the SOFC acts as a turbine reheater. However, this configuration would be impractical at off-design as the HPT outlet flow would be at unacceptably low pressures and temperatures to be delivered to the SOFC. As such, the maximum thermal efficiency was limited to 67.8% by placing the SOFC between the combustor and the HPT.

The integrated aircraft-cycle studies highlighted that little or no benefits would be achieved with a hybrid SOFC/GT cycle on both the T&W and BWB airframes—even at a SOFC power density of 1 kW/kg. Compared to the best Brayton cycle, the 12% reduction in SFC of the distributed-fans propulsions system is offset by the propulsion system weight. At SOFC power densities below 1 kW/kg the fuel cell hybrid cycle would always perform worse than the best Brayton cycle in terms of aircraft endurance.

These results neglected the SOFC stacking effects, which would result in non-uniform three-dimensional temperature and current density distributions. As such, the present cycle efficiencies and aircraft endurances results should be regarded as optimistic. However, the cycle design-point efficiency could still be improved by either linking the SOFC stacks in series or integrating the SOFC with a wave rotor with internal combustion, which could replace the traditional constant-pressure combustor. Further studies are required to assess if the performance benefits—at an aircraft-integrated level—justify such a complex cycle architecture.

Part III

Power Management and Distribution

Chapter 7

Energy Management

7.1 Introduction

Energy management proved to be a solution to extend endurance on small UAVs and to meet the future environmental goal of civil aviation. Energy management is a strategy adopted by hybrid-electric propulsion systems, which integrate thermal and electrical power sources. The synergy between different power sources is such that in specific applications either the mission can be extended or a fuel saving can be achieved for a given mission.

The aim of this chapter is to assess the potential of energy management on low-speed HALE UAVs. A review of hybrid-electric systems is initially presented, which is then followed by a comprehensive analysis of energy management for aircraft applications. The methodology that was built by the author is then introduced. The details of how the battery model was chosen and integrated with the aircraft and the engine are explained. The results present the outcome of the series-hybrid and climb-and-glide energy management strategies on the tube-and-wing and BWB airframes. Prior to the concluding remarks, the limitations to the present study are exposed along with a qualitative assessment of the further non-performance benefits of the energy management.

In this chapter, the energy management strategies were applied only for the distributed fans case. The same engine baseline cycle that was used in chapter 4 is considered. Another key assumption is that energy management was applied only to the loiter segment, the longest and most critical flight segment.

7.1.1 Hybrid-electric systems

A hybrid electric (HE) system can be defined as a system in which energy is provided by two or more types of storage and generation devices. Hybrid-electric propulsion systems include a combination of thermal engines (gas turbines, piston engines) and at least one source of electric power that is used to generate thrust such as fuel cells, batteries, and capacitors [Mavris and Perullo 2014].

The benefits of the HE systems are well known in the automotive industry, where on top of emission benefits petrol-fuelled hybrid-electric vehicles (HEV) achieved fuel consumptions comparable to that of a diesel-powered car. HEVs can be classifed into four main kinds: series hybrid, parallel hybrid, series-parallel hybrid and complex hybrid [Chau and Wong 2002]. However, the architectures that Chau and Wong propose would not be adequate for hybrid turboelectric distributed propulsion systems as there is no mechanical link between the core engine and the propulsors (see appendix C). As such, the power flow could be bidirectional in both the series-hybrid and parallel-hybrid arrangements for a turboelectric distributed propulsion system, whereas this would be the case only for the parallel-hybrid arrangement in a HEV.

For a turboelectric distributed propulsion system, the series-hybrid architecture would include a battery between the AC/DC converter and the DC/AC converters that transfer the power to the motors (fig. 7.1). The battery would act as a buffer between the engine and the propulsors. Thus, the engine power setting could be decoupled from the propulsors required power.

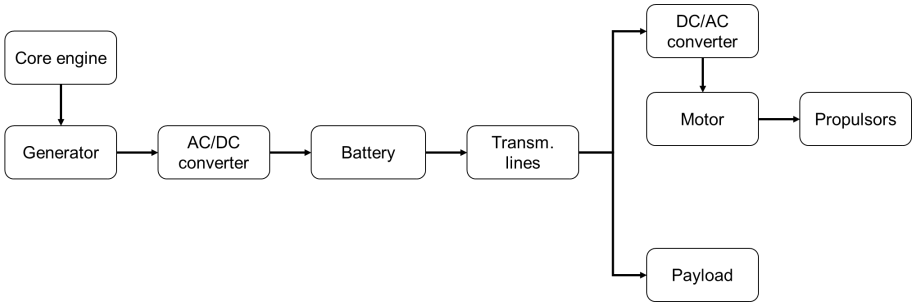

Figure 7.1: Series hybrid turboelectric distributed propulsion architecture

The series-hybrid architecture would allow any sudden increase in the engine power to be "filtered" and not be transferred as excess power directly to the propulsors. It could be particularly useful in the case of engine over-speeding, such as the ones due to a fuel metering or inlet guide vane mal-schedule, or shaft failure events. Also, it could allow the engine power setting to be selected independently from that of the

propulsors. Section 7.2.1.1 explains more details about the advantages that might arise.

As the name suggests, in the parallel hybrid architecture the battery is used in parallel with the core engine to supply power to the propulsors (fig. 7.2). In principle, this architecture allows the engine to be downsized and optimised for the low-power flight segments such as cruise. This architecture could be particularly suitable for short-range commercial aircraft as explained in section 7.1.2.2.

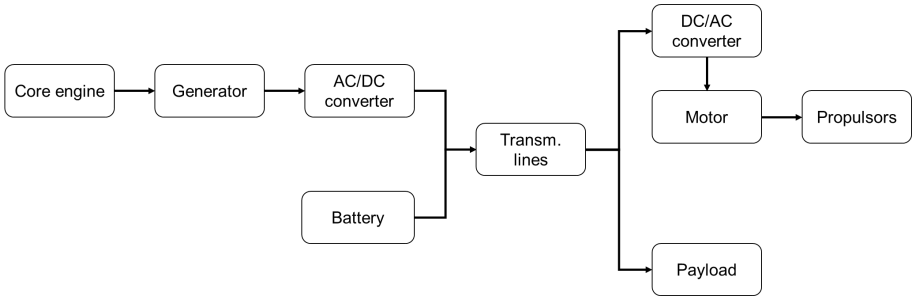

Figure 7.2: Parallel hybrid turboelectric distributed propulsion architecture

A further architecture that can be defined is the combined series-parallel hybrid turboelectric distributed propulsion system (fig. 7.3), which integrates the benefits of both the series- and parallel-hybrid arrangements. As explained in section 7.2.1.2, this architecture would allow the engine to be operated at a fixed power setting throughout the loiter by means of altitude variations.

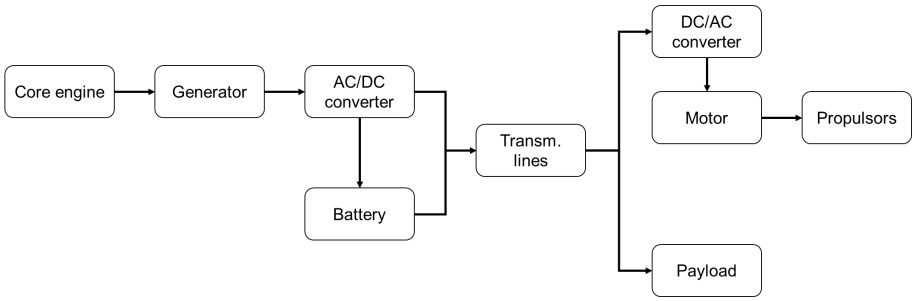

Figure 7.3: Series-parallel hybrid turboelectric distributed propulsion architecture

7.1.2 Energy management strategies

The main difference between energy management strategies for automotive and airborne application lies in the influence of the battery weight and the lack of historical data. Ground-based HEV studies [Borhan et al. 2009; Brahma, Guezennec and Rizzoni 2000; Chan-Chiao et al. 2001] highlighted how it is possible to determine

an optimum energy management strategy if the power demand as function of time is known. This could be achieved by means of analytical optimisation methods, instantaneous minimisation methods, and heuristic (or rule-based) methods [Serrao, Onori and Rizzoni 2011]. However, in aero applications the energy management is further complicated by the fact that the battery weight influences the aircraft mass reduction. Standard appropriate sizing methodologies have not yet been identified, and the optimal energy usage profile might change depending on the aircraft class and mission.

7.1.2.1 UAVs energy management strategies

Most UAVs energy management strategies focus on small unmanned aircraft, with take-off masses in the order of tens of kilograms. This results in low powers to be managed compared to the 200 kW that was set for the current project, not mention that an 800 kg payload would be unfeasible to carry.

In 2014, the Qinetiq Zephyr flew for 11 days solely based on solar power by means of efficient energy management. Excess solar energy would be stored in batteries during the day, which could then be used to sustain flight during the night. As suggested by Xian-Zhong et al. 2013, this energy management could be improved by allowing altitude to be varied (figure 7.4). Excess sun power could partly be used to climb at a higher altitude (while still charging the batteries), gravitational gliding could be used to reach a minimum altitude, and then the battery energy could be used for level flight. The same 11-day endurance requirement could be met by reducing the battery weight by up to 23.5% with this energy management strategy. However, this energy management strategy could hardly be adopted with larger HALE UAVs—the Zephyr weighs only 53 kg—as powers in the order of hundreds of kilowatts cannot be generated with solar energy given the limited wing surface area [Le Boulaire 2014].

Powerplant hybridisation was also found to offer benefits with a parallel-hybrid battery-thermal engine arrangement. Hung and Gonzalez 2012 demonstrated a 6.5% fuel burn reduction by using a battery in parallel with an internal combustion engine compared to the internal-combustion-engine-only configuration. However, the benefits referred to a small fixed-wing UAV with a fuel consumption in the order of 15-16 grams.

Karunarathne, Economou and Knowle 2011 recorded a 2.6% energy saving in a

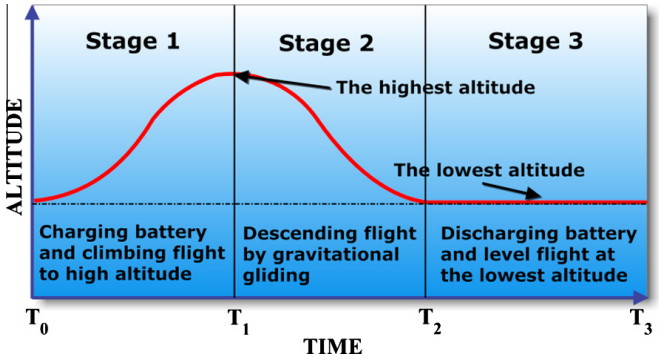

Figure 7.4: Optimal flight path and energy management strategy for solar-powered HALE UAV [Xian-Zhong et al. 2013]

parallel-hybrid battery-PEM fuel cell arrangement by dynamically controlling the power flow according to the aircraft demand. The battery would assist the fuel cell in the start up phase. Once the fuel cell reached a steady state condition, the excess power could be used to charge the battery. Additionally, the energy from both the fuel cell and the battery could be used during the power peaks. It has to be noticed, however, that this UAV had a total mass of 17.8 kg and a maximum required power of 1 kW. The use of PEM fuel cell would be questionable for powers close to a megawatt, whereas an integrated solid oxide fuel cell (SOFC)/gas turbine power plant may be more appropriate.

Bradley et al. 2009 studied a parallel hybrid arrangement so that a battery pack could assist either a piston engine or a PEM fuel cell. A climb-glide energy management strategy was proposed, where a climb phase would initially occur due to the combined power output of the battery and either the piston engine or the fuel cell. A glide phase would follow once the battery is emptied. No benefits were found for the fuel cell hybrid system, where the steady-level flight with no battery always outperformed any energy management strategy with and without altitude variation. Benefits were found with the climb-glide energy management strategy for the piston engine case, as the piston engine operates more efficiently at an increased power output. Still, the UAV under consideration had an overall mass of 12.5 kg with a 142 W power demand. For powers close to a megawatt a piston engine might be replaced by a gas turbine, whose off-design performance due to the altitude effect may offset any benefit of this energy management strategy.

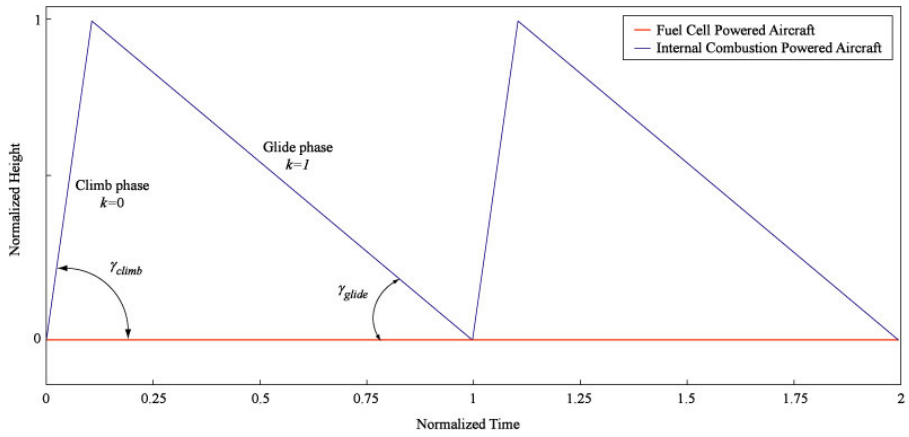

Figure 7.5: Optimal period flight paths for fuel cell and internal combustion powered aircraft [Bradley et al. 2009]

7.1.2.2 Large aircraft energy management strategies

Large aircraft energy management studies mainly focus on short-range parallel-hybrid aircraft (Airbus A320 or Boeing B737 type). Even with very optimistic assumptions on the energy density of the battery, its weight would likely offset any fuel flow reduction due to engine downsizing on long-range aircraft (fig. 7.6).

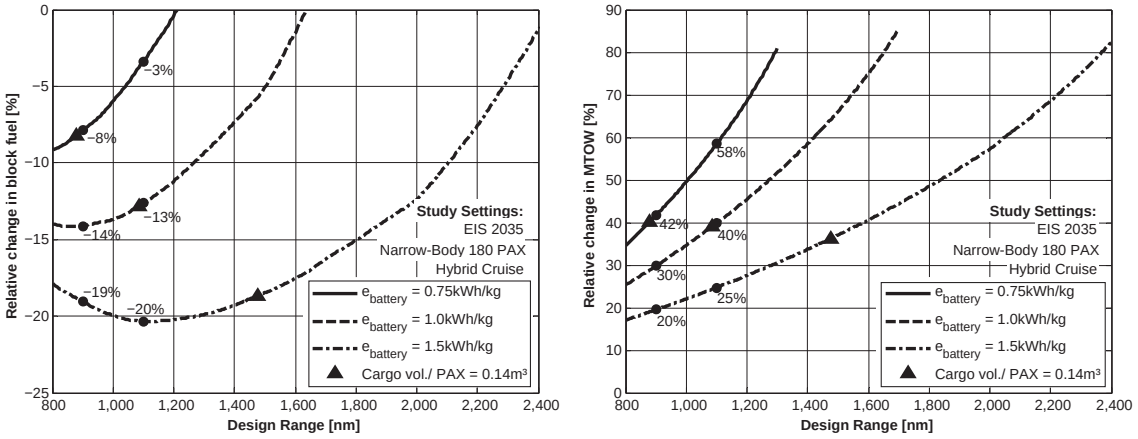

Figure 7.6: Relative change in block fuel (left) and MTOW (right) as a function of design range and battery energy density [Pornet et al. 2014a]

Bradley and Droney 2011 achieved a 63.4% fuel burn reduction with a parallel-hybrid architecture on a 154-passenger aircraft with a range of 900 nm. A tube and wing airframe was considered, and these benefits were on top of advancements in aircraft structures and aerodynamics. This hybrid arrangement comprised an electric motor mounted on the low-pressure shaft so that the fan could be driven by both turbine and battery power. A battery mass of 9,480 kg (13.5% of the maximum take-off weight) and a battery energy density of 750 Wh/kg were considered. This

63.4% fuel burn reduction is due to the gas turbine engine downsizing. In fact, the battery power can be used to boost the engine performance when high thrust levels are required (e.g. take-off and top-of-climb). Consequently, the thermal engine can be sized for cruise conditions only.

Figure 7.7: N+3 High L/D "SUGAR Volt" [Bradley and Droney 2011]

Pornet et al. 2014b reported a block fuel burn reduction up to 16% for a 900 nm mission on a 180-passenger aircraft with a mix of fuel energy to electrical energy of 82:18%. A battery mass of 8900 kg and a battery energy density of 1 kWh/kg were considered. Similarly to the aforementioned study, the fan was assumed to be driven by both turbine and battery power.

Figure 7.8: Bauhaus Luftfahrt Ce-Liner [Steiner et al. 2014]

In another study, the authors also formalised a set of algebraic expressions to parametrically describe dual-energy hybrid-electric aircraft [Isikveren et al. 2014]. It was found that such a dual-energy system can be represented by two independent non-dimensional variables: the supplied power ratio (Φ) and the activation ratio

(ϕ). In fact, the degree of hybridisation (DoH) for power was found to be a function of the supplied power ratio only. Conversely, the DoH for energy was found to be a function of both the supplied power ratio and the activation ratio.

The supplied power ratio Φ was defined as the ratio of the power supplied by two energy sources "a" and "b" (eq. 7.1). It measures the split between the two energy sources in terms of total installed power without including any transmission loss.

$$\Phi = \frac{P_{SUP,b}}{P_{SUP,a}} \tag{7.1}$$

The activation ratio ϕ was defined as the ratio of the time-weighted average of the energy source "'b" power control factor $\overline{w}$ upon the sum of the time-weighted average of both energy sources "a" and "b" power control factors (eq. 7.2). In simple terms, the activation ratio represents how often the second energy source is used throughout the mission. It is evident that different mission power profiles could lead to the same value of activation ratio as energy is assessed as the integral of power over time (eq. 7.3).

$$\phi = \frac{\overline{w_b}}{\overline{w_a} + \overline{w_b}} \tag{7.2}$$

$$E_{tot} = P_{SUPmax,a} \int_0^T \overline{w_a} dt + P_{SUPmax,b} \int_0^T \overline{w_b} dt \tag{7.3}$$

The authors also defined an energy specific air range (ESAR), which units nm/kWh and represents the distance travelled per kWh of energy. This figure of merit was then expressed as function of Φ and ϕ, the two independent variables of the dual-energy system (fig. 7.9). It can be seen that high values of Φ and low values of ϕ are required to positively affect the ESAR. Thus, high values of installed electric power and low utilisation (i.e. light battery weight) are required to achieve an increase in ESAR.

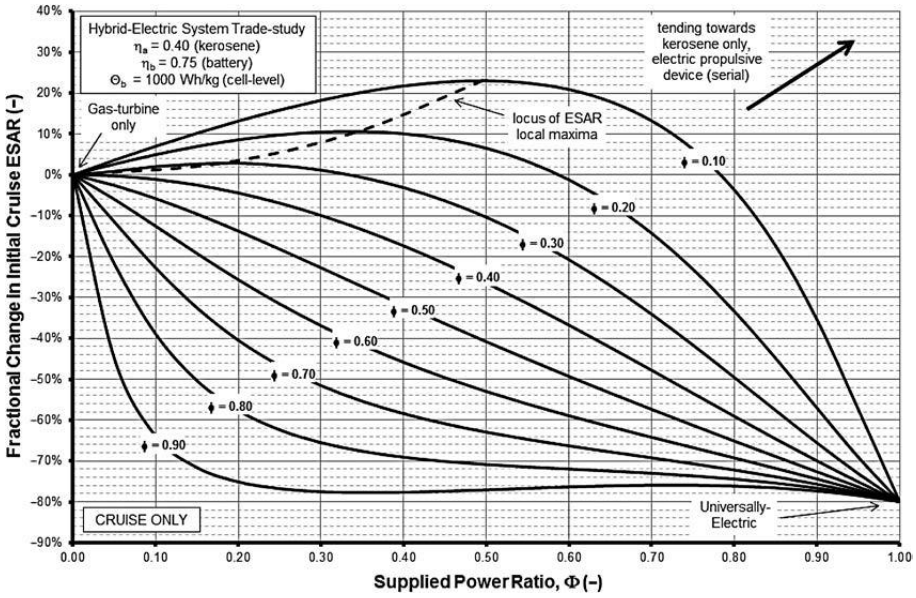

Figure 7.9: ESAR onion curves of a hypothetical hybrid-electric storage-propulsion-power system [Isikveren et al. 2014]

7.2 Methodology

The aim of the present study was to build a methodology to integrate the airframe, the core engines, the distributed fans, and the battery (fig. 7.10). Only with an integrated multidisciplinary and multifidelity methodology it is possible to capture the synergies between the individual parts of the systems.

The aircraft thrust needs to be translated into a power requirement throughout the loiter for the battery to discharge current to the propulsors at a calculated voltage. Similarly, to charge the batteries the engine power needs to be known in the different segments of the loiter if altitude and Mach are varied. The aircraft geometry must be reshaped to account for the battery volume and the reduced fuel load, and its performance need to differentiate between battery charging and discharging modes as both altitude and engine fuel flow would be affected by the energy management.

The present methodology initially focuses on the energy management strategies that were identified as suitable for a low-speed HALE UAV (sect. 7.2.1). The battery model that was selected for this project is then introduced, which allows the battery performance and weight to be assessed (sect. 7.2.2). The integration aspects between the different disciplines are finally described in section 7.2.3.

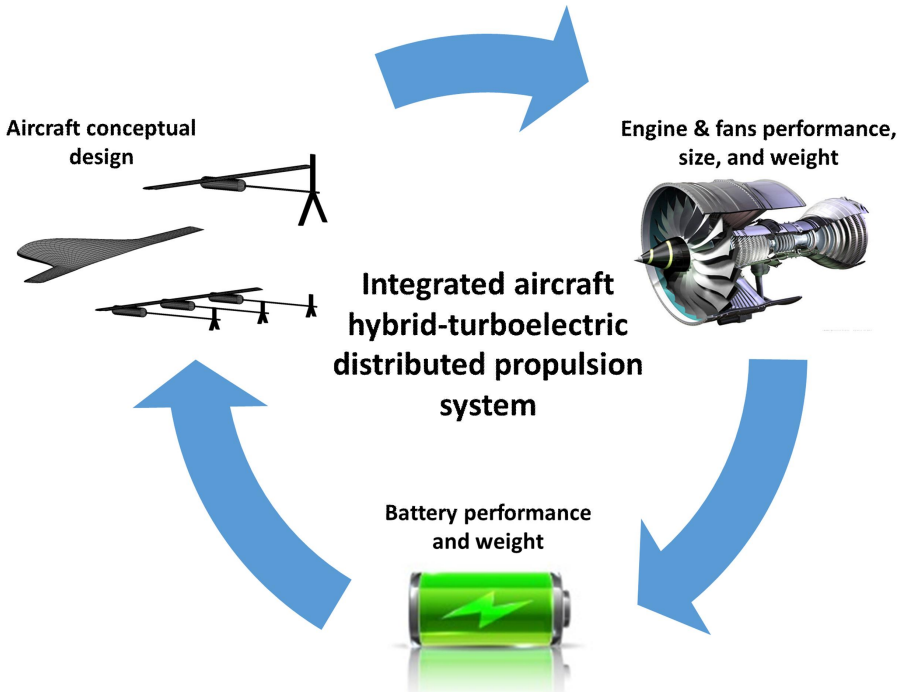

Figure 7.10: Visual representation of the methodology that integrates aircraft, engine, distributed fans, and battery calculations

7.2.1 Low-speed HALE UAV energy management strategies

Two energy management strategies were selected for the present research: the series-hybrid and the climb-and-glide. This choice was a trade-off between the current UAV specifications—which feature an unusual payload weight of 800 kg and power of 200 kW—and the public domain information about energy management.

7.2.1.1 Series-hybrid: the engine is relighted only to charge the batteries

Offsetting the off-design SFC penalty is the rationale behind the series-hybrid strategy. The gas turbine engine could be used at design-point only to recharge the batteries by relying on a series-hybrid architecture (fig. 7.1). Once the batteries are charged, the engine would be shut down and the electric propulsors would be powered by the batteries only. As the batteries are depleting, the engine could then be relighted to recharge them. This energy management strategy is graphically represented by the power-flow diagram in figure 7.11.

In principle, the engine is used for only a fraction of the total endurance and is run in the most efficiency way (i.e. its design point). Thus, if the battery is

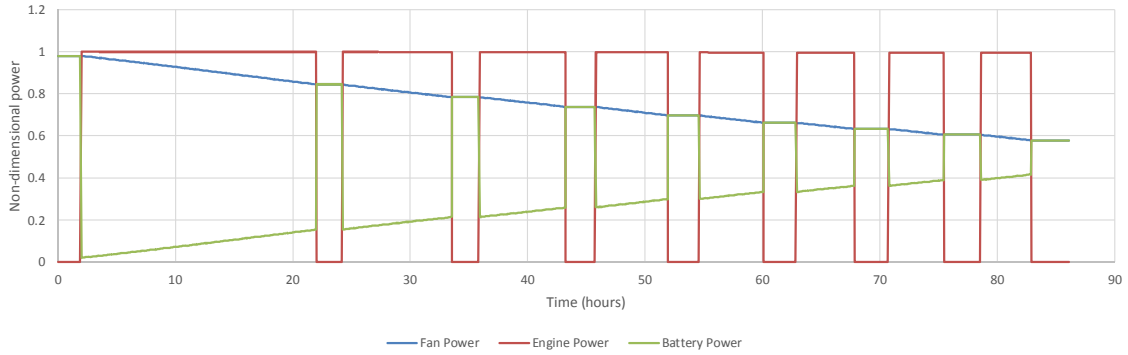

Figure 7.11: Series-hybrid fan system, engine and battery non-dimensional power profile as a function of time for the 15,000 kg T&W airframe with a battery energy density of 2 kWh/kg and a 10% battery fraction. Power is non-dimensional with respect to the design-point power of 955.5 kW

lightweight and has enough capacity the reduced fuel load and the deadweight effect should be counteracted by the engine off-design SFC mitigation. The "deadweight" effect refers to the greater empty mass of the aircraft because of the batteries, which negatively affects the mission fuel burn.

This series-hybrid energy management strategy presents many challenges in addition to the future development of battery technology:

Electrical transmission cooling Liquid hydrogen fuel is not extracted by the tanks when the engine is not running. Thus, the electric system would be left uncooled. A possible solution could be the coolant recirculation, so that hydrogen could be used even when the engine is not demanding fuel. This could be achieved, for example, either by using a higher heat capacity coolant such as slush hydrogen (a mixture of liquid and solid hydrogen) or by oversizing the cooling system so that more hydrogen can be circulated. With this approach the cooling system should be sized in a way that liquid hydrogen can be recirculated long enough for the batteries to be depleted and the engine relighted.

Engine relight There are two main challenges related to engine relight: combustion and fatigue life.

- About the combustion process, there has to be enough mass flow in the combustion chamber to have flow recirculation (or pressure drop) in the primary zone. Today's large turbofan engines are able to be relighted in at the most 90 seconds at an altitude of 39,000 ft. In a HALE UAV the engine is smaller so less mass flow is required in absolute terms, which is a positive factor.

However, low-speed HALE UAVs loiter at Mach 0.2 – 0.3, which is about four to three times lower than the Mach 0.8-0.85 of large civil aircraft. Also, at 50,000 ft the air density is about 40% lower than that at 39,000 ft.

- The engine start-up exposes the gas generator to a range of vibrations that may compromise its fatigue life. Although today's large aero engines can be relighted at altitude to meet the certification requirements, no current design is relighted multiple times during cruise.

A relight penalty should be included in the series-hybrid calculations. In principle, this should include the reduction of engine life and the energy required to relight the engine. An accurate representation of such a penalty would go beyond the scope of this research. A simplification was made to preliminary test the feasibility of the series-hybrid concept.

First of all, the impact on engine life was neglected. It is a reasonable assumption within the time-frame of a single mission so long as the engine is relighted a limited number of times. Further investigations would be required to assess how many missions one engine could complete.

Secondly, it was assumed that the engine is electrically-started with a motor mounted on the high-pressure shaft, and such energy would come from the battery. This contribution was calculated by assuming an engine relight work (eq. 7.4) and a relight time of 90 seconds, which together leads to a relight power that can be fed to the battery to discharge it. The relight work is the work that the engine requires to be accelerated from an initial to a final rotational speed. The inertia depends on its mass and its inner and outer radius by simplifying its design to that of hollow disc (eq. 7.5). In reality, fuel is consumed to restart the combustion process although the engine may not be producing a sensitive power output. This component of fuel that is burnt during the relight process varies from engine to engine almost in a random fashion and could not be predicted with current methods [Zachos 2014].

$$work = \frac{inertia\ (\omega_f^2 - \omega_i^2)}{2} \tag{7.4}$$

$$inertia = \frac{M\ (r_{outer}^2 - r_{inner}^2)}{2} \tag{7.5}$$

7.2.1.2 Climb-and-glide

In a climb-and-glide arrangement the engine and the battery could be used in parallel so that when both are providing power the aircraft climbs. When the batteries are depleted the aircraft would then glide as the gas turbine power output reduces due to the altitude effect. This solution is similar to what was proposed by Bradley et al. 2009. However, gravitational gliding was replaced by a controlled descent so that the engine would not cause windmilling drag. In principle, this extra drag term might cause the aircraft to lose altitude faster and negatively impact endurance. This energy management strategy is schematically represented by the power-flow diagram of figure 7.12 and by the altitude chart of figure 7.5. The architecture that enables this energy management strategy is the series-parallel hybrid arrangement (fig. 7.3).

From figure 7.12 it is possible to notice that the engine and the battery powers show a maximum and then decrease. This is because the aircraft is initially descending and its power output increases as altitude reduces. The battery power also increases because the battery itself is charged by the engine, and as its SOC increases its charging power becomes greater. The fans power is initially smaller compared to that of the engine and of the battery because only a small fraction of the engine power is delivered to the fans when descending. This is because the primary purpose of the descend phase is to charge the batteries.

The fan power peaks when the aircraft starts climbing, and it consequently reduces as the altitude decreases over time. After its peak, the engine power reduces for the same reason. However, the battery power becomes negative because it discharges to support the core engine in the climb phase. The climb performance sets the minimum battery capacity and consequently its weight for a given energy density. This is because the engine is operated at a constant power setting and alone it would not be able to make the aircraft climb. It is for this reason that the minimum battery mass that was considered was a 6% fraction of the take-off mass (for a 2 kWh/kg energy density).

Conversely, the limiting factor for the series-hybrid energy management strategy would be the initial discharge at the beginning of the loiter when the fans require more power than during the rest of the loiter. This constraint proved to be less demanding than that of the climb requirement, which is why the minimum battery mass fraction that was considered was lower (4% of the take-off mass) than that of

the climb-and-glide strategy.

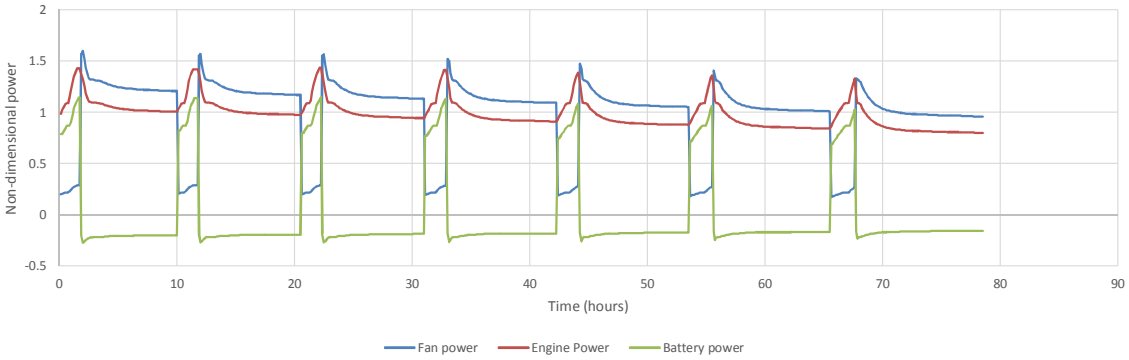

Figure 7.12: Climb-and-glide fan system, engine and battery power non-dimensional profile as a function of time for the 15,000 kg T&W airframe a battery energy density of 2 kWh/kg and a 4% battery fraction. Power is non-dimensional with respect to the design-point power of 955.5 kW

The benefits of the climb-and-glide energy management strategy should arise by operating the engine at constant power setting. However, the gas turbine and the propulsors would still experience an off-design due to the altitude effect. Being a parallel arrangement, in principle it should be possible to downsize the gas generator to reduce its fuel flow. Nonetheless, a small gas turbine engine may result in a longer time-to-climb. This would result in a higher fraction of the total time flown spent at a lower altitude where the drag is higher. Also, the climb-and-glide energy management solution poses a challenge in terms of flight control as it may interfere with the cruise path of civil aircraft (depending on the application of the present low-speed HALE UAV).

7.2.2 Battery modelling & sizing

An electrical model for lithium-ion batteries was selected [Chen and Rincon-Mora 2006; Vratny et al. 2013]. Lithium-ion batteries were chosen due their high energy density, high efficiency, long cycle life, and low self-discharge rate. On the other hand, lithium-ion battery properties deteriorate with cycling due to degradation effects and increased internal resistance.

Battery models can be classified into three categories: electrochemical, mathematical, and electrical models. Electrochemical models are generally used for detailed battery design as they relate micro- and macroscopic aspects. This option was not selected as their calculations would be too long compared to the convergence time of

the aircraft platform of the present research. Also, their fidelity would be higher than that required at a conceptual design phase. Mathematical models employ empirical equations or mathematical methods that are generally application-dependent. Also, their results can be inaccurate with an error of 5% to 20%.

Electrical models use a circuit-equivalent approach and represent the battery as a network of voltage sources, resistors, and capacitors (fig. 7.13). They are usually quite accurate (error between 1% and 5%) and their charge/discharge calculations last a matter of seconds. Chen and Rincon-Mora 2006 proposed a simplified electrical model that neglects the effects of self-discharge, cycle number, and temperature. However, this model is comprehensive enough to capture all the dynamic characteristics of a battery, from non-liner open-circuit voltage to storage time-dependent capacity and transient response. This model was validated with less than 0.4% error with experimental results, and so it accurately predicts battery runtime and current-voltage performance.

The selected electrical model is accurate and computationally-fast enough to be integrated in the aircraft platform. Single-variable functions dependent on the battery state-of-charge (SOC) were used to represent the open circuit voltage V_{OC}, the series resistor R_{Series}, and the RC network ($R_{Transient,S}$, $C_{Transient,S}$, $R_{Transient,L}$, $C_{Transient,L}$) as shown in figure 7.13.

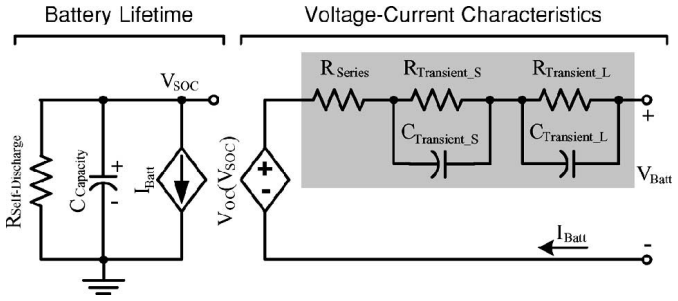

Figure 7.13: Battery model schematic proposed by Chen and Rincon-Mora 2006

On top of the runtime and current-voltage characteristics, the battery capacity also needs to be included in the integrated system representation. This can obtained by the knowing the battery weight and energy density (ρ_{bat}), which are the battery handles of the integrated methodology. In fact, the capacity of the battery, which units Ah, can be obtained by these two quantities by also knowing the operating voltage and the number of battery packs as shown in eq. 7.6 [Vratny et al. 2013].

$$C_{battery} = \frac{M_{bat} \;\; \rho_{bat}}{packs \;\; V} \tag{7.6}$$

7.2.3 Aircraft, battery and engine integration

The aircraft conceptual design methodology explained in chapter 4 was modified to include a fully-automated link with the battery electrical model. Specifically, the aircraft performance module was modified to include the interaction with the battery charge and discharge calculations (fig. 7.14). Also, the "endurance build-up" convergence algorithm was translated into a "battery cycle build-up" approach.

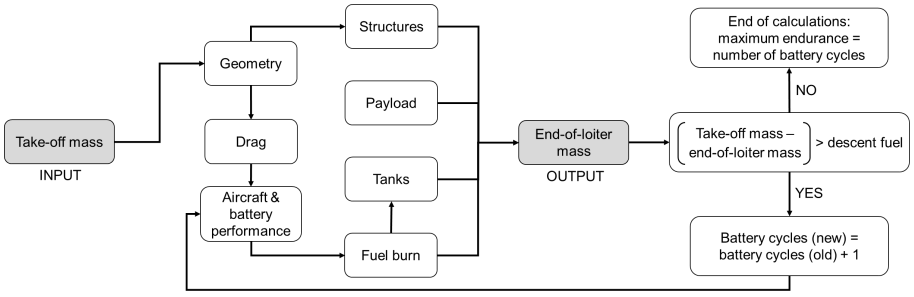

Figure 7.14: Layout of the integrated aircraft/battery iterative calculations

A battery cycle is defined as the sum of the charge and discharge time. The aircraft flies as long as the hybrid-electric propulsion system can afford to add up charge and discharge cycles. As no fuel is left, the battery cycles reached the maximum—ultimately the battery is recharged with the engine, which consumes fuel—and a final discharge of the batteries can be performed. As such, the maximum endurance can be defined as the sum of the battery cycles time plus the final discharge time until the batteries are emptied (minus the fuel required to complete the descent phase).

The integration between the aircraft and the battery model occurs so that the instantaneous aircraft power demand is fed to the battery model. Thus, by knowing the battery initial SOC and voltage—which needs to be guessed and iteratively changed—as well as the power demand it is possible to calculate the variation of state-of-charge ΔSOC for a given time step (fig. 7.15). This same approach could also work to recharge the battery if the aircraft power is replaced with the engine power and the ΔSOC is taken with a positive rather than a negative sign.

It has to be noticed that in the series-hybrid energy management strategy fuel is

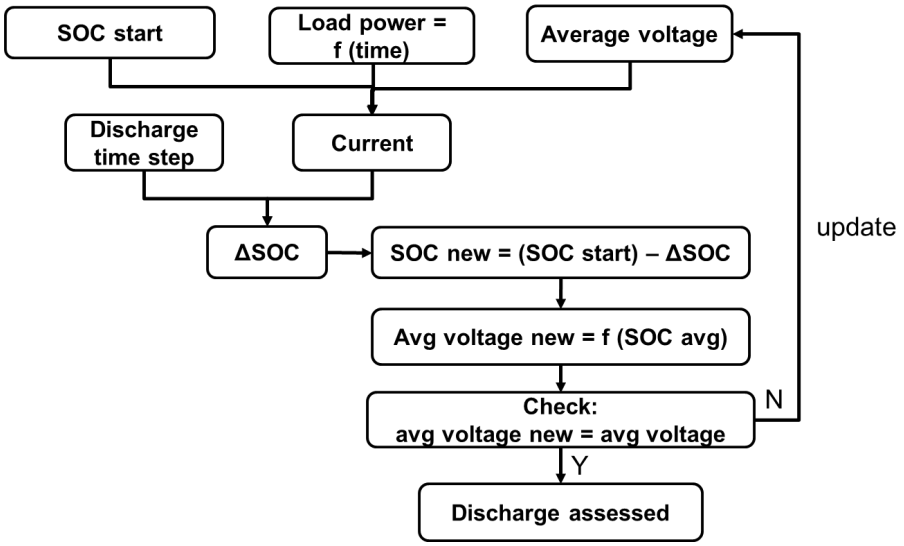

Figure 7.15: Battery discharge calculations flowchart. The same framework of calculations can work for recharging the battery if the ΔSOC is taken with the positive rather than the negative sign and the load power equals the engine power.

burned and Mach reduces (as altitude and angle of attack are kept constant) solely when the engine is charging the batteries (fig. 7.16). When the UAV is running on battery-only no fuel in consumed and so the discharge calculations are unrelated to the loiter fuel burn calculations. Also, the battery SOC was kept between 20% and 80% throughout each charge/discharge cycle to preserve the battery life. Beyond these limits the battery might be affected by irreparable damages that would shorten its operational life [Castano et al. 2015; Vratny et al. 2013].

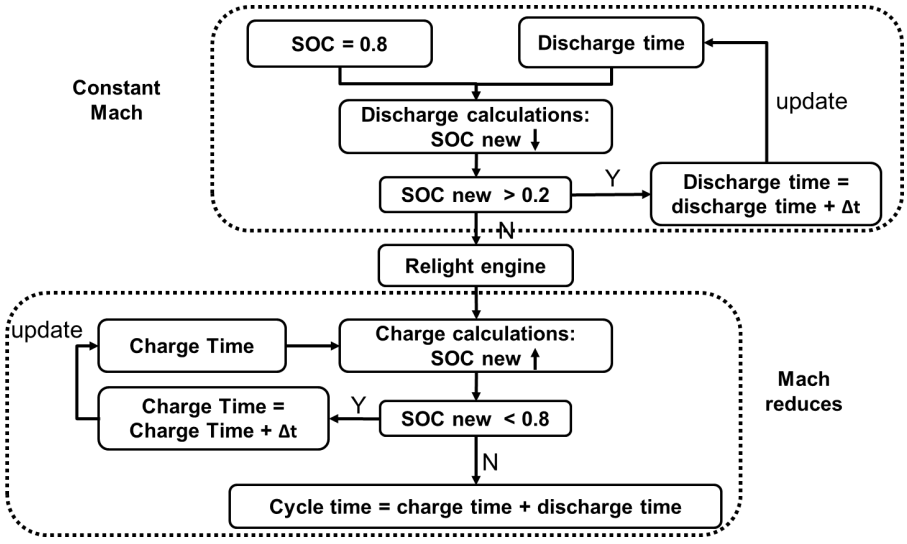

Figure 7.16: Series-hybrid aircraft-engine-battery calculations layout

An automated link between the aircraft and engine platform was also established.

This was achieved by means of maps representing the core engine and propulsors characteristics throughout the loiter. If the battery model is simple enough to be coded in the same language as the aircraft tool, this was not the case with the propulsion system. Cranfield's Turbomatch software was used to simulate the gas turbine and distributed fans performance. In addition to being written in a different programming language from the aircraft tool, it would take quite an effort to have a real-time interaction between the two software. As such, a simpler approach was chosen.

Aircraft thrust was translated into a battery power requirement by means of the power maps that were generated with Turbomatch (fig. 7.17). These off-design maps refer to the power the propulsors require to sustain flight, which is not to be confused with aircraft power expressed as the product of thrust and flying speed. Similarly, fuel flow and thrust were also mapped as they are required for the aircraft performance and fuel burn calculations (figs. 7.18 and 7.19). Power, available thrust and fuel flow were mapped as a function of altitude and Mach to explore the potential of both the climb-and-glide and series-hybrid energy management strategies.

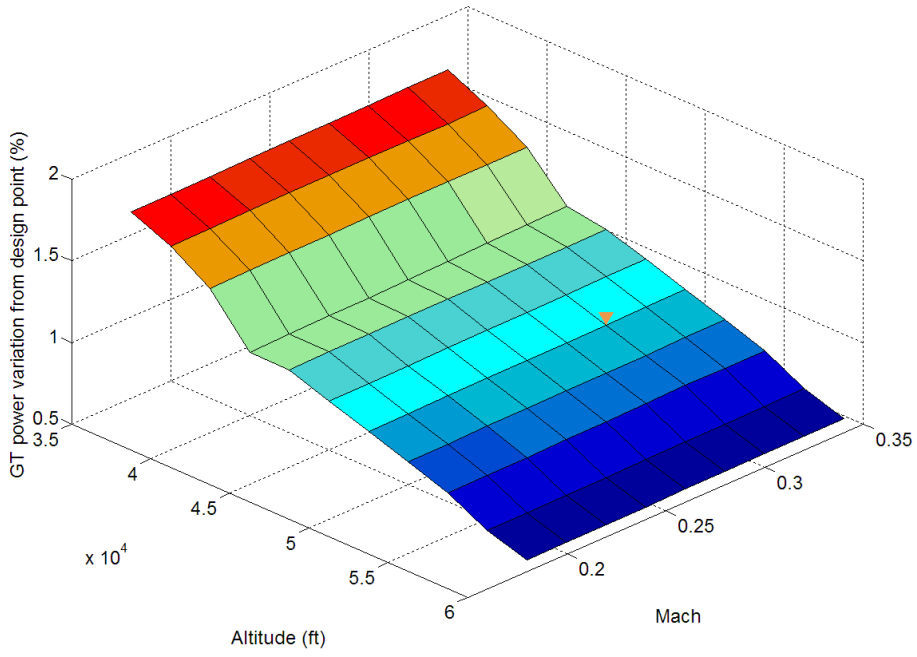

Figure 7.17: Gas turbine relative power variation from design point as function of altitude and Mach (the triangle represents the design point)

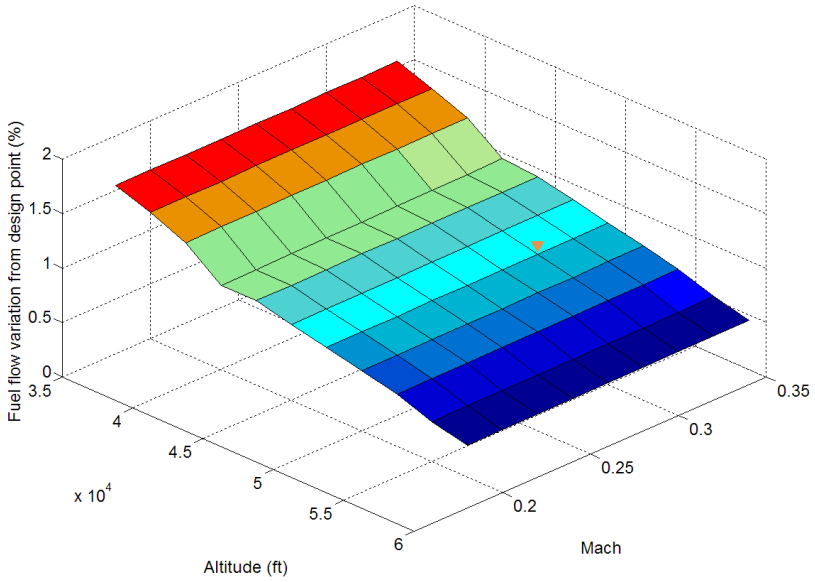

Figure 7.18: Gas turbine relative fuel flow variation from design point as function of altitude and Mach (the triangle represents the design point)

7.3 Results

The present results show the outcome of the integrated studies about the series-hybrid and climb-and-glide energy management strategies. Both the tube-and-wing and BWB airframes were considered. The main handle of these studies are the battery mass and its energy density. The first is expressed in percentage as a fraction of the aircraft take-off mass. In fact, it is typical of aircraft designers to relate the main aircraft masses (fuel, structures, payload, etc.) to the take-off mass in the form of a fraction, which can be either expressed in a decimal or percentage form. The battery energy density is a technological parameter that, for a given weight, defines the capacity of the battery pack (eq. 7.6). Values between 0.6 kWh/kg and 2 kWh/kg were considered. Public literature studies included power densities between 0.3 kW/kg and 1.3 kW/kg, which correspond to an energy density between 0.7 kWh/kg and 2 kWh/kg [Bradley and Droney 2011; Pornet et al. 2014a,b; Vratny et al. 2013]. State-of-the-art lithium-ion batteries have an energy density of approximately 0.2 kWh/kg at a pack level [Vratny et al. 2013].

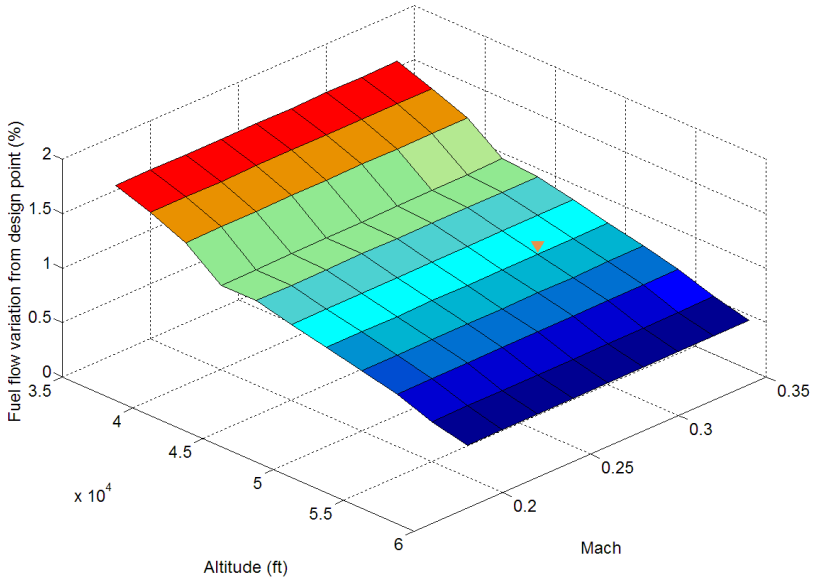

Figure 7.19: Propulsion system relative thrust variation from design point as function of altitude and Mach (the triangle represents the design point)

7.3.1 Series hybrid

7.3.1.1 Tube-and-wing airframe

The series-hybrid energy management strategy was found to offer an increase of 9 hours (or 9.5%) with a 4% battery mass when a battery energy density of 2 kWh/kg is used (fig. 7.20). This refers to the tube-and-wing airframe with a take-off mass of 15,000 kg. To achieve this benefit, the engine needs to be relighted 26 times, roughly once every four hours. As it will be explained below, endurance is a trade-off between battery weight and off-design SFC mitigation for a given battery energy density.

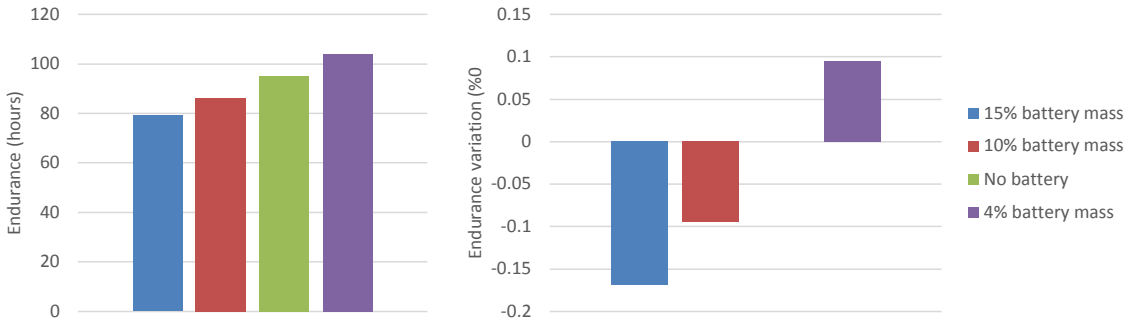

Figure 7.20: Endurance and endurance variation as a function of battery mass for the 15,000 kg T&W airframe with a battery energy density of 2 kWh/kg

This benefit is highlighted by the cumulative fuel burn trend (fig. 7.21). When a battery is used, the slope of the cumulative-fuel-burn line becomes smaller and smaller compared to the no-battery case as the aircraft accumulates flying hours. This suggests that, initially, by mitigating the off-design SFC penalty it is possible to offset two negative effects of carrying a battery. Firstly, the reduced fuel fraction (i.e. less fuel mass is available), and secondly the battery "deadweight" effect, which means that more fuel is burned per unit time as the aircraft empty mass is greater.

Afterwards, the slope of the cumulative-fuel-burn line becomes smaller than the no-battery case. This means that eventually avoiding the off-design SFC penalty more than offsets the heavier aircraft empty mass on a fuel-burn-per-unit-time basis. However, if the battery is too heavy—as in the 10% battery mass case—it displaces too much fuel mass for the maximum endurance to increase. This occurs despite the greater battery capacity being available, which should be expected in a series-hybrid energy management strategy where the battery is simply a buffer between the core engine and the propulsors. Conversely, if the battery is light enough there is sufficient fuel available to achieve a greater endurance although a smaller capacity is considered.

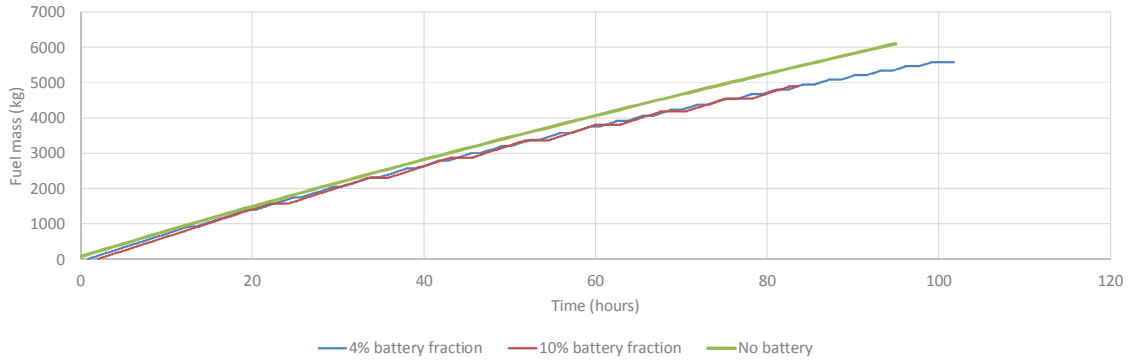

Figure 7.21: Cumulative fuel burn as a function of time for the 15,000 kg T&W airframe with a battery energy density of 2 kWh/kg

Other than displacing fuel, from an aircraft design perspective the presence of the battery has a negligible impact on endurance. Looking at figure 7.22, it is clear that the configuration with the lightest structures and the highest aerodynamic efficiency is the one with the heaviest battery mass. This is due to reduced fuselage size when less hydrogen is stored. However, the arrangement that gives the best maximum endurance is the closest to the baseline no-battery case in terms of fuel/structural mass and L/D. Thus, aircraft aerodynamics and structural improvements play a secondary effect compared to the off-design SFC mitigation, fuel mass reduction, and empty weight increase.

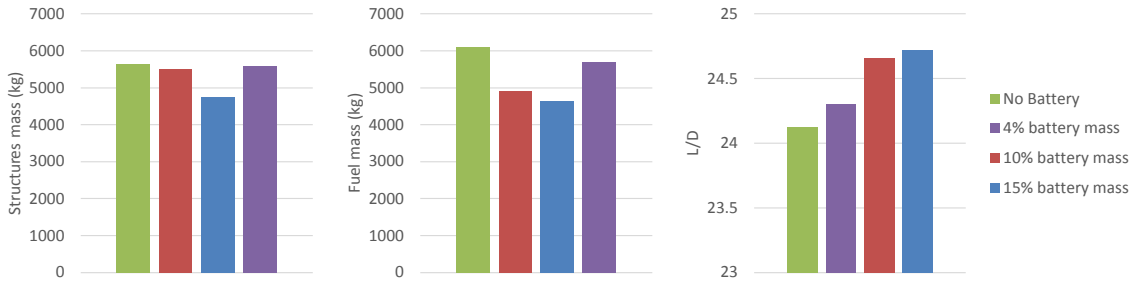

Figure 7.22: Structural mass (left), fuel mass (middle) and L/D (right) as function of battery fraction for the 15,000 kg T&W airframe with a battery energy density of 2 kWh/kg

The main outcome of this study is that the series-hybrid energy management strategy can be a viable solution only under very aggressive battery energy density assumptions (fig. 7.23). In fact, only at 2 kWh/kg of energy density an endurance improvement can be identified. For values smaller than that, no tangible benefits could be found. It has to be noticed that if the energy density is too small, for a given battery weight the capacity would be too small to provide power to the propulsors at the start of the loiter. This is why in figure 7.23 the 0.6 kWh/kg curve stops at 1500 kg and does not continue to smaller weights.

The outcome of this study was not affected by the aircraft take-off mass. In fact, even at smaller take-off masses the optimum battery fraction is still 4% for the 2 kWh/kg battery energy density under consideration (7.24). Thus, the results confirmed that even in the case of integrated hybrid-electric aircraft-battery-engine studies relating the battery weight to the take-off mass is a reasonable choice.

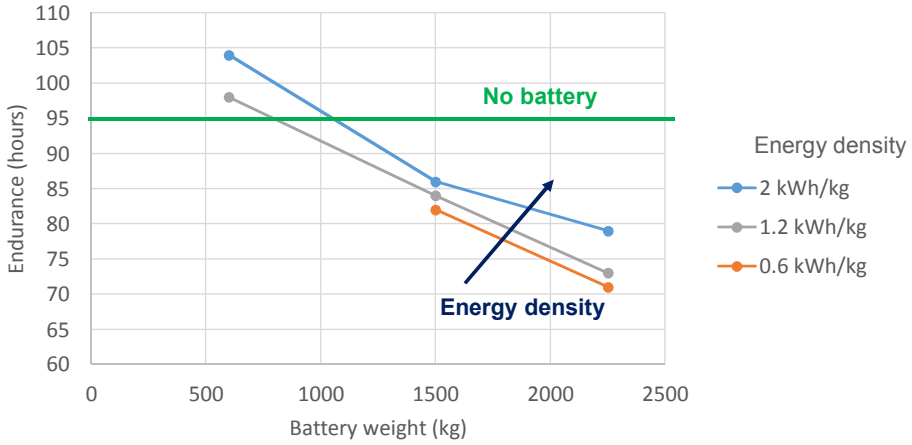

Figure 7.23: Endurance as function of battery weight and battery energy density for the 15,000 kg T&W airframe

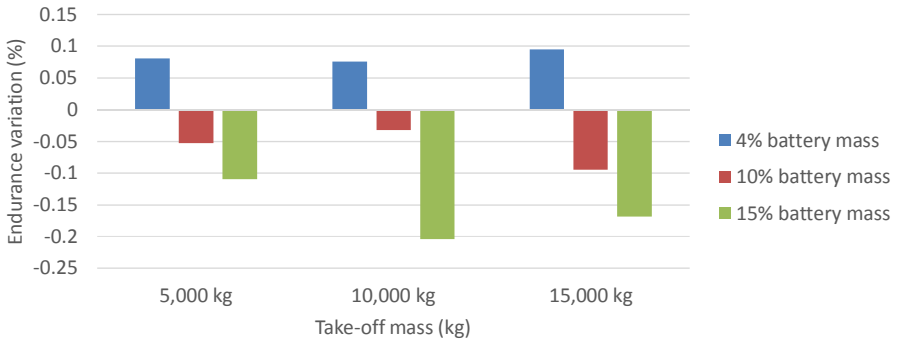

Figure 7.24: Endurance as function of take-off mass and battery weight for the T&W airframe

7.3.1.2 BWB airframe

The series-hybrid energy management strategy was found to offer no benefit on the BWB airframe (fig. 7.25). This is because for the BWB airframe, differently from the tube-and-wing airframe, the aircraft geometry is negatively affected by the battery volume. A take-off mass of 15,000 kg and a battery energy density of 2 kWh/kg were considered for the study.

An optimum wing loading could still be found when varying the battery mass. As it was explained in chapter 4, this is a trade-off between the centrebody and outer wing split of the total wing area. Such a trade-off is dependent on the internal volume requirement, which is affected by the battery volume that varies with its mass. The greater the battery mass and volume, the smaller the centrebody, and the bigger the outer wing, which results in a increased structural mass. The combined effect of the heavier structures (+2.9%) and the decreased fuel mass (-8.5%) offset the SFC penalty mitigation and the better L/D (+9.8%)—even at a 4% battery mass (fig. 7.26).

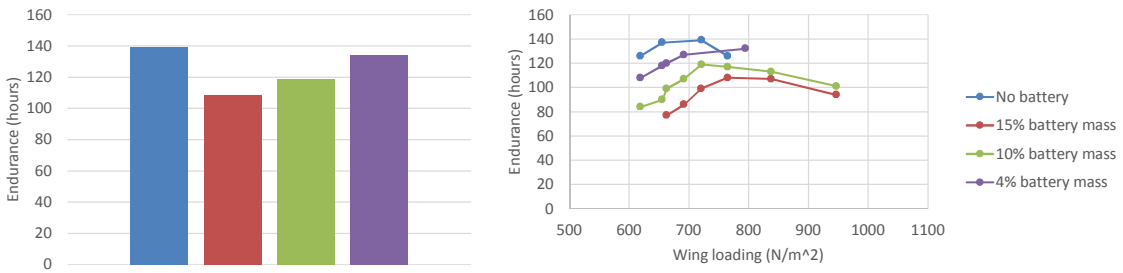

Figure 7.25: Endurance and endurance variation as a function of battery mass for the 15,000 kg BWB airframe with a battery energy density of 2 kWh/kg

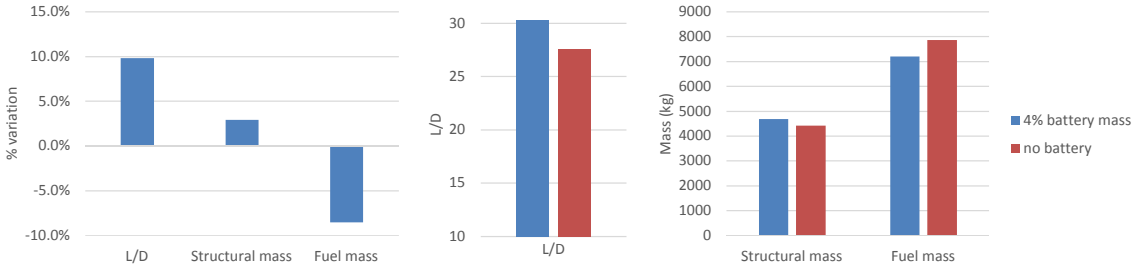

Figure 7.26: Variation of (left) and absolute (middle and right) L/D, structural mass and fuel mass as function of battery fraction for the 15,000 kg BWB airframe with a battery energy density of 2 kWh/kg

7.3.2 Climb and glide

7.3.2.1 Tube-and-wing airframe

The climb-and-glide energy management strategy was tested on the tube-and-wing airframe and found to offer no endurance benefit (fig. 7.27). This occurs independently of the GT-battery power split and the battery mass. This is mainly due to the fact that the gas turbine engine, although being operated at a given power setting, still experiences an off-design because of the altitude effect. A take-off mass of 15,000 kg and a battery energy density of 2 kWh/kg were considered.

As explained in section 7.2.1.2, both the engine and the battery are used at full power setting during the climb phase. When descending, a fraction of the engine power is fed to the batteries with the remaining power being supplied to the distributed fans. As such, the "80-20" figures refer to an 80% of power fed to the battery and 20% delivered to the fans.

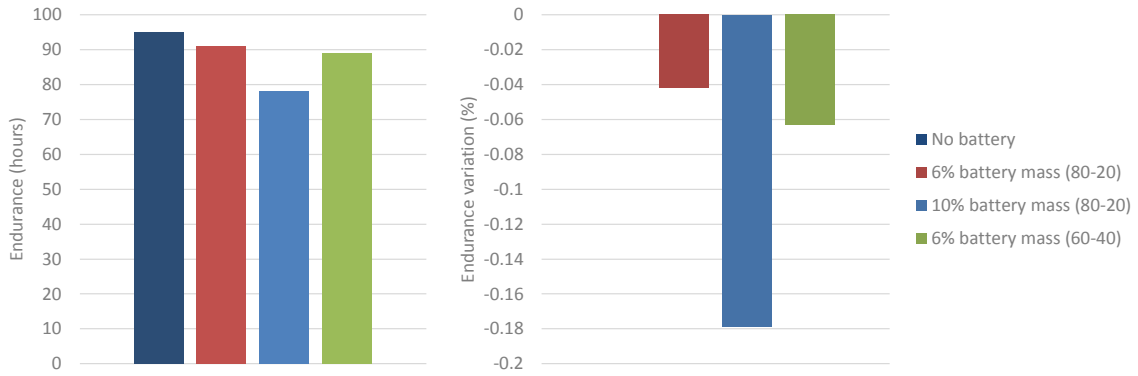

Figure 7.27: Endurance and endurance variation as a function of battery mass for the 15,000 kg T&W airframe with a battery energy density of 2 kWh/kg

The impact of the climb-and-glide approach on the maximum endurance can

be visualised from the cumulative fuel burn trends (fig. 7.28). In fact, its slope is unaffected by the climb-and-glide strategy so that the reduced fuel load because of the battery weight results in a shorter endurance. The fact that the cumulative fuel burn slope is unaffected suggests that the off-design penalty due to the altitude effect offsets the benefit of operating the core engine at a fixed power setting.

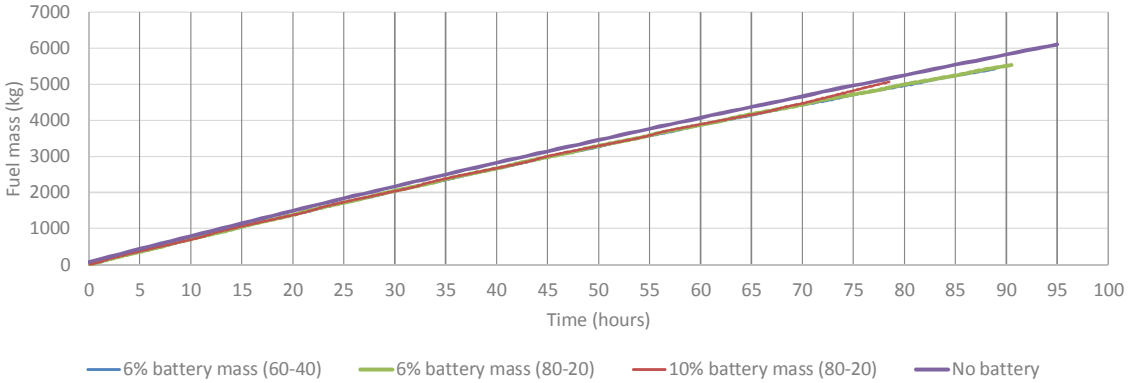

Figure 7.28: Cumulative fuel burn as a function of time for the 15,000 kg T&W airframe with a battery energy density of 2 kWh/kg

The core engine and the distributed fans were still sized for the top-of-climb case. Undersizing the core engine was not considered a viable option because, as it can be seen from figures 7.29 and 7.30, the combined engine/battery power already results in a time-to-climb of about 6-7 hours throughout the mission. A smaller core engine would lead to a greater time-to-climb, so that the aircraft would spend more time at a lower altitude where the increased drag would lead to a greater fuel consumption. Conversely, a bigger core engine would lead to a shorter time-to-climb by, at the same time, resulting in a greater fuel flow. Thus, undersizing or oversizing the core engine would not improve the impact on endurance.

It is possible to notice that with more power fed to the fans (from 20% to 40% of the GT power) the altitude variations reduce (fig. 7.29). This is because the distributed fans deliver more thrust. However, this results in a slightly shorter endurance as the batteries take longer to recharge and more time is spent during the descent phase. With an increase in battery mass (from 6% to 10%) the altitude variations become greater (fig. 7.30). This is due to the increase battery capacity as it takes longer to recharge it. The reduced fuel mass and the battery "deadweight" effect result in a shorter endurance.

The aerodynamic efficiency is positively affected by the climb-and-glide strategy as the aircraft spends more time at a lower altitude (fig. 7.31). As the wing is sized for high altitude (50,000 ft), a lower lift coefficient is required to fly at a lower

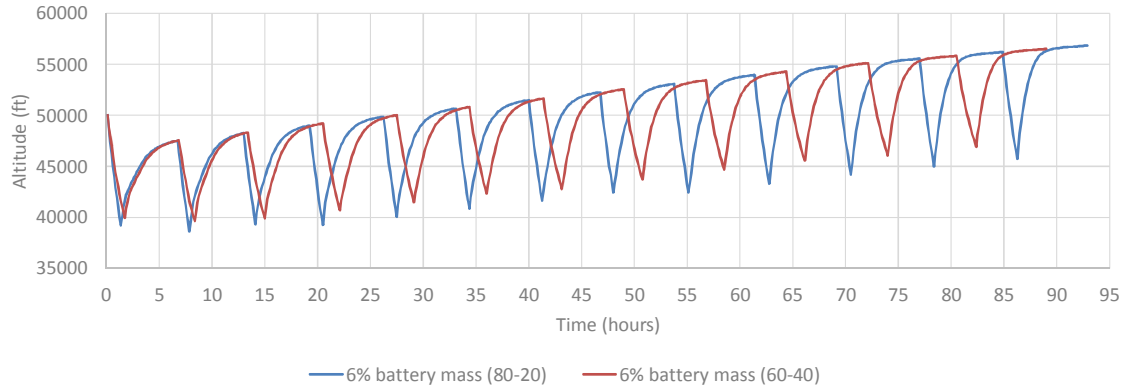

Figure 7.29: Altitude as a function of time for the 15,000 kg T&W airframe with a battery energy density of 2 kWh/kg

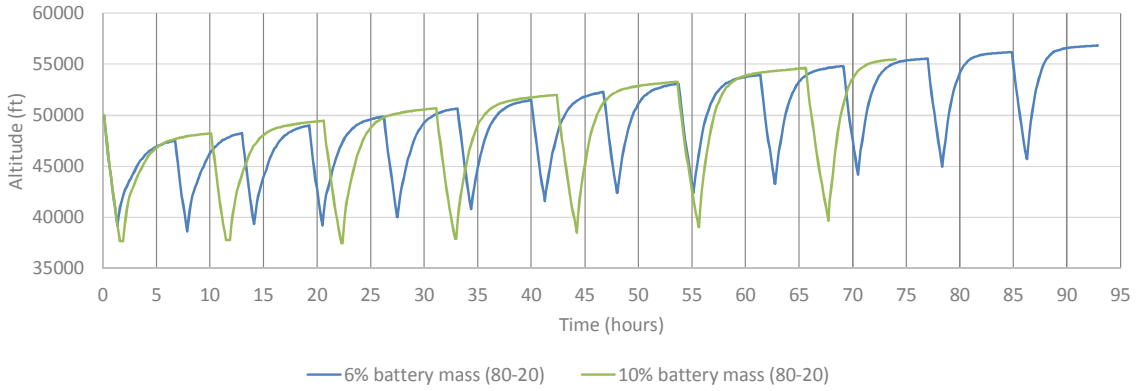

Figure 7.30: Altitude as a function of time for the 15,000 kg T&W airframe with a battery energy density of 2 kWh/kg

altitude due to increased air density. This results in a reduction in lift-induced drag, which depends on the square of the lift coefficient. However, this improvement in L/D is more than offset by the altitude effect on the engine performance together with the negative effects of the aircraft carrying a battery.

As expected, the propulsors thrust decreases when charging the batteries and increases when climbing (fig. 7.32). The thrust profiles were interpolated from the map of figure 7.19 for a given altitude and Mach by the aircraft conceptual design and performance tool throughout the loiter.

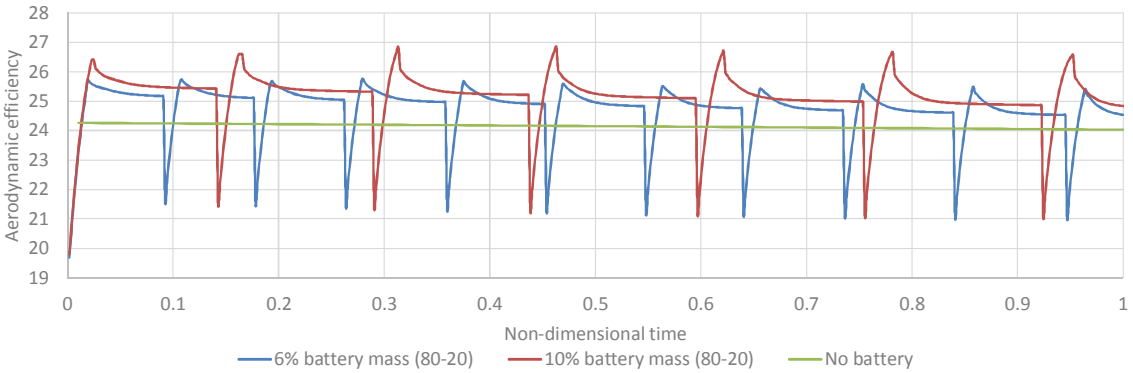

Figure 7.31: L/D as a function of time for the 15,000 kg T&W airframe with a battery energy density of 2 kWh/kg

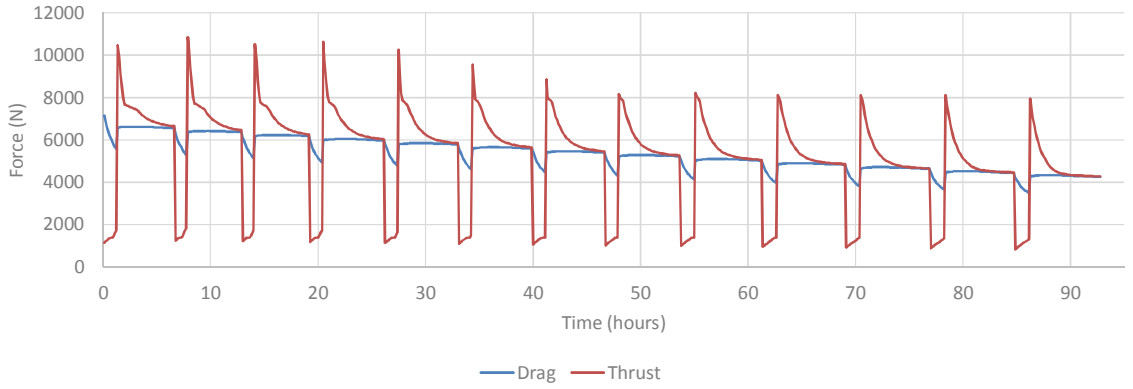

Figure 7.32: Thrust and drag as a function of time for the 15,000 kg T&W airframe with a battery energy density of 2 kWh/kg

7.4 Further considerations on the benefits of energy management

Energy management offers benefits that go beyond an endurance improvement and that should be further discussed. Section 7.3 highlighted that the series-hybrid energy management strategy offers performance benefits only with very optimistic assumptions on the battery energy density. Also, no endurance benefits were found for the climb & glide energy management strategy. Although their detailed analysis would go beyond the scope of this research, there are also operational, environmental, and reliability considerations that need to be taken into account.

7.4.1 Operational flexibility

The series-hybrid energy management strategy mitigates the system heat signature when the core engine is off and only the battery provides power to the propulsors. This could be useful for military applications, particularly for high-speed HALE UAVs. The heat signature may not be significant in a turboshaft engine if a propeller-powered aircraft was considered for a low-speed application. However, part of the thrust is still delivered by the core in a high-BPR turbofan such as the present turboelectric distributed propulsion system. The battery and the electrical transmission system would still have their own heat signature, although that should be easier to be mitigated as they are embedded in the airframe.

7.4.2 Environmental benefits

Both the series-hybrid and the climb-and-glide options allow emissions to be mitigated. Firstly, they allow the same or a greater endurance to be achieved with a reduced fuel mass, meaning that less fuel is burned and fewer emissions are released. Secondly, the series-hybrid architecture allow emissions to be further reduced as the aircraft is operated on battery only for part of the loiter. These benefits would refer only to the aircraft emissions, and it is clear that for the overall emissions to be reduced hydrogen must be sourced from renewable sources.

In addition, the series-hybrid architecture allows contrails formation to be mitigated when the engine is not used. Contrails are more likely to occur at low exhaust temperatures for given ambient pressure, temperature, and humidity. The exhaust temperatures of large commercial engines are likely to decrease in the near future as turbofans are moving to lower specific thrusts. Decreasing the flight altitude could be a viable solution due to the higher ambient temperature, although it would result in an increased fuel consumption due to the greater aircraft drag [Noppel 2007]. Energy management might be a solution to avoid such a fuel penalty and still be able to mitigate the contrails formation.

It might be argued that either there are not many UAVs in operation or that particularly for military applications emissions and contrails may not be a priority. However, the UAV market is expected to double in the next decade and hybrid-electric systems are also currently investigated for large aircraft.

7.4.3 Reliability

In a turboelectric distributed propulsion system there should be more than one generator per core engine for reliability purposes and to cope with failure scenarios. However, a battery would be more reliable than a generator given the fact that energy is delivered through a chemical reaction rather than by having rotating parts. Thus, if a hybrid electric architecture is considered there may not be the need for a auxiliary generators. A detailed analysis of the systems failure modes is required to assess this opportunity.

7.5 Limitations to the present study

Several assumptions limit the conclusions and the feasibility of this study. Some of them are related to either the design or the modelling of the individual elements of the system, whereas others concern the study as a whole.

7.5.1 Battery modelling and assumptions

The battery model was able to account for its efficiency as a function of how much energy is stored, i.e. its state of charge. This was a fundamental effect to capture given the fact that the battery would be constantly charging and discharging at different SOCs. However, the present model is not able to account for its voltage selection. To a certain extent, for a given capacity the battery voltage can be varied by changing the number of cells that are linked either in series or in parallel. The battery voltage might then be optimised for its integration with the electrical transmission system as its weight is very sensitive to its operating voltage due to the solid-state switch power converters (appendix C).

The results of the present study were also influenced by the lower and upper bounds for the SOC, which were set at 20% and 80%. This choice was made to preserve the battery life as the charge/discharge cycles may irreversibly damage the cells outside these boundaries. On the other hand, if the SOC boundaries could be "relaxed" more energy could be stored for a given battery weight. Thus, a shorter battery life would lead to the same endurance with a reduced fuel mass (or a greater maximum endurance could be achieved with the same fuel mass). As such, there

should ba a trade-off between the battery replacement cost and the fuel penalty of carrying a constrained-capacity battery. A model to incorporate the effects of the charge/discharge cycles on the battery life as well as cost considerations should be included.

7.5.2 Electric transmissions system assumptions

A sensitivity analysis would also be required to assess the influence of the electric system weight and efficiency on the energy management integrated studies. The electric transmission system weight and efficiency, which are discussed in appendix C, should be mainly considered as a technological target. Thus, further studies should also include their variation as it may cancel out the benefits identified by the present studies—even with very aggressive battery energy densities.

7.5.3 Results analysis and presentation

A remark must also be made on how the results were exposed. This study was presented in terms of battery mass—expressed as a function of the take-off mass—and energy density. Also, the results mainly focused on the integrated system performance, which is ultimately represented by aircraft parameters such as endurance, L/D, and the fuel/structural fractions. This choice was based on factors such as ease of integration of the different technologies, at a computational level, and ensuring that the results could be readily interpreted by a wider audience. However, more focus could be devoted to the battery parameters. For example, future studies could show the system results as a function of the calculated battery efficiency. In addition, it would be insightful to formulate an approach to interpret the results in terms of energy and power similarly to what was proposed in [Isikveren et al. 2014]. First of all, the formulation should account for the different installed powers of the battery, the core engine, and the propulsors. Secondly, a measure of how efficiently the fuel energy is converted into electric energy when charging and discharging the battery should be identified.

7.6 Concluding remarks

The aim of this chapter was to establish a methodology to asses the impact of the energy management strategies on the endurance of the present low-speed HALE UAVs. The current methodology can be applied to any choice of airframe, engine cycle, and propulsor. Energy management strategies were also identified by the author as current solutions focus on either small UAVs or short-range commercial aircraft. In these cases either the power to be managed is too small or the time flown is too short. Conversely, in a low-speed HALE UAV both the power to be managed is high and the time flown is long.

Two energy management strategies were identified and assessed: a series-hybrid approach and a climb-and-glide strategy. The engine is relighted only when the batteries are depleted in the series-hybrid solution. Conversely, in the climb-and-glide approach the core engine is used in parallel with the battery to initially climb. A descent phase then follows where the batteries are recharged.

The series-hybrid strategy was found to offer a 9.5% endurance improvement on the tube-and-wing airframe with a 4% battery mass and an energy density of 2 kWh/kg—about 10 times greater than today's technology. A similar benefit was obtained on all the considered take-off masses: 5000, 10000, and 15000 kg. This is because the off-design SFC penalty is mitigated, which counteracts the reduced fuel mass and increased aircraft empty weight. However, this benefit would not occur at reduced energy densities or at higher battery fractions. Also, the series-hybrid was found to provide no benefit on the BWB airframe. This is because the wing planform reshaping, coupled with the reduced fuel mass and increased aircraft empty weight, offset the off-design SFC penalty.

The climb-and-glide energy management strategy was found to offer no benefits on the tube-and-wing airframe regardless of the battery fraction or the power split between the gas turbine and the distributed fans during the descent phase. This is because the core engine still experiences an off-design due to the altitude effect. A take-off mass of 15000 kg and a battery energy density of 2 kWh/kg were considered. As such, the climb-and-glide approach would not offer any benefit also on the BWB airframe.

Energy management also offers benefits that go beyond an endurance improvement. Operational flexibility could be added for military applications by reducing

the overall system heat signature. Environmental benefits could be achieved in terms of aircraft emissions and contrails mitigations. The overall system reliability might also improve as the battery could replace the auxiliary generators that may otherwise be necessary for redundancy.

Chapter 8

Distributed propellers slipstream-wing interaction

8.1 Introduction

Distributed propellers are able to increase the wing maximum lift coefficient up to 5 and above. This would allow the wing to be downsized as effectively it would be able to produce more lift per unit area (i.e. the wing loading increases). A smaller wing is also a lighter wing, which allows more fuel to be stored for a given take-off mass. An increase in range or endurance could then be achieved or, vice versa, the same mission could be completed with a smaller fuel load. Also, a lighter wing reduces the aircraft empty mass, which means that the aircraft would carry less deadweight throughout the mission. This would result in a fuel burn reduction per unit time.

The aim of this chapter is to assess the potential of distributing motor-driven propellers on low-speed HALE UAVs. A review of the previous work on distributed propellers is initially presented, which was structured based on the benefits offered by such a technology: lift-augmentation, lift-induced drag reduction, and propulsors power drop. The integrated methodology that was built by the author is then introduced. This allows the mutual interactions between the airframe, the engine, and the distributed propellers to be captured.

The results show the outcome of the design space exploration study, which described the integrated-system design and performance based on the three main propeller design variables: its radius, RPM, and number of propulsors (which fixes its

unit thrust). The results also show the integration of the distributed propellers with the series-hybrid energy management strategy (introduced in chapter 7) and with the Brayton and wave rotor cycles (see chapter 5). Prior to the concluding remarks, the limitations to the present study are exposed along with a qualitative assessment of the further non-performance benefits of the distributed propellers.

8.1.1 Previous work on distributed propellers

8.1.1.1 Distributed propellers increase lift

The benefits of distributed propellers have been recently investigated on general aviation aircraft. Patterson and Daskilewicz 2014 studied the lift-augmentation effect due to distributed propellers on the Cirrus SR22, a four-seat general aviation aircraft. The study highlighted that a maximum lift coefficient of over 5.2 could be achieved by distributing small motor-driven propellers on the wing leading edge. The distributed propeller version of the Cirrus SR22 was renamed Leading Edge Asynchronous Propellers Technology (LEAPTech) concept.

The increased lift coefficient allowed the wing to be sized for cruise conditions only. Thus, its surface area can be reduced so that the wing aspect ratio can be increased without incurring in a heavier wing mass (fig. 8.1). The study showed that by increasing the lift coefficient from 0.3 to 0.77 the wing area reduces from $13.5m^2$ to $5.1m^2$. This also allowed the wing aspect ratio to be increased from 13.1 to 17.4, leading to an aerodynamic efficiency increase from 11 to 20—nearly doubled (table 8.1). It is for this reason that Stoll et al. 2014 referred to this concept as a "drag reduction" solution.

A key feature of the aforementioned study is that the cruise propellers were

Parameter	**Cirrus SR22**	**LEAPTech**
Gross weight (kg)	1540	1300
Wing area (m^2)	13.5	5.1
Wingspan (m)	11.7	9.4
Wing aspect ratio	13.1	17.4
$C_{L,cruise}$	0.3	0.77
Cruise L/D	11	20

Table 8.1: Comparison between the Cirrus SR22 aircraft and the LEAPTech concept with leading-edge distributed propellers [Stoll et al. 2014]

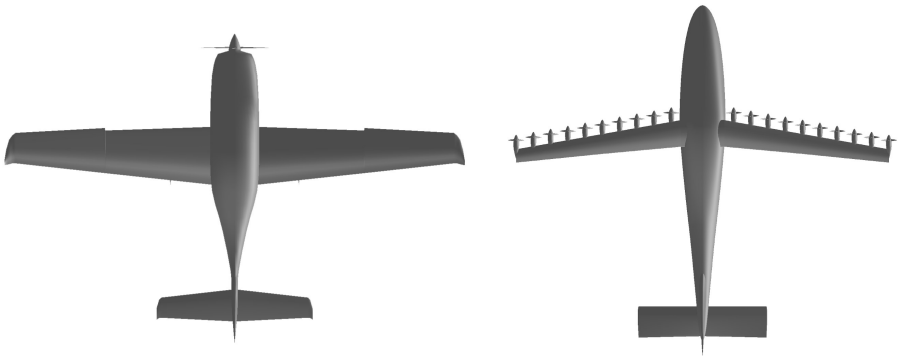

Figure 8.1: Top-view comparison between the Cirrus SR22 aircraft and the LEAPTech concept [Stoll et al. 2014]

different from the take-off propellers. In fact, distributed propulsion allows many propulsors to be installed so that each of them could be optimised for different parts of the mission. As such, most of the distributed propellers were designed for low-speed operations (e.g. take-off). The authors found that a high-solidity and low-diameter design was the most efficient way to augment lift at low speeds [Borer, Moore and Turnbull 2014]. These low-speed propellers could then be folded at high-speed cruise conditions so that the aircraft could be operated just with a couple of propellers optimised for this flight segment (fig. 8.2). These were designed according to the more typical minimum-induced loss approach.

Different methodologies, which are characterised by different levels of fidelity, were investigated to estimate the lift-augmentation effect. Starting with simulations, the authors relied on a higher-order vortex lattice method (distributed vorticity elements) to model the wing and lifting line theory for the propellers [Patterson and German 2014]. Such methods are computationally inexpensive as their calculation time ranges between seconds and minutes [Patterson and Daskilewicz 2014], making them suitable at the conceptual design stage. However, these methods are still inappropriate for design space exploration studies where many different system architectures need to be assessed.

The authors also proposed a set of simplified correlations to model the lift curve slope and the zero-lift angle of attack when the propellers are installed on the wing leading edge [Patterson and German 2015]. These are based on two-dimensional aerodynamic models that aim to provide a quick estimate of the lift-augmentation effect. The drawback of these correlations is their accuracy as they were mainly developed for a designer to build intuition on the lift-augmentation effect. Also, these correlations are application specific as they would be unsuitable to study

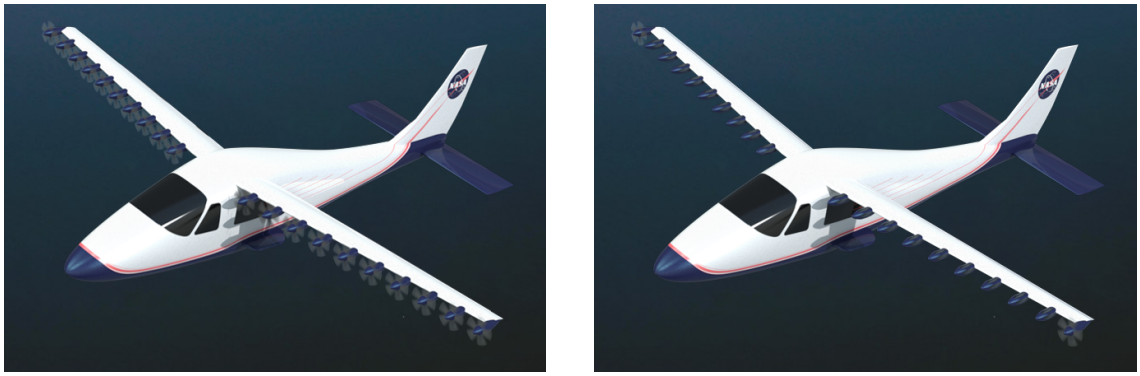

Figure 8.2: NASA Leading Edge Asynchronous Propellers Technology (LEAPTech) concept [Patterson and German 2015]

distributed propellers that are not meant to increase lift.

Computational fluid dynamics (CFD) simulations were also carried out and validated with experimental results [Stoll 2015]. The accuracy of CFD results could be attractive, particularly in the case of complex flow phenomena such as the wing-propeller interaction. However, the computational expense makes CFD suitable only for detailed studies where both the wing geometry and the propellers design are defined.

8.1.1.2 Distributed propellers reduce lift-induced drag

Jameson found that distributed propellers can also reduce lift-induced drag in addition to augment lift [Jameson 1969]. The author modelled the wing according to the lifting line theory, and the propellers were modelled as an axial flow with uniform velocity (fig. 8.3). Thus, the inviscid and incompressible flow did not include the swirl effect due to the slipstream rotation.

The leading-edge mounted propellers were modelled as a uniform wide jet with no gaps between the propulsors. Eliminating the gaps between the individual jets would maintain a continuous circulation along the wing span. This results in a substantial increase in the efficiency of the propellers installation effect than if the propellers were considered as separate jets. According to the author, eliminating these gaps can be considered a valid assumption as long as the mutual distance between the propellers is, at the most, a tenth of their radius.

The reason why lift-induced drag reduces may not be immediately apparent. A reduced frontal area of mass flow is required as the wing generates lift with the

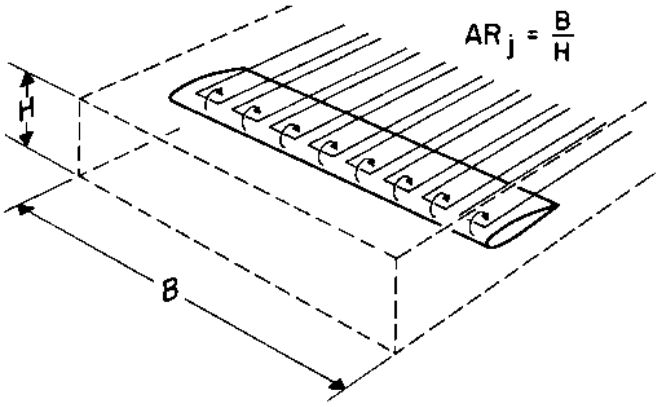

Figure 8.3: Wing spanning a rectangular jet of width B, height H, and aspect ratio $AR_j = B/H$. The lifting-line ideal horseshoe vortex distribution is also shown [Jameson 1969]

propellers slipstream. This is a consequence of mass flow conservation: the area has to reduce compared to the freestream case if the wing encounters a mass of air with a greater speed due to the slipstream. The frontal area reduction implies that the vertical distance between the air particles and the wing surface reduces. Thus, the particles have a lower potential energy, which means that they can be turned more efficiently by the wing airfoil. This is the reason why the author concludes that it is easier to deflect a flow that is closer to the wing [Jameson 1969].

An improved turning effectiveness implies that the inefficiencies in generating lift, or the lift-induced drag, are reduced. At a low Mach number, this argument is valid as long as the slipstream velocity is reasonably close to the flight speed. If the velocity increment imparted by the propeller is too great the turbulent flow would offset the aforementioned benefits.

This effect can also be visualised in terms of wing "effective" aspect ratio. The wing imparts a greater vertical speed to the air—the downwash—when the propeller is leading-edge mounted. The same would happen if the same wing area needed to generate the same lift with a reduced aspect ratio.

Lift generation is proportional to the vertical velocity that the wing imparts to the air. This is the integral of the downwash of a wing section throughout the wing span (eq. 8.1). The overall vertical speed V_V remains unchanged if the wing needs to generate the same amount of lift. However, if the wingspan b reduces the local vertical speed v_V needs to increase for the integral to lead to the same V_V. This is why a reduced wing aspect ratio, which leads to a reduced wing span for a given wing area, results in a greater local downwash v_V. Thus, distributed propellers

would reduce the effective aspect ratio of the wing due the increased vertical velocity that the wing imparts to the air. Lift-induced drag would be penalised as it depends on the wing aspect ratio.

The lift-induced drag changes as a trade-off between the reduction in effective aspect ratio and the increase in wing turning effectiveness. Lift-induced drag should reduce at small velocity increments imparted by the propeller as the increase in wing turning effectiveness counteracts the reduction in wing effective aspect ratio. Conversely, the reduction in effective aspect ratio would prevail at high velocity increments and consequently penalise lift-induced drag.

$$V_V = \int_{-b/2}^{b/2} v_V \, dy \tag{8.1}$$

The methodology of Jameson to assess the wing-propeller interaction, which is extensively described in [Jameson 1970], showed a good agreement when validated with wind-tunnel testing experimental results (fig. 8.4). The results indicate that the author's theoretical approach fits both the lift-coefficient curve as function of the angle of attack and the aircraft drag polar. Figure 8.4 refers to an unflapped wing, which is usually what is used by UAVs given their simple design. However, for a flapped wing the author's theoretical method can underpredict the lift coefficient for a given angle of attack or drag coefficient by up to 7% with a flap deflection of 40°.

The author also built some simplified analytical correlations that approximate the theoretical results with a maximum error of 3%. These are particularly useful for design space exploration studies given their trade-off between accuracy and simplicity (see section 8.2.3). The main limitation of these correlations is that they are valid for a wing chord that is less than twice the jet height. However, this is a constraint of the simplified correlations themselves and not of the lifting line theory from which they were extrapolated.

8.1.1.3 Propellers power reduces as their number increases

Distributed propellers have the potential to reduce the overall power that the aircraft demands from the propulsion system to sustain flight—for a given thrust

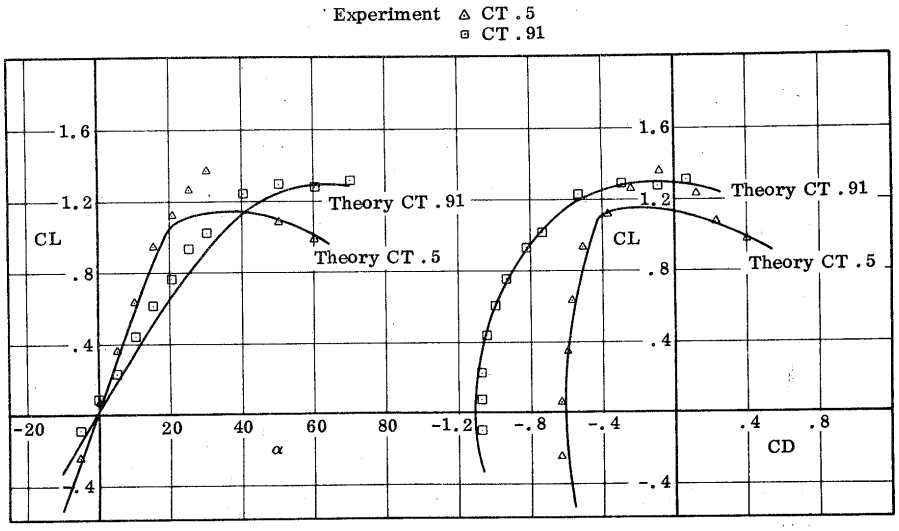

Figure 8.4: Validation of the theoretical results of Jameson with experimental results for an unflapped wing [Jameson 1969]

requirement—in addition to aerodynamic benefits. This would lead to a reduced fuel flow and consequently to a lower mission fuel burn if the electric power is generated on-board by a thermal engine. Alternatively, a greater range or endurance could be achieved by the aircraft for the same fuel mass.

The fact that the overall power that the propellers require to deliver a certain thrust reduces as their number increases was recorded in [Konishi and Fujimoto 2014]. Both their experiments and simulations confirmed that the minimum power requirement is attained when the power is equally distributed between a main nose-mounted propellers and two wing-mounted sub-propellers. Delivering all the required thrust with either the main propeller or just the two sub-propellers would always result in a higher overall power requirement.

Although not reported in the public domain, this could be the reason why the Aerovironment Global Observer included multiple propellers (four to eight propellers depending on the prototype version) in its design.

8.2 Methodology

The aim of the present study was to build a methodology to integrate the airframe, the core engine, and the distributed propellers (fig. 8.5) Such a multidisciplinary and multifidelity methodology is essential to capture the synergies between the in-

dividual components. For example, only with a fully integrated multidisciplinary methodology it is possible to resize the aircraft wing based on the how propellers properties affect its lift and drag. Similarly, only by integrating the propellers with the core engine it is possible to calculate its fuel flow reduction when the number of propellers is increased due the propulsors power drop.

The present methodology section initially focuses on the individual disciplines, with emphasis on the propellers design, weight and performance (sections 8.2.1 and 8.2.2) and how their slipstream affects the wing both in terms of lift-augmentation (sect. 8.2.3.1) and lift-induced drag reduction (sect. 8.2.3.2). After that, the integration aspects between the individual disciplines are presented (8.2.4). Emphasis is placed on the airframe-propellers and the engine-propellers integration as the airframe-engine integration was discussed in chapter 4. The architecture of the distributed propellers system along with the key assumptions behind the core engine and the electric transmission system are explained in the appendixes B and C.

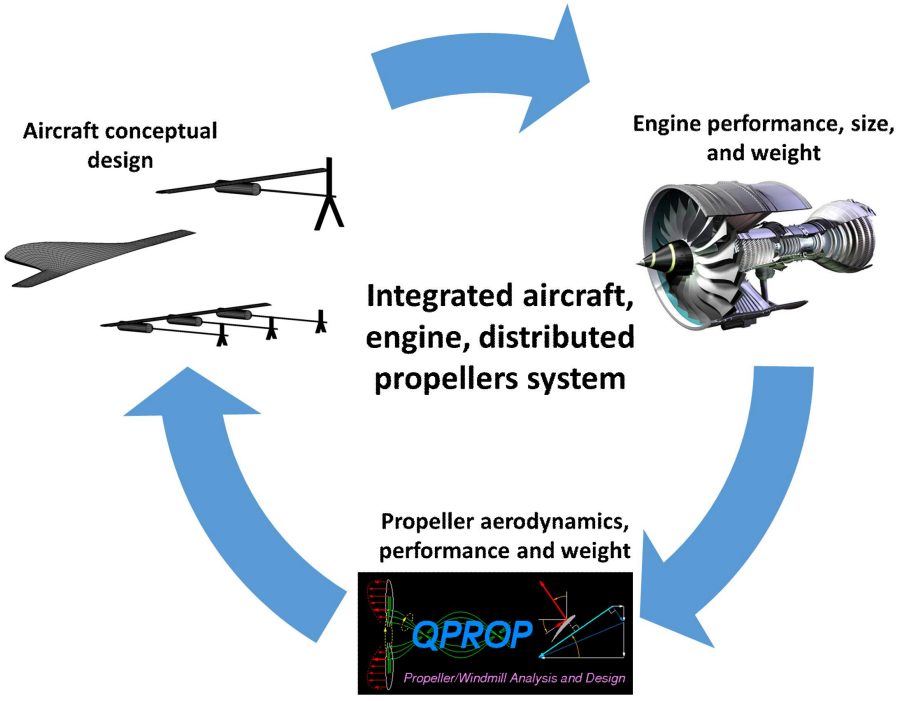

Figure 8.5: Visual representation of the methodology that integrates the present aircraft platform, Turbomatch engine simulations, and QMIL/QPROP propeller calculations

8.2.1 Propeller design & performance

The propeller design and performance were assessed with the QMIL/QPROP software. For a given airfoil, QMIL allows the blades to be designed for minimum induced losses by taking as inputs the following design parameters:

- RPM
- Hub and tip radius
- Thrust (or power) requirement
- Number of blades
- Altitude and flight speed
- Airfoil properties

The airfoil properties that need to be included in the analysis are its lift coefficient and drag polar curves. The output of QMIL, which becomes the input of QPROP, is the blade geometry represented by the chord and pitch distribution as a function of the radius.

The Clark Y airfoil was selected for the present project, which offers an improved efficiency at low blade pitch and low flight speed [Freeman 1931]. These would be the typical flight conditions and blade geometry of a HALE UAV. It was important to choose an airfoil that is well suited for the low Reynolds number conditions. This criterion was considered sufficient for the present project as it aims to carry out a design space exploration study. In reality, for a final aircraft design the propeller-airfoil choice would be dependent on the designer's personal experience.

The blade number was set to two, which is a sensible choice at the early stage of aircraft design [Falk 1943]. A low number of blades avoids an increase in weight and complexity in addition to be a particularly suitable choice for a low speed aircraft. Nonetheless, within the present project the number of propellers that was considered would be well above the norm of two to four propulosors. If more propellers are considered, then for a given thrust requirement the loading on the propeller disc would reduce. A smaller disc loading may lead to an unfeasible propeller design if too many blades are considered. This is simply the author's hypothesis, and further studies are required to assess the effect of blade number.

Based on the aforementioned assumptions, it can be concluded that the main design handles for the propeller blade are its RPM, radius, and thrust requirement. In fact, the airfoil and blade number were fixed in addition to the flight conditions. The propeller power requirement would be usually considered if a piston engine is driving the propeller. However, the thrust requirement was found to be a more convenient choice as the aircraft thrust is known and the number of distributed propellers was considered as a handle of the study.

QPROP was used to evaluate the performance of the propeller geometries generated with QMIL. The software relies on a classical blade-element/vortex formulation, which was originally developed by Betz, Goldstein, and Theodorsen [Drela 2006]. Blade element theory represents the foundation of almost every modern method for preliminary propeller analysis. The fundamental assumption of blade element theory is that the propeller blade can be discretised into 2D strips—or blade elements—whose performance can be considered independent. The integration of the individual airfoil properties along the radius, where each of them can have a different angle of attack, leads to the overall blade performance.

Blade element theory can assess the propeller viscous losses as it incorporates the airfoil properties by means of its lift-slope and drag-polar curves. However, it is unable to calculate the momentum losses—due to the blade imparting a velocity differential to the flow—and the tip losses. The QPROP formulation includes analytical correlations to account for the tip losses, where a local wake advance ratio is used instead of the propeller advance ratio [Smedresman, Yeo and Shyy 2011]. Also, momentum losses are accounted with an empirical correlation that relates the circumferentially-averaged tangential velocity of the blade to that of the flow [Drela 2006].

Propeller performance are usually represented by non-dimensional coefficients. The power and the thrust coefficients are simply the non-dimensional forms of the propeller power and thrust according to equations 8.2 and 8.3. The advance ratio represents the horizontal distance covered by the propeller in one rotation (eq. 8.4). The propeller efficiency is the ratio of the aircraft power (i.e. thrust times flight speed) upon the power that the propeller requires to generate that thrust (eq. 8.5). The disc loading represents the power per unit of diameter squared (eq. 8.6), which is the analogous of the fan pressure ratio for a turbofan engine.

$$C_P = \frac{P}{\rho\, RPM^3\, D^5} \tag{8.2}$$

$$C_T = \frac{T}{\rho\ RPM^2\ D^4} \tag{8.3}$$

$$J = \frac{V_0}{RPM\ D} \tag{8.4}$$

$$\eta_{prop} = \frac{T\ V_0}{P} = \frac{C_T\ J}{C_P} \tag{8.5}$$

$$\frac{P}{D^2} = \frac{C_P}{J^3}\ \rho\ V_0^3 \tag{8.6}$$

8.2.2 Propeller weight estimation

The propeller weight was estimated by means of the analytical correlation suggested in [Morris 1979]. It is a simple correlation that relates the propeller blades weight to their diameter, tip speed and disc loading (eq. 8.7).

$$M_{prop} = const\ D^{2.48808}\ V_{tip}^{0.30}\ (P/D^2)^{0.2925} \tag{8.7}$$

The equation was originally built to estimate the mass of high-speed open-rotor blades, which for a given propeller disc area they are expected to be lighter than a simple propeller blade for a HALE UAV given their advanced technology. However, the correlation was built in 1979, and so a lighter blade should be comparable to modern standards to due the advancements in materials. This was verified by comparing the analytically predicted weight and that of a first-principle approach. It was possible to estimate the blade surface area by assuming that its perimeter is roughly 2.2 times its chord, and by taking the propeller hub and tip diameters from a design of the present study. A material density was assumed by considering a full composite blade, which led to an estimate of the blade weight.

8.2.3 Propeller slipstream-wing interaction

The model of Jameson was selected to assess the slipstream-wing interaction due to its trade-off between accuracy and simplicity [Jameson 1969, 1970]. A qualitative explanation of the theoretical background was explained in section 8.1.1.2. The following sections enter into the details of the methodology for both the lift-augmentation and lift-induced drag-reduction effects.

8.2.3.1 Lift-augmentation & wing sizing

The lift-augmentation effect on the wing sizing is graphically described in figure 8.6. The amount of wing area covered by the propellers required to sustain flight depends on the lift-coefficient due to the slipstream effect $C_{L,prop}$. This depends on three main parameters: the clean-wing angle of incidence, the clean-wing area, and the propeller exit speed V_{prop}. The clean-wing angle of incidence was calculated with Javafoil, which is a panel-method software for airfoil and wing calculations.

As it was described in chapter 4, the wing is sized to fly at a minimum speed of Mach 0.25 at 50,000 ft with a maximum C_L of 1.3. Thus, Javafoil was used to find which angle of attack, for a given wing aspect ratio, would provide a C_L of 1.3. The propeller exit speed V_{prop}—which is mainly a function of its RPM, radius, and thrust—was calculated with the QMIL/QPROP companion (section 8.2.1).

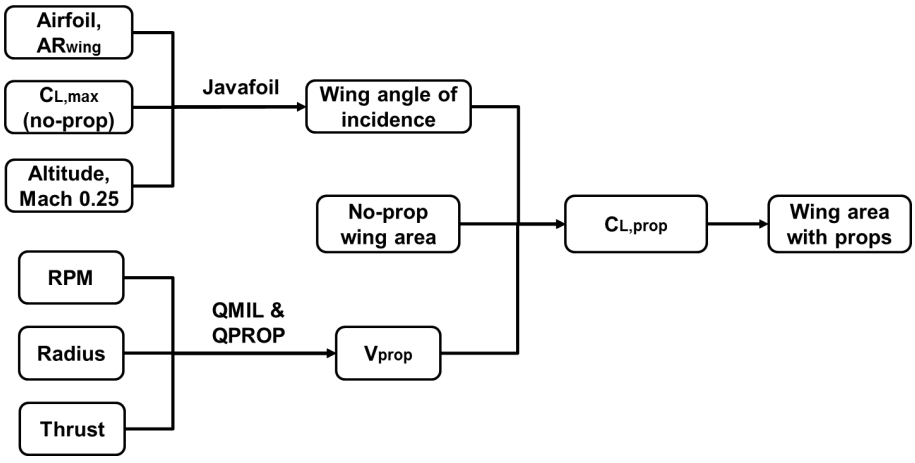

Figure 8.6: Wing sizing flow chart to include the slipstream effect

In reality, not all the wing span can be covered by the propellers because of the fuselage presence. Also, the number of propellers is considered a main handle of the design space exploration study. This means that for a low number of propellers

an additional part of the wing would be unaffected by the slipstream. It was then assumed that the wing could be split in two portions, one influenced by the propellers and one that generates lift with the freestream flow. The two effects were linearly superimposed (eq. 8.8)

$$VSC_L = (S - S_{wj})V_0^2 C_{L,no\ props} + S_{wj}V_{jet}^2 C_{L,props} \tag{8.8}$$

According to Jameson, the $C_{L,props}$ depends on two terms (eq. 8.9). The first term directly accounts for the slipstream effect. The second term includes the difference between the wing freestream characteristics ($a_{no\ props}\alpha_{no\ props}$) and the properties of the part of the wing covered by the propellers as if it was an isolated platform in a freestream ($a_{iso}\alpha_{iso}$). In equation 8.9 α refers to the wing angle of attack and a refers to the slope of the lift-slope curve as a function of α. For the present analysis it was assumed that for a rectangular wing with constant airfoil and twist α_{iso} equals $\alpha_{no\ props}$.

The ratios a_{props}/a_{iso} and $a_{no\ props}/a_{iso}$ can be calculated as a function of the aspect ratio of the wing part immersed in the jet $AR_{w,jet}$, the velocity ratio $\mu = V_0/V_{jet}$, and the aspect ratio of the jet AR_{jet} (eqs. 8.10, 8.11, and 8.12). Thus, the lift slope is affected by the propeller properties (shape, speed) and by the non-dimensional extent of the wing area wetted by the slipstream (its aspect ratio). Conversely, a_{iso} is solely a function of the aspect ratio of the wing immersed in the jet (eq. 8.12). It should not be expected to be a function of the velocity ratio or of the jet shape as a_{iso} refers to the part of wing covered by the propellers as if it was immersed in a freestream flow.

$$C_{L,props} = a_{props}\alpha_{props} + \frac{V_0^2}{V_{jet}^2}(a_{no\ props}\alpha_{no\ props} - a_{iso}\alpha_{iso}) \tag{8.9}$$

$$\frac{a_{props}}{a_{iso}} = \frac{1}{1 + \left(\frac{a_{iso}}{a_{static}} - 1\right)\left(\frac{1-\mu^2}{1+AR_{jet}\mu^2}\right)} \tag{8.10}$$

$$\frac{a_{static}}{a_{iso}} = \frac{AR_{w,jet} + 2}{AR_{w,jet} + 2AR_{jet} + \frac{2.5}{1+AR_{jet}}} \tag{8.11}$$

$$a_{iso} = 2\pi \frac{AR_{w,jet}}{AR_{w,jet} + 3\frac{AR_{w,jet}^2+2}{AR_{w,jet}^2+1.5}} \tag{8.12}$$

8.2.3.2 Lift-induced drag reduction

Similarly to the lift-slope coefficient, the induced drag factor of the part of the wing wetted by the slipstream K_{props} is expressed as a ratio between its value and that of the same part of the wing wetted by the propellers as it if was immersed in freestream flow K_{iso} (eq. 8.13). This ratio depends on the wing geometry and the slipstream shape and velocity ratio (eqs. 8.14 and 8.15).

K_{iso} is solely a function of $AR_{w,jet}$ and, as expected, it is independent of the jet shape (eq. 8.15). A closer look to its equation reveals a marked similarity with the expression of the lift-induced drag factor of a wing wetted by freestream flow [Raymer 1992], although a span efficiency factor is not explicitly included. A detailed analysis of these correlations unveils that a thinner jet (small AR_{jet}) and/or an increased fraction of the wing covered by the propellers (big $AR_{w,jet}$) reduce the lift-induced drag factor K_{props}.

$$\frac{K_{props}}{K_{iso}} = \frac{\frac{K_{static}}{K_{iso}} + \left(1 + AR_{jet} + \frac{K_{static}}{K_{iso}}\right)\mu^2}{1 + AR_{jet}^2} \tag{8.13}$$

$$\frac{K_{static}}{K_{iso}} = 0.76\left(AR_{jet} + e^{-AR_{jet}}\right) + 0.53 \tag{8.14}$$

$$K_{iso} = \frac{1 + 0.006AR_{w,jet}}{\pi AR_{w,jet}} \tag{8.15}$$

8.2.4 Aircraft-engine-propellers integration

A methodology to integrate the engine and the propellers properties was required to carry out the design space exploration exercise. In principle, two solutions could be adopted. Either a fully automated link between the various software is built, or their output need to be represented in a way that captures all the interrelations between the different disciplines. The second approach was chosen due to its simplicity compared to integrate software written in different programming languages

representing completely different disciplines. Also, such approach forces the user to make all the variables of the integrated system explicit. This avoids the risk of modelling solutions that may be unfeasible or of not uncovering potential synergies.

8.2.4.1 Design point

The propellers design-point properties are mainly a function of its radius, thrust, and RPM (section 8.2.1). As such, its power, efficiency, and velocity differential ΔV were translated into maps that are function of these variables (figs. 8.7, 8.8, and 8.9). The power map was necessary to size the core engine, whose fuel flow and mass can be expressed as a function of its design-point power output. The ΔV map was necessary to determine the size and aerodynamic properties of the wing. On the other hand, the efficiency map offers an insight into how the propeller design is affecting its power requirement.

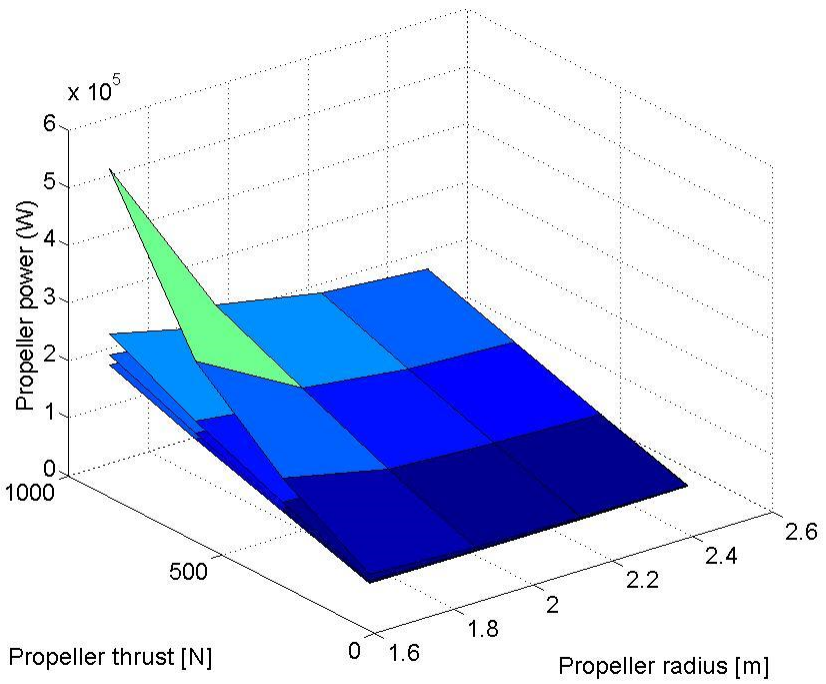

Figure 8.7: Single propeller design point power as function of thrust, radius, and RPM. The RPM varies from 650 (top surface) to 1000 (bottom surface)

The propeller power decreases with an increase in its radius and RPM, and it increases with an increase in its thrust (fig. 8.7). For a given thrust requirement, when the propeller radius increases its losses are mitigated and so its efficiency

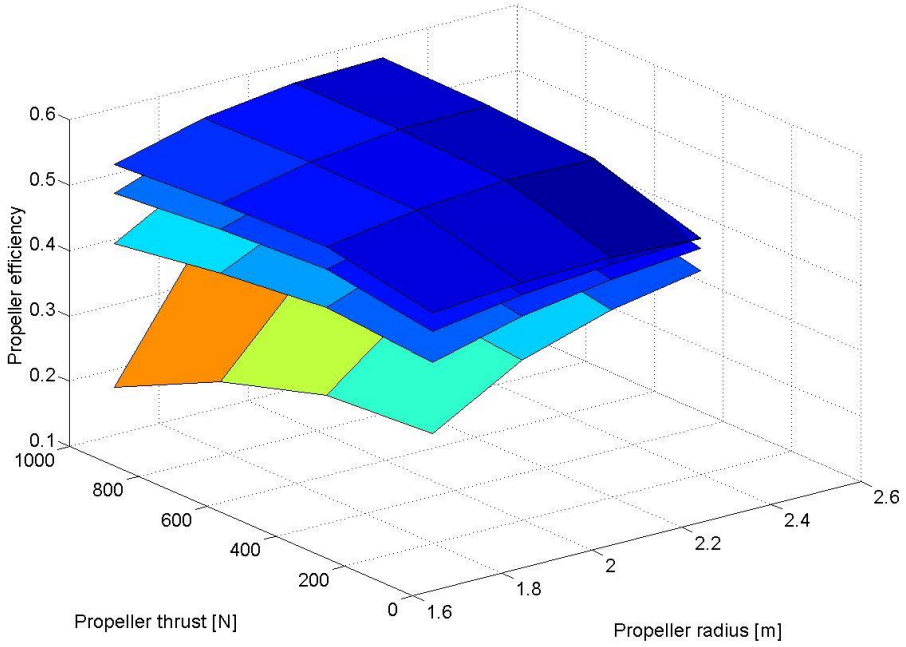

Figure 8.8: Propeller design point efficiency as function of thrust, radius, and RPM. The RPM varies from 650 (bottom surface) to 1000 (top surface)

improves (fig. 8.8). In fact, the tip losses decrease similarly to what would occur in a wing whose aspect ratio is increased. Momentum losses also reduce as the same thrust is distributed on a greater propeller disc area (i.e. its disc loading decreases). This would lead to a propeller design with a lower increase in axial and tangential velocities imparted to the flow. Viscous losses should increase due to the reduction in blade chord, although their effect is offset by reshaping the propeller chord and pitch distribution.

Changing the RPM has a direct impact on the propeller torque. For a given power, when the RPM increases the torque should decrease as power is simply expressed by their product. If the propeller is re-designed, however, the torque decreases faster than the RPM increases. This is due to the fact that at a higher RPM the propeller can be designed to mitigate the tip losses more efficiently than in the low-RPM case (fig. 8.8). Ultimately, the tip losses are due to the flow that goes from the pressure to the suction side (the opposite of the direction of rotation). However, at high RPM the flow is more forced to follow the blade rotation rather than going the opposite way. For a given radius, this RPM change effect is more pronounced at higher propeller unit thrusts. This is due to the increase in disc loading, which makes the propeller less efficient (fig. 8.8).

The propeller ΔV increases with an increase in thrust or a decrease in radius, and

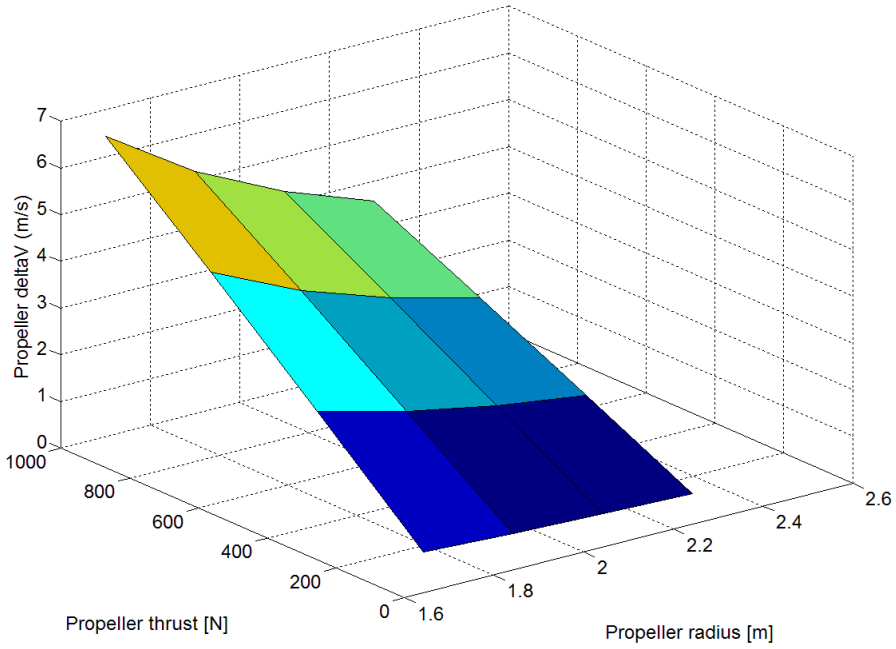

Figure 8.9: Single propeller design point ΔV as function of thrust and radius

it is unaffected by its RPM (fig. 8.9). When the thrust increases the ΔV increases as more thrust needs to be delivered by the same propeller disc area. This can only be achieved by an increase in disc loading, which results in a greater flow exit speed. Similarly, the same would happen in a fan if its pressure ratio is increased. Vice versa, for a given thrust the ΔV decreases with an increase in radius as the disc loading decreases.

The RPM has a negligible effect on the propeller ΔV as its blades are redesigned every time. In fact, when the RPM increases the blade pitch angle decreases. If the pitch angle was the same, the increase in RPM would lead to an increase in ΔV which would lead to a greater thrust for a given disc area.

8.2.4.2 Off-design

The propeller off-design properties are usually represented by maps of thrust coefficient, power coefficient, and efficiency as a function of the advance ratio. However, when multiple propeller designs are considered it would be inconvenient to integrate all the maps for the purpose of off-design calculations. Thus, it was decided to compare the propeller maps for designs at the opposite ends of the spectrum. If a small difference were to be found, then a common representation could be used for

all the propeller designs.

Maps of variation of thrust/power coefficient, efficiency, and ΔV as a function of the variation of advance ratio were built. The variation of each parameter was expressed as the difference between that parameter and its value at design point, the whole difference being divided by the value at design point itself. Thus, it represents the variation of the considered parameter from its design-point value.

Four different designs were considered: a high-RPM case with a small radius and a low-RPM case with a big radius, both for a high and low thrust. The radius varied from 1.7 to 2.3m, the RPM from 650 to 1000, and the thrust from 150 to 1000 N. These ranges were constrained by the feasibility of the propeller design as for values outside of these boundaries QPROP would not return a solution.

It was found that the variation of the propeller performance coefficients from their respective design point value follows the same trend for all the considered cases (fig. 8.10, 8.11, and 8.12). This means that although the propeller maps change when the propeller design changes, their relative variation from the respective design point is similar. As such, the traditional propeller maps were replaced with the proposed variation-percentage maps. This was assumed to be applicable to any propeller design in the selected range given the fact that the trends are consistent when comparing the boundaries of the intervals.

A similar approach was also used to represent the propeller velocity differential ΔV (fig. 8.13). In fact, ΔV reduces as the flight speed reduces, which affects the aerodynamic properties of the wing. It was essential to capture this effect since the loiter performance were discretised in one-hour steps (see chapter 4). Similarly, by computing the aircraft thrust at each time-step it was possible to assess the propeller power variation throughout the loiter. The link with the core engine was established by building curves of off-design fuel flow as a function of the power output.

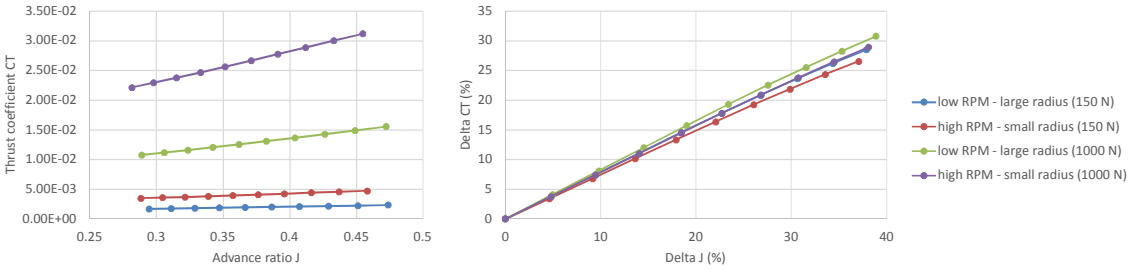

Figure 8.10: Comparison of propeller thrust coefficient and thrust coefficient variation percentage from design point for four selected cases

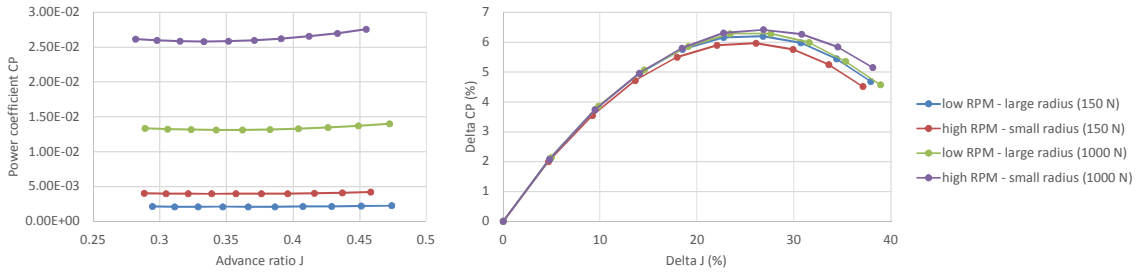

Figure 8.11: Comparison of propeller power coefficient and thrust coefficient variation percentage from design point for four selected cases

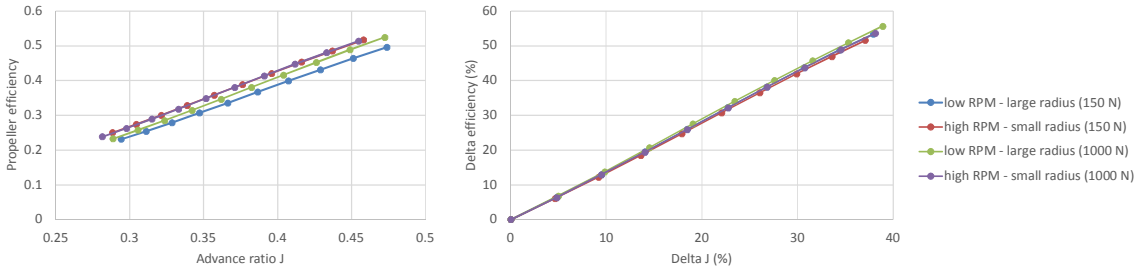

Figure 8.12: Comparison of propeller efficiency and efficiency variation percentage from design point for four selected cases

8.3 Results

A design space exploration study was carried out to assess the influence of the main design parameters of the distributed propellers (radius, thrust, RPM) on the design and performance of the integrated system. The propeller-thrust handle was replaced by the number of propellers, defined as the aircraft thrust divided by the single-propeller thrust. Directly using the thrust of the single propeller may lead to a non-integer number of propellers.

The distributed propellers were integrated only on the T&W airframe. In fact, the BWB airframe proved to be unfeasible to design for a maximum wing lift coefficient greater than one. This was due to the hydrogen volumetric requirement, which fixes the centrebody surface area (see chapter 4). Also, the same baseline engine cycle that was used to compare the airframes with the distributed fans was adopted (OPR = 28, TET = 1300 K). As such, the different propulsors will be directly comparable.

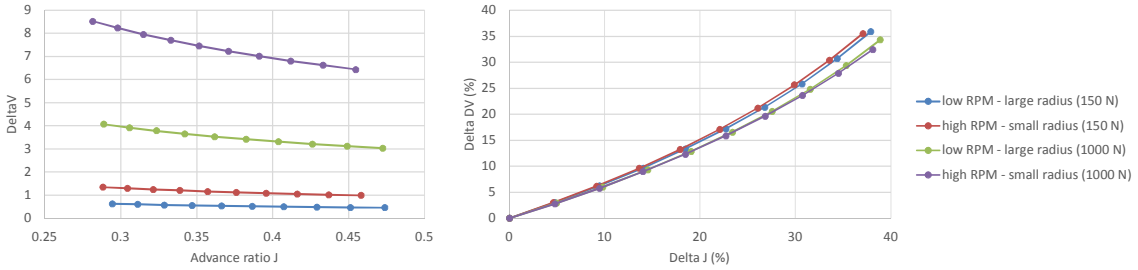

Figure 8.13: Comparison of propeller ΔV and ΔV variation percentage from design point for four selected cases

8.3.1 Slipstream-wing interaction methodology validation

The lift-augmentation and drag-reduction analytical correlations were modelled and found to be in close agreement with the results from [Jameson 1970]. The reference curves are the slope of the (C_L, α) curve and the inverse of the Oswald span efficient factor (fig. 8.14). It has to be noticed that Jameson referred to C_D as the wing lift-induced drag coefficient and not as the overall wing drag coefficient. Thus, multiplying π and the wing AR by $C_D/(C_L)^2$ leads to $1/e$, where e is the Osvald span efficiency factor that represents how close the lift distribution is to the ideal elliptical one [Raymer 1992].

8.3.2 Propeller radius & RPM effect

An increase in propeller radius and RPM was found to have a beneficial impact on endurance (fig. 8.15a). Notably, endurance nearly doubles moving from the smallest radius (1.7m) and the lowest RPM (650) to the biggest radius (2.1m) and the highest RPM (1000). The results assume a fixed number of propeller and wing aspect ratio, which are equal to 12 and 30 respectively.

The endurance improvement is mainly driven by the reduction in the distributed-propellers power when either the radius or the RPM increase. In fact, when the radius increases the propeller disc loading reduces, which improves the propeller efficiency. The increase in RPM has a similar effect on efficiency as it reduces the propeller torque. A greater RPM has a minor effect on power as the propeller radius increases (fig. 8.15c). This is because at a high RPM the flow is already forced to follow the blade rotation, and so the tip-losses mitigation would not be as pronounced as at low rotational speeds.

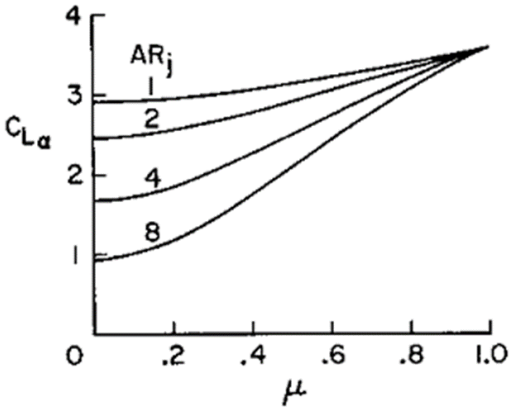

(a) (C_L, α) curve slope [Jameson 1970]

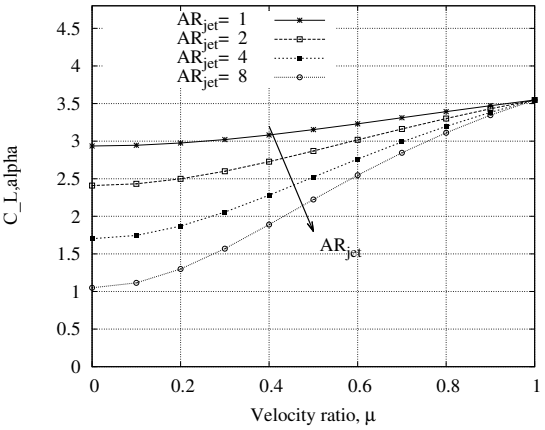

(b) (C_L, α) curve slope

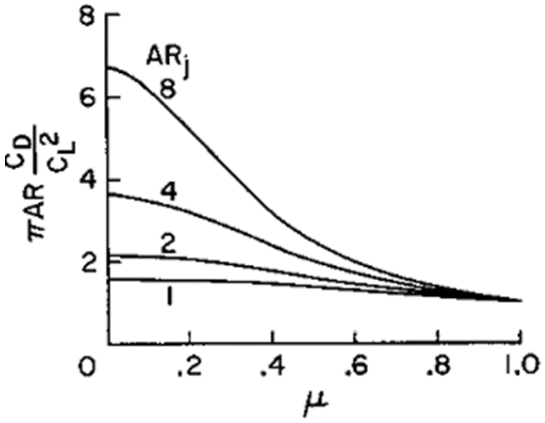

(c) $\pi\ AR\ C_{D,i}/(C_L)^2$ curves [Jameson 1970]

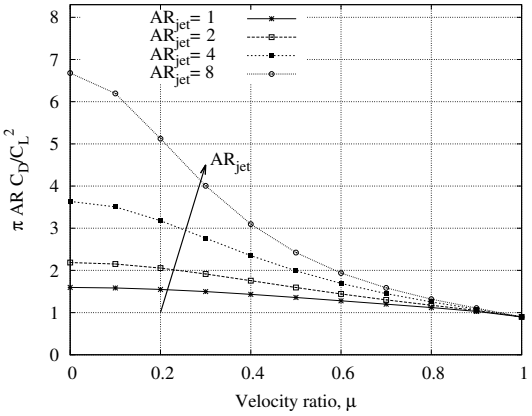

(d) $\pi\ AR\ C_{D,i}/(C_L)^2$ curves

Figure 8.14: Comparison of the present simulation results with the results from [Jameson 1970] for the operational curves of lift slope and $\pi\ AR\ C_{D,i}/(C_L)^2$ for a rectangular wing of aspect ratio = 4

The distributed-propellers power-drop translates into a fuel flow reduction as the engine can be downsized (fig. 8.15d). The fuel flow trends are consistent with the power variation trends, although the relative variation is not the same. For instance, for a radius of 1.7m power reduces from 1.8 MW to 900 kW (-50%) when the RPM increases from 650 to 1000. However, fuel flow reduces from 0.033 kg/s to 0.020 kg/s (-39%). This variation is intrinsic of the engine thermodynamics as the turbomachinery isentropic efficiency was kept constant.

The airframe is affected by a change in propeller radius, whereas the RPM effect is negligible. For a given radius, a change in RPM would not affect neither the fraction of the wing covered by the propellers nor their ΔV. Thus, both the aircraft aerodynamics and structures would not change.

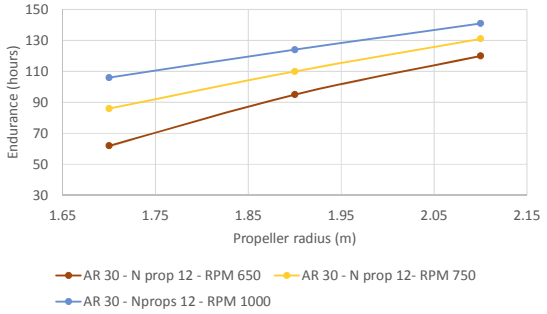

(a) Endurance as function of propeller radius and RPM

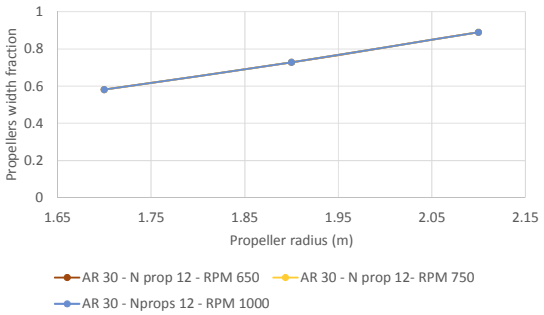

(b) Propellers width fraction as function of radius and RPM

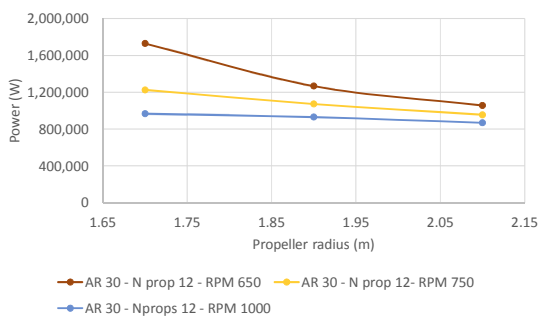

(c) Distributed propellers power as function of propeller radius and RPM

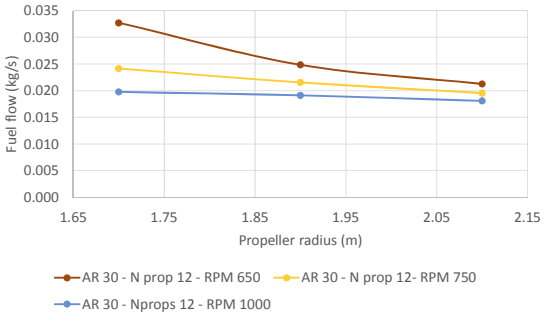

(d) Engine fuel flow as function of propeller radius and RPM

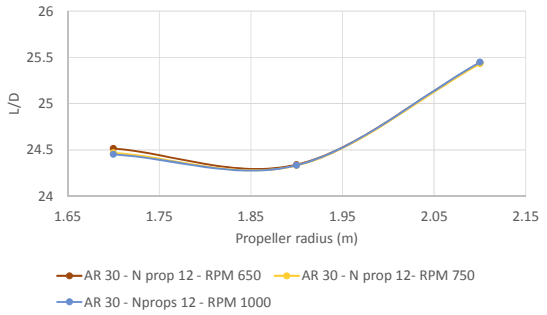

(e) L/D as function of propeller radius and RPM

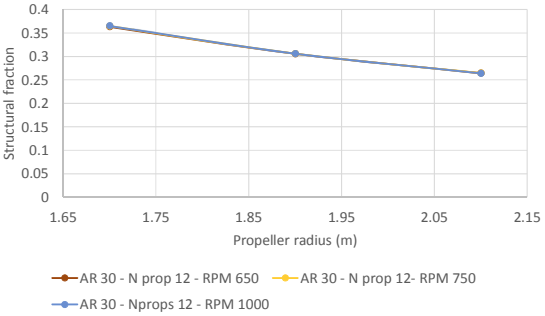

(f) Aircraft structural fraction as function of propeller radius and RPM

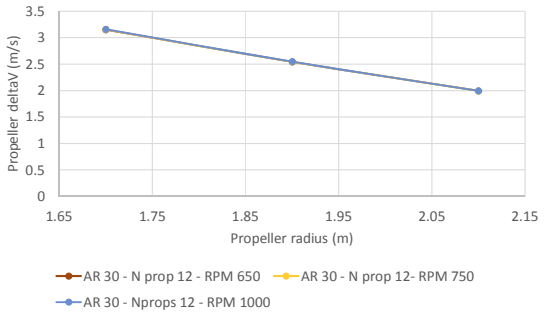

(g) Propeller ΔV as function of propeller radius and RPM

Figure 8.15: The effect of propeller RPM and radius selection on the design and performance of the integrated system (wing AR = 30 & 12 propellers)

Conversely, increasing the propeller radius has a more pronounced effect. The fraction of the wing covered by the propellers increases when a bigger radius is considered for a given number of propellers (fig. 8.15b). As reported in [Jameson 1969], when the slipstream covers a greater fraction of the wing the lift-augmentation effect becomes more noticeable. This leads to a greater lift coefficient and a smaller wing area, which is why the aircraft structural fraction reduces as the propeller radius increases (fig. 8.15f). The reduced structural fraction offers a double benefit: more fuel can be stored and less deadweight is carried throughout the mission.

The aerodynamic efficiency reaches a minimum and then increases when the radius increases (fig. 8.15e). This is because two opposite effects occur. First of all, when the wing area reduces the overall wetted area reduces and so the overall drag should reduce. The same effect was recently observed in distributed propellers studies for general aviation aircraft [Stoll et al. 2014]. Also, with the present slipstream-wing interaction model the overall drag reduces due to a reduction in lift-induced drag (see section 8.2.3.2). However, a second effect that occurs is that the length of the wing chord becomes smaller as the wing area reduces (for a given wing aspect ratio). This leads to a greater parasite drag due to the Reynolds number effect.

Initially, when the propeller radius increases the wing chord reduction slightly offsets the drag-reduction benefits of the distributed propellers as they cover a greater fraction of the wing. However, as 70% to 80% of the wing is affected by the distributed propellers (fig. 8.15b) the drag reduction benefits prevail.

It can be concluded that the endurance of the integrated system increases with an increase in propeller radius and RPM. This is mainly driven by the fact that the overall power that the propulsors require to deliver thrust reduces, which is the reason why both the power and the endurance charts show convergent trends. The reduced power requirement leads to a smaller engine, which in turns consumes less fuel. A contribution also comes from the lighter aircraft structures (which allows more fuel to be stored and less deadweight to be carried throughout the mission) and the improved aerodynamic efficiency.

8.3.3 Number of propellers effect

Increasing the number of propellers from 8 to 12 and 16 improved the endurance of the integrated system for a given RPM (750) and wing aspect ratio (30). Similarly to the RPM increase, an increase in number of propellers leads to a smaller power

required by the propulsors to deliver thrust (see section 8.3.2). Consequently, fuel savings can be achieved by downsizing the engine. However, the loiter lift-to-drag ratio is also affected by the propellers number as it varies from 19 to 30 (fig. 8.16e). It is because of the combination of these two effects that when the number of propellers changes the difference between the maximum and minimum values of endurance (fig. 8.16a) is greater than the same difference when the RPM changes (fig. 8.15a).

The improvement in aerodynamic efficiency is mainly driven by a reduction in lift-induced drag (fig. 8.16f), whereas the wing area and consequently the aircraft structural fraction are negligibly affected by the number of propellers (fig. 8.16h). The reduction in lift-induced drag depends on the propeller ΔV becoming smaller and smaller as the number of propellers increases (fig. 8.16g). The ΔV can only reduce if thrust is distributed to more propellers as the propulsor disc loading decreases.

The reason why the structural fraction is minimally affected by the number of propellers is because the greater fraction of the wing covered by the propellers is offset by the decrease in ΔV. These two opposite effects lead to a similar wing lift coefficient, and consequently to the same wing area and structural fraction.

It can be concluded that the endurance of the integrated system increases as a greater number of propellers is considered due to the propulsors-power drop and the improved aerodynamic efficiency. Both effects are driven by the reduction in the propulsors disc loading, which leads to a more efficient propeller design and allows the wing to be fully covered by the propellers.

8.3.4 Wing aspect ratio effect

The endurance of the integrated system increases when a greater wing aspect ratio is considered if the propeller radius is large enough to cover the whole wing span (fig. 8.17a). The results assume a fixed number of propellers (12) and RPM (750).

As the wing aspect ratio is solely an aircraft parameter, the propulsors power and consequently the engine fuel flow are unaffected (figs. 8.17c and 8.17d). The benefits come from a reduction in wing surface area when the propellers cover a greater fraction of the wing span. When the wing aspect ratio increases, this condition can be met only with a greater propeller radius (figs. 8.17b). This is because when the

wing aspect ratio increases the wing span is bigger, and so it can be fully covered

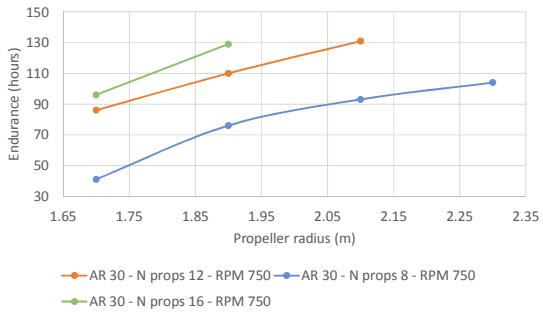

(a) Endurance as function of number or propellers

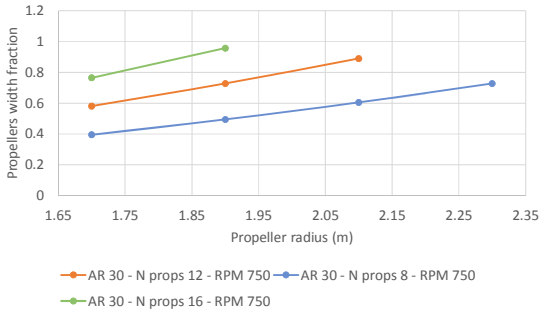

(b) Propellers width fraction as function of number or propellers

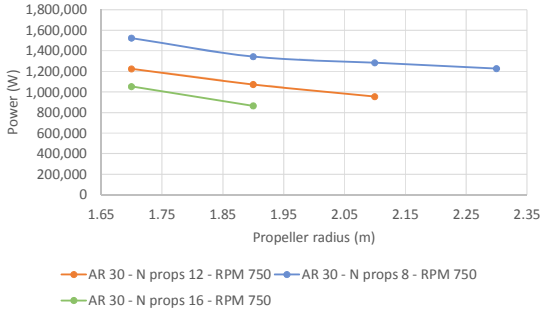

(c) Distributed propellers power as function of number or propellers

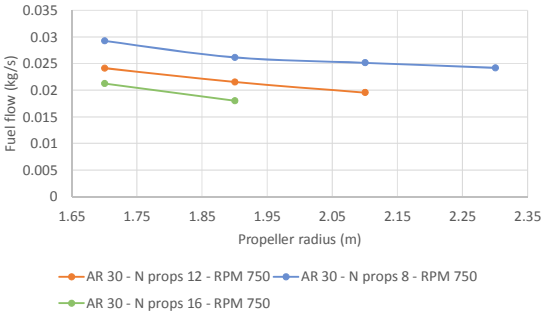

(d) Engine fuel flow as function of number or propellers

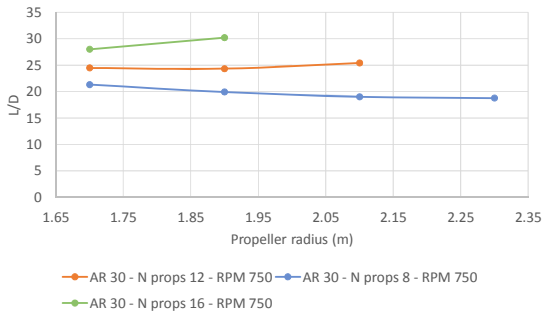

(e) L/D as function of number or propellers

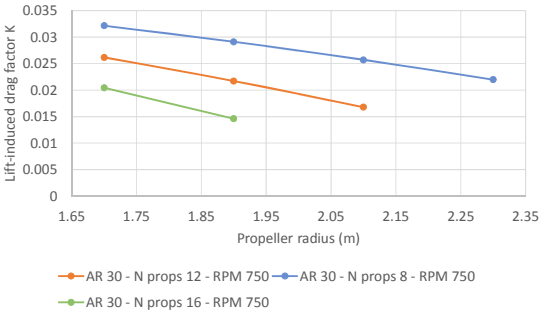

(f) Aircraft structural fraction as function of number or propellers

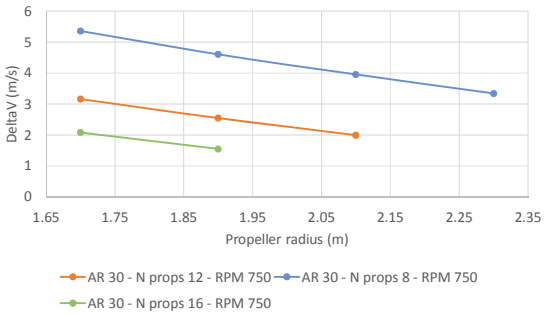

(g) Propeller ΔV as function of number or propellers

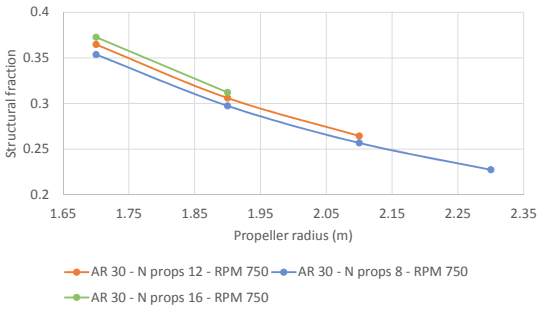

(h) Aircraft structural fraction as function of number or propellers

Figure 8.16: The effect of propellers number and radius on the design and performance of the integrated system (wing AR = 30 & RPM = 750)

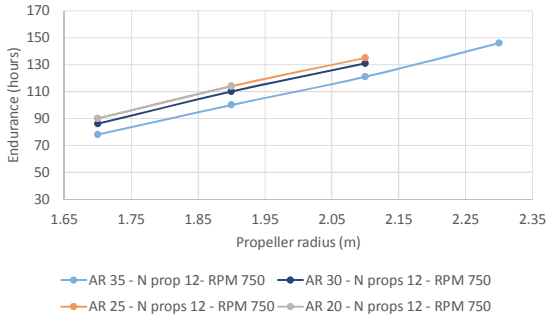

(a) Endurance as function of number or propellers

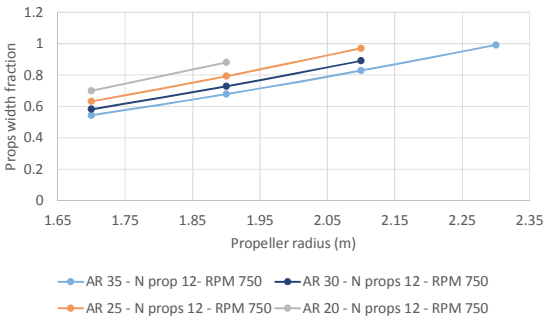

(b) Propellers width fraction as function of number or propellers

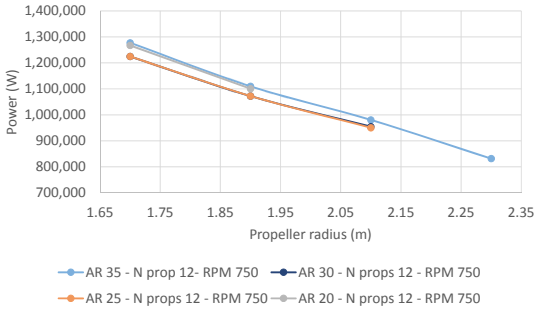

(c) Distributed propellers power as function of number or propellers

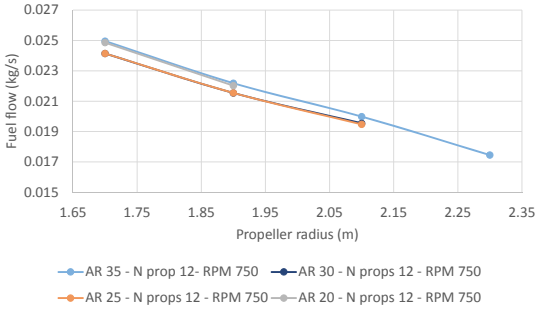

(d) Engine fuel flow as function of number or propellers

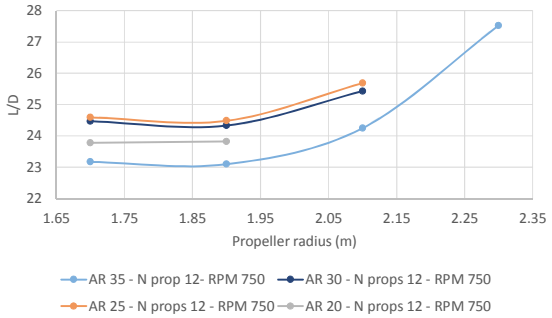

(e) L/D as function of number or propellers

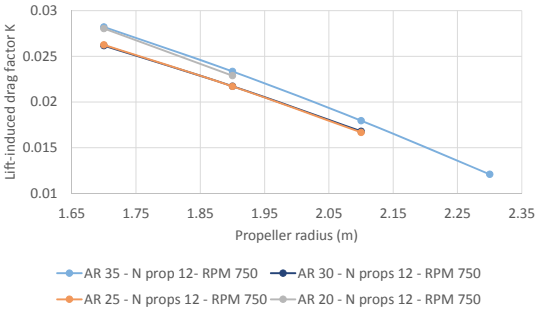

(f) Lift-induced drag factor K as function of number or propellers

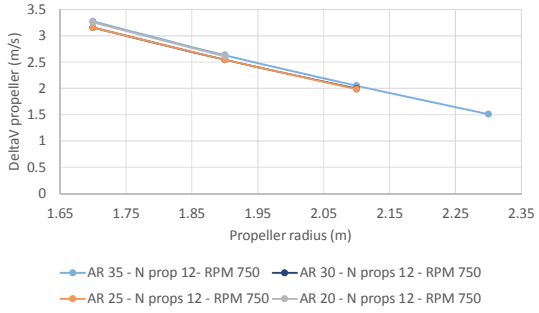

(g) Props ΔV as function of their number

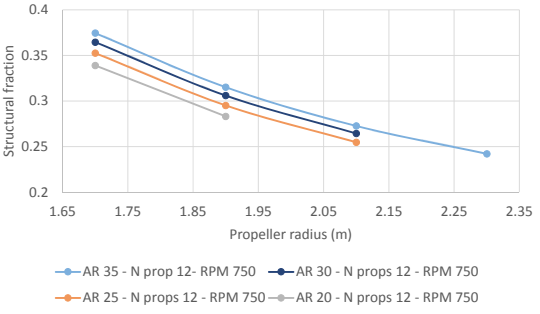

(h) Structural fraction vs props number

Figure 8.17: The effect of wing aspect ratio and propeller radius on the design and performance of the integrated system (12 propellers & RPM = 750)

only with larger propellers if their number is fixed.

The reduction in wing area leads to an aircraft drag and wing mass reduction. The smaller drag is a combination of both the reduced wing wetted area and the lift-induced drag if the propellers are large enough to cover wing span (fig. 8.17e). Similarly to the results of section 8.3.2, a minimum L/D can be observed and at a high propeller radius the reduction in lift-induced drag offsets the smaller wing chord. The wing mass reduction leads to a reduced structural fraction, which allows more fuel to be stored for a given take-off mass and less deadweight to be carried throughout the mission (fig. 8.17h).

8.3.5 Comparison between distributed fans and distributed propellers

The distributed propellers were found to offer a +58% (over 2 days) endurance improvement compared to the distributed fans case for a given take-off mass, type of airframe and engine cycle (table 8.2). The T&W airframe was considered, and the turboshaft performance parameters are OPR = 28 and TET = 1,300 K. It has to be noticed that while the type of airframe and engine cycle were the same, in reality the airframe and the engine were not the same design. In fact, both the airframe and the engine were rescaled depending on the considered propulsor type. About the propulsors, the fan was characterised by a BPR of 20 and an optimum FPR of 1.2. The propeller design was optimised for the best endurance and it was characterised by radius of 2.3m, an RPM of 1,000, and a number of propulsors equal to 12.

The effect of rescaling the airframe can be noticed from the difference in wing area when a different propulsor type is used. The wing area reduced by 52% when the distributed propellers were used compared to the distributed fans. This a direct consequence of the propellers lift-augmentation effect as the wing can be sized for a higher lift coefficient of 2.7 rather than 1.3. Consequently, the aircraft structural mass reduces by 35% as the wing is the main structural component. This offers a double benefit: more fuel can be stored and the aircraft empty mass can be reduced. The fuel fraction improves by 26%, which is different from the reduction in structural mass. This is due to the fact that when more fuel is stored the mass of the fuel tanks also increases.

Parameter	Dfans	Dprops	Δ
Take-off mass (kg)	15,000	15,000	–
Endurance (days)	4	6.25	+58%
Endurance (hours)	95	150	+58%
Wing area (m^2)	223.7	107.8	-52%
Wing mass (kg)	4507	2486	-45%
Aircraft structural fraction	0.37	0.24	-35%
Aircraft fuel fraction	0.46	0.58	+26%
Wing aspect ratio	22	35	+56%
Loiter L/D	24	27.5	+15%
$C_{L,max}$	1.3	2.7	+108%
$C_{L,cruise}$	0.86	1.73	+101%
Top-of-climb propulsors power (kW)	955.5	788	-18%
Top-of-climb propulsor efficiency	0.90 (ise)	0.84	-6.7%

Table 8.2: Comparison between the distributed fans (Dfans) and distributed propellers (Dprops) case for the 15,000 kg T&W airframe. The same GT cycle (OPR=28, TET=1,300 K) was considered.

The optimum wing aspect ratio of the wing increases from 22 to 35 when the propellers are used. This is due to the fact that as the wing area reduces a higher aspect ratio can be achieved without incurring in a structural penalty. The combination of the increased wing aspect ratio, reduced wing area, and the slipstream effect led to a +15% improvement in aerodynamic efficiency. A wing aspect ratio of 35 is still in the range of the previous HALE UAV designs, and as such it was assumed to be feasible in terms of wing design.

Looking at the different propulsors, it can be noticed that the propellers require 18% less power than the fans although they are less efficient. This means that the engine would be downsized when the propellers are used, leading to a reduction in fuel flow and consequently of fuel burn. The power reduction is due to the fact that 12 propellers were considered. The same would not be true at high disc loadings if two or four propellers were to be considered. Conversely, the fans power remain unaffected by their number being a compressing device. These distributed propellers benefits are also complemented by their simpler design, which translates into ease of manufacturing. Fans are generally more difficult to design, although being shrouded rotors their efficiency is higher.

It is possible to conclude that the distributed propellers, compared to the distributed fans, lead to an endurance improvement due to the fact that the wing is downsized and their power to sustain flight reduces. The wing area reduces as a consequence of the lift-augmentation effect, which leads to aerodynamic and struc-

tural benefits. The power that the propellers require to deliver thrust is smaller because of two reasons. Power reduces as the number of propellers increases, and the improved aerodynamic efficiency leads to a lower design-point thrust requirement. Conversely, the distributed fans did not offer any synergy with the airframe as they were considered as podded on the wing.

8.3.6 Integration of engine cycles and energy management

The distributed propellers were also integrated with the energy management series-hybrid strategy. Their performance was compared with the baseline distributed fans configuration (fig. 8.18). Different cycles were considered as it was illustrated in chapter 5. The aim was to show the effect of increasing the core engine OPR and TET for the Brayton cycle, and to benchmark its performance against the wave rotor with internal combustion (WRIC) cycle.

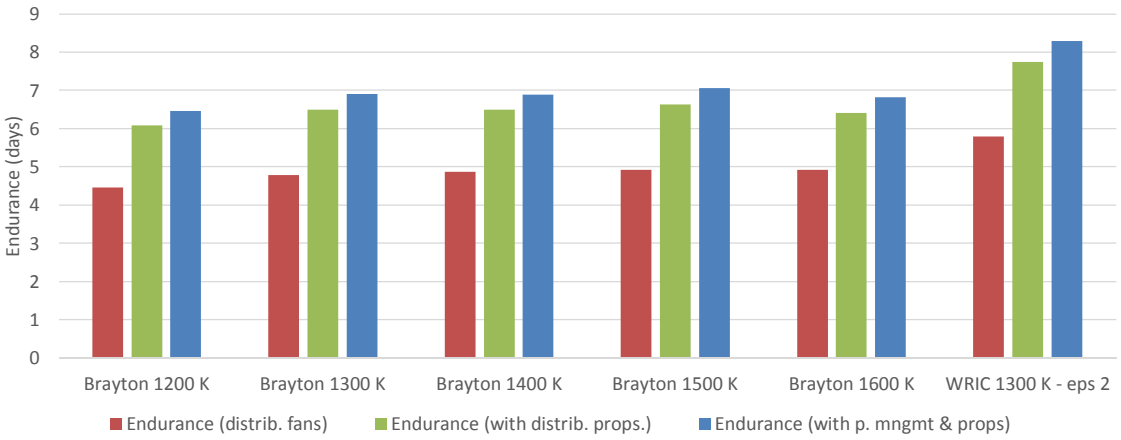

Figure 8.18: 15,000 kg T&W airframe endurance as a function of the Brayton and the wave rotor cycles. The distributed fans case is compared to that of the distributed propellers with and without the series-hybrid energy management strategy

For a given cycle, the distributed propellers lead to an endurance increase between 1.5 and 2 days compared to the baseline distributed fans case. As expected, the benefits of the distributed propellers are independent of the selected cycle. Also, for both the distributed propellers and the distributed fans there is no apparent benefit in moving towards high-temperature and high-pressure cycles. This is because the theoretical thermal efficiency improvement is degraded by the reduced turbomachinery blade height (see chapter 5).

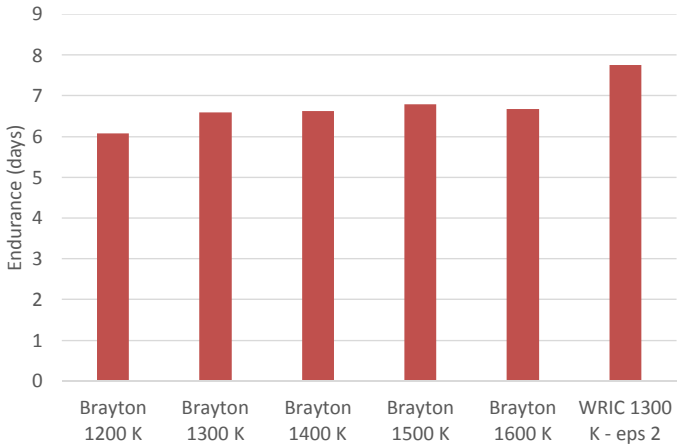

Figure 8.19: 15,000 kg BWB endurance as a function of the Brayton and the wave rotor cycles for the distributed fans case

It is also possible to notice that the series-hybrid energy management strategy offers a limited benefit regardless of the considered cycle. The results refer to a 4% battery mass and a 2 kWh/kg energy density (see chapter 7). The energy management contribution is in the order of half of a day of endurance improvement, which is three to four times less than what the distributed propellers could achieve. This should not be surprising given the fact that including a battery improves the propulsion system SFC and at the same time it increases the aircraft empty mass. Conversely, the distributed propellers improve the propulsion system SFC and allow more fuel to be stored. The first effect is due to the power reduction when the propulsors number increases, and the second effect is a consequence of the wing downsizing due to the lift-augmentation effect.

From a target perspective, an important conclusion of this study is that the T&W airframe was able to meet the 7–10 days endurance requirement due to the integration of the WRIC cycles and the distributed propellers. Including the effect of the series-hybrid energy management strategy would allow the aircraft to breach the eight-day endurance threshold.

It is also worth noticing that, for a given cycle, the distributed propellers literally turns the T&W airframe into a BWB airframe from a performance perspective as the endurances become comparable (fig. 8.18 and 8.19). Ultimately, the BWB offered a better endurance because of the improved aerodynamic and structural efficiency. The first effect is due to its high volumetric efficiency, defined as the surface to volume ratio. The second one is due to the bending relief effect on the centrebody. Thus, it should not be surprising that by means of aerodynamic and structural

improvements the T&W airframe performance became comparable to that of the BWB airframe. However, the BWB airframe proved to be less flexible than the T&W airframe given that fact that the both the effects of the energy management strategies and of the distributed propellers would either not offer any benefit or be unfeasible.

8.4 Limitations to the present study

Several assumptions limit the conclusions and the feasibility of this study. Some of them are related to either the design or the modelling of the individual elements of the system, whereas others concern the study as a whole.

8.4.1 Propellers modelling assumptions

Looking at the propellers, their design is usually based on experience. Although the selected Clark Y airfoil is reasonable for HALE operations, a more detailed study is required to assess if it is a suitable choice. This could be addressed by interviewing subject-area experts and by repeating the design space exploration study with different airfoils. Similarly, another design choice was the fixed-pitch blade, which is acceptable at a conceptual design stage due to its simplicity. However, a priori it is not known whether the propeller off-design may improve the endurance of the system if a variable pitch or a combination of variable pitch and variable RPM are considered. Similar arguments are also true for the number of blades, which was fixed to two for simplicity.

Other aspects that should be addressed are related to the propeller aerodynamics. At the very low disc loadings the velocity differential that is imparted to the air is very small, in the order of 1 or 2 m/s. In the literature there are examples of propellers that generate a ΔV of about 4 m/s at cruise conditions, such as the example of [Stoll et al. 2014]. However, if the viscosity effect was accounted with fully viscous flow calculations (i.e. CFD) it might be that even at very low disc loadings the losses in the propeller would result in a higher ΔV than what was computed with QPROP. In fact, QPROP accounts for viscosity by including the airfoil (C_L, α) and drag-polar curves that are computed with Xfoil.

8.4.2 Slipstream-wing interaction assumptions

The slipstream-wing interaction model that was used for this project is also subject to its own limitations. It represents a one-way interaction between the slipstream and the wing, where the slipstream influences the wing and not vice versa. This assumption can be considered acceptable at a conceptual design stage by assuming that both the propeller hub and the motor behind it fit in the wing leading edge. Consequently, the interference drag between the wing and the propeller could be considered negligible compared to the lift-augmentation and drag-reduction benefits. Higher fidelity methods will be required to prove this hypothesis true.

Detailed calculations will also be required to assess the impact of the propeller swirl, which is neglected by the selected method and may affect the wing angle of attack. The fact that viscosity was ignored is also another fundamental assumption as viscosity effects can play an important role in HALE operations due to the low Reynolds number. On the other hand, at very low-subsonic speeds such as Mach 0.2 – 0.3 compressibility effects are negligible.

8.4.3 Electric transmission system assumptions

The electrical system is the key technology enabler to distribute the propellers on the wing. Its architecture and the assumptions that were adopted for this study were explained in appendix C. As such, parametric studies are required to assess the sensitivity of the electric system to its weight and efficiency. It may not be feasible to install the motors on the wing should their weight be too heavy. This would compromise its structural integrity due to the excessive static and/or dynamic loads. Similarly, an increase in the transmission system losses would result in a fuel burn penalty as the core engine would need to be oversized.

8.4.4 Airframe assumptions

The wing structural correlations are also a weakness of the present study. The optimum wing aspect ratio of the clean wing was limited to 22. For values above that, the structural mass penalty would offset the aerodynamic benefit. However, in the past there were HALE UAVs designed with a wing aspect ratio in excess of 30. As part of the benefit of distributing propellers comes from a drag reduction,

this benefit would reduce if the baseline aircraft could afford a greater aspect ratio for the same wing mass. Still, the distributed propellers would still offer benefits compared to the fan alternative as their power reduces when their number increases.

8.4.5 Results analysis and presentation

A remark also needs to be made on the study as a whole. A lot of emphasis was place on analysing the performance of the integrated system, and so the results highlighted the endurance improvements and what was driving them. More effort could be devoted to the individual components of the system. For instance, the results could have been presented from a propeller performance or a wing aerodynamics perspective. It could be useful, for example, to repeat part of the study with a fixed-wing geometry to clearly distinguish the drag reduction due to the a decrease in lift-induced drag and due to the wing downsizing as a consequence of the lift-augmentation effect.

In addition, from a propeller designer perspective the results could be shown in terms of propeller disc loading and efficiency. This would have highlighted that the optimum propeller design in terms of efficiency would not automatically lead to the best endurance. However, it was the author's preference to present the results in a way that gives an insight on how a designer might approach the integrated-system-design problem. As such, it was decided to present the results in terms of radius, RPM, and propellers number (which replaces thrust), which are the main design parameters of the propellers. Also, it has to be noticed that the present study would be of interest of experts and researchers that may not be familiar with the propeller performance. Radius, RPM, and propeller numbers as variables are easier to be interpreted by a larger audience.

8.4.6 Reliability

Lastly, when distributing the propellers the system performance benefits are traded with an increase in complexity and risk. The whole concept relies on an advanced electrical transmission system, which could be more or less reliable than a simple gearbox. Maintenance issues, life expectancy, and failure modes need to be carefully addressed.

8.5 Concluding remarks

The aim of the present chapter was to establish a methodology to assess the impact of distributing motor-driven propellers on the design and performance of the present low-speed HALE UAVs. Although the current methodology could be applied to any airframe, it would be unfeasible to redesign the BWB airframe with the propellers due to the hydrogen volumetric requirement that fixes the centrebody surface area. This would lead to a delta wing design, which is unsuitable for low speeds. As such, the distributed propellers results only refer to the T&W airframe.

A design space exploration study was carried out to assess the sensitivity of the integrated aircraft system to the main design parameters of the propeller: its radius, RPM, and number of propulsors (which fixes its unit thrust). The propeller radius was varied from 1.7 to 2.3m, the RPM from 650 to 1,000, and the number of propulsors between 8 and 16. These ranges were considered as the software used to model the propulsors would not return a propeller design outside of these boundaries.

It was found that the system endurance increases by 1.5 to 2 days for a given engine cycle—nearly a 60% improvement compared to the baseline distributed-fans case. This is due to the combination of aircraft weight, aerodynamics, and engine rescaling effects. The lift-augmentation effect leads to a smaller wing area, which, coupled with the reduction in lift-induced drag due to the improved wing turning effectiveness, results in an improved aircraft aerodynamic efficiency. The smaller wing area also allows more fuel to be stored as the structures become lighter and the aircraft empty mass reduces. Also, when multiple propellers are considered their power requirement reduces, which means that the engine can be downsized and consume less fuel.

The distributed-propellers technology was also found to offer a three to four times greater benefit compared to the series-hybrid energy management strategy—regardless of the considered engine cycle. This is because the presence of the battery could improve the propulsion system SFC at the expense of a reduction in fuel mass and an increase in aircraft empty weight. Conversely, the distributed propellers make the propulsion system more fuel efficient by at the same time allowing more fuel to be stored and decreasing the aircraft empty mass—in addition to the aerodynamic benefits of the slipstream-wing interaction.

It can be concluded that the distributed propellers technology should be fur-

ther investigated for HALE UAVs and perhaps for other low-subsonic application such as prop-powered regional aircraft. However, the 60% endurance improvement is susceptible to many risks and uncertainties, particularly about the electric transmission system (weight, losses, and reliability) and the slipstream-wing interaction. Higher-fidelity studies are required to address them.

Chapter 9

Summary and Conclusions

The aim of the present thesis is to build a multi-disciplinary and multi-fidelity methodology to capture the synergies offered by integrating advanced and disruptive aircraft technologies. Hydrogen fuel, unconventional airframes, and distributed propulsion were selected to meet the 7-10 days long-endurance requirement when carrying an 800 kg payload that requires 200 kW of power. The individual technologies by themselves enhance the performance of a HALE UAV. However, their integration leads to synergies that improve the endurance of the system so that it would be greater than what could be achieved by simply superimposing the individual technologies.

The integrated HALE UAV under consideration comprises three main areas of analysis: the airframe, the distributed propulsion system, and the energy management system. Their mutual interactions affect the integrated aircraft power requirement, production, management, and distribution.

It is worth noticing that such a methodology could not be identified in the public domain. The present literature does not give an indication or design rule about how an integrated system should be designed to maximise the benefits offered by the integration synergies. There are also many uncertainties on what are the key variables that mostly influence the design and performance of the integrated aircraft system.

The aim of the present methodology is to capture the integration synergies for the purpose of design space exploration studies. Assuming a fixed design for any of the considered sub-systems would not allow the benefits of the aforementioned

technologies to be fully quantified. Below is a summary of the main findings that arose from the design space exploration.

9.1 Power requirement

A flexible aircraft platform was built to assess the effect of integrating a distributed propulsion system on the design and performance of a HALE UAV. Three airframes were considered, namely a baseline tube-and-wing (T&W), a triple-design and a blended wing body (BWB) airframe. The main conclusions on the airframes study are exposed below.

Propulsion system mass flow scaling increases endurance by 30%. The figure refers to the distributed-fans tube-and-wing airframe when its take-off mass is increased from 5,000 kg to 15,000 kg. This is due to the propulsion system specific fuel consumption (SFC), which drops as its greater intake mass flow allows more energy to drive the fan system. It has to be noticed that the fans power is as big as the payload power, and so the greater mass flow allows a higher fan pressure ratio to be achieved. It can be concluded that assuming a constant SFC is no longer a valid assumption when designing integrated aircraft systems.

BWB airframe improves maximum endurance by two days (+ 30%) with uncertainty on its structural efficiency. The BWB structural mass might be heavier than what predicted by the current study despite its improved structural and aerodynamic characteristics. This is due to the installation of the hydrogen tanks, which would interfere with the structures layout and was not modelled in the present study.

BWB airframe is also sensitive to its wing lift coefficient choice at design point, which is lower than that of the tube-and-wing airframe. This means that it could not benefit from the lift augmentation of distributed propellers.

The triple-fuselage design was found to offer no endurance benefit for a low-speed HALE UAV. This is because the drag penalty of the extra fuselages counteracts the wing bending relief due to distributing masses away from the aircraft centreline.

It can be concluded that detailed studies on the hydrogen tanks installation are required to assess the effective endurance benefits of the BWB airframe when

compared to the T&W baseline.

9.2 Power production

Wave rotor with internal combustion (WRIC) and solid oxide fuel cell (SOFC) were both considered in the form of hybrid cycles with gas turbine components. The impact of the cycle selection on the aircraft endurance was assessed for the distributed fans case. This is a trade-off between engine weight, drag, and SFC. The main findings of the cycles study are presented in the following paragraphs.

Hybrid WRIC/GT cycles offered an endurance benefit of 6%-18% on the T&W airframe and of 5%-14% on the BWB airframe compared to the best Brayton cycle. The WRIC/GT cycles reduce the propulsion system weight, drag, and SFC as the wave rotor bypass increases. This is different to what occurs in a Brayton cycle, where the increase in TET leads to lower weight and drag but to a higher SFC. In addition, the lower-bound of the wave rotor endurance benefits is aligned to the 8% endurance improvement that would occur if a stage of centrifugal compressor were to be added.

The WRIC/GT endurance benefits were achieved with a TET limit of 1,300 K for the WRIC/GT cycles. This is because the WRIC delivery pressure is higher than that of the high-pressure compressor exit flow, so that its air could not be used to cool the turbine blades. However, there are other strategies that could be adopted—such as extracting work from the WRIC to lower its exit pressure—to increase the cycle TET.

The WRIC integration challenges may also lead to emissions benefits. Careful wave rotor and ducts design is required to supply unsteady flow to a turbine. However, the intrinsic combusted gas recirculation of a wave rotor could also reduce emissions, which would be important for civil applications should future regulations set targets on them.

Hybrid SOFC/GT cycles were found to offer no endurance benefits on both the T&W and BWB airframes compared to the best Brayton cycle. This is because the 12% lower SFC is not enough to offset the heavier propulsion system mass—which would be two times bigger than that of the Brayton cycle engine even with a SOFC power density of 1 kW/kg.

It can be concluded that hybrid WRIC/GT cycles should be further investigated for higher TETs. Sensitivity studies on the pressure losses within the ducts are also required, although a pessimistic 6.5% pressure loss was already included in the present study. Hybrid SOFC/GT studies should not be further investigated for low-speed HALE UAVs.

9.3 Power management and distribution

The effects of power management and distribution were investigated by assessing different energy management strategies and the lift-augmentation of distributed propellers. Only the tube-and-wing airframe was considered for the distributed propellers due to the wing lift coefficient limitations of the BWB airframe. The following conclusions can be drawn.

Distributed propellers improved the T&W endurance by 1.5 to 2 days for a given engine cycle—nearly a 60% improvement compared to the distributed fans case. This is because the lift-augmentation of the propellers leads to a smaller wing area, which, coupled with the reduction in lift-induced drag, results in an improved aircraft aerodynamics efficiency. The smaller wing area also allows more fuel to be stored as the aircraft structures become lighter. Also, when multiple propellers are considered their power requirement reduces, which means that the engine can be downsized to consume less fuel.

Relighting the engine to be run at design point and recharge the batteries offered an endurance benefit of 9.5% on the T&W airframe with a 4% battery mass and a battery energy density of 2 kWh/kg. This is because mitigating the extra fuel burn due to the engine off-design SFC penalty offsets the weight of the battery—regardless of the aircraft take-off mass. However, no benefits were found for an energy density of 1 kWh/kg, which is already four to five times greater than today's technology.

The climb-and-glide energy management strategy was found to offer no endurance benefit with a battery energy density of 2 kWh/kg. This is because the engine still experiences an off-design due to the altitude effect. A full parametric study on the aircraft take-off mass, the battery mass fraction, its energy density, and the power split between the fans and the battery during the glide/charge phase was conducted.

Hybrid systems could also improve system reliability and emissions. A battery might replace the need for a redundant generator. In addition, with the series-hybrid architecture aircraft emissions and contrails could be mitigated when the aircraft is operated on battery-only. Redundancy and emissions considerations might be important for civil applications should future regulations set targets on them.

It can be concluded that the distributed propellers technology should be further investigated for low-speed HALE UAVs and perhaps for other low-subsonic appplications (e.g. regional aircraft). Their benefits are three to four times greater than that of the series-hybrid energy management strategy and of the wave rotor cycles. However, the 60% endurance improvement is susceptible to many risks and uncertainties, particularly about the electric transmission system (weight, losses, reliability) and the slipstream-wing interaction. Higher-fidelity studies are required to address them.

Appendix A

Take-off Mass Build-up Approach for Endurance Aircraft

The iterative layout shown in figure A.1 was initially adopted by the author and found to be unsuitable for an endurance aircraft. This method is usually referred to as the take-off mass build approach. In simple words, this numerical approach answers the question "for a given mission, which take-off mass will meet this requirement?".

The name comes from the fact that the take-off mass of the aircraft is iteratively changed for a given mission requirement. This calculation framework is usually adopted to design large aircraft, and it usually converges within a few iterations if a reasonable initial guess for the take-off mass is assumed. Existing aircraft designs usually provide enough information to make a reasonable first guess.

However, this calculations framework proved to be unsuitable for the conceptual design of endurance aircraft. In fact, when the endurance requirement increases divergent trends were predicted (fig. A.2). The results diverge to take-off masses that are too great for a HALE UAV carrying 800 kg of payload. Also, these trends were not affected by other parameters such as the loiter SFC or the storage system gravimetric efficiency.

It was then decided to change the approach to the endurance-aircraft conceptual design problem. Rather than iterating on the take-off mass for a given endurance requirement, for a given take-off mass the maximum endurance of the system was determined. Although the individual aircraft disciplines are the same (drag, per-

formance, structures, etc.), this framework of calculations was found to be more stable. Its convergence time, however, is dependent on the initial endurance guess, and unfortunately previous designs are unavailable to estimate it. Thus, a trial-and-error approach was required.

The "endurance build-up" approach (fig A.3) convergence criteria works on the descend fuel. Starting with an underestimate of the maximum endurance, the aircraft would be left with too much fuel complete the descent phase. Thus, the endurance requirement can be iteratively increased until the fuel that aircraft is left with at the end of the loiter matches the fuel required to complete the descend phase.

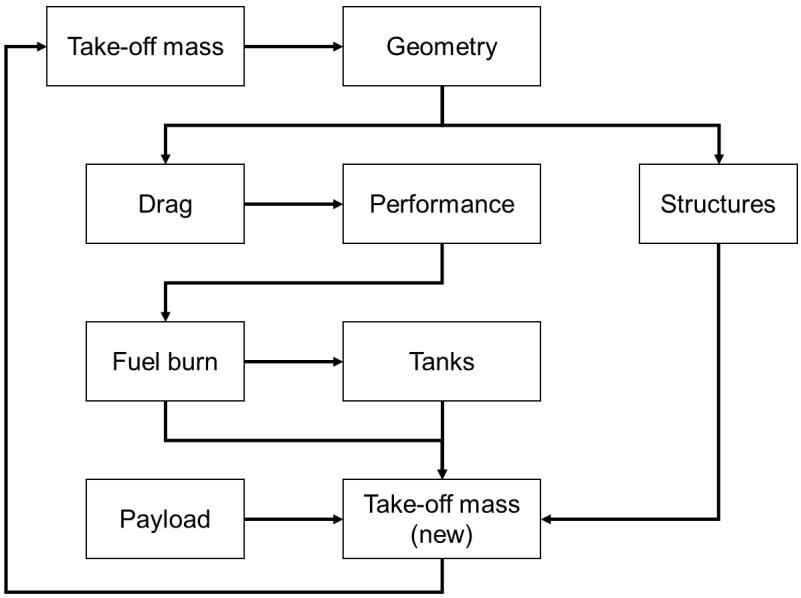

Figure A.1: Take-off mass build-up approach iterative method layout for aircraft conceptual design calculations

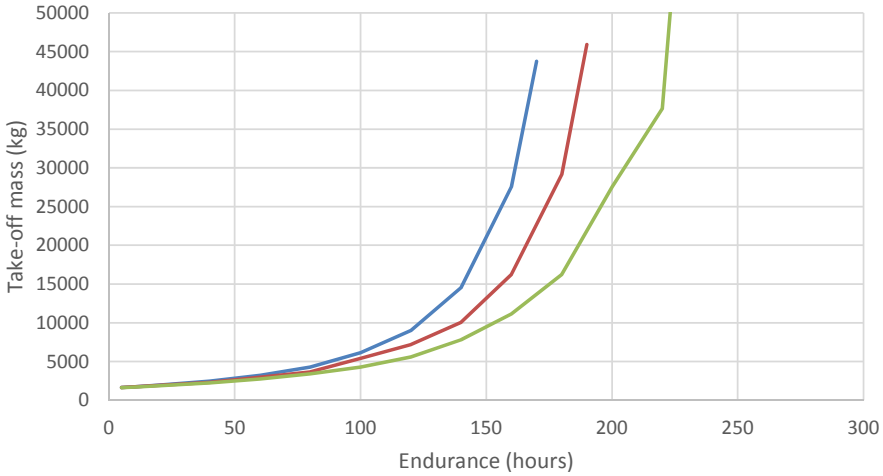

Figure A.2: Trends of take-off mass as a function of endurance computed with the calculation layout of figure A.1. Loiter SFC decreases when moving from the blue curve to the green curve.

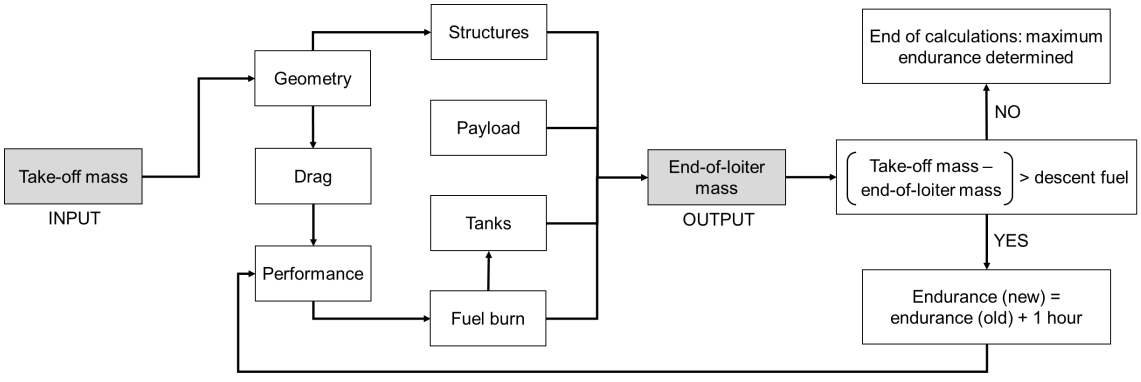

Figure A.3: Iterative method layout for long-endurance aircraft conceptual design

Appendix B

Core Engine and Distributed Fans Size and Weight Assumptions

Engine sizing and weight calculations were essential to estimate the turbomachinery blade height and gas turbine mass. Determining the height of the HPC outlet is essential to ensure that the size constraints are met. In fact, below 9 mm of blade height the compressor polytropic efficiency can degrade by approximately 10% to 13% compared to a baseline design with no degradation [Kyprianidis and Rolt 2014]. In addition, estimating the engine mass is essential for integrated airframe-engine studies. Ultimately, for a given take-off mass the presence of the engine results in a reduced fuel mass and an increase in airframe empty weight. Both factors need to be accounted for accurate aircraft performance calculations.

The engine performance properties have to be known to predict its size and weight. The core engine and distributed fans performance were assessed with Turbomatch, Cranfield University gas turbine engine performance simulation software. Turbomatch allows design and off-design calculations to be performed and it also has multi-fuel capabilities.

The engine sizing calculations were carried out according to the preliminary design guidelines suggested in [Ramsden and Macmanus 2011]. Their procedure allows the engine main gas path to be sized in term of hub, mean, and tip radius (fig. B.1).

About the compressors design, an inlet hub-to-tip ratio of 0.65 was assumed for the low-pressure (LP) one. A constant-hub layout was adopted for both the LP and

HP compressors to achieve an exit hub-to-tip ratio lower than 0.9. In fact, it was found that the constant-tip and the constant-mean-diameter options would not meet the exit hub-to-tip ratio constraint. As suggested by the authors, the shaft rotational speed was chosen to ensure a blade-tip Mach number lower than 1.3 and constant axial velocity throughout the stages was assumed [Ramsden and Macmanus 2011]. For the turbine designs, the number of stages was chosen to achieve stage loadings below 2.5 and flow coefficients between 0.4 and 0.6, which are typical design values. The distributed fans were preliminary sized by following the compressor guidelines and by assuming a hub-to-tip ratio of 0.4.

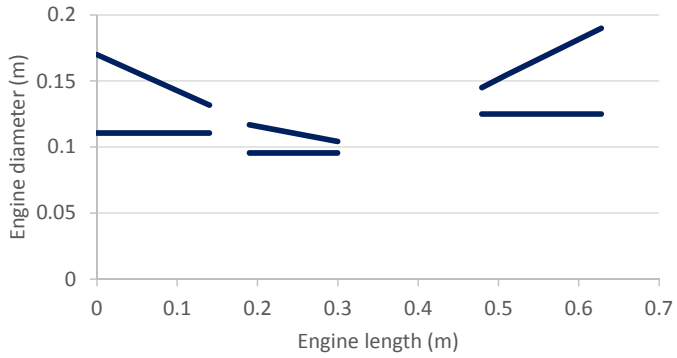

Figure B.1: Example of the preliminary design of turbomachinery components

The core engine and distributed fans sizing allowed their weight to be determined by means of empirical expressions [D. A, Lieblein and Krebs 1971]. Analytical correlations were selected as their simplicity make them suitable at the conceptual design stage. A more detailed weight estimation procedure could be used for future studies, where each turbomachinery component is broken down its constituent parts (disks, casing, blade, etc.) and their masses are individually assessed.

According to the selected analytical method, the compressors, turbines, and distributed fans masses can be individually assessed by knowing their length, mean diameter, and number of stages. These properties should be known after performance and sizing calculations. The weight estimation accounts for the rotor and stator blades, disks, and casing. Similarly, the weight of the combustion chamber was assessed based on its mean diameter and an empirical constant.

Appendix C

Turboelectric Distributed Propulsion Layout and Electric System Specifications

The turboelectric distributed propulsion concept relies on an advanced electric-based transmission system to link the core engine with the propulsors. There are several advantages with an electric transmission system. To start with, it allows the propulsors to be distributed nearly anywhere on the airframe, which adds another degree of freedom at the conceptual design stage. This could open the door to aerodynamic and structural synergies between the propulsion system and the airframe. The electric transmission can also be used as a variable-ratio gearbox, meaning that the propulsors speed would be independent from that of the core engine, provided that a suitable architecture is defined. Thus, the motors and propulsors speed could be optimised for different mission requirements (e.g. noise, emissions, efficiency) in different flight segments.

Today's electric machines are known to be heavy and subject to non-negligible transmission losses. The main assumption behind the selection of a turboelectric distributed propulsion system is that their weight and efficiency will improve in the near future [Brown 2011]. Superconductivity is a very attractive option, as it allows current to be transferred at near-zero losses when cryocooled. In addition to the presence of liquid hydrogen as a primary fuel, this is the reason why the electric system architecture was assumed to be superconducting for the present project.

However, it has to be noticed that progress in conventional electric machines will

also occur in the near future, and the final decision on whether or not superconductivity will be required may also depend on other factors such as reliability and ease of manufacturing. This last point is particularly crucial as the losses of the superconducting filaments can be assumed to be near-zero only at a thickness that cannot be manufactured according to the current standards [Felder, Brown and Kim 2011].

The superconducting electric system architecture shown in figure C.1 was selected for the present turboelectric distributed propulsion system. First of all, it would be beyond the scope of this project to define the "ultimate" electric system architecture. Many considerations such as the voltage selection and the fault currents require a much more detailed approach [Armstrong, Blackwelder and Ross 2014; Davies et al. 2015; Jones et al. 2015]. Thus, the present architecture needs to be intended as a top-level arrangement of the components that are required to transmit the power from the engine to the propulsors.

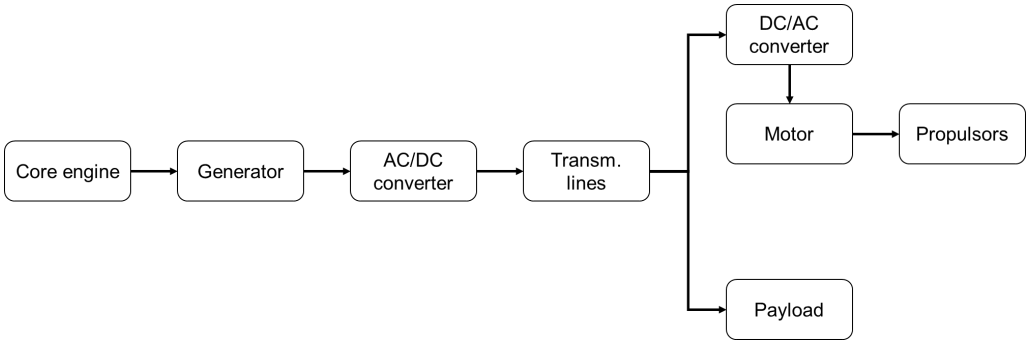

Figure C.1: Layout of the superconducting electric system for turboelectric distributed propulsion

The present electric system architecture includes an AC generator, a rectifier (or AC/DC converter), DC superconducting transmission lines, inverters (DC/AC converter), and AC motors. Many reasons and assumptions lie behind this choice. Looking at the generator, it was assumed to be AC as it would be more reliable than having a DC output directly from the generator itself. The output of a generator is AC by the intrinsic nature of current generation: either the magnetic field or the

Component	**Efficiency (%)**	**Power density (kW/kg)**
Generator with AC/DC converter	99.28	41.6
Motor	99.97	22.0
DC/AC converter	99.93	15.45

Table C.1: MgB_2-based liquid-hydrogen cooled electrical system weights and efficiencies [Felder, Brown and Kim 2011]

conducting coil have to be variable for the current to flow in a conducting material. If a "switch" was mounted directly on the generator itself, which is usually referred to as a commutator, it could be possible to have a DC output from the generator. However, rectifiers (AD/DC converters) are usually a much simpler, cheaper, and more reliable solution in non-superconducting electric systems. It was assumed that the same assumption could be valid even with superconducting machines given the lack of information about it.

Superconducting transmission lines need to be DC to avoid AC superconducting losses. It is interesting to notice that the opposite would happen with a non-superconducting architecture as the DC lines are subject to a voltage drop over long distances. Alternatively, a high-voltage DC solution could be adopted.

The motors were assumed to be AC so that their speed could be changed by varying the current frequency throughout the DC/AC conversion process. It is due to this conversion from AC to DC and then from DC to AC that the speed of the core engine, and so of the generator, can be decoupled from that of the motors. This is because there is a direct relationship between the current frequency and the motor/generator rotational speed [Hardy-Bishop 2003].

However, the voltage selection plays an important role in the weight of a variable system frequency. As it was reported in [Jones et al. 2015], the weight of the converters can become approximately three to four times heavier than the electric machines (motors, generator) at a DC distribution voltage of 10 to 20 kV (fig. C.2). Even at smaller voltages, the weight of the converters is still two times greater than the electric machines. Thus, detailed electric system architecture studies should aim at minimising the number of required converters as at the moment they are the dominating weight of the electric system.

It is also worth noticing that these studies refer to solid-state switch converters, which represent today's technology and are not superconducting. They are known as the most suitable technology to convert power from AC to DC (and vice versa), and no alternative options have been found so far. Therefore, it will be a priority to identify new solid-state switching technologies, materials, and topologies to reduce their weight and losses [Armstrong, Blackwelder and Ross 2014].

The component power densities of table C.1 were assumed for the present project. The choice was based on a lack of information about the weight and efficiencies of superconducting machines as at the moment they are still in the early development

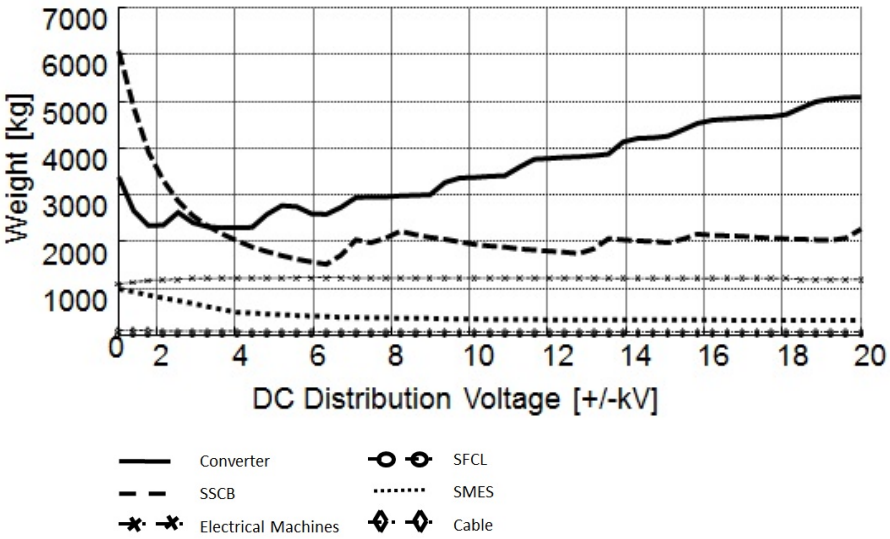

Figure C.2: Sensitivity of the weight of the turboelectric distributed propulsion system to the DC distribution voltage [Jones et al. 2015]

stages. About the transmission lines, their weight was arbitrarily assumed to be a 10% of the overall electric machines and converters weight. The proposed values should be looked at as targets. On one side, there is a lot of uncertainty about whether they can or cannot be achieved. On the other side, uncertainty also means potential for further development.

It can be immediately seen that the overall efficiency of the transmission system is above 99%, which is quite an optimistic assumption. The same argument holds true for the power densities, as non-superconducting electric machines would be two three times less power dense than what reported in table C.1 [Schiltgen et al. 2012].

Bibliography

A

Abbott, I. H. and A. E. Von Doenhoff (1959). *Theory of wing sections*. Dover Publications Inc.

Aguiar, P., D. J. L. Brett and N. P. Brandon (2008). "Solid oxide fuell cell/gas turbine hybrid system analysis for high-altitude long-endurance unmanned aerial vehicles". In: *International Journal of Hydrogen Energy*.

Akbari, P. and M. R. Nalim (2009). "Review of recent development in wave rotor combustion technolgy". In: *J. of Propulsion and Power*.

Akbari, P., R. Nalim and N. Mueller (2006). "A review of wave rotor technology and its applications". In: *ASME J. of Engineering for Gas Turbine Power*.

Altman, A. (2000). "A conceptual design method for low speed high altitude long endurance unmanned aerial vehicles". PhD thesis. Cranfield University, Department of Air Vehicle Technology.

Ameyugo, G. (2007). "Distributed propulsion and future aerospace technologies". EngD thesis. Cranfield University, School of Engineering.

Armstrong, M., M. Blackwelder and C. Ross (2014). "Sensitivity of TeDP microgrid systems weight and efficiency to operating voltage". In: *50th AIAA/ASME/SAE/ASEE Joint Propulsion Conference*.

Austin, R. (2010). *Unmanned Aicraft Systems – UAV design, development and deployment*. John Wiley & Sons Ltd.

B

Boggia, S. and A. Jackson (2002). "Some unconventional aero gas turbines using hydrogen fuel". In: *ASME Turbo Expo*. GT-2002-20412.

Boggia, S., A. Jackson and R. Singh (2001). “Unconventional cycles for aero gas turbine engines burning hydrogen”. In: *International Symposium on Air Breathing Engines*. ISABE-2001-1245.

Borer, N. K., M. D. Moore and A. R. Turnbull (2014). “Tradespace exploration of distributed propulsors for advanced on-demand mobility concepts”. In: *14th AIAA Aviation Technology, Integration, and Operations Conference*.

Borhan, H. A. et al. (2009). “Predictive energy management of a power-split hybrid electric vehicle”. In: *Proceedings of the American Control Conference*.

Bradley, M. K. and C. K. Droney (2011). *Subsonic ultra green aircraft research: phase I final report*. Tech. rep. NASA/CR–2011-216847.

Bradley, T. H. et al. (2009). “Energy management for fuel cell powered hybrid electric aircraft”. In: *7th International Energy Conversion Engineering Conference*.

Brahma, A., Y. Guezennec and G. Rizzoni (2000). “Optimal energy management in series hybrid vehicles”. In: *Proceedings of the American Control Conference*.

Brasseur, G. P. et al. (1998). “European scientific assessment of the atmospheric effects of aircraft emissions”. In: *Atmospheric Environment*.

Brenner, M. W. et al. (2012). “Conceptual design framework for blended wing body aircraft”. In: *12th AIAA Aviation Technology, Integration, and Operations (ATIO) Conference and 14th AIAA/ISSM*.

Brewer, G. D. (1991). *Hydrogen aircraft technology*. CRC Press.

Brown, G. V. (2011). “Weights and efficiencies of electric components of a turboelectric aircraft propulsion system”. In: *49th AIAA Aerospace Sciences Meeting including the New Horizons Forum and Aerospace Exposition*.

Bu, F. et al. (2012). “A stand-alone dual stator-winding induction generator variable-frequency AC power system”. In: *IEEE Transactions on Power Electronics*.

Burmeister, W. (2004). *Hydrogen project at Munich airport*. Tech. rep. International Energy Agency.

C

Campanari, S. and P. Iora (2004). “Definition and sensitivity analysis of a finite volume SOFC model for a tubular cell geometry”. In: *Journal of Power Sources*.

Campanari, S. and P. Iora (2005). “Comparison of Finite Volume SOFC Models for the Simulation of a Planar Cell Geometry”. In: *Fuel Cells*.

Castano, S. et al. (2015). “Dynamical modeling procedure of a Li-ion battery pack suitable for real time applications”. In: *Energy Conversion and Management*.

Chan-Chiao, L. et al. (2001). “Energy management strategy for a parallel hybrid electric truck”. In: *Proceedings of the American Control Conference*.

Chau, K. T. and Y. S. Wong (2002). “Overview of power managemnt in hybrid electric vehicles”. In: *Energy conversion and management*.

Chen, M. and G. A. Rincon-Mora (2006). “Accurate electrical battery model capable of predicting runtime and I-V performance”. In: *IEEE Transactions on Energy Conversion*.

Choi, S. and B. V. Sankar (2008). “Gas permeability of various graphite/epoxy composite laminates for cryogenic storage systems”. In: *Composites*.

Choi, S. et al. (2008). “Multifidelity design optimization of low-boom supersonic jets”. In: *Journal of Aircraft*.

Clem, J. R. and A. P. Malozemoff (2010). “Theory of ac loss in power transmission cables with second generation high temperature superconductor wires”. In: *Supercond. Sci. Technol.*

Colozza, A. J. (2002). *Hydrogen storage for aircraft applications overview*. Tech. rep. NASA/CR–2002-211867.

Corchero, G and J. L. Montañes (2005). “An approach to the use of hydrogen for commercial aircraft engines”. In: *Proc IMechE Part G: J Aerospace Engineering*.

Costamagna, P. and K. Honegger (1998). “Modeling of solid oxide heat exchanger intergated stacks and simulation at high fuel utilisation”. In: *Journal of Electrochemical Society*.

Costamagna, P. et al. (2004). “Electrochemical model of the integrated planar solid oxide fuel cell (IP-SOFC)”. In: *Chemical Engineering Journal*.

Cryoplane (2003). *Liquid hydrogen fuelled aircraft – system analysis*. Tech. rep. European Community, Competitive and Sustanaible Growth Programme.

D

Dahl, G. and F. Suttrop (1998). “Engine control and low-NO_x combustion fo rhydrogen fuelled aircraft gas turbines”. In: *Int. J. Hydrogen Energy*.

Daly, M. (2012). *Jane’s all the world’s aircraft: unmanned, 2012 – 2013*. IHS.

Daumling, M. et al. (2000). “Ac loss in superconducting power cables”. In: *Studies of High Temperature Superconductors*.

Davies, K. M. et al. (2015). “Fault behaviour of a superconducting turboelectric distributed propulsion aircraft network, a comprehensive study”. In: *Interna-*

tional Conference on Electrical Systems for Aircraft, Railway, Ship Propulsion and Road Vehicles (ESARS).

De La Cruz Arevalo, M. A. (2015). "Performance assessment of hydrogen fuelled distributed propulsion HALE UAV with a constant volume combustion wave rotor". MSc thesis. Cranfield University, School of Aerospace, Transport and Manufacturing.

Doty, F. D. *Our Transportation Energy Future.*

Doty, F. D. (2004a). *A Realistic Look at Hydrogen Price Projections.*

Doty, F. D. (2004b). *Future Fuels.*

Drela, M. (2006). *QPROP formulation.* `http://web.mit.edu/drela/Public/web/qprop/qprop_theory.pdf`.

Dye, S., A. Kopelove and G. L. Mills (2010). "Integrated and load responsive multilayer insulation". In: *AIP Conf. Proc.*

Dye, S., A. Kopelove and G. L. Mills (2012). "Novel load responsive multilayer insulation with high in-atmosphere and on-orbit thermal performance". In: *Cryogenics.*

E

ESDU (2008). *Equations for calculations of international standard atmosphere and associated off-standard atmospheres.* Tech. rep. ESDU 77022.

F

Falk, K. H. (1943). *Aircraft propeller handbook.* Ronald Press Company.

Felder, J. L., G. V. Brown and H. D. Kim (2011). "Turboelectric distributed propulsion in a hybrid wing body aircraft". In: *ISABE.*

Felder, J. L., M. T. Tong and J. Chu (2012). "Sensitivity of mission energy consumption to turboelectric distributed propulsion design assumptions on the N3-X hybrid wing body aircraft". In: *48th AIAA/ASME/SAE/ASEE Joint Propulsion Conference.*

Felder, J. L. et al. (2011). "An examination of the effect of boundary layer ingestion on turboelectric distributed propulsion systems". In: *49th AIAA Aerospace Sciences Meeting.*

Fielding, J. P. and S. H (2006). "FLAVIIR, an innovative university/industry research program for collaborative research and demonstration of UAV technologies". In: *25th International congress of the aeronautical sciences*.

Freeh, J. E., J. W. Pratt and J Brouwer (2004). "Development of a solid oxide fuel cell gas turbine hybrid system model for aerospace applications". In: ASME Turbo Expo.

Freeman, H. B. (1931). *Comparison of full scale propellers having raf-6 and clark y airfoil sections*. Tech. rep. DTIC document.

G

Gates, T. S., R. W. Grenoble and K. S. Whitley (2004). "Permeability and lifetime durability of polymer matrix composites for cryogenic fuel tanks". In: *AIAA/ASME/ASCE/AHS/ASC Structures, Structural Dynamics, and Material Conference*.

Geng, T. and M. R. Nalim (2004). "Statistical design-of-experiments for wave ejector performance improvement". In: *42nd AIAA Aerospace Sciences Meeting*.

Glaister, D. et al. (2011). "Long term cryogenic storage technologies overview for NASA exploration applications". In: *AIAA Thermophysics Conference*.

Godula-Jopek, A., W. Jehle and J. Wellnitz (2012). *Hydrogen storage technologies – New materials, transport, infrastracture*. John Wiley & Sons Ltd.

Gohardani, A. S. (2011). "Modelling framework of advanced all electrical power and propulsion systems for future aircraft". PhD thesis. Cranfield University, School of Engineering.

Green, J. E. (2008). "Laminar flow control – back to the future". In: *36th AIAA Fluid Dynamics Conference and Exhibition*.

Gruber, C. and R. Wurster (2002). *Hydrogen-fueled buses: the Bavarian Fuel Cell Bus Project*. Tech. rep. International Energy Agency.

Guerreiro, J. F., J. A. Pomilio and T. D. C. Busarello (2013). "Design of a multilevel active power filter for more eletrical airplane variable frequency systems". In: *IEEE Aerospace Conference*.

H

Haglind, F., A. Hasselrot and R. Singh (2006). "Potential of reducing the environmental impact of aviation by using hydrogen, Part I, II and III". In: *The Aeronautical Journal*.

Haldar, P. et al. (2005). "Improving performance of cryogenic power electronics". In: *IEEE Transactions on Applied Superconductivity*.

Hasselgreaves, J. E. (1969). *A correlation of tip-clearance/efficiency measurements on mixed-flow and axial flow turbomachines*. Tech. rep. NEL report no. 423.

Himansu, A. et al. (2006). "Hybrid solid oxide fuel cell gas turbine system design for high altitude long endurance aerospace missions". In: International Conference on Fuel Cell Science.

Howe, D. (1996). "The prediction of aircraft wing mass". In: *Proc IMechE Part G: J Aerospace Engineerings*.

Howe, D. (2000). *Aircraft conceptual design synthesis*. Professional Engineering Publishing.

Howe, D. (2001). "Blended wing body airframe mass prediction". In: *Proc IMechE Part G: J Aerospace Engineerings*.

Hung, J. Y. and L. F. Gonzalez (2012). "Design, simulation and analysis of a parallel hybrid electric propulsion system for unmanned aerial vehicles". In: *28th International Congress of the Aeronautical Science*.

I

IEA (2012). *Key world energy statistics 2012*. International Energy Agency.

Isikveren, A. T. et al. (2014). "Pre-design strategies and sizing techniques for dual-energy aircraft". In: *Aircraft Engineering and Aerospace Technology International Journal*.

J

Jackson, A. (2008). *Hydrogen data*. Email exchange with the International Energy Agency.

Jackson, A. J. B. (2009). "Optimisation of aero and industrial gas turbine design for the environment". PhD thesis. Cranfield University, School of Engineering.

Jameson, A. (1969). "The analysis of propeller-wing interaction". In: *NASA Symposium Proceedings SP-228*.

Jameson, A. (1970). *Analysis of wing slipstream flow interaction*. Tech. rep. NASA CR1630.

Jenkinson, L., P Simpkin and D. Rhodes (1999). *Civil jet aircraft design*. Arnold Publishers.

Jenkinson, L. R. and J. F. Marchman (2003). *Aircraft Design Projects for engineering students*. AIAA Education Series.

Johnson, T. F., D. W. Sleight and R. A. Martin (2013). "Structures and design phase I summary for the NASA composite cryotank technology demonstration project". In: *AIAA/ASME/ASCE/AHS/ASC Structures, Structural Dynamics, and Material Conference*.

Jones, C. E. et al. (2015). "A pre-design sensitivity analysis tool for consideration of full-electric aircraft propulsion electrical power system architecture". In: *International Conference on Electrical Systems for Aircraft, Railway, Ship Propulsion and Road Vehicles (ESARS)*.

Jones, S. M. and G. E Welch (1996). "Performance benefits for wave rotor-topped gas turbine engines". In: *International Gas Turbine and Aeroengine Congress*.

K

Karunarathne, L., J. T. Economou and K. Knowle (2011). "Power and energy management system for fuel cell unmanned aerial vehicle". In: *IMEechE Part G: J of Aerospace*.

Khandelwal, B. et al. (2013). "Hydrogen powered aircraft: the future of air tranport". In: *Progress in Aerospace Sciences*.

Kirner, R. (2014). "An investigation into the benefits of distributed propulsion on advanced aircraft configurations". PhD thesis. Cranfield University, School of Engineering.

Konishi, N. and H. Fujimoto (2014). "Range extension control system for electric airplane with multiple motors by optimization of thrust distribution considering propellers efficiency". In: *Industrial Electronics Society, IECON 2014 – 40th Annual Conference of the IEEE*.

Koster, J. N., S. Balaban and D. R. Hillery (2011). "Rapid, international design and test of a hybrid-powered blended wing body unmanned aerial vehicle". In: *11th AIAA Aviation Technology, Integration, and Operations (ATIO) Conference*.

Kyprianidis, K. G. and A. M. Rolt (2014). "On the optimization of a geared fan intercooled core engine design". In: *Journal of Engineering for Gas Turbines and Power*.

L

Lakshminarayana, B. (1970). "Methods for predicting the tip clearance effects in axial flow turbomachinery". In: *Journal of Basic Engineering*.

Lan, C. E. and J. Roskam (1980). *Aircraft aerodynamics and performance*. Roskam aviation and engineering corporation.

Larminie, J. and A. Dicks (2003). *Fuel Cell Systems Explained*. John Wiley and Sons Ltd.

Lawson, C. (2012). "Aircraft performance, lecture notes". Cranfield University.

Le Boulaire, T. (2014). "Distributed propulsion hydrogen-fuelled UAVs – gas turbine hybrid cycles performance assessment: integration of solar energy". MSc thesis. Cranfield University, School of Engineering.

Lefebvre, A. H. and D. R. Ballal (2010). *Gas turbine combustion, alternative fuels and emissions*. CRC Press.

Leifsson, L. et al. (2013). "Multidisciplinary design optimization of a blended wing body transport aircraft with distributed propulsion". In: *Journal of Aerospace Science and Technology*.

Li, H., P. Akbari and M. R. Nalim (2007). "Air standard thermodynamic analysis of gas turbine engines using wave rotor combustion". In: *43rd AIAA/ASME/SAE/ASEE Joint Propulsion Conference*.

Li, Y. et al. (2009). "The capacity optimization for the static excitation controller of the dual-stator-winding induction generator operating in a wide speed range". In: *IEEE Transactions on Industrial Electronics*.

Liebeck, R. H. (2004). "Design of Blended Wing Body Subsonic Transport". In: *Journal of Aircraft*.

Lucintel (2011). *Growth opportunity in global UAV market*. Lucintel Brief, Presentation.

Lukaczyk, T. et al. (2015). “SUAVE an open source environment for multi-fidelity conceptual vehicle design”. In: *16th AIAA/ISSMO Multidisciplinary analysis and optimization conference*.

Luongo, C. A. et al. (2009). “Next generation more-electric aircraft: a potential application for HTS superconductors”. In: *IEEE Transaction on Applied Superconductivity*.

M

Maack, M. H. and T. H. Schucan (2006). *Ecological City Transport System*. Tech. rep. International Energy Agency.

Maniaci, D. C. (2008). “Relative Performance of a liquid hydrogen-fueled commercial transport”. In: *AIAA Aerospace Sciences Meeting and Exhibit*.

Marquart, S. et al. (2005). “An upgraded estimate of the radiative forcing of cryoplane contrails”. In: *Meteorologische Zeitschrift*.

Mastropasqua, L. (2014). “Modelling of SOFC for performance simulation of advanced power cycles”. MSc thesis. Cranfield University, School of Engineering.

Maughmer, M. D. and D. M. Somers (1989). “Design and experimental results for a high-altitude, long-endurance airfoil”. In: *J. of Aircraft*.

Mavris, D. and C. Perullo (2014). *A modelling and simulation framework for vehicle sizing of turboelectric distributed propulsion and hybrid-electric architectures*. Disruptive Green Propulsion Technologies - Beyond The Competitive Horizon London Conference, Presentation.

Mills, G. L., B. Buchholtz and A. Olsen (2012). “Design, fabrication and testing of a liquid hydrogen fuel tank for long duration aircraft”. In: *AIP Conf. Proc.*

Moir, I. (1998). “The all-electric aircraft – major challanges”. In: *IEEE Colloquium on All Electric Aircraft*.

Moren, D. A. and M. A. Hoffman (2005). “Clarifying the Butler-Volmer equation and related approximations for calculating activation losses in solid oxide fuel cell models”. In: *Journal of Power Sources*.

Morring, F. (2013). “NASA sees potential in composite cryotank”. In: *Aviaiton Week*.

Morris, S. J. (1979). *Performance estimation of highly loaded eight-blade propeller combined with an advanced technology turboshaft engine*. Tech. rep. NASA TM80075.

Mourouzidis, C. (2015). *Axial turbomachinery polytropic efficiency for the 2025-2035 timeframe*. Private conversation.

N

Nalim, M. R. (2003). US Patent no. 2003/0079713.

Nickol, C. L. et al. (2007). *High Altitude Long Endurance UAV Analysis of Alternatives and Technology Requirments Development*. Tech. rep. NASA/TP-2007-214861.

Noji, H. (2011). "AC losses in multilayer power transmission cables comprised of YBCO tapes". In: *Physica C*.

Noppel, F. G. (2007). "Contrail and cirrus cloud avoidance technology". PhD thesis. Cranfield University, School of Engineering.

Noppel, F. G. (2011). "Comparison of unconventional aero engine architectures". PhD thesis. Cranfield University, School of Engineering.

O

Oh, H. W., E. S. Yoon and M. K. Chung (1997). "An optimum set of loss models for performance prediction of centrifugal compressors". In: *IMechE Proceedings*.

Osamura, K. et al. (2011). "Prototype of SC inverter". In: *IEEE Transactions on Applied Superconductivity*.

P

Palethorpe, B. (2008). *Very long endurance propulsion system – a fuel cell based power generation system for a high altitude and long endurance UAV*. Tech. rep. Rolls-Royce plc.

Patterson, M. D. and M. J. Daskilewicz (2014). "Conceptual design of electric aircraft with distributed propellers: multidisciplinary analysis needs and aerodynamic modeling development". In: *52nd AIAA Aerospace Sciences Meeting*.

Patterson, M. D. and B. J. German (2014). "Wing aerodynamic analysis incorportating one-way interaction with distribtued propellers". In: *14th AIAA Aviation Technology, Integration, and Operations Conference*.

Patterson, M. D. and B. J. German (2015). "Simplified aerodynamics models to predict the effects of upstream propellers on wing lift". In: *53rd AIAA Aerospace Sciences Meeting*.

Paxson, D. E. and T. A. Kaemming (2012). "Fouundational performance analysis of pressure gain combustion thermodynamic benefits for gas turbine". In: *50th AIAA Aerospace Sciences Meeting*.

Payzer, R. J. and S. W. Renninger (1979). "Hydrogen fuelled high bypass turbofans in subsonic aircraft". In: *International Symposium on Hydrogen in Air Transportation*.

Poling, B. E., J. M. Prausnitz and J. P. O'Connel (2001). *The properties gases and liquids, fifth edition*. McGraw Hill.

Pornet, C. et al. (2014a). "Integrated fuel-battery hybrid for a narrow-body sized transport aircraft". In: *Aircraft Engineering and Aerospace Technology International Journal*.

Pornet, C. et al. (2014b). "Methodology for sizing and performance assessment of hybrid energy aircraft". In: *Journal of Aircraft*.

Pratt, J. W. et al. (2011). *Proton Exchange Membrane Fuel Cells for Electrical Power Generation On-Board Commercial Aircraft*. Tech. rep. SAND2011-3119. Sandia National Laboratories.

R

Ramage, M. P. et al. (2004). *The hydrogen economy*. National Academies Press.

Rapp, D. (2007). *Transporting hydrogen to the moon or mars and storing it there*. `http://www.spaceclimate.net/Hydrogen.25.web.pdf`.

Raymer, D. P. (1992). *Aircraft design: a conceptual approach*. AIAA Education Series.

Righi, M. (2014). "Performance analysis of hybrid cycles using unsteady flow devices for a hydrogen fuelled distributed propulsion HALE UAV". MSc thesis. Cranfield University, School of Engineering.

Risch, T. et al. (2009). "X-48B Flight Test Progress Overview". In: *47th AIAA Aerospace Sciences Meeting*.

Robinson, C. J. (1982). *A review of the effect of rotor tip clearance on axial compressor performance*. Tech. rep. RCR 90830.

Roland Berger (2013). *Top management issues radar 2013, Aerospace and Defence industry*. Roland Berger Strategy Consultants Survey.

Romeo, G., G. Frulla and E. Cestino (2006). "Design of a high-altitude long-endurance solar-powered unmanned air vehicle for multi-payload and operations". In: *Proc IMechE Part G: J Aerospace Engineering*.

Rosero, J. A. et al. (2007). “Moving towards a More Electric Aircraft”. In: *IEEE A&E systems magazine*.

Roskam, J. (1985). *Airplane design, part V: component weight estimation*. Roskam aviation and engineering corporation.

Roth, B. and R. Giffin III (2010). “Fuel cell hybrid propulsion challenges and opportunities for commercial aviation”. In: 46th AIAA/ASME/SAE/ASEE Joint Propulsion Conference.

S

D. A, S., S. Lieblein and R. P. Krebs (1971). *Empirical Expressions for Estimating Length and Weight of Axial-Flow Components of VTOL Powerplants*. Tech. rep. NASA-TM-X-2406.

Saravanamutoo, H. I. H. (1987). “Modern turboprop engines”. In: *Prog. Aerospace Sci.*

Schiltgen, B. et al. (2012). “Benefits and concerns of hybrid electric distributed propulsion with conventional electric machines”. In: *48th AIAA/ASME/SAE/ASEE Joint Propulsion Conference*.

Schmidt, M. J. P. (1985). “Blade tip clearance effects on an axial flow compressor rotor”. PhD thesis. Cranfield Institute of Technology.

Selimovic, A. (2002). “Modelling of solid oxide fuel cells applied to the anaysis of integrated systems with gas turbines”. PhD thesis. Lund Institute of Technology.

Selimovic, A. and J. Palsson (2002). “Networked solid oxide fuel cell stacks combined with a gas turbine”. In: *Journal of Power Sources*.

Serrao, L., S. Onori and G. Rizzoni (2011). “A comparative analysis of energy management strategies for hybrid electric vehicles”. In: *Journal of dynamic systems, measurement, and control*.

Simbolotti, G. (2007). *Hydrogen production and distribution – energy technology essentials*. Tech. rep. International Energy Agency.

Smedresman, A., D. Yeo and W. Shyy (2011). “Design, fabrication, analysis, and testing of a micro air vehicle propeller”. In: *29th AIAA Applied Aerodynamics Conference*.

Smith, B. D et al. (2012). “Scaling study of wave rotor turbo normalization for internal combustion engine”. In: *48th AIAA/ASME/SAE/ASEE Joint Propulsion Conference*.

Sosunov, V. and V. Orlov (1990). “Experimental turbofan using liquid hydrogenn and liquid natural gas as fuel”. In: *AIAA/SAE/ASME/ASEE Joint Propulsion Conference*.

Steffen, C. J., J. E. Freeh and L. M. Larosiliere (2005). “Solid oxide fuel cell gas turbine hybrid cycle technology for auxiliary aerospace power”. In: ASME Turbo Expo.

Steiner, H. et al. (2014). “Optimum nuber of engines for transport aircraft employing electrically powered distributed propulsion”. In: *CAES Aeronautical Journal*.

Stoll, A. M. (2015). “Comparison of CFD and experimental results of the LEAPTech distributed electric propulsion blown wing”. In: *15th AIAA Aviation Technology, Integration, and Operations Conference*.

Stoll, A. M. et al. (2014). “Drag reduction through distributed electric propulsion”. In: *14th AIAA Aviation Technology, Integration, and Operations Conference*.

Sullivan, R. M. et al. (2006). *Engineering analysis studies for preliminary design of lightweight cryogenic hydrogen tanks in UAV applicatons*. Tech. rep. NASA/TP–2006-214094.

Svensson, F. (2005). “Potential of reducing the environmental impact of civil subsonic aviation by using liquid hydrogen”. PhD thesis. Cranfield University, School of Engineering.

T

Tang, H. et al. (2012). “High altitude low Reynolds number effect on the matching performance of a turbofan engine”. In: *Proc IMechE Part G: J Aerospace Engineering*.

Tenney, D. R. (2008). *Evaluation of advanced composite structures technologies for application to NASA’s vision for space exploration*. Tech. rep. NASA.

Tenney, D. R. et al. (2009). *NASA composite materials development: lessons learned and future challanges*. Tech. rep. NASA.

Thiow Yong Dennis, L. (2007). “A methodological approach for conducting a business case analysis of the global observer joint capability tehncology demonstration”. MSc thesis. Naval Postraduate School.

Thompson, D. J., J. Feys and M. D. Filewich (2011). “The design and construction of a blended wing body UAV”. In: *49th AIAA Aerospace Sciences Meeting including the New Horizons Forum and Aerospace Exposition*.

Torenbeek, E. (1976). *Synthesis of Subsonic Airplane Design*. Delft University Press.

V

van Zon, N. (2012). “Liquid hydrogen powered commercial aircraft”. In: *Space for Innovation, Technical University of Delft.*

Velicki, A. and D. A. Hansen (2011). *Hydrogen fuelled blended wing body ring tank.* Patent, the Boeing Company.

Verstraete, D. et al. (2010). “Hydrogen fuel tanks for subsonic transport aircraft”. In: *Int. J. of Hydrogen Energy.*

Verstraete, D. (2009). “The potential of liquid hydrogen for long range aircraft propulsion”. PhD thesis. Cranfield University, School of Engineering.

Vicker, J. (2013). *NASA Composite cryotank project – Structures for launch vehicles.* Composite Australia Conference, Presentation.

Vratny, P. C. et al. (2013). “Battery pack modelling methods for universally electric aircraft”. In: *4th CEAS Air and Space Conference.*

Vysotsky, V. S. et al. (2013). “Hybrid energy transfer line with liquid hydrogen and superconducting MgB_2 cable – first experimental proof of concept”. In: *IEEE Transaction on Applied Superconductivity.*

W

Wang, D. et al. (2005). “A novel stand-alone dual stator-winding induction generator with static excitation regulator”. In: *IEEE Transactions on Energy Conversion.*

Ward, C. M. and R. J. Miller (2012). “Performance analysis of an ejector enhanced pressure gain combustion gas turbine”. In: *50th AIAA Aerospace Sciences Meeting.*

Waters, D. F. and C. P. Cadou (2003). “Engine-integrated solid oxide fuel cells for efficient electrical power generation on aircraft”. In: 52nd AIAA Aerospace Sciences Meeting.

Weber, K. F. and P. H. Snyder (1998). “Wave rotor to high pressure turbine transition duct flow analysis”. In: *34th AIAA/ASME/SAE/ASEE Joint Propulsion Conference.*

Welch, G. E., S. M. Jones and D. E. Paxson (1997). “Wave-rotor-enhanced gas turbine engines”. In: *J. of Eng. Gas Turbine Power.*

Welch, G. E., J. W. Slater and J. Wilson (2007). “Wave rotor transition duct experiment”. In: *45th AIAA Aerospace Sciences Meeting.*

Westenberger, A. (2003). “Hydrogen fuelled aircraft”. In: AIAA/ICAS International Air, Spance Symposium and Exposition: The Next 100 Years.

Wheeler, P. W. et al. (2012). “An overview of the more electric aircraft”. In: *Proc IMechE Part G: J Aerospace Engineering*.

Williams, D. (2011). “Propulsion system performance and integration, volume 2 – airframe engine integration”. Cranfield University.

Wilson, J. and D. E. Paxson (1996). “Optimization of wave rotors for use as gas turbine engine topping cycles”. In: *Journal of Propulsion and Power*.

Wilson, J. R. (2013). “UAV Roundup 2013”. In: *Aerospace America (an AIAA journal)*.

X

Xian-Zhong, G. et al. (2013). “Energy management strategy for solar-powered high altitude long endurance aircraft”. In: *Energy conversion and management*.

Y

Yu, Y. H. (2000). “Rotor blade-vortex interaction”. In: *Progress in Aerospace Science*.

Yuan, W. (2011). *Second-generation high temperature superconductors coils and their applications for energy storage*. Springer-Verlag London Limited.

Z

Zachos, P. K. (2014). *Engine relight challenges*. Private conversation.